Investigation of the Phase Space Distribution of Electron Bunches at the FLASH-Linac Using a Transverse Deflecting Structure

Dissertation
zur Erlangung des Doktorgrades
des Fachbereichs Physik
der Universität Hamburg

vorgelegt von

Michael Röhrs
aus Buchholz

Hamburg
2008

Gutachter der Dissertation:	Prof. Dr. Peter Schmüser Prof. Dr. Gerhard Mack
Gutachter der Disputation	Prof. Dr. Peter Schmüser Prof. Dr. Shaukat Khan
Datum der Disputation	6. Mai 2008
Vorsitzende des Prüfungsausschusses	Prof. Dr. Caren Hagner
Vorsitzender des Promotionsausschusses	Prof. Dr. Joachim Bartels
Dekan der Fakultät für Mathematik, Informatik und Naturwissenschaften	Prof. Dr. Arno Frühwald

Abstract

The operation of a high-gain free-electron laser (FEL) puts stringent demands on the peak current, transverse emittance and energy spread of the electron beam. At the Free Electron Laser in Hamburg (FLASH), a transverse deflecting structure (TDS) has been installed to investigate these electron beam parameters. The radio-frequency electromagnetic field in the TDS is utilized to deflect the beam electrons vertically as a function of time so that the charge distribution in the longitudinal-horizontal plane can be imaged with optical transition radiation screens. Using this technique, the single-bunch current profile was measured with an unprecedented resolution of about 10 μm (30 fs) under FEL operating conditions. A precise single-shot measurement of the energy distribution along a bunch was accomplished by using the TDS in combination with an energy spectrometer. Appropriate variations of the focal strengths of quadrupole magnets allowed for the measurement of the horizontal emittance as a function of the longitudinal position within a bunch (slice emittance) with a longitudinal resolution in the order of 10 μm. While the slice emittance in the peak current region was measured to be significantly larger than deduced from properties of the FEL radiation, tomographic methods revealed a bunch region of small horizontal emittance and high current. The observed increase in slice emittance in the peak current region was found to be caused by coherent emission of synchrotron radiation within bending magnets.

Zusammenfassung

Der Betrieb eines hochverstärkenden Freie-Elektronen Lasers (FEL) stellt hohe Anforderungen an Peakstrom, transversale Emittanz und Energieschärfe des Elektronenstrahls. Zur Untersuchung dieser Strahlparameter ist am Freie-Elektronen Laser in Hamburg (FLASH) eine transversal ablenkende Wanderwellenstruktur (TDS) installiert worden. Das hochfrequente elektromagnetische Feld in der TDS wird genutzt, um die Elektronen vertikal in linearer Abhängigkeit von ihrer Ankunftszeit abzulenken, so dass die Ladungsverteilung in der longitudinal-horizontalen Ebene durch Leuchtschirme abgebildet werden kann. Auf diese Weise konnte das Stromprofil einzelner Elektronenpakete unter FEL-Betriebsbedingungen mit einer bisher unerreichten Auflösung von etwa 10 μm (30 fs) gemessen werden. Eine präzise Messung der Energieverteilung entlang einzelner Elektronenpakete wurde durch die kombinierte Nutzung der TDS und eines Energiespektrometers erreicht. Eine geeignete Variation der Fokussierungsstärke von Quadrupolmagneten erlaubte die Messung der horizontalen Emittanz in Abhängigkeit von der longitudinalen Position (Scheibenemittanz) mit einer longitudinalen Auflösung von etwa 10 μm. Während im Bereich des maximalen Stroms eine deutlich größere Scheibenemittanz gemessen wurde, als aus den Eigenschaften der FEL-Strahlung hervorgeht, konnte durch die Anwendung tomographischer Methoden ein Bereich im Elektronenpaket mit kleiner horizontaler Emittanz und hohem Strom gefunden werden. Der beobachtete Anstieg der Scheibenemittanz im Bereich des maximalen Stroms konnte auf kohärente Emission von Synchrotronstrahlung in Dipolmagneten zurückgeführt werden.

Contents

Chapter 1

Introduction

The electromagnetic radiation emitted by ultra-relativistic electrons in magnetic fields (synchrotron radiation) has become a standard diagnostic tool in a variety of fields of research, both basic and applied research in the chemical, materials, biotechnology and pharmaceutical industries. High intensities at short wavelengths down to the X-ray regime allow researchers to probe the structure of a wide range of samples with a resolution down to the level of atoms and molecules. The radiation generated by bunched electron beams has a temporal structure on the scale of nanoseconds and below, allowing for observation of processes taking place on such time-scales.

While experiments with synchrotron radiation were initially carried out parasitically at circular accelerators used for high-energy or nuclear physics, numerous projects worldwide are now dedicated solely to the delivery of high-quality synchrotron radiation. So-called third generation light sources are electron storage rings augmented with insertion devices (wiggler and undulator magnets) in which magnetic fields of alternating polarity induce intense radiation pulses. Recent advances in accelerator and undulator magnet technology nowadays allow for the construction of free electron lasers (FELs) based on self-amplified spontaneous emission (SASE). These are often called fourth generation light sources. For many experiments, the relevant figure of merit is the brilliance or spectral brightness of the radiation beam. SASE FELs achieve a peak brilliance which exceeds third generation synchrotron radiation sources by several orders of magnitude (see Fig. 1.1).

The requirements placed on the driving electron beam in fourth generation light sources are extremely demanding and can currently only

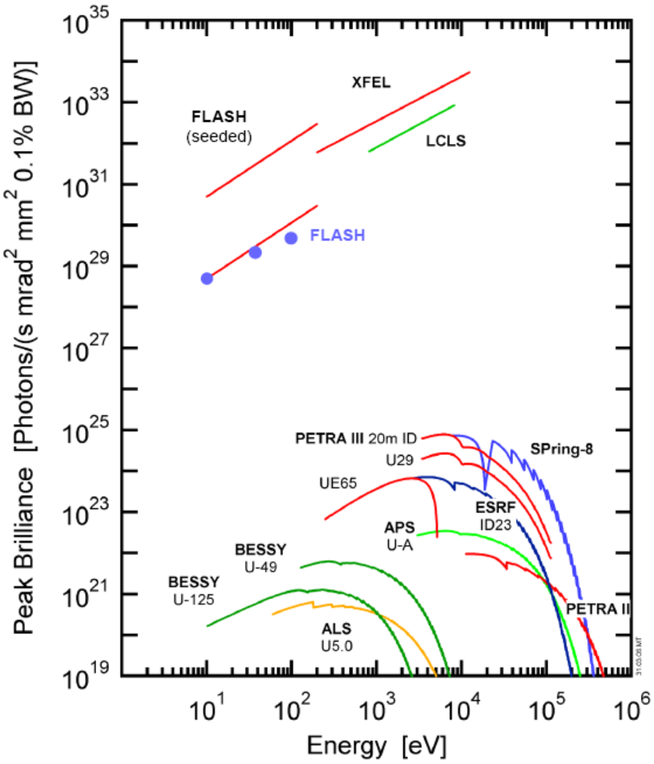

Figure 1.1: Peak brilliance of SASE FELs versus 3rd generation Synchrotron Radiation light sources [1]. Blue spots indicate the experimental performance of the Free-Electron Laser in Hamburg (FLASH). The brilliance is defined as the number of photons in 10^{-3} ω *frequency bandwidth (BW) centered around the angular frequency* $\omega =$ *energy*/$\hbar$ *emitted per second into a solid angle of 1* $\mathrm{mrad}^2\cdot\mathrm{mm}^2$.

be achieved in linear accelerators (linacs) with high-brightness electron sources. During the passage through a linac of some hundreds of meters, or even several kilometers length, the electron beam is subject to disturbances which need to be controlled. Accurate diagnostic tools for probing the electron beam are therefore essential for operating and optimizing FELs. In contrast to storage rings, where the particle beam reaches a kind of equilibrium state after many turns, significant fluctuations of beam parameters from shot-to-shot in linacs necessitate diagnostic devices with single-bunch resolution. Furthermore, at current machines like the Free-Electron Laser in Hamburg (FLASH), the requirements for the electron beam can only be achieved within a small longitudinal section of each electron bunch comprising about 15 % of the total bunch charge[1]. Probing this

---

[1] So-called higher-harmonic RF structures allow to circumvent this problem. A corresponding upgrade of FLASH with a third-harmonic structure is planned.

lasing bunch section requires a time-resolution on the femtosecond scale, making accurate beam diagnostics a challenge to develop.

Transverse deflecting structures, which were developed at SLAC in the 1960s for separating charged secondary particles of different masses, are very powerful electron beam diagnostic tools. The high-frequency electromagnetic field within a transverse deflecting structure (TDS) deflects the electrons of a passing bunch transversely as a function of time so that the longitudinal profile of a bunch can be viewed by a screen placed in the beamline. In combination with tomographic reconstruction techniques, a TDS allows for the determination of the charge density distribution of a bunch in phase space with unprecedented accuracy. For this reason, in many current FEL projects, a TDS is installed in the driving accelerator. The first operational experience with a TDS in a free electron laser has been gained at the FLASH facility at DESY. In this thesis, the first TDS experimental results obtained under FEL operating conditions in the FLASH facility are presented. These results include the single-bunch longitudinal charge density profile, charge density distribution in longitudinal phase space, and density distribution in horizontal phase space as a function of longitudinal position within the bunch.

In the remainder of the introduction, the working principle of FELs is briefly reviewed. Emphasis is put on the impact of electron beam parameters on the lasing process. In chapter 2, the dynamics of electron bunches in linear accelerators is described and concepts required in the remainder of the thesis are introduced. Chapter 3 deals with methods for analyzing the electron distribution in transverse phase space, in particular the tomographic methods that were applied. Details of the FLASH facility, the TDS and the experimental setup used for the measurements can be found in chapters 4 and 5. Experimental results collected during most basic linac operational conditions are presented in chapter 6, while chapter 7 presents experimental results under FEL operating conditions. A comparison of the experimental results with those of numerical simulations is given in chapter 8.

1.1 The principle of Free-Electron Lasers

This section is meant to provide an intuitive understanding of the physics of FELs, with a focus on the impact of electron beam parameters on the FEL process. Details and derivations of the presented formulas can be found in references [2, 3, 4].

Undulator magnets

FEL radiation is generated in undulator magnets. Undulator magnets consist of a periodic arrangement of permanent magnets with alternating polarity (Fig. 1.2). In planar undulator magnets, the magnetic field B in the symmetry plane $y = 0$ is approximately a harmonic field given by

$$B = B_0 \sin(k_u z) \cdot e_y, \tag{1.1}$$

where B_0 is the peak magnetic field, e_y the unit vector in vertical direction and $k_u = 2\pi/\lambda_u$ with the period λ_u of the magnet arrangement. Electrons passing an undulator magnet along the undulator axis ($x = 0$, $y = 0$) are forced to move on an oscillating path in the symmetry-plane $y = 0$. Neglecting the longitudinal force due to the horizontal velocity components, the trajectory of an electron with energy[2] $\gamma_r m_e c^2$ and velocity $\beta_r c$ can be expressed by

$$x(z) = \frac{K}{\beta_r \gamma_r k_u} \cdot \sin(k_u z) \tag{1.2}$$

with the dimensionless undulator parameter

$$K = \frac{e B_0}{m_e c\, k_u}. \tag{1.3}$$

Here, it is assumed that the particle trajectory fulfills the initial conditions $x(0) = 0$ and $x'(0) = dx/dz(0) = K/(\beta_r \gamma_r)$. For ultra-relativistic particles with $\beta_r \approx 1$, the maximum horizontal offset x_{max} and the maximum angle x'_{max} with respect to the undulator axis are then given by

$$x_{max} \approx \frac{K}{\gamma_r k_u} = \frac{\lambda_u K}{2\pi \gamma_r} \tag{1.4}$$

$$x'_{max} \approx \frac{K}{\gamma_r}. \tag{1.5}$$

---

[2] The index r for “relativistic” is used to distinguish the relativistic parameters β_r and γ_r from parameters related to the design of accelerators introduced in chapter 2.

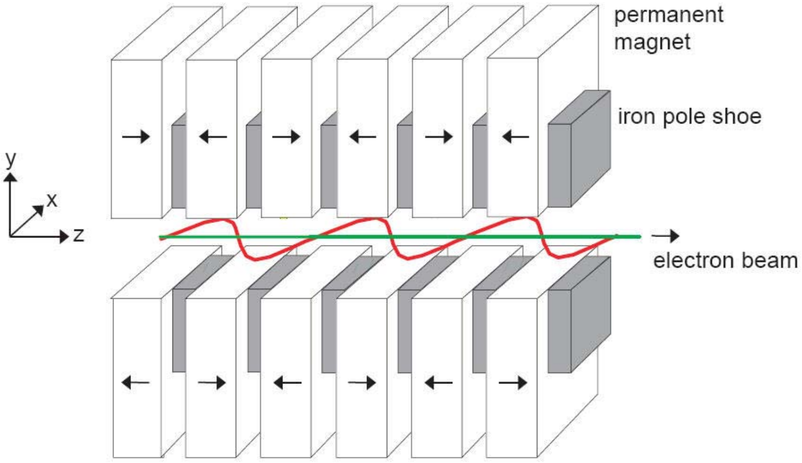

Figure 1.2: Schematic of a planar undulator magnet and the oscillating trajectory of a passing electron beam. A sine-like vertical magnetic field is generated by a periodic arrangement of permanent magnets of alternating polarity installed between iron pole shoes [2].

Owing to the sine-like particle trajectory, the longitudinal particle velocity component v_z is a periodic function of z with a period $\lambda_u/2$. The mean or effective longitudinal velocity $\bar{v}_z$ is given by

$$\bar{v}_z = \left(1 - \frac{1}{2\gamma_r^2}\left(1 + \frac{K^2}{2}\right)\right) c \equiv \bar{\beta}_r c. \tag{1.6}$$

The synchrotron radiation emitted by a relativistic electron moving along an undulator magnet is concentrated in a narrow cone of opening angle $1/\gamma_r$, which is centered around the instantaneous tangent to the particle trajectory [3]. In case the effective longitudinal velocity $\bar{v}_z$ is only slightly smaller than the speed of light, which is the case for large γ_r and small K (cf. Eq. (1.6)), the radiation detected by an observer at an angle $\Theta \ll 1$ with respect to the undulator axis is a superposition of the contributions from several oscillations along the trajectory. A coherent superposition is obtained at a wavelength λ_l equal to the distance an electron falls behind per period λ_u. This distance is determined by $\bar{v}_z$ (Eq. (1.6)) and the angle Θ, and can approximately be expressed by

$$\lambda_l \approx \frac{\lambda_u}{2\gamma_r^2}\left(1 + \frac{K^2}{2} + \gamma_r^2\Theta^2\right). \tag{1.7}$$

The overlap of the electromagnetic fields generated along the trajectory increases with decreasing angle x'_{max} of the electron trajectory. After a sufficiently large number of periods λ_u, the continuous spectrum of synchrotron radiation becomes sharply peaked at the wavelength λ_l and higher harmonics[3] due to interference in case

$$x'_{max} \lesssim \frac{1}{\gamma_r}. \tag{1.8}$$

According to Eq. (1.5) this is equivalent to $K \lesssim 1$, which is a defining property of undulator magnets. The undulator parameter of the magnets used at FLASH is $K = 1.23$ and the period $\lambda_u = 27$ mm.

Power amplification

Undulator radiation is linearly polarized with the electric field vector in the plane of the sine-like particle trajectory. As a consequence, there is an energy exchange between an electron and a co-moving radiation field. The rate of change of the particle energy E is given by

$$\frac{dE}{dt} = -ev_x(t)\mathcal{E}_x(t), \tag{1.9}$$

where $\mathcal{E}_x(t)$ is the electric field and $v_x(t)$ the horizontal velocity component of the particle. A sustained energy transfer along the undulator is obtained if the electric field $\mathcal{E}_x$ and the horizontal velocity component v_x oscillate synchronously, which is the case if condition (1.10) is fulfilled on the undulator axis:

$$\lambda_l \approx \frac{\lambda_u}{2\gamma_r^2}\left(1 + \frac{K^2}{2}\right). \tag{1.10}$$

Given a plane electromagnetic wave with wavelength λ_l (radiation beam), this relation imposes a condition on the particle energy. The energy fulfilling condition (1.10) for a given wavelength λ_l will be called reference energy. Due to the energy transfer between an electron and a co-moving radiation beam, an electron having initially the reference energy will obtain a slightly detuned energy, which in turn changes the effective longitudinal velocity according to Eq. (1.6) and thus the rate of energy change. This

---

[3] Higher harmonics occur due to deviations of the trajectory from the sine-like shape. Due to symmetry-properties of these deviations only odd higher harmonics are possible.

interdependence of energy and rate of energy change leads to an oscillation in particle energy as well as effective longitudinal velocity along the undulator magnet, which is the basis for FELs.

The electrons of a bunch with a length $\sigma_z \gg \lambda_l$ will partly gain and partly loose energy due to the interaction with a radiation beam, depending on the difference between the phase of the horizontal oscillation and the phase of the electric field of the radiation beam. It can be shown, however, that in case the mean energy of the electron bunch is slightly above the reference energy, energy is effectively transferred to the electromagnetic field. This amplification effect is utilized in so-called low-gain FELs, in which the radiation is produced in a short undulator magnet and stored in an optical cavity comprising the undulator magnet. Electron bunches are repeatedly injected into the undulator in synchronism with the radiation pulse so the radiation beam and the electron beam spatially overlap. The gain in intensity of the radiation that can be reached is in the order of a few percent per undulator passage, and becomes very large after a sufficient number of turns. Low-gain FELs are suited for wavelengths in the infrared and visible regime, for which mirrors with high reflectivity that are required for an optical cavity are available. They are typically used in conjunction with electron storage rings or energy recovery linacs.

In so-called high-gain FELs, each radiation pulse is generated by a single passage of an electron bunch through a long undulator magnet. Along the magnet, the oscillation in effective longitudinal velocity induced by a co-moving radiation beam leads to a periodic modulation of the particle density within the bunch with a period λ_l (microbunching). The modulation gives rise to stimulated emission, which in turn amplifies the density modulation. This process leads to an exponential growth in radiation power $P \propto exp(z/L_g)$ at the fundamental wavelength λ_l and higher harmonics[4]. Here, L_g is called the power gain length, which is determined by properties of the undulator and the electron beam. The growth in radiation power approaches a saturated regime after typically about twenty gain lengths (saturation length). Saturation occurs since the emission of radiation leads to a decrease in particle energy and an increase in energy spread, both impeding the FEL process. Furthermore, repulsive Coulomb forces counteract the microbunching process.

---

[4] Only odd higher harmonics are amplified, see e.g. [2].

High-gain FELs principally allow an operation at wavelengths down to the hard X-ray regime, since optical cavities are not needed. They can be driven by a so-called seed laser, which provides an initial electromagnetic wave with a well-defined wavelength which is then amplified.

In SASE FELs, the amplification process develops from spontaneous undulator radiation of the electron beam. The radiation wavelength (fundamental harmonic) of SASE FELs is determined by the particle energy and can thus be tuned by changing the electron beam energy. Temporally, the radiation is a superposition of wave trains of a certain coherence length, randomly distributed over the length of an electron bunch. Typically, the bunch length is such that there are a few coherence regions or “longitudinal modes” in the radiation.

1.2 Requirements on the electron beam in high-gain free-electron lasers

High-gain FELs put stringent requirements on the driving electron beam. Adverse beam properties lead to an increase in gain length so a saturated regime may eventually not be reached within the finite length of the undulator magnet. For a mono-energetic beam with design energy, an approximative one-dimensional (the transverse extension of the beam is neglected) analytical treatment yields the gain length

$$L_{g0} \propto \gamma_r n_e^{-1/3} \tag{1.11}$$

where n_e is the electron density. By including the effects of energy spread, transverse size and transverse divergence of the electron beam, the gain length $L_g = \chi L_{g0}$ is increased by a factor $\chi > 1$ compared to this ideal case, as will be discussed in more detail below. The dependence on γ_r in Eq. (1.11) shows that in order to reach saturation within an undulator magnet of reasonable length, the requirements on the beam become the more demanding the higher the particle energy.

In case of a beam with non-vanishing energy spread, only the particles within a narrow energy window contribute constructively to the FEL gain process. The influence of a non-vanishing energy spread can be determined analytically within the framework of a one-dimensional approximation. It is convenient to express the energy spread in terms of the dimensionless parameter

$$\rho_{FEL} = \frac{1}{4\pi\sqrt{3}} \frac{\lambda_u}{L_{g0}}, \tag{1.12}$$

which is called FEL parameter because of its fundamental importance. An RMS energy spread of $\sigma_E/E = 0.5\rho_{FEL}$ leads to an increase in gain length of $L_g/L_{g0} \approx 1.25$ with L_{g0} the gain length of a monoenergetic beam, which is conventionally considered as upper limit for a tolerable increase in gain length.

A transverse beam divergence[5] $\sigma_{x'} = \sqrt{\langle x'^2 \rangle}$ with $x' = dx/dz$ reduces the mean effective longitudinal particle velocity $\langle \bar{v}_z \rangle$. Concerning the synchronism of particle oscillation and electromagnetic wave, a beam divergence is thus equivalent to an energy spread. By demanding the equivalent energy spread to be smaller than $0.5\rho_{FEL}$ as above, one obtains the condition

$$\sigma_{x'}^2 < \frac{\rho_{FEL}}{2\gamma_r^2}. \tag{1.13}$$

A corresponding condition is demanded for the divergence $\sigma_{y'}$ in vertical direction.

The transverse size $\sigma_x = \sqrt{\langle x^2 \rangle}$ affects the FEL process in two ways. From the relation $L_{g0} \propto n_e^{-1/3}$ (cf. Eq. (1.11)) follows $L_{g0} \propto \sigma_x^{2/3}$. Thus a small transverse beam size appears to be preferable. However, a small transverse beam size is accompanied by strong diffraction effects of the radiation beam, which reduce the overlap of radiation and electron beam. The transverse RMS size of the radiation beam increases by a factor of two after a distance L_R called Rayleigh length, which depends on the transverse size of the beam according to

$$L_R = \frac{4\pi\sigma_x^2}{\lambda_l}. \tag{1.14}$$

A Rayleigh length smaller than the ideal gain length L_{g0} leads to a significant increase of the true gain length L_g. On the other hand, if the ideal gain length is much smaller than the Rayleigh length, the power gain is hardly hampered by diffraction, since the power gain in the center of the radiation beam over-compensates the losses due to diffraction (gain guiding). Given L_{g0}, this means that the transverse size of the electron beam

---

[5] It is assumed that $\langle x' \rangle = 0$ and $\langle x \rangle = 0$.

has to be chosen sufficiently large, which is in contrast to the requirement mentioned above. A choice of a Rayleigh length of $L_R \approx 2L_{g0}$ is generally considered to be a reasonable compromise. Using Eqs. (1.12) and (1.14), this yields the condition

$$\sigma_x^2 \approx \frac{\lambda_u \lambda_l}{8\pi^2\sqrt{3}\rho_{FEL}}. \tag{1.15}$$

Transverse size and divergence of the electron beam are typically controlled by quadrupole magnets installed at regular intervals on top or in-between undulator magnets. In order to be able to fulfill conditions (1.13) and (1.15) simultaneously by beam focusing, the product must satisfy

$$\sigma_x \sigma_{x'} < \frac{\lambda_l}{4\pi}, \tag{1.16}$$

where $\lambda_u/(\sqrt{3}\gamma_r^2) < \lambda_l$ (for small undulator parameters K) was used. The product on the left hand side of Eq. (1.16) is an upper limit for the transverse beam emittance $\epsilon_x = \sqrt{\langle x^2\rangle\langle x'^2\rangle - \langle xx'\rangle^2}$, which is a fundamental beam parameter that will be discussed in detail in chapter 2. The term on the right hand side in Eq. (1.16) is equal to the product $\sigma_x^l \cdot \sigma_\Theta^l$ of transverse size and divergence of the radiation beam which is determined by diffraction. Equation (1.16) thus states that the electron beam emittance has to be smaller than the "emittance" of the radiation beam.

The quantitative dependence of the gain length L_g on the transverse emittance can only be determined numerically. Figure 1.3 shows the computed gain length as a function of the normalized transverse emittance (emittance ϵ_x times γ_r) using undulator parameters of FLASH and a particle energy of 1 GeV according to reference [2]. The criterion (1.16) yields an upper limit of 1 μm for the normalized emittance in this case. In this example an increase in emittance leads to an increase in gain length by roughly the same factor, which illustrates the importance of this parameter for the FEL process.

Above it is assumed that the centroid of the electron beam $\langle x\rangle$ has zero offset with respect to the undulator axis. In reality, centroid offsets are inevitable. In order to not impede the FEL process by reducing the overlap between electron and radiation beam, the maximum deviations should be significantly smaller than the diameter of the beam. With typical beam diameters in the order of 100 μm at energies in the order of 1000 MeV, this

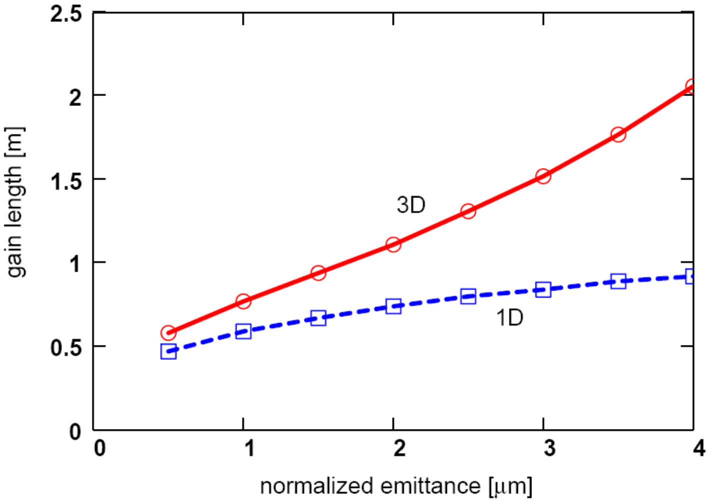

Figure 1.3: Computed 3D power gain length L_g (solid red curve) and 1D power gain length L_{g0} (dashed blue curve) as a function of the normalized emittance. The calculations are done for an energy of 1 GeV using parameters of FLASH and a peak current of 2500 A [2]. The gain length L_{g0} was determined within the framework of the one-dimensional approximation taking into account the change in charge density accompanying a variation in emittance.

means that the orbit should be aligned with an accuracy in the order of 10 μm over several gain lengths. This puts stringent requirements on the field quality and mechanical accuracy of the undulator. Furthermore, the orbit of the electron beam has to be precisely aligned to the undulator axis by steering magnets. Deviations occuring slowly over many gain lengths are less critical due to the principle of gain guiding.

Chapter 2

Transverse particle dynamics in linear accelerators

2.1 Transverse particle dynamics in linear approximation

In particle accelerators, electromagnetic guide fields force the beam particles to move on trajectories close to a design orbit. The guide fields are typically stationary magnetic fields transverse to the direction of motion. The simplest beam transport systems consist of dipole magnets, which define the design orbit for a reference particle with the nominal momentum, and quadrupole magnets to keep all particles close to the design orbit. Typically, the design orbit lies within a plane, which is assumed to be the horizontal plane, and all quadrupole magnets are oriented in such a way that the motion transverse to the direction of motion of the reference particle is decoupled in horizontal and vertical direction[1]. The magnetic field within the plane of the design orbit is then purely vertical.

It is convenient to describe the motion of individual particles in terms of coordinates related to the design orbit. The instantaneous position of an particle can be specified by the curvilinear-orthogonal coordinates (x, y, s), where s is the distance along the design orbit from some arbitrary reference point $s_0 = 0$ to the point on the design orbit nearest the particle. The horizontal and vertical displacements are then perpendicular to the tangent at the design orbit at s and are specified by the corresponding coordinates x and y in a local right-handed rectangular coordinate system,

---

[1] The assumption that the motion is decoupled is not mandatory. Linear transverse beam dynamics including coupling is described e.g. in [5].

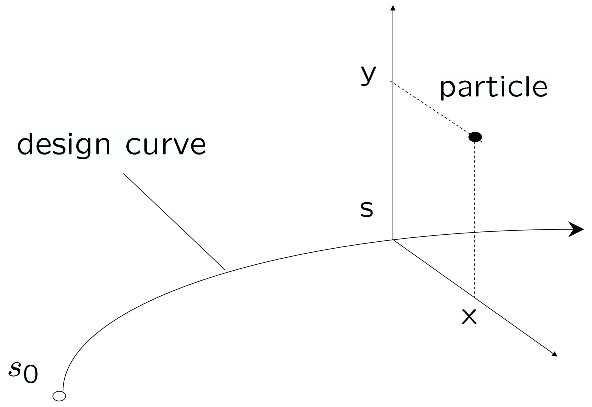

Figure 2.1: Design orbit and coordinate system.

see Fig. 2.1. Excluding particle acceleration, the guide field of a linear beam transport system as described above with a design orbit in the horizontal plane can approximately be expressed by

$$B_y(x,s) = B_y(0,s) + \left.\frac{\partial B_y}{\partial x}\right|_{(0,s)} \cdot x \tag{2.1}$$

$$B_x(y,s) = \left.\frac{\partial B_x}{\partial y}\right|_{(0,s)} \cdot y. \tag{2.2}$$

With $\vec{\nabla} \times \vec{B} = 0$ follows

$$\frac{\partial B_y}{\partial x} = \frac{\partial B_x}{\partial y}. \tag{2.3}$$

The guide field can thus be described by the two quantities $B_y(0,s)$ and $\left.\frac{\partial B_y}{\partial x}\right|_{(0,s)}$. Choosing s as an independent coordinate instead of time and retaining only terms up to first order in x, y and their derivatives, the equations of motion for an electron with charge $(-e)$ and design momentum p_0 are

$$\frac{d^2x}{ds^2} = -K_x(s) \cdot x \tag{2.4}$$

$$\frac{d^2y}{ds^2} = -K_y(s) \cdot y \tag{2.5}$$

with

$$K_x(s) = \frac{1}{\rho^2(s)} + \frac{e}{p_0}\left.\frac{\partial B_y}{\partial x}\right|_{(0,s)} \tag{2.6}$$

$$K_y(s) = -\frac{e}{p_0}\left.\frac{\partial B_y}{\partial x}\right|_{(0,s)}, \tag{2.7}$$

where $\rho(s)$ is the local bending radius in the horizontal plane [5]. For an electron with slightly deviating momentum

$$p = p_0 \cdot (1+\delta), \tag{2.8}$$

the equations of motion are [5]

$$\frac{d^2x}{ds^2} = -K_x(s) \cdot x + \frac{\delta}{\rho(s)} \tag{2.9}$$

$$\frac{d^2y}{ds^2} = -K_y(s) \cdot y. \tag{2.10}$$

Again, terms of second and higher order in (x, y, δ) (including combinations) and their derivatives are neglected.

These equations describe the so-called betatron motion due to linear focusing. They are examples of Hill's differential equation [6]. Within sections where $K_{x/y}(s)$ is positive and constant, as within focusing fields of quadrupole magnets, the equations of motion correspond to that of a one-dimensional harmonic oscillator. Note that due to relation (2.3) focusing in the horizontal plane includes defocusing in the vertical plane and vice versa (neglecting "geometric focusing" due to the bending radius). Reference [5] shows that a proper arrangement of alternating high gradient quadrupole fields is nevertheless suited to keep particles close to the design trajectory simultaneously in both transverse planes.

To solve Hill's equation, two standard methods are commonly used. The first one reflects the fact that the function $K(s) = K_x(s)$ is specified piecewise by the sequence of magnets and drift sections rather than as a global function[2]. The solutions are therefore assembled from local solutions by means of transfer matrices. The second one originates from circular accelerators, where the requirement of long-term stability of particle trajectories allows to describe the focusing characteristics of the entire magnet configuration via so-called beta functions.

---

[2] From now on only the horizontal plane is considered. Everything applies correspondingly to the vertical direction.

2.1.1 Transfer matrices

The general solution $x(s)$ of the homogenous Hill equation

$$\frac{d^2x}{ds^2} + K(s) \cdot x = 0 \tag{2.11}$$

within an interval $s_0 \leq s \leq L$ and its derivative $x'(s)$ can be expressed in terms of linearly independent solutions $u_1(s)$ and $u_2(s)$ as

$$\begin{aligned} x(s) &= a_1 u_1(s) + a_2 u_2(s) && (2.12) \\ x'(s) &= a_1 u_1'(s) + a_2 u_2'(s), && (2.13) \end{aligned}$$

where a_1, a_2 are real constants. Eq. (2.12) can be written in matrix notation as

$$\left[\begin{array}{c} x(s) \\ x'(s) \end{array} \right] = \left[\begin{array}{cc} u_1(s) & u_2(s) \\ u_1'(s) & u_2'(s) \end{array} \right] \cdot \left[\begin{array}{c} a_1 \\ a_2 \end{array} \right], \tag{2.14}$$

or

$$X(s) = U(s) \cdot A. \tag{2.15}$$

The determinant of $U(s)$ does not depend on s:

$$\frac{d}{ds} \left[\det U(s) \right] = 0. \tag{2.16}$$

It is, moreover, non-zero as $u_1(s)$ and $u_2(s)$ are linearly independent and the determinant is just the Wronski determinant of these solutions. The matrix $U(s)$ is therefore invertible, and multiplication of Eq. (2.15) with $U(s)^{-1}$ yields at $s = s_0$

$$A = U(s_0)^{-1} \cdot X(s_0). \tag{2.17}$$

Inserting this expression into Eq. (2.15) yields a representation of the general solution in terms of the initial conditions $X(s_0)$ at s_0:

$$X(s) = M(s, s_0) \cdot X(s_0), \tag{2.18}$$

where

$$\begin{aligned} M(s, s_0) &= U(s) \cdot U(s_0)^{-1} && (2.19) \\ &= \left[\begin{array}{cc} C(s) & S(s) \\ C'(s) & S'(s) \end{array} \right]. && (2.20) \end{aligned}$$

The matrix $M(s, s_0)$ is called the transfer matrix from s_0 to s. From Eq. (2.16) follows

$$\det M(s, s_0) = 1. \tag{2.21}$$

The matrix elements $C(s)$ and $S(s)$ are called the cosine-like and sine-like principal solutions of the Hill equation satisfying the relations

$$\begin{aligned} C(s_0) &= 1 && (2.22)\\ C'(s_0) &= 0 && (2.23)\\ S(s_0) &= 0 && (2.24)\\ S'(s_0) &= 1. && (2.25) \end{aligned}$$

The representation (2.18) of the general solution is very useful in accelerator physics, since the function $K(s)$ is typically piecewise constant in very good approximation. The equation of motion can thus be solved locally yielding transfer matrices for the single intervals in which $K(s)$ constant, and the general solution can be calculated by matrix multiplication, i.e.

$$M(s_n, s_0) = M(s_n, s_{n-1}) \cdot ... \cdot M(s_1, s_0). \tag{2.26}$$

A solution of the inhomogeneous equation (2.9) can be found by using Green's functions, yielding a particular solution $\delta \cdot D(s)$ with [7, 8]

$$D(s) = S(s) \int_{s_0}^{s} \frac{1}{\rho(t)} C(t) dt - C(s) \int_{s_0}^{s} \frac{1}{\rho(t)} S(t) dt. \tag{2.27}$$

Physically, $\delta \cdot D(s)$ is the horizontal offset of an electron with relative momentum deviation δ from the design orbit at s, provided the electron was moving on the design orbit in a small interval around s_0. The function $D(s)$ is called the dispersion trajectory. The general solution of the inhomogeneous equation can be expressed using again matrix notation as

$$\begin{bmatrix} x(s) \\ x'(s) \\ \delta \end{bmatrix} = \begin{bmatrix} C(s) & S(s) & D(s) \\ C'(s) & C'(s) & D'(s) \\ 0 & 0 & 1 \end{bmatrix} \cdot \begin{bmatrix} x(s_0) \\ x'(s_0) \\ \delta \end{bmatrix}. \tag{2.28}$$

2.1.2 The beta function

The general solution of the homogenous Hill equation (2.11) can be expressed in phase-amplitude form by

$$x_{1,2}(s) = w(s) \cdot e^{\pm i\phi(s)}. \tag{2.29}$$

This ansatz satisfies the Hill equation, if the real-valued functions $w(s)$ and $\phi(s)$ fulfill

$$w''(s) + K(s)w(s) - \frac{1}{w^3(s)} = 0 \tag{2.30}$$

and

$$\phi'(s) = \frac{1}{w^2(s)}, \tag{2.31}$$

as can be verified by substitution. The two solutions $x_{1,2}(s)$ are then linearly independent, and Eq. (2.19) can be used to express the transfer matrix $M(s, s_0)$ in terms of the functions $w(s)$ and $\phi(s)$. In case of circular accelerators, the representation of the transfer matrix for one turn in this way allows to uniquely define an amplitude function $w(s)$, since the requirement of long-term stability imposes stringent conditions on the one-turn-matrix [5]. For historical reasons, this amplitude function is denoted as $\sqrt{\beta(s)}$, and $\beta(s)$ is referred to as the beta function. The beta function is commonly used also in case of linear accelerators, although it is not uniquely defined by the magnet configuration. Its definition in linear accelerators will be addressed at the end of this section. The general real-valued phase-amplitude solution can be expressed via the beta function as

$$x(s) = \sqrt{a \cdot \beta(s)} \cdot \cos(\phi(s) + \phi_0), \tag{2.32}$$

where a and ϕ_0 are real constants specifying the particular solution, and

$$\phi(s) = \int_{s_0}^{s} \frac{ds'}{\beta(s')} \tag{2.33}$$

is the betatron phase. The value of the beta function is a positive real number for all s so the betatron phase has no singularities. Two additional functions

$$\alpha(s) = -\frac{1}{2}\beta'(s) \tag{2.34}$$

$$\gamma(s) = \frac{1 + \alpha^2(s)}{\beta(s)} \tag{2.35}$$

derived from the beta function are commonly used to describe the betatron motion. Together, $\beta(s)$, $\alpha(s)$ and $\gamma(s)$ are referred to as the Courant-Snyder or Twiss parameters.

The beta function of a given accelerator completely describes the lateral focusing properties of the (linear) guide field and reveals significant characteristics of the particle trajectories. In particular, the maximum possible displacement of a particle from the design orbit at position s is given by $\sqrt{a\beta(s)}$. The instantaneous wavelength of the pseudo-harmonic oscillation described by Eq. (2.32) is given by

$$\begin{aligned} \lambda &= \frac{2\pi}{\phi'(s)} && (2.36) \\ &= 2\pi\beta(s). && (2.37) \end{aligned}$$

The local focusing properties can be deduced from Eq. (2.30).

The representation of the transfer matrix $M(s_2, s_1)$ via $\beta(s)$ and $\phi(s)$ is given by [7]

$$M(s_2, s_1) = \qquad (2.38)$$

$$\begin{bmatrix} \sqrt{\frac{\beta_2}{\beta_1}}(\cos(\Delta\phi) + \alpha_1 \sin(\Delta\phi)) & \sqrt{\beta_1\beta_2}\sin(\Delta\phi) \\ \frac{\alpha_1-\alpha_2}{\sqrt{\beta_2\beta_1}}\cos(\Delta\phi) - \frac{1+\alpha_1\alpha_2}{\sqrt{\beta_2\beta_1}}\sin(\Delta\phi) & \sqrt{\frac{\beta_1}{\beta_2}}(\cos(\Delta\phi) - \alpha_2 \sin(\Delta\phi)) \end{bmatrix},$$

where

$$\Delta\phi = \int_{s_1}^{s_2} \frac{ds}{\beta(s)} \qquad (2.39)$$

is the betatron phase advance from s_1 to s_2, and $\beta_1 = \beta(s_1)$ and correspondingly for all Courant-Snyder parameters.

The phase-amplitude solution allows an instructive interpretation, which can be seen by combining $x(s)$ and $x'(s)$ according to Eq. (2.32) to the expression

$$\gamma x^2 + 2\alpha x x' + \beta x'^2 = a. \qquad (2.40)$$

Eq. (2.40) defines an ellipse in so-called trace space coordinates (x, x') with area πa and center at $(0, 0)$. The particle motion can thus be interpreted as a movement around an ellipse in trace space, whose shape varies along the accelerator according to the corresponding transfer matrices while its

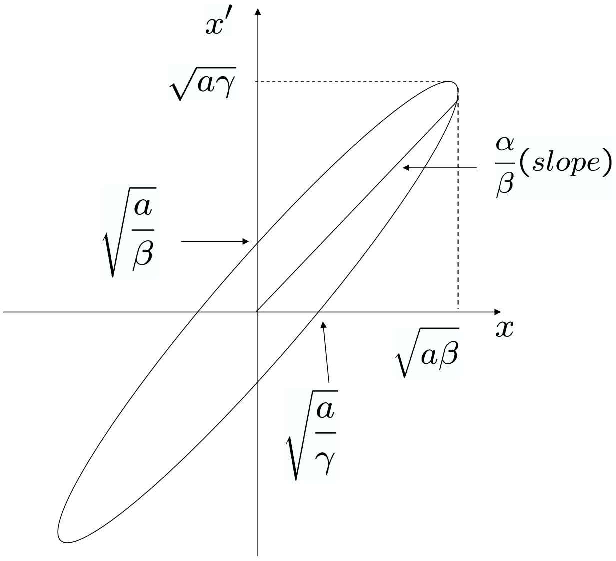

Figure 2.2: Ellipse characteristics related to Courant-Snyder parameters [9].

area remains constant. Because of its importance a is called the Courant-Snyder invariant. The relation of Courant-Snyder parameters to the ellipse geometry is sketched in Fig. 2.2.

To determine the transformation of Courant-Snyder parameters and thus the shape of the ellipse, it is helpful to write Eq. (2.40) in matrix notation as

$$X^T J X = a \tag{2.41}$$

with

$$X = \begin{bmatrix} x \\ x' \end{bmatrix} \tag{2.42}$$

and

$$J^{-1} = \begin{bmatrix} \beta & -\alpha \\ -\alpha & \gamma \end{bmatrix}. \tag{2.43}$$

Note that

$$\det(J) = \det(J^{-1}) = 1 \tag{2.44}$$

due to Eq. (2.35). When the trace space coordinates are transformed by multiplication with a transfer matrix $M = M(s_2, s_1)$, the new ellipse parameters are given by

$$J(s_2)^{-1} = M J(s_1)^{-1} M^T, \tag{2.45}$$

as can be verified through

$$X(s_1)^T \left[M^T(M^T)^{-1}\right] J(s_1) \left[M^{-1}M\right] X(s_1) = a. \tag{2.46}$$

Inserting the representation (2.20) of M in terms of principal solutions into Eq. (2.45) yields the following transformations of Courant-Snyder parameters:

$$\begin{bmatrix} \beta(s_2) \\ \alpha(s_2) \\ \gamma(s_2) \end{bmatrix} = \begin{bmatrix} C^2 & -2CS & S^2 \\ -CC' & (S'C + SC') & -SS' \\ C'^2 & -2S'C' & S'^2 \end{bmatrix} \cdot \begin{bmatrix} \beta(s_1) \\ \alpha(s_1) \\ \gamma(s_1) \end{bmatrix}. \tag{2.47}$$

The corresponding representation of the phase advance $\Delta\phi$ from s_1 to s_2 is given by [10]

$$\Delta\phi = \tan^{-1}\left(\frac{S}{C \cdot \beta(s_1) - S \cdot \alpha(s_1)}\right). \tag{2.48}$$

The transformation of Courant-Snyder parameters described by Eq. (2.47) is particularly important for linear accelerators, since the arbitrariness of the beta function reduces to the specification of initial values for α and β. Designing the optics of a linear accelerator thus includes a reasonable choice of these values. This choice is based on statistical properties of the electron distribution of single electron bunches as discussed in the following section.

2.2 Transverse emittance

The interpretation of the particle motion in terms of a transforming ellipse in trace space is particularly helpful for describing the development of an electron distribution $\rho(x, x')$ under the linear dynamics described above. Since the dynamics of a single electron is determined by its trace space coordinates (x, x'), every electron within a certain trace space area will stay within this area if the boundary is transformed according to the equation of motion. Since an elliptical area with center $(0, 0)$ remains elliptical as shown above, the transformation of a few ellipse parameters is suited to describe the envelope of an electron ensemble in trace space.

A trace space ellipse that is particularly useful and easy to determine is given by the covariance matrix $\sigma = COV(x, x') = COV(X)$ of the beam distribution via

$$X^T \sigma^{-1} X = 1. \tag{2.49}$$

The covariance matrix or beam matrix is defined as

$$\sigma = \begin{bmatrix} \langle x^2 \rangle & \langle x x' \rangle \\ \langle x x' \rangle & \langle x'^2 \rangle \end{bmatrix}, \tag{2.50}$$

where $\langle \, \rangle$ denotes averaging over the electron density distribution $\rho(x, x')$ and

$$\langle x \rangle = \langle x' \rangle = 0$$

has been assumed. The ellipse is referred to as RMS ellipse.

A transformation of the electron coordinates

$$X(s_2) = M \cdot X(s_1) \tag{2.51}$$

with a transfer matrix $M = M(s_2, s_1)$ yields a transformation of the beam matrix according to

$$\sigma(s_2) = M \sigma(s_1) M^T, \tag{2.52}$$

as can be verified by calculating $COV(MX)$. The transformation of $\sigma(s)$ is identical to that of $J(s)^{-1}$ (Eq. (2.45)). Thus one can define ellipse parameters $(\beta_e, \alpha_e, \gamma_e)$ in terms of covariances in correspondence to Eq. (2.43) by

$$\begin{bmatrix} \beta_e & -\alpha_e \\ -\alpha_e & \gamma_e \end{bmatrix} = \frac{\sigma}{\sqrt{\det(\sigma)}} \tag{2.53}$$

with the result that $(\beta_e, \alpha_e, \gamma_e)$ transform in the same way as Courant-Snyder parameters (β, α, γ). $(\beta_e, \alpha_e, \gamma_e)$ are referred to as beam ellipse parameters[3]. The quantity

$$\begin{aligned} \epsilon &= \sqrt{\det(\sigma)} \qquad (2.54) \\ &= \sqrt{\langle x^2 \rangle \langle x'^2 \rangle - \langle x x' \rangle^2} \qquad (2.55) \end{aligned}$$

is called the geometric RMS emittance [11][4]. The product $\pi\epsilon$ is the area of the RMS ellipse in trace space. The geometric emittance has units of length.

---

[3] The beam ellipse parameters are often also called Courant-Snyder or Twiss parameters. This will not be done here to avoid confusion.

[4] There is another definition of RMS emittance introduced by Lapostolle [12], who defines it as phase space area occupied by a “perfect equivalent beam” with uniform density distribution and the same covariances. This definition will not be used here.

If the actual beam ellipse parameters are the same as the Courant-Snyder parameters of the design optics, the beam is said to be "matched". In this case, the RMS emittance ϵ corresponds to a Courant-Snyder invariant and the beta function directly reveals the RMS beam size of a beam with known RMS emittance via

$$\epsilon\beta(s) = \langle x(s)^2 \rangle. \tag{2.56}$$

In case of a matched Gaussian bunch, the iso-density contours in trace space coincide with ellipses described by the Courant Snyder parameters.

Other definitions of transverse emittance

There are various definitions of beam emittance specific to particular purposes and beam properties. Generally, the emittance is a measure of the phase space or trace space volume (the difference is discussed below) occupied by a beam, mostly restricted to two-dimensional subspaces. For an ideal hard-edged beam, the emittance can simply be defined to be proportional to the total trace space volume occupied by the beam. For a particle distribution without well-defined cutoff, often the trace space volume populated by a certain fraction, e.g. 90% of the beam particles is taken to define the emittance. For Gaussian-like distributions, the RMS emittance introduced above is convenient. In case of a two-dimensional Gaussian trace space distribution, 39.3% of all particles are contained within an RMS ellipse. The ellipse is sometimes scaled to include a larger fraction of the particles, e.g. in case of proton beams the "2σ-emittance" is conventionally used.

For non-Gaussian beams, the RMS emittance may be misleading since the fraction of particles contained within the RMS ellipse may strongly deviate from the quoted value. Moreover, the ellipse area may comprise sections with very low or even vanishing particle density if the distribution is deformed accordingly. In these cases, a more detailed analysis of the trace space distribution is necessary to define a meaningful emittance related to the particles of interest. This is particularly important in case of single-pass FELs with strongly distorted trace space distributions and will be addressed in detail in chapter 7.

Conservation of transverse emittance

The phase space volume occupied by a beam bunch is conserved under very general conditions. For a beam subject to external electromagnetic forces described by a Hamiltonian, the Liouville theorem [13] can be applied if internal forces are neglected. In this particular case, the theorem states that the phase space density within an arbitrary six-dimensional phase space volume transformed according to the Hamiltonian is constant in time. If the dynamics in the two-dimensional horizontal and vertical subspaces and the longitudinal subspace is decoupled, which is a convenient but particularly in linear accelerators sometimes violated assumption (see below), the same applies to these two-dimensional subspaces. A change of the phase space density may occur due to internal processes, such as Coulomb forces and radiation processes.

Ideally the bunch emittance is proportional to the phase space volume occupied by the bunch particles. In this case the emittance is a key parameter of a beam and a measure of the "beam quality", meaning the deviation of beam particle parameters from reference parameters. In reality this is, however, often not the case. Depending on the exact definition of emittance, there are mechanisms leading to emittance growth without changing the phase space volume occupied by a bunch.

An important issue in this respect are the underlying variables. Liouville's theorem is based on a description in canonically conjugate variables. The canonical transverse momentum P_x conjugate to the spatial position coordinate x in presence of an electromagnetic field is given by [3]

$$P_x = p_x + q \cdot A_x \tag{2.57}$$

with the horizontal vector potential component A_x, particle charge q and horizontal kinetic momentum $p_x = \gamma_r m \frac{dx}{dt}$, where m is the mass of the particle. In case the magnetic field is purely transverse to the direction of movement as in case of linear transport lines discussed here, the transverse components of the vector-potential $\vec{A}$ vanish and the transverse kinetic momentum p_x is conjugate to the transverse position x. Thus the local particle density in kinetic transverse phase space (x, p_x) is conserved. The same applies to trace space (x, x') only if there is no acceleration. In this case the canonical transverse momentum p_x is proportional to the angle x', yielding a canonical transformation to conjugate variables x and x'.

Otherwise the angle coordinate x' scales like $1/\gamma_r$. In order to define an emittance invariant under acceleration, the angle-coordinate x' in trace space can be replaced by the invariant ratio p_x/m_ec. With

$$\frac{p_x}{m_ec} = \gamma_r\beta_r x' \tag{2.58}$$

and $\beta_r \approx 1$ one obtains the invariant normalized transverse emittance $\gamma_r\epsilon$, where ϵ is the corresponding geometric emittance in trace space. If the beam is not mono-energetic the gamma-factor refers to the average energy. This implies that the normalized emittance may change slightly along a beamline, but typically the energy variance is small enough so this effect is negligible.

Conservation of the normalized transverse RMS emittance is additionally only guaranteed within the framework of the linear approximation. Any transverse force depending in a non-linear way on transverse coordinates may change the RMS emittance.

Important sources for two-dimensional transverse RMS emittance growth in the linear electron accelerators considered in this thesis are coherent synchrotron radiation effects within dipoles, wake fields and, particularly at low energies, repulsive Coulomb forces. These issues are discussed in detail in section 4.1.4. There are other sources for RMS emittance growth which are typically not significant in case of linear accelerators but important in circular accelerators, as for instance higher order magnetic fields leading to “beam filamentation” and thus to a dilution of the average phase space density within the RMS ellipse, and “chromatic” effects due to a non-vanishing energy spread.

2.3 Normalized coordinates and beam mismatch

Typically, the beam ellipse parameters $(\beta_e(s_0), \alpha_e(s_0), \gamma_e(s_0))$ at a point $s = s_0$ of a transport line are not perfectly matched to the design parameters $(\beta(s_0), \alpha(s_0), \gamma(s_0))$. In order to describe the development of such “mismatched” beam ellipse parameters, it is convenient to introduce so-called normalized coordinates (u, v) as described in the following.

Normalized coordinates

Given the design Courant-Snyder parameters $(\beta(s), \alpha(s), \gamma(s))$, the transformation to normalized coordinates can be expressed via [14]

$$\begin{bmatrix} u(s) \\ v(s) \end{bmatrix} = S \cdot \begin{bmatrix} x(s) \\ x'(s) \end{bmatrix} \tag{2.59}$$

with

$$S(s) = \begin{bmatrix} \frac{1}{\sqrt{\beta(s)}} & 0 \\ \frac{\alpha(s)}{\sqrt{\beta(s)}} & \sqrt{\beta(s)} \end{bmatrix}. \tag{2.60}$$

Inserting the general solution (2.32) for $x(s)$ and $x'(s)$ in terms of betatron functions yields

$$\begin{aligned} u(s) &= \sqrt{a} \cdot \cos(\phi(s)) & (2.61) \\ v(s) &= -\sqrt{a} \cdot \sin(\phi(s)) & (2.62) \\ &= \frac{du}{d\phi}. & (2.63) \end{aligned}$$

Thus, electron trajectories describe a circle in the (u, v)-plane with radius $\sqrt{a}$. With ϕ as independent variable, this is in analogy to a description of a one-dimensional harmonic oscillator.

A transfer matrix $M(s_2, s_1)$ in trace space corresponds to a transfer matrix

$$\tilde{M}(s_2, s_1) = S(s_2) \cdot M(s_2, s_1) \cdot S^{-1}(s_1) \tag{2.64}$$

in the (u, v)-plane. The transformation yields a rotational matrix

$$\tilde{M}(s_2, s_1) = \begin{bmatrix} \cos(\phi) & \sin(\phi) \\ -\sin(\phi) & \cos(\phi) \end{bmatrix}. \tag{2.65}$$

Mismatch parameter and mismatch phase

The transformation from trace space coordinates (x, x') to normalized coordinates (u, v) by multiplication with a matrix S according to Eq. (2.59) defines a transformation of RMS ellipse parameters $(\beta_e, \alpha_e, \gamma_e)$ of a particle distribution in trace space. Since $\det(S) = 1$, the transformation is in analogy to the transformation induced by linear beam transfer (Eq. (2.45)) given by

$$\tilde{J}^{-1} = SJ^{-1}S^T \tag{2.66}$$

with

$$J^{-1} = \begin{bmatrix} \beta_e & -\alpha_e \\ -\alpha_e & \gamma_e \end{bmatrix} \tag{2.67}$$

and

$$\tilde{J}^{-1} = \begin{bmatrix} \tilde{\beta_e} & -\tilde{\alpha_e} \\ -\tilde{\alpha_e} & \tilde{\gamma_e} \end{bmatrix}. \tag{2.68}$$

In particular, one obtains

$$\tilde{\beta_e} = \frac{\beta_e}{\beta}. \tag{2.69}$$

In case $(\beta_e, \alpha_e, \gamma_e)$ are equal to the design Courant-Snyder parameters (β, α, γ), the resulting parameters $(\tilde{\beta_e}, \tilde{\alpha_e}, \tilde{\gamma_e})$ describe a circle in the (u, v)-plane with a radius of $\sqrt{\epsilon}$, ϵ denoting the RMS emittance. In case $(\beta_e, \alpha_e, \gamma_e)$ deviate from the design parameters, an ellipse with the same area $\pi\epsilon$ as the circle will be obtained, since $\det(S) = 1$. The ellipse will be called mismatch ellipse. The "deformation" of the mismatch ellipse is a measure for the deviation of the RMS ellipse parameters $(\beta_e, \alpha_e, \gamma_e)$ from the design Courant-Snyder parameters. The deformation can be described by the ratio of the length of the semi-major axis to the radius of the circle. The square of this ratio is called mismatch parameter M [14] (Fig. 2.3).

The mismatch parameter can be determined from the RMS ellipse parameters and the design Courant-Snyder parameters via [14, 15][5]

$$M = B + \sqrt{B^2 - 1} \tag{2.70}$$

with

$$\begin{aligned} B &= \frac{1}{2}(\beta_e\gamma - 2\alpha_e\alpha + \beta\gamma_e) && (2.71) \\ &= \frac{1}{2}\left(\tilde{\beta_e} + \tilde{\gamma_e}\right). && (2.72) \end{aligned}$$

---

[5] In the literature, sometimes B is called mismatch parameter [16].

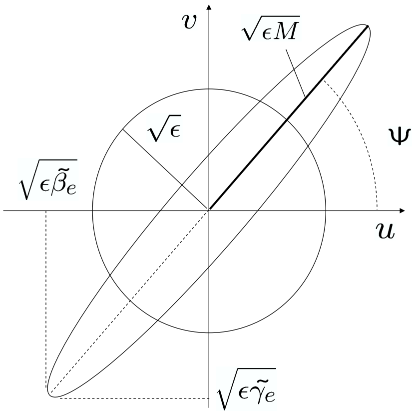

Figure 2.3: Mismatch ellipse defined by parameters $(\tilde{\beta}_e, \tilde{\alpha}_e, \tilde{\gamma}_e)$*. The circle is obtained by applying the transformation to normalized coordinates* (u, v) *to the design Courant-Snyder parameters* (β, α, γ)*. The mismatch ellipse is the result of a corresponding transformation of mismatched RMS ellipse parameters.* ϵ *denotes the RMS emittance. The mimatch ellipse can be described by the mismatch parameter* M *and the mismatch phase* Ψ*.*

The orientation of the mismatch ellipse at $s = s_0$ can be described by the angle Ψ_0 between the semi-major axis and the u-axis in the right half plane (Fig. 2.3). It is related to the parameters $(\tilde{\beta}_e, \tilde{\alpha}_e, \tilde{\gamma}_e)$ of the mismatch ellipse via

$$\tan(2\Psi_0) = \frac{-2\tilde{\alpha}_e}{\tilde{\beta}_e - \tilde{\gamma}_e}. \tag{2.73}$$

Here, the solution within the interval $[-\pi/2, \pi/2]$ with opposite sign of $\tilde{\alpha}_e$ has to be taken in order to obtain the angle indicated in Fig. 2.3 [14].

As shown above, the transfer matrices in normalized coordinates are rotational matrices. The axis of the mismatch ellipse rotates clockwise by an angle $-\Delta\phi = -(\phi(s) - \phi(s_0))$ (with the usual convention for positive angles) as the bunch proceeds along the beamline from s_0 to s. The shape of the ellipse and therefore the mismatch parameter are unaffected, whereas the angle Ψ_0 changes. An invariant under linear beam transfer describing the orientation of the mismatch ellipse can be defined by

$$\Psi = \Psi_0 + \phi(s). \tag{2.74}$$

Ψ will be called mismatch phase [14]. It corresponds to the angle Ψ_0 in Fig. 2.3 at $s = 0$.

Given the Courant-Snyder parameters of an accelerator, mismatch parameter and mismatch phase uniquely determine the RMS ellipse parameters at all points of the beamline. They can in particular be used to describe the ratio $\beta_e(s)/\beta(s) = \tilde{\beta}_e(s)$, which is given by [15]

$$\frac{\beta_e(s)}{\beta(s)} = B + \sqrt{B^2 - 1} \cdot \cos(2(\phi(s) - \Psi)). \tag{2.75}$$

$\beta_e(s)$ thus oscillates with a frequency twice the betatron frequency around the design value $\beta(s)$ times the constant B. This oscillation is called “beta-beating”. The maximum of the ratio $\beta_e(s)/\beta(s)$ is given by M.

Deformation parameter and deformation phase

Mismatch parameter M and mismatch phase Ψ describe the deviation of ellipse parameters from design parameters. The same formalism can be applied in order to compare two arbitrary sets of ellipse parameters. It will turn out to be useful to compare the ellipse parameters of subsets of the particles within a bunch with the overall bunch ellipse parameters. In analogy to M and Ψ, the quantities m and ψ are introduced for this purpose. m and ψ will be called deformation parameter and deformation phase, respectively.

Chapter 3

Transverse phase space diagnostics

The transverse phase space distribution of an electron beam can be explored by measuring its spatial projections either at different positions of a beamline, or at one position for different focal strength of quadrupoles upstream of the observation point. Least square methods allow to determine important quantities as transverse emittance and beam ellipse parameters. The detailed distribution in phase space can be obtained by tomographic reconstruction techniques.

Throughout this chapter it will be assumed that the transverse dynamics can be described by the linear approximation introduced in chapter 2. In particular, it is assumed that the particle motion in horizontal and vertical direction is decoupled, and that the beam particles are of constant energy. Only the horizontal direction will be considered. Everything applies in the same way to the vertical direction.

3.1 Determination of transverse beam parameters

The geometrical RMS emittance is defined by

$$\epsilon \;=\; \sqrt{det(\sigma)},$$

σ denoting the covariance matrix of the beam (beam matrix)

$$\sigma = \begin{bmatrix} \langle x^2 \rangle & \langle xx' \rangle \\ \langle xx' \rangle & \langle x'^2 \rangle \end{bmatrix}$$

(cf. section 2.2). The beam matrix transforms along a linear beamline without acceleration according to

$$\sigma(s) = M\sigma(s_0)M^T,$$

where M is the transfer matrix from s_0 to s. The emittance is conserved during this transformation due to $\det(M) = 1$. The emittance is thus determined if the beam matrix is known at one position (here: s_0) of the beamline. At the same time, the ellipse parameters $(\beta_e, \alpha_e, \gamma_e)$ at s_0 are determined via

$$\left[\begin{array}{cc} \beta_e & -\alpha_e \\ -\alpha_e & \gamma_e \end{array}\right] = \frac{\sigma(s_0)}{\sqrt{det(\sigma(s_0))}} = \frac{\sigma(s_0)}{\epsilon}.$$

Knowledge of the ellipse parameters at one position allows to match the beam to a design optics by adapting the focal strengths of appropriate quadrupoles.

The element $\sigma_{1,1} = \langle x^2 \rangle$ of the beam matrix can be measured directly with standard diagnostic devices[1] (cf. chapter 4). Since $\sigma_{1,1}(s)$ at position s is a function of the elements of $\sigma(s_0)$ according to Eq. (3.1), the entire beam matrix $\sigma(s_0)$ can be deduced from measurements of $\sigma_{1,1}(s)$ at different positions of the beamline. $\sigma_{1,1}(s)$ is explicitly given by

$$\sigma_{1,1}(s) = \left(\begin{array}{ccc} M_{1,1}^2, & 2M_{1,1}M_{1,2}, & M_{1,2}^2 \end{array} \right) \left(\begin{array}{c} \sigma_{1,1}(s_0) \\ \sigma_{1,2}(s_0) \\ \sigma_{2,2}(s_0) \end{array} \right), \tag{3.1}$$

where matrix notation is used and $\sigma_{i,j}$ and $M_{i,j}$ indicate the elements of the matrices M and σ. This notation can be used to express the squared beam sizes $\sigma_{1,1}^{(i)} = \sigma_{1,1}(s_i)$ at positions $s_1, s_2, ...s_n$ by

$$\left(\begin{array}{c} (\sigma_{1,1}^{(1)}) \\ (\sigma_{1,1}^{(2)}) \\ \vdots \\ (\sigma_{1,1}^{(n)}) \end{array} \right) = \left(\begin{array}{ccc} (M_{1,1}^{(1)})^2 & 2M_{1,1}^{(1)}M_{1,2}^{(1)} & (M_{1,2}^{(1)})^2 \\ (M_{1,1}^{(2)})^2 & 2M_{1,1}^{(2)}M_{1,2}^{(2)} & (M_{1,2}^{(2)})^2 \\ \vdots & & \\ (M_{1,1}^{(n)})^2 & 2M_{1,1}^{(n)}M_{1,2}^{(n)} & (M_{1,2}^{(n)})^2 \end{array} \right) \left(\begin{array}{c} \sigma_{1,1}(s_0) \\ \sigma_{1,2}(s_0) \\ \sigma_{2,2}(s_0) \end{array} \right), \tag{3.2}$$

where $M^{(i)}$ denotes the transfer matrix from s_0 to s_i. The matrix equation can be written in short hand notation as

$$\Sigma = R \cdot o. \tag{3.3}$$

---

[1] It is also possible to measure the beam divergence directly by sending the beam through apertures of known size before measuring the transverse size of the “beamlets”. This technique will not be considered here. For details see e.g. [17].

In case $n = 3$, the solution vector o containing the elements of the beam matrix at s_0 (the reconstruction point) is determined by the vector Σ of squared beam sizes via

$$o = R^{-1} \cdot \Sigma, \tag{3.4}$$

provided the matrix R is invertible.

In practice, the squared beam sizes $\sigma_{1,1}(s_i)$ are not determined exactly, but contain measurement errors. Equation 3.3 does not hold exactly in this case, which is expressed by a non-vanishing residual vector

$$r = R \cdot o - \Sigma. \tag{3.5}$$

In case of an overdetermined system with $n > 3$, a solution vector o can be determined such that the residual vector r is minimized in a least squares sense. This method is described in more detail in the next section.

It is not required that the measurements of beam sizes are done at different positions of the beamline. If diagnostic devices to measure the beam size are not installed at the appropriate positions, it may be advantageous to measure at one position s for different transfer matrices $M^{(i)}(s, s_0)$ from s_0 to s. This can be accomplished by varying the focal strength of quadrupoles located between s_0 and s. Such measurements are loosely called “quadrupole scans”.

3.1.1 Least squares method

The vector Σ is in general subject to statistical measurement errors. For simplicity, it is at first assumed that the errors can be expressed in a covariance matrix $V[\Sigma]$ of the form

$$V[\Sigma] = \Delta^2 \cdot I_n, \tag{3.6}$$

where I_n is the unit matrix of rank n and Δ^2 the variance of the squared beam sizes $\Sigma_i = (\sigma_{1,1}^{(i)})$. The general case of an arbitrary covariance matrix $V[\Sigma]$ is considered below. Moreover, it is assumed that there are no systematic errors, i.e. the expectation values of the elements of Σ are identical with the true beam sizes squared. The least squares solution of Eq. (3.3) with $n > 3$ is then obtained by minimizing the expression

$$S = r^T r = \sum_{j=1}^{n} r_j^2 \tag{3.7}$$

with $r = R \cdot o - \Sigma$. The minimum of S is determined by the condition

$$\frac{\partial S}{\partial o_i} = 0 \tag{3.8}$$

for $i = 1...3$, leading to the equation

$$R^T R \cdot \hat{o} - R^T \Sigma = R^T \cdot r = 0 \tag{3.9}$$

with $\hat{o}$ the “best estimate” for the vector o (normal equation). In case $R^T R$ is invertible, this yields the solution

$$\hat{o} = (R^T R)^{-1} R^T \Sigma. \tag{3.10}$$

The covariance matrix $V[\hat{o}]$ of $\hat{o}$ due to measurement errors of Σ is given by error propagation,

$$V[\hat{o}] = J V[\Sigma] J^T \tag{3.11}$$

with $J = (R^T R)^{-1} R^T$, yielding

$$V[\hat{o}] = \Delta^2 (R^T R)^{-1}. \tag{3.12}$$

The resulting errors of the emittance and the ellipse parameters can be estimated by error propagation as well. In particular, the variance σ_ϵ^2 of the emittance is given by

$$\sigma_\epsilon = B V[\hat{o}] B^T \tag{3.13}$$

with

$$B = \frac{1}{2\epsilon} \left(\hat{o}_3, -2 \cdot \hat{o}_2, \hat{o}_1 \right). \tag{3.14}$$

Until now, only the special case of uncorrelated errors of the same absolute value Δ has been considered. The formalism can be generalized to include the case of an arbitrary covariance matrix $V[\Sigma]$ by minimizing the expression

$$S = r^T W r \tag{3.15}$$

with $W = V[\Sigma]^{-1}$ and $r = R \cdot o - \Sigma$ [18]. For uncorrelated errors Δ_i of Σ_i, this corresponds to a minimization of

$$S = \sum_{i=1}^{n} \frac{r_i^2}{\Delta_i^2}. \tag{3.16}$$

The best estimate $\hat{o}$ for the parameter vector o in a least squares sense is given by

$$\hat{o} = (R^T W R)^{-1} R^T W \Sigma, \tag{3.17}$$

and the covariance matrix $V[\hat{o}]$ of $\hat{o}$ by [18]

$$V[\hat{o}] = (R^T W R)^{-1}. \tag{3.18}$$

In practice, statistical errors can be estimated by the variance of measured beam sizes. Aside from statistical errors, the result may be subject to systematic errors both of the beam size vector Σ, e.g. due to calibration errors of the measurement devices, and the matrix R due to errors of the transfer matrices. Systematic errors typically lead to an increase of elements of the residual vector r and can be identified and occasionally be corrected in this way. In contrast to statistical errors, an accurate estimation of systematic errors is hardly possible. They are therefore not included in the least-square formalism. Systematic errors are specific for the particular experimental setup and are discussed in detail in chapter 5 for the setup used here.

The least-square formalism is covered in detail, for instance, in references [18, 19].

Optimum arrangement of measurement stations

Equation (3.12) shows that measurement errors Δ may be magnified if the elements of the matrix $(R^T R)^{-1}$ are large, which is the case when the inversion of the matrix $R^T R$ is imprecise. It is therefore important to choose an appropriate matrix R.

The design of a measurement arrangement is typically done on the basis of a design optics. Some intuitive arguments will be given here on how an appropriate arrangement can be chosen.

An arrangement of measurement stations is characterized by the set of transfer matrices from one point of the machine (for convenience the position of the first station) to the other measurement stations. It is instructive to use normalized coordinates with respect to the design optics, so the transfer matrices are rotational matrices. The arrangement is then described by a set of angles $\Delta\phi_i$, indicating the phase advance from the first station to the other stations. A beam is investigated by measuring the spatial profiles (projection onto the horizontal axis), in particular the RMS widths, at the different stations. In between the measurement the beam distribution is rotated by angles $\Delta\phi_{i+1} - \Delta\phi_i$ in normalized phase space.

A first conclusion from these considerations is that measurement stations separated by 180° phase advance are redundant since the spatial profiles are point symmetric with respect to their center and the width is the same. The measurement stations can thus be arranged such that the betatron phase advance between the first and the last station is less than 180°. The optimum arrangement of a fixed number n of stations within this interval depends on the exact criterion chosen. Typically, the most important parameter of such a measurement is the error σ_ϵ of the resulting emittance. Thus a reasonable criterion is to minimize the error magnification $e_{mag} = \sigma_\epsilon/\Delta$. This magnification does not only depend on the matrix R, but also on properties of the beam matrix elements (cf. Eq. (3.13)). The beam matrix elements can be characterized by the mismatch parameter M and the mismatch phase Ψ with respect to the design optics (cf. section 2.3). The dependence on these parameters is apparent, since they determine the shape and the orientation of the RMS ellipse in normalized phase space at the measurement stations. For a fixed mismatch parameter M, the error magnification e_{mag} is a periodic function of the mismatch phase Ψ with a period of 180°. If subsequent measurement stations are separated by $180°/n$, this period is reduced to $180°/n$. In order to guarantee a reliable emittance measurement, it thus appears to be reasonable to choose an equidistant arrangement of measurement stations covering 180°. Simulations of emittance measurements with different arrangements of measurement stations indeed show that the error magnification for a given mismatch parameter M can be minimized in this way [20] (see also section 5.3.1).

These considerations are only valid within the framework of a given design optics. The design optics is meaningful in this context, if the beam ellipse parameters are typically close to the design parameters. An arrangement of measurement stations can then be characterized by specifying the error magnification e_{mag} of the emittance error for a certain mismatch parameter M, indicating the “acceptance” of the arrangement for mismatched beams.

A change of transfer matrices by a scan of the focusing strengths of quadrupoles can be considered in the same way by constructing an equivalent transfer line. Correspondingly, the statements given above apply to the phase advance from the reconstruction point to the measurement station during the scan.

3.1.2 Reconstruction of phase space trajectories

A phase space trajectory $(x(s), x'(s))$ with initial coordinates (x_0, x'_0) evolves according to

$$\left[\begin{array}{c} x(s) \\ x'(s) \end{array} \right] = M(s, s_0) \cdot \left[\begin{array}{c} x(s_0) \\ x'(s_0) \end{array} \right], \tag{3.19}$$

provided only quadrupole fields are present (dipole fields define the reference trajectory). In analogy to Eq. (5.8), spatial offsets $x(s_i)$ at positions $s_i > s_0$ can be expressed in the form

$$\left(\begin{array}{c} x(s_1) \\ x(s_2) \\ \vdots \\ x(s_n) \end{array} \right) = \left(\begin{array}{cc} M^{(1)}_{1,1}) & M^{(1)}_{1,2} \\ M^{(2)}_{1,1}) & M^{(2)}_{1,2} \\ \vdots & \\ M^{(n)}_{1,1}) & M^{(n)}_{1,2} \end{array} \right) \left(\begin{array}{c} x_0 \\ x'_0 \end{array} \right), \tag{3.20}$$

where $M^{(i)}$ denotes the transfer matrix from s_0 to s_i. Thus, the initial coordinates (x_0, x'_0) at s_0 can be reconstructed from at least two measurements of spatial offsets $x(s_i)$ from the design orbit at positions s_i. The least square method is applicable in case of $n > 2$ in the same way as in case of emittance measurements. Such a reconstruction can be applied to determine the trajectory of the center of mass of a bunch. Moreover, difference trajectories, e.g. of two bunches, can be reconstructed in the same way through measurements of differences $\Delta x^{(i)}$ in spatial offset.

3.2 Phase space tomography

Transverse profiles of a particle beam at different positions of a linear transfer line allow to determine the transverse emittance as shown above. They can in principle serve also for a reconstruction of the two-dimensional phase space distribution of the beam. Such a reconstruction is possible by computerized tomography, which generally allows to reconstruct a two-dimensional object, e.g. a density distribution, from one-dimensional projections performed at different angles.

3.2.1 The Radon transform

Tomographic reconstructions are based on the Radon theorem:

The value of a two-dimensional function at an arbitrary point is uniquely determined by the integrals along the lines of all directions passing the point [21].

The relation between the function and the set of line integrals is provided by the Radon transform of the function, which is defined as follows. Consider a two dimensional function $f(x, y)$ of the Cartesian coordinates (x, y). Rotation of the coordinate system by an angle Θ about its origin yields new coordinates (x_Θ, y_Θ) as illustrated in Fig. 3.1. A line α parallel to the y_Θ-axis with $y_\Theta = 0$ at $\hat{x}_\Theta$ is defined by the condition

$$x \cdot \cos(\Theta) + y \cdot \sin(\Theta) = \hat{x}_\Theta. \tag{3.21}$$

The line integral of the function $f(x, y)$ along this line is given by

$$\begin{aligned} \int_\alpha f(x,y) ds &= \int_{-\infty}^{\infty}\int_{-\infty}^{\infty} f(x,y) \cdot \delta(x \cdot \cos(\Theta) + y \cdot \sin(\Theta) - \hat{x}_\Theta)\, dx\, dy \\ &\equiv P(\Theta, \hat{x}_\Theta), \end{aligned}$$

where δ denotes the Dirac δ-function. $P(\Theta, \hat{x}_\Theta)$ is called the Radon transform of $f(x, y)$. The function $P_{\Theta_0}(\hat{x}_\Theta) = P(\Theta_0, \hat{x}_\Theta)$ is the projection of the function $f(x, y)$ onto the x_Θ-axis at the angle Θ_0.

The Fourier transforms $\tilde{P}_\Theta(\omega) = \tilde{P}(\Theta, \omega)$ of the projections $P_\Theta(\hat{x}_\Theta)$ are related to the Fourier transform $\tilde{f}(u, v)$ of $f(x, y)$ according to the Fourier slice theorem. The theorem states that

$$\tilde{P}_\Theta(\omega) = \tilde{f}(\omega \cdot \cos(\Theta), \omega \cdot \sin(\Theta)) \tag{3.22}$$

[22]. The function $f(x, y)$ can be reconstructed from the Fourier transforms $\tilde{P}_\Theta(\omega)$, explicitly

$$f(x,y) = \int_0^\pi \int_{-\infty}^{\infty} \tilde{P}(\Theta, \omega) e^{2\pi i (x\omega\cos(\Theta) + y\omega\sin(\Theta))} \omega \, d\omega \, d\Theta. \tag{3.23}$$

$f(x, y)$ is thus uniquely determined by its Radon transform.

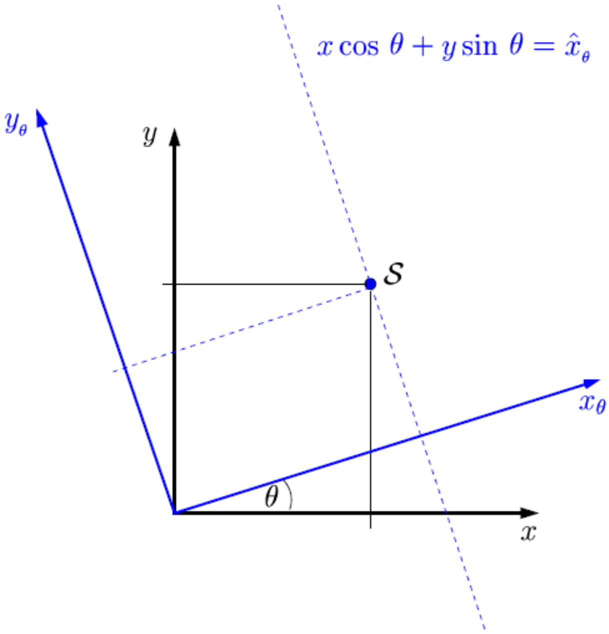

Figure 3.1: Transformation of coordinates due to rotation of the coordinate system about the origin by an angle Θ *[25]. Lines parallel to the* y_Θ*-axis are defined by Eq.* (3.21).

In tomographic applications, there is a discrete set of angles Θ_j, $j = 1...J$ at which projections are measured. Furthermore, each projection is usually a non-continuous, binned distribution $P_j(m_j)$ with $m_j = 1...N_j$ and N_j the number of bins at the angle Θ_j. The aim of a tomographic reconstruction is to approximately determine a function $f(x, y)$, usually representing a density distribution, from a discrete set of binned projections $P_j(m_j)$. Geometrically, discrete sets of angles and bins as described above provide a subdivision of a certain area of the (x, y)-plane into polygons, as is illustrated in Fig. 3.2.

Several algorithms have been invented for computerized tomographic reconstructions, such as Filtered Backprojection [23] and Algebraic Reconstruction Technique [24]. For the purpose of beam diagnostics, the Maximum Entropy algorithm described in the following sections is particularly well-suited.

3.2.2 Maximum entropy principle

The reconstruction of a two-dimensional distribution from a finite set of projections as described above is not unique. As a consequence, there is

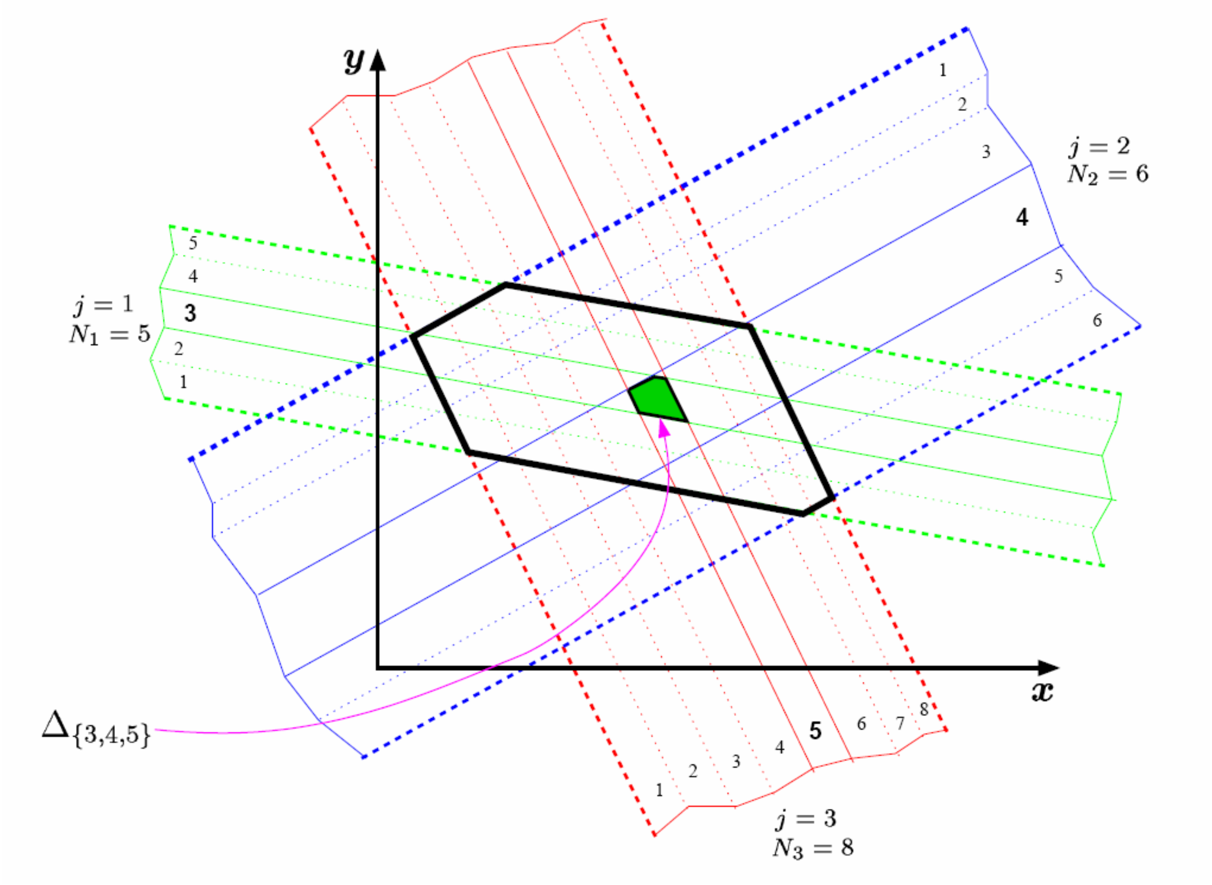

Figure 3.2: Subdivision of a region of the (x, y)*-plane into polygons [25]. The region surrounded by the bold line is sampled by* $J = 3$ *projections. Each projection is binned into intervals* $m_j = 1...N_j$*. The polygons* $\Delta_{\{m_1,m_2,m_3\}}$ *are determined by the corresponding binning-indices* m_1, m_2, m_3 *.*

a need for a mechanism for constructing an estimate of the distribution which is in agreement with the set of projections. In case the projections are the only information available, the maximum entropy principle provides a natural way for doing this.

The maximum entropy principle can be introduced here as follows. A distribution $f(x, y)$ defined in a region D of the (x, y)-plane is assumed to be normalized to yield $\int_D f(x, y)\ dx\ dy = 1$, so it allows an interpretation as probability density distribution. The entropy H of $f(x, y)$ can then be defined by

$$H = \int_D -f(x, y) \cdot ln(f(x, y))\ dx\ dy. \tag{3.24}$$

In case there are several distributions which fulfill the boundary conditions imposed by measured projections, the solution in the sense of the maximum entropy principle is given by the distribution with the largest entropy.

When there are no boundary conditions, the entropy assumes its maximum for a uniform distribution $f(x, y) = \text{const}$. The basic property of the maximum entropy solution is that it incorporates only variations in $f(x, y)$ which are forced by constraints. Maximization of entropy thus corresponds to a minimization of structure. This means in particular that the algorithm by construction minimizes artefacts and allows reliable statements on the object of investigation.

In the framework of the geometric interpretation given above, one consequence of the maximum entropy principle is that $f(x, y)$ is constant within each polygon. The problem thus reduces to finding the value f_ν, $\nu = 1, 2, \ldots$ for each polygon such that the constraints are fulfilled and the overall entropy is maximized.

The rationale of the maximum entropy principle is covered in detail in references [26, 27, 28].

3.2.3 Reconstruction algorithm

Mathematically, finding the solution with maximum entropy that approximately (in a least-squares sense) fulfills the boundary conditions is a constrained optimization problem, which can be solved by the method of Lagrange multipliers. Applying this method yields a representation of the function values f_ν as a product

$$f_\nu = \prod_{j=1}^{J} h_{jm_j(\nu)}. \tag{3.25}$$

Here, $m_j(\nu)$ is the binning index that corresponds to the polygon with index ν at the rotation angle Θ_j. Each factor $h_{jm_j(\nu)}$ is proportional to $P_j(m_j(\nu))$. The proportionality constant depends on all other factors h_{gm_g} with $g \neq j$. The factors $h_{jm_j(\nu)}$ can be adapted iteratively until the projection data are reproduced reasonably well. Details on the algorithm can be found in references [29, 30, 25, 31].

An important property of the algorithm is that it is not restricted to rotations, but works for arbitrary linear transformations of a two-dimensional function $f(x, y)$ [30]. It is thus directly applicable to phase space tomography in a linear transfer line of an accelerator. However, a reconstruction based on arbitrary linear transformations is not related to the Radon theorem, so the accuracy of such a reconstruction may be principally limited.

An implementation of the MENT algorithm written by J. Scheins [25] in C++ is used at FLASH for tomographic reconstructions [32]. The program extracts data from an input file providing one-dimensional density profiles $P_x^{(1)}(x)...P_x^{(J)}(x)$ and a corresponding set of transformation matrices $M_1...M_J$. The reconstructed two-dimensional distribution is provided in the form of a digital image, where the intensity of each pixel is calculated from the corresponding polygon fragments covering the pixel area. The user can choose the number of iterations of the algorithm in order to control the calculation time. The results are typically in good agreement after about 10 iterations [25]. The capability of the algorithm is illustrated in Fig. 3.3.

3.2.4 Phase space tomography using normalized coordinates

The transformations induced by a linear beam transfer line can be reduced to rotations by introducing normalized coordinates with respect to a design optics (cf. section 2.3). Accordingly, the one-dimensional profiles $P_x^{(i)}(x)$ have to be transformed to profiles $P_u^{(i)}(u)$ in normalized coordinates according to

$$P_u^{(i)}(u) = \frac{P_x^{(i)}(x)}{\sqrt{\beta_x(s_i)}}, \tag{3.26}$$

where $\beta_x(s_i)$ is the value of the design beta function at position s_i of a measurement station. The multiplication with $1/\sqrt{\beta_x(s_i)}$ cancels the effect of shearing in phase space that may be induced by beam transfer.

The representation in normalized coordinates allows an interpretation in terms of the Radon theorem, and an intuitive approach to the question which transformations are appropriate to obtain an accurate reconstruction. As in case of emittance measurements, it turns out that a rotation in normalized phase space over an interval of 180° is sufficient. Without additional information about the density distribution, an equidistant arrangement of measurement stations is favorable.

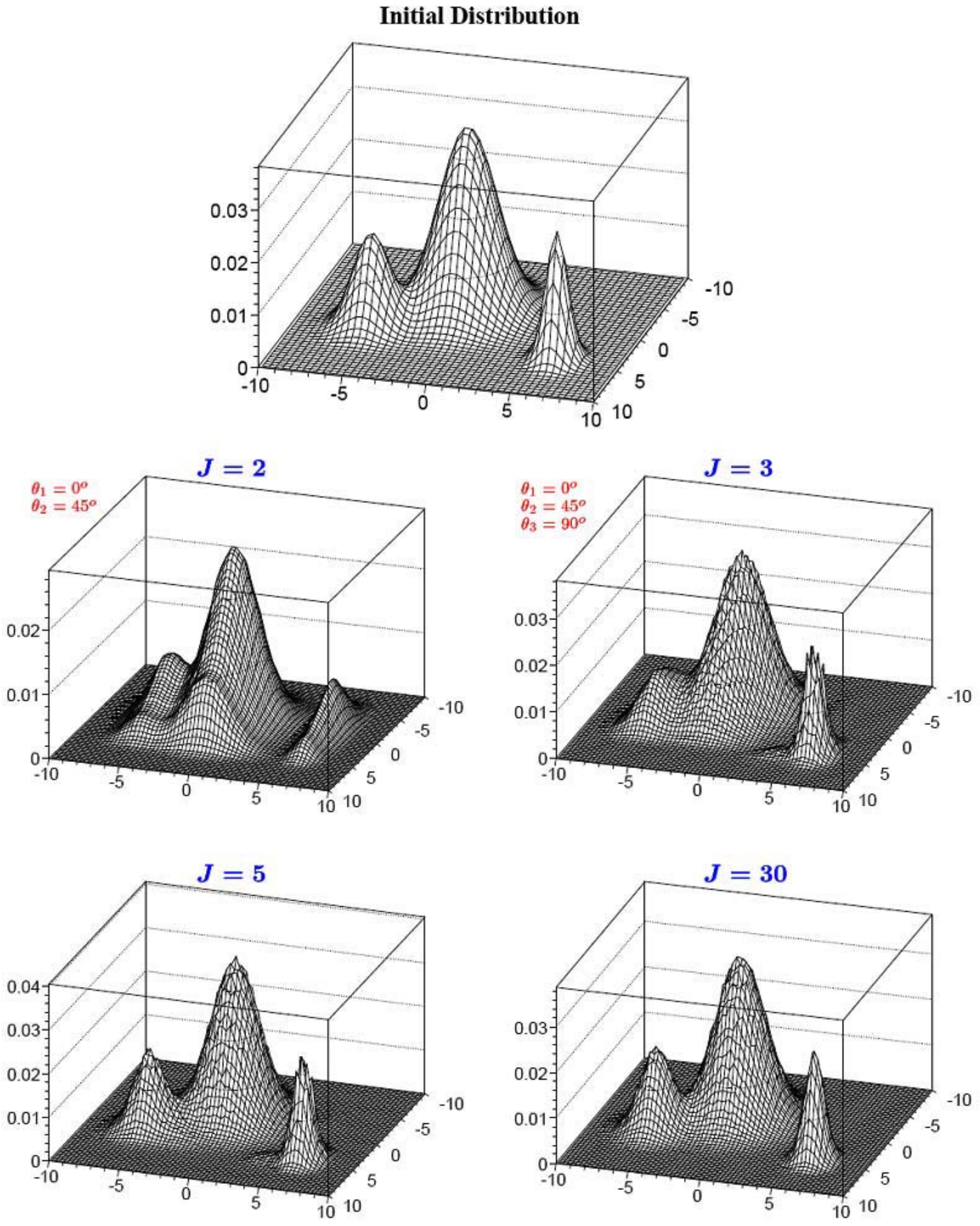

Figure 3.3: Illustration of the capability of the Maximum Entropy algorithm [25]. The initial distribution (top) is a superposition of three Gaussian distributions. The reconstructed distributions are shown for different numbers of projections of $J = 2, 3, 5, 30$ *performed at different rotation angles.*

3.2.5 Higher-dimensional tomographic reconstructions

The Radon theorem can be generalized to higher dimensions by considering the integral of a function over hyperplanes [24]. Thus, an n-dimensional function can be reconstructed from $(n-1)$-dimensional projections.

In practice, a tomographic reconstruction of a three-dimensional object is performed by dividing the object into slices corresponding to intervals in the third dimension, and applying a two-dimensional reconstruction to each slice. Effectively, this corresponds to a reconstruction of a three-dimensional distribution from two-dimensional projections.

A three-dimensional tomographic phase space reconstruction can be applied to the distribution of a particle beam in (x, x', ζ)-space, where ζ is the internal longitudinal bunch coordinate. The internal longitudinal position can be resolved for instance by inducing a longitudinal energy gradient onto the bunch and dispersing it transversally as a function of energy by a bending magnet [33]. A second possibility is to use a transverse deflecting structure, as will be described in chapters 4 and 5.

A reconstruction of a density distribution in four-dimensional transverse phase space (x, x', y, y') from two-dimensional spatial projections is not possible, since the reconstruction problem is severely under-determined. Nevertheless, the maximum entropy principle can be utilized to determine a four-dimensional distribution which reproduces measured spatial projections. A corresponding algorithm is presented in references [34, 35]. This should not be confused with a tomographic reconstruction, since the accuracy is principally limited. The four-dimensional transverse beam distribution is not of prime interest at linac-driven FELs since the coupling between both transverse planes is negligible for a well-aligned accelerator.

Chapter 4

Experimental setup

4.1 The Free Electron Laser in Hamburg

4.1.1 Overview

The Free-Electron Laser in Hamburg (FLASH) is an FEL user facility providing radiation at a fundamental wavelength which can be tuned from 47 nm down to 6 nm. The radiation is generated by Self-Amplification of Spontaneous Emission (SASE) in ultra-relativistic electron bunches. Aside from being a user facility, FLASH serves as a pilot project for the planned European X-ray FEL [36, 37].

FLASH is an upgrade of the TESLA Test Facility (TTF) linac, which was built to perform tests related to the TESLA Linear Collider Project. Already at an early stage, TTF was additionally used to drive an FEL. In 2001, it became the first SASE FEL reaching saturation at a fundamental wavelength of 98 nm [38, 39]. The facility was redesigned and augmented by additional accelerator modules, and lasing in a saturated regime at fundamental wavelengths down to 13 nm was reported in 2006 [1]. Another upgrade allowed to generate FEL radiation at 6.5 nm in 2007.

A schematic of FLASH is shown in Fig. 4.1. The first part of the facility is a linear accelerator (linac) providing ultra-relativistic electron bunches. The linac is composed of a laser-driven photocathode mounted in a 1.3 GHz copper cavity (RF gun), six superconducting accelerator modules (ACC1 to ACC6), and two magnetic chicanes called bunch compressors BC2 and BC3 for historical reasons. The RF gun generates electron bunches with a charge in the range of 0.5 to 1 nC and an energy of ≈ 4.5 MeV. A dipole magnet allows to deflect the electron beam into a dump for commissioning purposes. The beam energy is boosted to about 130 MeV in module ACC1.

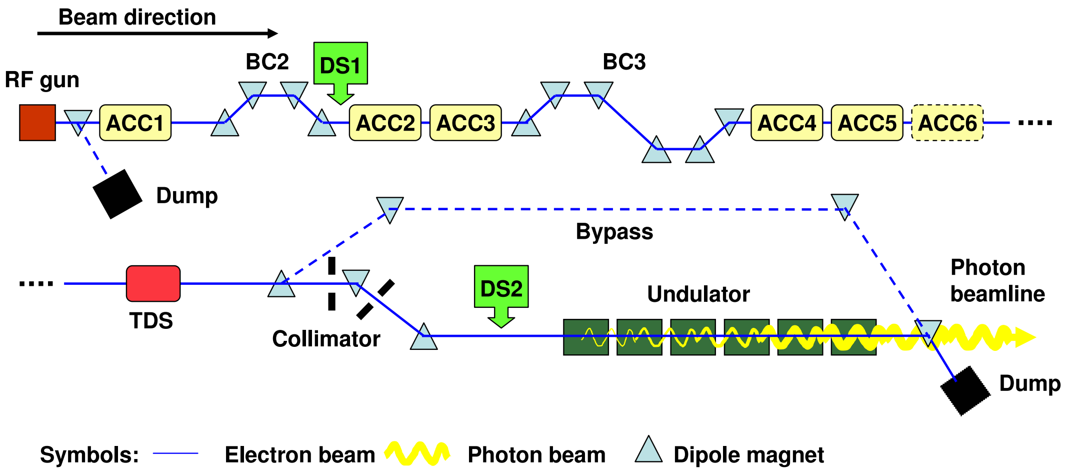

Figure 4.1: Schematic layout of FLASH (not to scale). The linac (top) is composed of an RF gun, six accelerating modules ACC1 to ACC6, and two bunch compressors BC2 and BC3. Two diagnostic sections for emittance measurements (DS1 and DS2) are installed. A transverse deflecting structure (TDS) is located at the end of the linac. Six undulator magnets are used to generate FEL radiation. The total length of the facility (excluding the experimental hall) is about 250 m.

The module can be used to induce a longitudinal energy gradient onto the bunches which leads to bunch shortening in BC2. Modules ACC2/3 further accelerate the beam to about 380 MeV, before the bunches are longitudinally compressed a second time in BC3. The accelerator modules ACC4 to ACC6 allow to reach a final particle energy of up to 1 GeV. Details on the linac can be found in [40].

At the end of the linac, six 4.5 m long undulator magnets are installed in which the FEL radiation is generated. The undulator magnets are preceded by a collimator system to protect them from radiation damage. The collimator system comprises several apertures in the straight and in the dispersive section allowing to absorb off-orbit as well as off-energy particles [41]. The energy acceptance is ±3 % [42]. Downstream of the undulator segments, a dipole magnet deflects the electron beam into a dump, while the radiation propagates in a photon beamline to the experimental hall. The undulator section can be bypassed to facilitate machine commissioning and tests of accelerator components.

Diagnostic sections (DS1 and DS2) for emittance measurements and beam matching are installed downstream of BC2 and upstream of the undulator magnets. A transverse deflecting structure (TDS) is located at the end of the linac directly downstream of module ACC6. The detailed setup

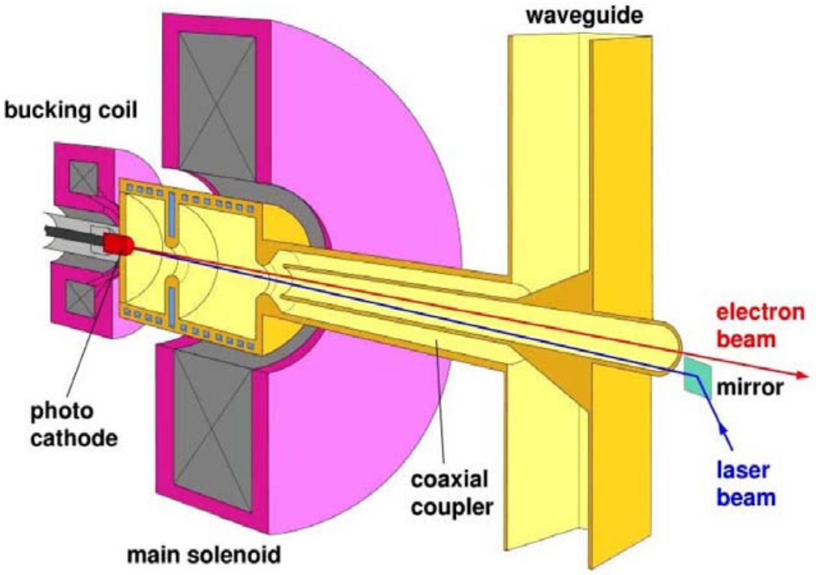

Figure 4.2: Scheme of the RF electron gun of FLASH. The photocathode is mounted at the back of a $1\frac{1}{2}$-cell copper cavity. A laser beam is reflected onto the cathode by a small mirror outside the beam axis. The RF power for the cavity is fed into the structure through a coaxial coupler at the exit. The cavity is surrounded by a solenoid (main solenoid) providing transverse focusing. A second solenoid at the back of the cathode (bucking coil) compensates the field of the main solenoid at the cathode. Great care has been taken to built an axially symmetric structure to minimize transverse field asymmetries.

around the TDS will be shown in section 4.2.

4.1.2 The RF gun

A schematic of the RF-gun is shown in Fig. 4.2. The electron source is a cesium-telluride (Cs_2Te) photocathode mounted in the backplane of a $1\frac{1}{2}$-cell copper RF cavity. The cathode is illuminated by laser-pulses with a wavelength of 262 nm which liberate electrons by photo emission. The quantum efficiency of the cathode is in the order of 1 to 5 % [43]. The longitudinal intensity profile of the laser pulses is Gaussian with a duration of about 4.4 ps (RMS). A “flat top”- distribution with a diameter of typically 3 mm is realized transversely using an iris [43]. The laser generates trains (macropulses) of up to 800 pulses (micropulses), each micropulse providing a bunch of electrons. The micropulse repetition rate is typically 1 MHz. The macropulse repetition rate can be set to 2, 5 or 10 Hz. During the measurements presented in this thesis, a macropulse repetition rate of 5 Hz

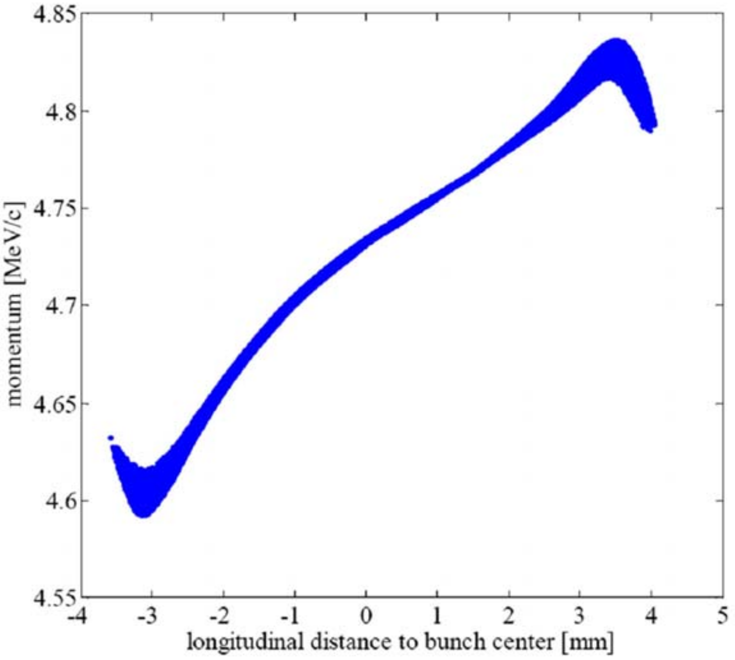

Figure 4.3: Typical electron distribution in longitudinal phase space downstream of the RF gun (simulation). The bunch head is on the right hand side.

with either one bunch or two bunches per macropulse was used.

The RF cavity has a resonance frequency at 1.3 GHz. The resonance frequency depends critically on the temperature which is stabilized to about 0.02°C by a water cooling system. The peak longitudinal electric field at the position of the cathode amounts to 42 MV/m. The RF gun can be operated with an RF pulse length of up to 900 μs at a repetition rate of 10 Hz [44]. Laser and RF of the cavity are synchronized within less than 170 fs (RMS), which corresponds to a phase jitter of 0.08° at 1.3 GHz [45]. The nominal operation point of the RF gun with respect to the first electrons emitted by the cathode is 38° from the zero-crossing phase of the longitudinal electric field. Although this phase is within the rising edge of the accelerating field, electrons at the front of a bunch gain more energy than those at the back mainly due to the traveling time from the half to the full cell [46] (cf. Fig. 4.3).

The electrons of a bunch interact with each other owing to their electric charge. The effective force on an electron resulting from the interaction with all the other particles is called space charge force. Space charge forces are strong at positions with a large gradient in particle density. In the rest frame of a bunch, space charge forces result from pure Coulomb fields. In the laboratory frame, they are a combination of electric and magnetic forces. At high energies, the transverse electric forces are partly compensated by magnetic forces so the transverse space charge force is proportional to the inverse of the beam energy squared [7]. Space charge forces are therefore of particular importance in the low-energy section of the linac. In order to counteract transverse space charge forces and to minimize space charge induced emittance growth, the RF cavity is surrounded with a solenoid coil which provides transverse focusing. The field of the solenoid at the position of the cathode is compensated by a second solenoid (bucking coil).

Bunches leaving the gun have a Gaussian longitudinal charge density profile with a length of roughly 2 mm (RMS) with a peak current of less than 100 A. The normalized transverse emittance is about 2 μm. The bunch charge can be varied and is typically in the range of 0.5 to 1 nC with shot-to-shot fluctuations of about 1 % (RMS) [47]. A more detailed characterization of the RF gun can be found in [44, 48].

4.1.3 Beam acceleration

An accelerator module is composed of 8 superconducting cavities manufactured from pure niobium and a pair of superconducting quadrupole magnets at the exit. Cavities and quadrupole magnets are cooled to 2 K and 4.5 K, respectively, by a cryogenic system using superfluid and liquid helium. The cavities are 9-cell standing wave structures of 1.03 m length and an iris radius of 35 mm. They are operated with an accelerating electric field of up to 25 MV/m.

Each cell of a cavity is excited in a TM_{010}-mode. The mode is characterized by a longitudinal electric field which is almost homogenous over the aperture of the structure. The resonance frequency ν_0 of this mode is 1.3 GHz. The fields within the 9-cell structure couple in such a way that neighboring cells are 180° out of phase (π-mode). The length of the cells is chosen such that a relativistic particle needs half an RF period to traverse one cell. As a result, the particle experiences the same accelerating force in each cell.

The mean accelerating field $\mathcal{E}_{acc}$ acting on a relativistic charged particle traversing a cavity is given by

$$\mathcal{E}_{acc} = \frac{1}{L_c} \int_{-L_c/2}^{L_c/2} \mathcal{E}_0 \cdot \cos\left(\omega_0 t(z)\right) dz, \tag{4.1}$$

where L_c is the cavity length, $\mathcal{E}_0$ the amplitude of the longitudinal electric field, $t(z) \approx z/c + t_0$ with an arbitrary constant t_0, and $\omega_0 = 2\pi\nu_0$. The maximum accelerating field $\mathcal{E}^0_{acc}$ is obtained for $\omega_0 t(z) = 0$ in the center of each cell. A particle is said to be accelerated "on-crest" in this case. If the particle injection is delayed by Δt with respect to on-crest acceleration, the particle is said to be accelerated "off-crest" at an RF phase $\phi = \omega_0 \Delta t$. The accelerating field seen by such a particle is given by

$$\mathcal{E}_{acc} = \mathcal{E}^0_{acc} \cdot \cos(\phi), \tag{4.2}$$

as can be verified by transforming Eq. (4.1). The same terms are used in case of electron bunches and refer to the bunch center (mean longitudinal electron position).

The RF phases of the cavities are regulated via the klystrons powering them. Four klystrons with a power of 5 to 10 MW are used, one for the RF gun, one for module ACC1, one for modules ACC2 and ACC3, and one for modules ACC4 to ACC6. As a consequence, only four phases can be chosen independently. The on-crest phase of the modules can be determined by measuring the horizontal charge density distribution at positions with a significant dependence of the horizontal beam position on the beam energy (horizontal dispersion). The standard deviation of the particle energy within a bunch is minimized at the on-crest phase, and consequently the horizontal bunch width is minimized in presence of dispersion. Corresponding measurements can be carried out using optical transition radiation (OTR) screens (cf. section 4.1.7) located within the bunch compressor chicanes and in the collimator section.

Aside from a longitudinal electric field, particles not moving on-axis through an RF cavity are subject to radial forces due to a radial electric field component $\mathcal{E}_r$ and an azimuthal magnetic field B_φ, where cylindrical coordinates (r, φ, z) are used. The forces provide focusing at the entrance of a cell and defocusing at its exit in case of on-crest operation. Due to acceleration within the cell, there is an overall focusing force (RF focusing). The strength of RF focusing depends on the ratio of the energy gain per cell to the particle energy. It is thus of particular importance at low energies. The transverse dynamics in cavities including RF focusing as well as the attenuation of angles x', y' through acceleration can be described accurately by linear transfer matrices [49]. More details on superconducting accelerator structures can be found in references [50, 51, 52].

4.1.4 Bunch compression

High peak currents in the order of a few kiloamperes are generated by longitudinal bunch compression at particle energies of more than 100 MeV. Compression of ultra-relativistic particle bunches can only be accomplished by introducing a dependence of the path length on the internal longitudinal position of bunch particles, since the differences in velocity resulting from slightly different particle energies are insignificant. This is realized in two steps. At first, a nearly linear correlation between energy and internal longitudinal position is imprinted onto a bunch through off-crest acceleration. Afterwards the particles are sent through a magnetic chicane introducing different path lengths depending on the particle energy. The principle of the compression process is illustrated in Fig. 4.4.

At FLASH, a two-stage compression system is used (cf. Fig. 4.1). The first stage is the magnetic chicane BC2 consisting of four horizontally deflecting dipoles. All dipoles are connected to the same power supply. The nominal deflection angle Θ_0 in each dipole is 18° at a beam energy E_0 of 130 MeV. The deflection results in a maximum offset (bump amplitude) of 320 mm from the beam axis. The difference Δs in path length between the beam trajectory through the chicane and the straight trajectory is about 85 mm [53].

The second stage (BC3) consists of six horizontally deflecting dipoles, also connected to one power supply. Here, the nominal deflection angle is $\Theta_0 = 3.8°$ at $E_0 = 380$ MeV. The bump amplitude amounts to 191 mm. The deflection leads to an additional path length of $\Delta s \approx 24$ mm [53].

Bunch compression in linear approximation

The bunch length of $\sigma_\zeta \approx 2$ mm (RMS) downstream of the gun corresponds to a standard deviation of the RF phase in module ACC1 of $\approx 3.2°$. The energy gained by the bunch electrons thus significantly depends on their internal position ζ within the bunch in case of off-crest acceleration. In a small interval around $\zeta = 0$ (mean longitudinal electron position), this dependence can be described by a linear "energy chirp factor"

$$h = \left. \frac{d(\Delta E/E_0)}{d\zeta} \right|_{\zeta=0}, \tag{4.3}$$

where ΔE denotes the energy gain in the module and E_0 the nominal energy downstream of the module. The relative energy deviation

$$\delta = (E - E_0)/E_0. \tag{4.4}$$

of an electron with energy E can thus be written in the form

$$\delta(\zeta) = h \cdot \zeta + \delta_i, \tag{4.5}$$

where δ_i is the initial energy deviation of the electron divided by E_0.

The path length difference Δs introduced by a magnetic chicane like BC2 and BC3 with respect to the straight trajectory depends on the bending angle Θ in the dipoles of the chicane. It can be shown that

$$\Delta s(\Theta) \propto \Theta^2 \tag{4.6}$$

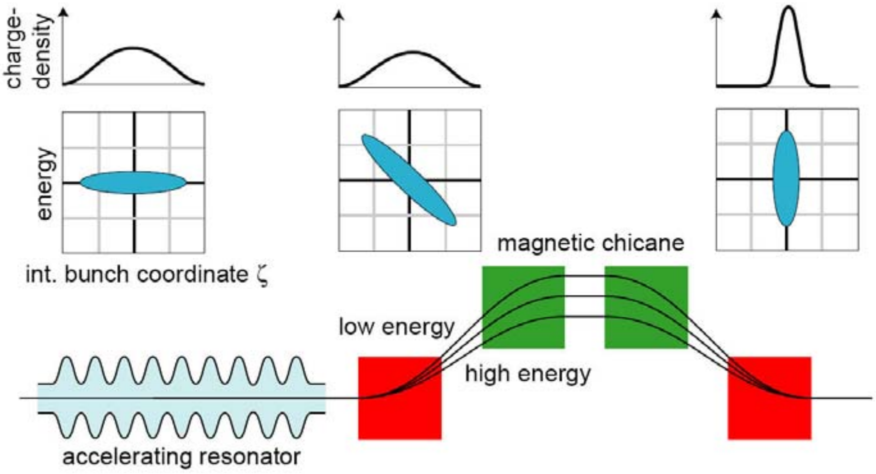

Figure 4.4: Principle of longitudinal compression of a relativistic electron bunch [2]. The bottom row shows an accelerating cavity and the four dipole magnets of a magnetic chicane. The top figures show the longitudinal bunch charge distribution and the correlation between the internal position of an electron inside the bunch and its relative energy deviation before the cavity (left), behind the cavity (middle), and behind the magnetic chicane (right). In the RF cavity the particles are accelerated off-crest so the trailing electrons receive a larger energy gain than the leading ones. In the magnetic chicane the electrons at the tail move on a shorter orbit than those at the head and catch up with them.

for $\Theta \ll 1$ [54]. Since $\Theta \propto 1/E$ with E denoting the particle energy, the deflection angle $\Theta(\delta)$ as a function of the relative energy deviation δ is given by

$$\Theta(\delta) = \frac{\Theta_0}{(1+\delta)}, \tag{4.7}$$

where Θ_0 is the nominal deflection angle at energy E_0. Inserting expression (4.7) into (4.6) and expanding the term $1/(1+\delta)^2$ into a Taylor series around $\delta = 0$ yields

$$\Delta s(\delta) \propto \Theta_0^2 \left(1 - 2\delta + 3\delta^2 + ...\right). \tag{4.8}$$

The internal bunch coordinate ζ of an electron with relative energy deviation δ thus is changed behind a magnetic chicane according to

$$\begin{aligned} \Delta\zeta(\delta) &= \Delta s(\delta) - \Delta s(\delta = 0) \\ &\propto 2\Theta_0^2 \left(\delta - \frac{3}{2}\delta^2 + ...\right). \end{aligned} \tag{4.9}$$

Introducing a proportionality constant[1] R_{56}, this relation can be written as

$$\Delta\zeta(\delta) \approx R_{56} \cdot \delta - \frac{3}{2} R_{56} \cdot \delta^2. \tag{4.10}$$

Within small longitudinal bunch sections, the relative energy deviation is typically less than 1 % so the quadratic and higher order terms can be neglected. The leading term describes a shearing of a particle distribution in the (ζ, δ)-plane according to

$$\begin{pmatrix} \zeta \\ \delta \end{pmatrix} \longmapsto \begin{pmatrix} \zeta + R_{56} \cdot \delta \\ \delta \end{pmatrix}. \tag{4.11}$$

Inserting expression (4.5) yields

$$\zeta \longmapsto (1 + hR_{56}) \cdot \zeta + R_{56} \cdot \delta_i. \tag{4.12}$$

The RMS length σ_ζ of the considered bunch section thus becomes

$$\sigma_\zeta = \sqrt{(1 + hR_{56})^2 \cdot (\sigma_\zeta^0)^2 + R_{56}^2 \cdot \langle \delta_i^2 \rangle}, \tag{4.13}$$

---

[1] The notation R_{56} is standard and stems from a matrix formalism. $\alpha = -R_{56}$ is called momentum compaction factor.

where σ_ζ^0 denotes the length prior to compression and $\langle \zeta \cdot \delta_i \rangle = 0$ has been assumed. The term $R_{56}^2 \cdot \langle \delta_i^2 \rangle$ is typically small and plays a minor role. The ratio $C = \sigma_\zeta^0 / \sigma_\zeta$ is called compression factor (here: local compression factor). The bunch length is reduced (compression factor > 1) for $1 + hR_{56} < 1$. The minimum length is achieved for $1 + hR_{56} = 0$ (full compression). For $1 + hR_{56} < 0$ (over-compression), the length is increased compared to full compression.

In case of BC2 and BC3, one obtains $R_{56} \approx 180$ mm and $R_{56} \approx 49$ mm, respectively [53]. Assuming on-crest operation of module ACC2/3, full compression occurs at an RF phase ϕ_{ACC1} of about $-11°$, while at $\phi_{ACC1} = 0$ the compression factor is equal to one.

The RF curvature causes strong variations of the local compression factor along a bunch. As a consequence, the longitudinal charge density distribution after compression may significantly deviate from a Gaussian distribution. Under FEL operating conditions, bunches are typically accelerated about $-8°$ off-crest in module ACC1. Regarding the standard deviation of the RF phase of the bunch particles of about $3°$, this means that the tail of a bunch is only slightly compressed, while the initial front is over-compressed. The bunch section subject to full compression is located at the bunch head and forms a spike in the current profile with a peak current of a few kiloamperes. Figure 4.5 shows results of particle tracking simulations illustrating the development of current profile and particle distribution in longitudinal phase space[2] in such a case.

Collective effects

The bunch compression process leads to a high peak current and high longitudinal gradients in charge density. As a result, strong longitudinal space charge forces occur around the high-current region and lead to a significant acceleration of particles at the leading edge and a deceleration of particles at the trailing edge of the current spike. Furthermore, the particles emit synchrotron radiation on the curved paths within the bending magnets of the magnetic chicanes and thus lose energy. Particles at the front of a bunch may interact with the radiation field generated by the bunch tail, since the

---

[2] The plane spanned by the internal bunch coordinate ζ and the particle energy E (or the relative energy deviation $\Delta E / E_0$) are loosely called longitudinal phase space in short-hand.

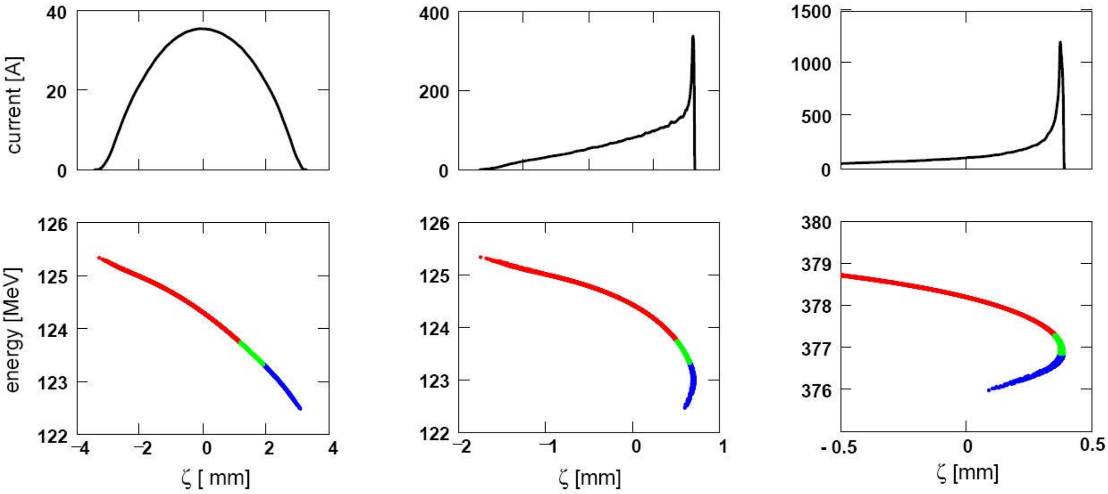

Figure 4.5: Electron beam current as a function of the internal bunch coordinate ζ (top row) and electron distribution in longitudinal phase space (bottom row) at different positions along the linac (simulation) [2]. Left: behind the first acceleration module. The bunch has a length of 1.3 mm (RMS) and a strong correlation between energy and longitudinal position due to off-crest acceleration. It can be seen that the energy chirp factor varies along the bunch. The different colors indicate the initial positions within the bunch (blue: head of bunch, green: middle section, red: tail). Middle: behind BC2. Full compression occurs at the bunch head resulting in a spike in the current profile. The peak current has grown from 35 A to 350 A. Right: behind BC3. The initial front of the bunch is over-compressed. The peak current amounts to 1250 A. The reference point $\zeta = 0$ is chosen to be the mean particle position.

photons move on a straight path through the magnet and may overtake the bunch electrons. These effects are particularly strong for wavelengths in the order of the bunch length since the particles radiate coherently in this case. Also substructures in the longitudinal charge density profile, in particular the sharp current spike discussed above, may lead to coherent emission and a significant energy loss of the coherently radiating particles [57, 58].

In particle tracking simulations including these collective phenomena, typically three strong effects can be distinguished: space charge forces between BC2 and BC3, space charge forces downstream of BC3, and coherent synchrotron radiation (CSR) within the bending magnets of BC3. These effects lead to characteristic deformations in longitudinal phase space which are illustrated in Fig. 4.6.

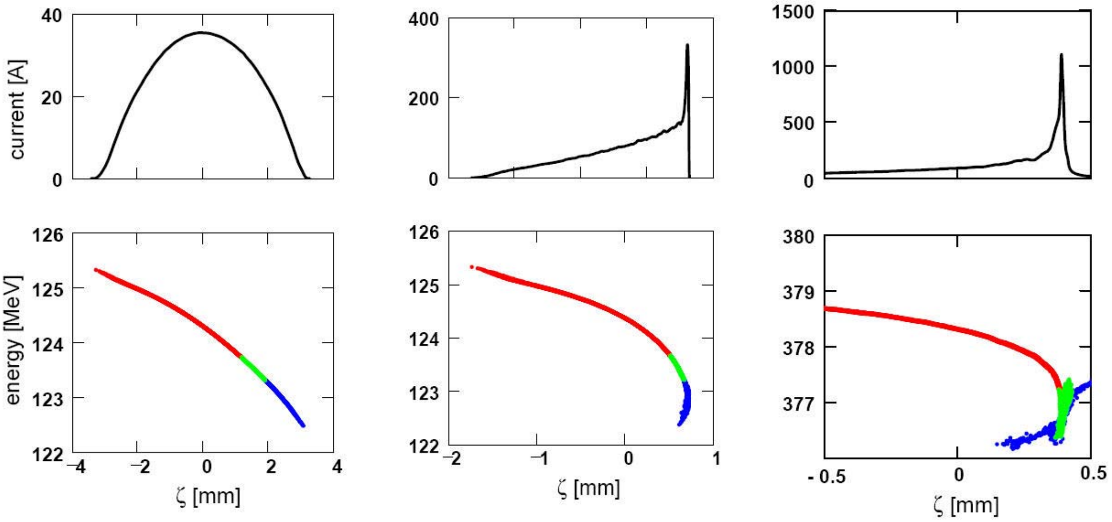

Figure 4.6: Influence of coherent synchrotron radiation and space charge forces on the bunch compression process [2]. The figure shows the current profile (top row) and the distribution in longitudinal phase space (bottom row) at the same positions as in Fig. 4.5. In contrast to the results shown in Fig. 4.5, collective effects are included. Upstream and downstream of BC2 (left and middle), the distribution in longitudinal phase space hardly deviates from the ideal one shown in Fig. 4.5. Strong distortions occur downstream of BC3 (right). The bunch section which is close to full compression (green region and part of the blue region) shows a significantly broadened energy distribution due to both CSR and space charge. In particular, a spike towards lower energies can be observed, which is mainly due to CSR. The small spike towards higher energies (green) indicates space charge forces downstream of BC3 and gets more pronounced as the bunch moves on. The bunch section close to full compression downstream of BC2 (blue region) exhibits a spike towards positive ζ due to space charge between BC2 and BC3: The forces lead to an energy broadening which involves a shearing in longitudinal phase space within BC3. The results were obtained by particle tracking simulations using the codes ASTRA [55] and CSRTrack [56].

4.1.5 The undulator section

Single-pass FELs require long undulator systems in order to reach saturation of the radiation power. At FLASH, six planar undulator magnets with a length of 4.5 m each are installed downstream of the linac. The magnets are composed of a periodic sequence of NdFeB (neodymium-iron-boron) permanent magnets with alternating polarity and iron pole shoes with a gap height of 12 mm in between, thus generating an alternating vertical magnetic field. The period of the magnetic field is $\lambda_u = 27.3$ mm. The peak magnetic field on the axis amounts to 0.47 T. Passing electrons perform an oscillation in the (x, z)-plane. Between the six undulator magnets, quadrupole magnets are installed for beam focusing. Beam position monitors and wire scanners are used for measuring the beam position and the transverse beam size (see the following sections). The quadrupole magnets are equipped with movers allowing a fine adjustment of their transverse position. More details on the undulator magnets can be found in reference [59].

4.1.6 Accelerator Magnets

Dipole and quadrupole magnets are installed at various positions along the linac. Dipole magnets are used to create a curved design orbit as in magnetic chicanes. Moreover, small dipole magnets are used to empirically adjust the beam orbit in horizontal and vertical direction. The latter ones will be called steering magnets, and the former ones bending magnets. Quadrupole magnets are used for beam focusing. They are combined with steering magnets which provide a correction dipole field.

Conventional dipole magnets consist of an iron yoke with two flat pole shoes surrounded by copper coils which excite a homogeneous magnetic field in the gap between the pole shoes (Fig. 4.7(a) and (b)). Conventional quadrupole magnets comprise four iron pole shoes with surrounding copper coils (Fig. 4.7(c)). The pole shoes have a hyperbolic surface contour in order to minimize higher harmonic fields. At FLASH, also superferric quadrupole magnets containing superconducting NbTi-coils are used. A doublet of superferric quadrupole magnets is installed at the exit of each cryomodule containing the accelerator structures. The entire magnets (including the iron yoke) are cooled to 4.5 K by liquid helium. A pair of superconducting horizontal and vertical steering magnets composed of

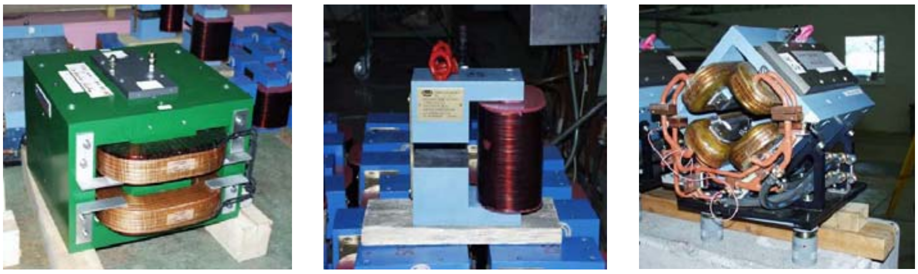
(a) (b) (c)

Figure 4.7: Photographs of conventional accelerator magnets used at FLASH [60]. (a): Bending magnet. (b): Steering magnet. (c): Quadrupole magnet.

NbTi coils is installed within the aperture of the quadrupole magnets [61]. More details on the magnets within the experimental beamline are given in section 4.2

4.1.7 Basic electron beam diagnostics

Toroids

Inductive toroidal current transformers (toroids) around the beam allow to measure the beam current of a macropulse and thus the bunch charge [62]. The core of the toroids is made from supermalloy (alloy of Ni,Mo,Fe) which provides a high magnetic permeability. The charge resolution is 2-3 pC [63]. Toroids are placed at regular intervals along the linac.

Beam position monitors

Beam position monitors (BPMs) are used to measure the transverse offset of the beam from the beam axis. Several types of BPMs are installed at FLASH. The ones most frequently used are button BPMs and stripline BPMs. In button BPMs, four electrodes (pick-up electrodes) are mounted in an orthogonal arrangement around the beam pipe, two of them being separated vertically and the other two horizontally. The beam centroid is evaluated by comparing the signals measured through the electrodes. Button BPMs are space saving and therefore installed in regions with limited space as the injector and the undulator section. A resolution down to 10 μm (RMS) for single bunches can be achieved with button BPMs [64].

Stripline BPMs have the same working principle, but use tube electrodes (striplines) with a length of 20 cm arranged parallel to the beam axis. They also allow a resolution in the order of 10 μm [65]. Stripline BPMs are installed at various positions along the linac, in particular within quadrupole magnets.

Within the superconducting accelerator modules, circular cavities (cavity BPMs) are used to measure the transverse beam position. A beam traversing the cavity off-axis excites a TM_{110} dipole mode, whose amplitude is measured. The amplitude is proportional to the beam displacement and the bunch charge. Cavity BPMs allow also a resolution in the order of 10 μm [66].

Optical transition radiation screens

Transition radiation is emitted whenever a relativistic charged particle passes the boundary of two media of different dielectric properties. The radiation is emitted both into the forward and the backward hemisphere of the boundary. In case of relativistic particles, the radiation in the forward hemisphere is emitted in a cone around the direction of movement of the particle. The radiation in the backward hemisphere is emitted in a cone around the direction of the specular reflection of the incoming particle. The radiation is radially polarized, with the electric field vector pointing towards the axis of the emission cone. The intensity correspondingly vanishes on-axis. The opening angle of the emission cone is in the order of $1/\gamma_r$, where γ_r denotes the relativistic Lorentz-factor. The spectrum of transition radiation is flat.

For the purpose of beam diagnostics, an aluminum-coated silicon wafer (screen) is placed in the beamline. The screen is rotated so the angle of incidence of the particle beam is 45°. The backward transition radiation propagates orthogonally to the beam direction. The transition radiation in the optical wavelength range (OTR) is recorded by a camera. The efficiency of OTR (measured by the number of emitted photons in the optical wavelength range per electron) for relativistic electrons is a few percent [67]. For a bunch charge of 1 nC, the number of emitted photons per bunch is thus in the order of 10^8, which results in a radiation intensity that is easily detectable with standard CCD devices. The intensity emitted from a small area of the screen is proportional to the total charge intercepting the screen in this area, as long as coherent emission does not occur. A camera image then yields the transverse intensity distribution of a bunch.

The spatial resolution that can be reached with OTR in case of ultra-relativistic particle beams is limited due to diffraction effects and the radial polarization of OTR, which leads to a specific angular intensity distribution. Owing to diffraction the small opening angle of the radiation lobes in the order of $1/\gamma_r$ implies that radiation of a wavelength λ originates from a region of transverse size at least in the order of $\gamma_r \cdot \lambda$. Due to long tails in the angular intensity distribution of the radiation lobes the resolution critically depends on the angular acceptance of the optical system used to detect the radiation [68, 69, 70, 71]. Typically, the resolution obtained with OTR is worse than the nominal resolution of the optical system [70, 72].

More details on OTR can be found in references [67, 73, 74].

Determination of the beam energy

The beam energy can be determined by measuring the transverse displacement of the beam downstream of a dipole magnet (energy spectrometer). Corresponding measurements can be performed within the bunch compressor chicanes and in the collimator section. At beam energies of several hundreds of MeV, this method allows for an accuracy of a few percent. Under FEL operating conditions, the final beam energy can be determined precisely from the radiation spectrum measured by means of grazing incidence spectrometer systems [75].

4.2 The experimental beamline

4.2.1 Overview

The experimental beamline is schematically shown in Fig. 4.8. A transverse deflecting RF structure (TDS) is installed downstream of the accelerating modules. The TDS transfers the longitudinal charge density profile of single bunches to a vertical charge density profile downstream of the structure by means of a rapidly varying electromagnetic field, similar as in conventional oscilloscope tubes. The transverse charge density distribution of single bunches can be measured with an OTR station (OTR-2) installed about 9 m downstream of the TDS. This arrangement allows for the measurement of the current profile of single bunches. Moreover, measuring the horizontal width along a bunch with different focusing strengths of the upstream quadrupole magnets (Q-ACC4 to Q-ACC6) permits to determine the horizontal slice emittance. The quadrupole between the TDS and the screen (Q-TDS) is vertically defocusing thus amplifying the divergence induced by the TDS. The screen of station OTR-2 is mounted horizontally off-axis. Single bunches are deflected onto the screen by a fast kicker installed 2 m in front of the TDS. This configuration renders the possibility of parasitic measurements by kicking single bunches out of a bunch train.

A second screen is installed in the collimator section downstream of a horizontally deflecting dipole. The dipole disperses bunch particles horizontally as a function of energy. When the TDS is switched on, the vertical

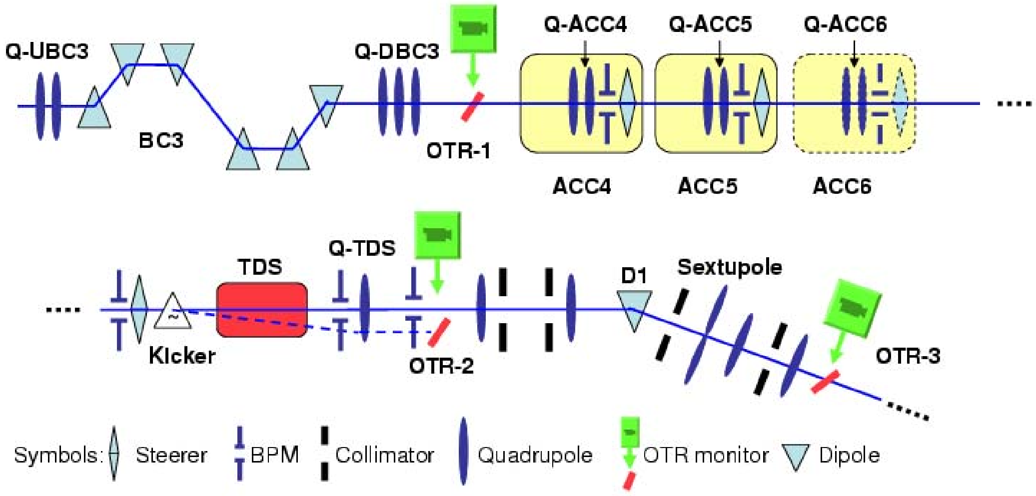

Figure 4.8: Schematic of the experimental beamline. The figure shows the section of the FLASH linac ranging from the second bunch compressor (BC3) to the collimator section (cf. Fig. 4.1). The TDS is installed downstream of the accelerating modules. The structure allows to deflect electrons vertically as a function of their longitudinal position within a bunch. A horizontal kicker steers single bunches horizontally onto an off-axis screen, on which the particle distribution in the horizontal-longitudinal plane (x, ζ) is measured. The horizontal slice emittance can be measured by changing the focusing strengths of the quadrupole magnets Q-ACC4 to Q-ACC6. The monitor OTR-3 located in a horizontally dispersive section permits to measure the charge density distribution of single bunches in longitudinal phase space. The beam can be matched to a special optics using the OTR station OTR-1 and the upstream quadrupole magnets Q-UBC3 and Q-DBC3. BPMs and steering magnets allow to adjust the beam orbit. Only a selection of BPMs, steering magnets and OTR stations installed in this segment of the linac is shown. Module ACC6 was installed in 2007 and not present during most of the measurements presented in this thesis.

particle position on the screen depends on the longitudinal position within a bunch, while the horizontal position depends on the energy. This configuration allows for single-shot measurements of the particle distribution in longitudinal phase space.

In order to optimize the resolution of the measurements, appropriate accelerator optics were prepared for the different measurements. The OTR station OTR-1 was used to measure horizontal and vertical ellipse parameters of the bunches by changing the focusing strengths of the upstream quadrupole magnets (Q-DBC3). The quadrupole triplet Q-DBC3 and the doublet upstream of BC3 (Q-UBC3) were used to match the beam ellipse parameters to the design values. BPMs and steering magnets installed along the beamline allowed to correct the orbit, in particular after changing the focusing strength of quadrupole magnets.

In the remainder of this section, the elements of the beamline are discussed. Details on the measurements as the optics, calibration measurements, beam matching and data analysis can be found in chapter 5.

4.2.2 Optical transition radiation monitors

Standard monitors

The optical transition radiation (OTR) monitors OTR-1, OTR-2 and OTR-4 (cf. Fig. 4.8) are of the standard type used at FLASH. A schematic of such a station is shown in Fig. 4.9. An aluminum-coated silicon screen is installed within the vacuum chamber with an angle of 45° with respect to the beam axis. The screen is mounted on a vertical mover and can be moved into and out of the beamline by remote control. The backward OTR generated when a bunch intercepts the screen leaves the vacuum chamber orthogonally to the beam axis through a silica window (DUV-200), which is resistant to X-rays and provides a good transmission in the visible wavelength range. The OTR is reflected downwards by a mirror, passes lenses and filters that may optionally be inserted, and is recorded by a CCD camera. This arrangement minimizes the exposure of the camera to X-rays. The camera is connected via a IEEE1394 (firewire) link to a personal computer located in the tunnel, which in turn is connected to a server located in the control room via local ethernet.

The camera (Basler A301f) is triggered externally in synchronism with the RF system of the accelerator. It has a CCD sensor consisting of 658×494 pixels with a size of $9.9 \times 9.9\ \mu$m, from which 640×480 pixels are used for the resulting images. The dynamic range of the output signal is 2^8, providing an 8 Bit intensity resolution. The camera is equipped with a remote gain and shutter control. Each image contains the integrated OTR intensity over one macropulse. Single-bunch imaging can be achieved by operating the machine with one bunch per macropulse.

Three different lenses (achromats) with a focal length of 250 mm, 200 mm and 160 mm can be inserted remotely. They provide nominal magnifica-

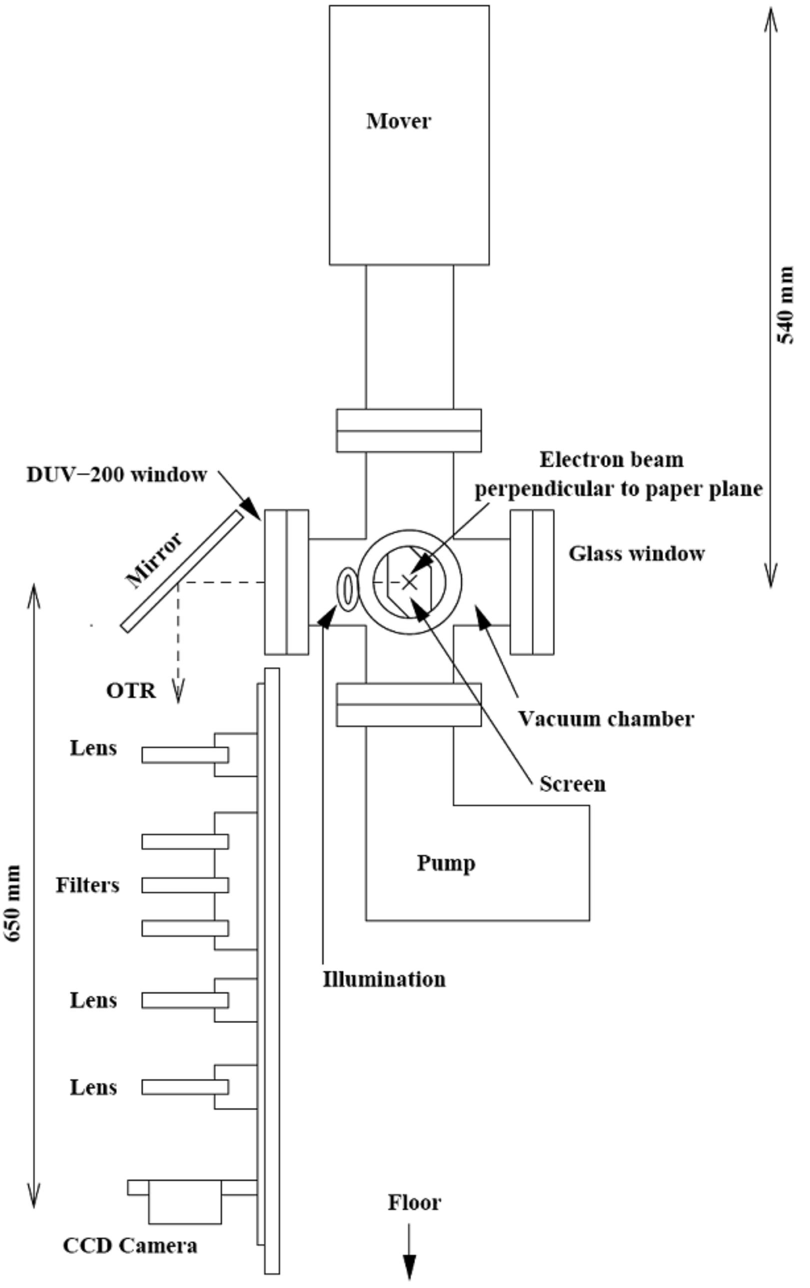

Figure 4.9: Schematic of a standard OTR monitor at FLASH [76].

tions of 1.0, 0.39 and 0.25, respectively. The corresponding calibration constants are 9.9, 25 and 39 μm/pixel. The resolution of the optical system (highest magnification) was measured to be 11 μm (RMS) [77]. A more detailed description of standard OTR monitors at FLASH can be found in references [32, 77, 76].

The monitor OTR-2

The OTR monitor OTR-2 (cf. Fig. 4.8) allows for a measurement of the transverse charge density distribution downstream of the TDS. In contrast to a standard OTR monitor, the screen is not centered on the beam axis, but has a horizontal offset. Bunches therefore have to be deflected onto the screen by a horizontal kicker. A schematic of the screen holder is shown in Fig. 4.10. Two screens, one on each side of the beam axis, allow measurements on both sides of the beam axis. In case of the measurements presented in this thesis, only the screen on the right hand side was used. The distance between both screens is 20 mm, leaving enough space for on-axis bunches to pass without being affected. The screens consist of aluminum-coated silicon wafers. Each screen has a width of 8 mm, a hight of 26.5 mm and a thickness of 0.280 mm.

Bunches steered towards the off-axis screen are absorbed by the downstream collimator system. A pre-collimator with a diameter of 30 mm is additionally installed directly behind the off-axis screen to stop secondary particles emitted from the screen and to avoid uncontrolled beam loss.

The OTR emitted by the screen leaves the vacuum chamber orthogonally to the beam direction and is reflected by a mirror so it enters a camera. In contrast to the standard OTR stations, the OTR is not deflected downwards, but horizontally so it propagates parallel to the beam to a camera located next to the beam axis.

The camera (Basler A311f) is triggered externally in synchronism with the TDS and the kicker. It contains a CCD sensor with 658×494 pixels of 9.9×9.9 μm size as in case of standard OTR monitors. The dynamic range of the output signal can be selected between 2^8 and 2^{12}. The minimum exposure time is 1 μs, which allows to image single bunches at a bunch repetition rate of 1 MHz. The camera is equipped with a lense having a focal length of 200 mm and a diameter of 50 mm. An aperture was installed to improve the depth of field, so the effective aperture of the lense is reduced to 25 mm. The distance between the lense and the screen along the optical axis amounts to about 600 mm.

Transverse distances on the screen were calibrated using bore holes on the screen holder (cf. Fig.4.10), which are separated by a distance of 5 mm horizontally and vertically. A calibration constant of 24.2 ± 0.5 μm/pixel was determined in vertical direction. In horizontal direction, the angle α of

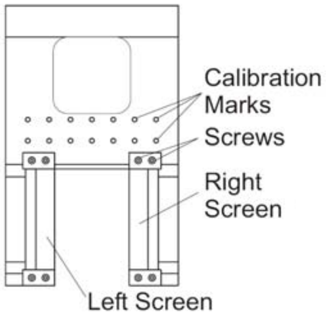

Figure 4.10: Technical drawing of the screen holder with two OTR screens (aluminum-coated silicon wafers). The screen holder provides boreholes with a distance of 5 mm for calibration purposes.

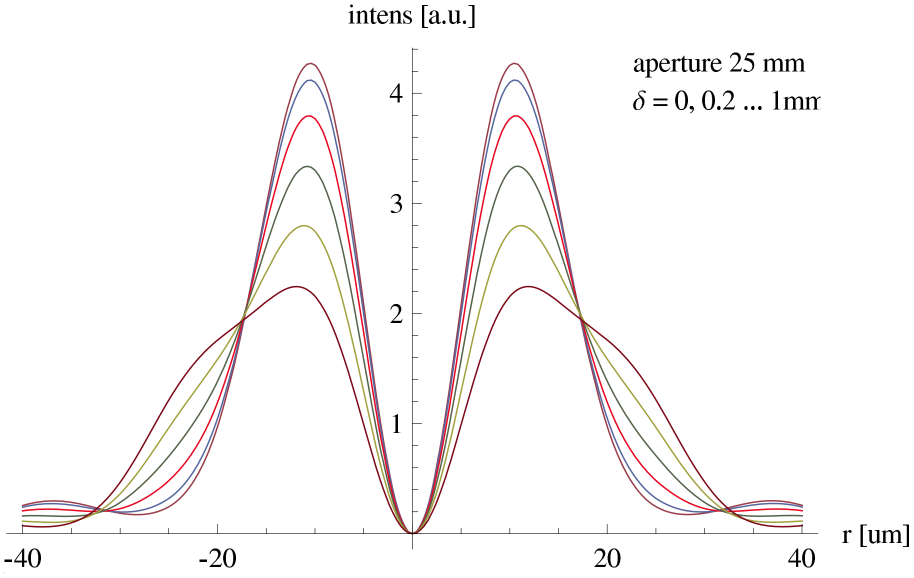

Figure 4.11: Point spread function of the optical system for OTR with $\lambda = 500$ nm and $\gamma_r = 1000$ for different distance errors $\delta = 0$ (top curve at the maxima) to $\delta = 1$ mm (bottom curve at the maxima) (courtesy: B. Schmidt [71]). The vertical axis shows the intensity in arbitrary units, the horizontal axis the radial distance r to the center of the intensity distribution in units of [μm].

the screen with respect to the beam axis has to be taken into account. By comparing the apparent distance of bore holes in horizontal and vertical direction in units of pixels, an angle of $\alpha = 48.1°$ was determined. A distance of 27.0 ± 0.6 μm orthogonal to the beam direction is imaged onto one pixel of the CCD camera. The total size of the camera window amounts to 12.9×15.5 mm.

The spatial resolution of the optical system was measured to be roughly 13 μm by using a sinusoidal test target precisely in focus [78]. Due to the angle α of the screen with respect to the beam axis, the distance from the screen surface to the lense depends on the horizontal position on the screen and changes by 5.6 mm when going from the left to the right edge. Due to these distance errors, the resolution is a function of the horizontal position. Furthermore, the particular properties of OTR have to be included. Figure 4.11 shows the calculated point spread function (response of the imaging system to a point source) for OTR at different distance errors δ up to 1 mm. The vanishing intensity at the center $r = 0$ results from the radial polarization of OTR (cf. section 4.1.7). The distance between the positions of the two intensity spikes at both sides of the minimum is roughly 20 μm independent of the distance error. The width of the intensity spikes continuously increases with increasing distance error, thus deteriorating the resolution. The resolution was estimated by convolving Gaussian test distributions with the presented point spread functions. The reconstructed standard deviation σ_{rec} can be approximated by an expression of the form

$$\sigma_{rec} = \sqrt{\sigma_{resol}^2 + \sigma_0^2}, \tag{4.14}$$

where σ_0 is the standard deviation of the test distribution and σ_{resol} an estimate for the RMS resolution. An RMS resolution of $\sigma_{resol} \approx 14$ μm was obtained for a perfect arrangement (distance error $\delta = 0$). For a distance error of $\delta = 5$ mm, which can be considered as an upper limit, a resolution of $\sigma_{resol} \lesssim 26$ μm was found [71].

4.2.3 Magnets

The Dipole magnet D1

The dipole magnet D1 (cf. Fig. 4.8) is a conventional magnet composed of an iron yoke and a copper coil. The pole shoes have a length $L = 0.4$ m and are separated by gap $h = 40$ mm. The maximum excitation current is $I_{max} = 200$ A. Neglecting hysteresis effects, the peak magnetic field is proportional to the exciting current. In order to elaborate the relation between exciting current I and magnetic field B_0 more accurately, the field strength was measured at different currents, yielding the relation [79]

$$B_0 = 0.0013\ \mathrm{T} + 0.0029\ \frac{\mathrm{T}}{\mathrm{A}} \cdot I, \tag{4.15}$$

where the first summand indicates the remanent field of the magnet at zero current. The corresponding bending angle α of a passing electron with momentum p is given by

$$|\alpha| \approx \frac{eB_0L}{p} \approx 0.2998 \cdot \frac{B_0\ [\mathrm{T}] \cdot L\ [\mathrm{m}]}{p\ [\mathrm{GeV/c}]}. \tag{4.16}$$

The nominal bending angle is 3.5°. The current can be controlled remotely in steps of 1 mA. In order to exclude hysteresis effects, the current can be changed to its maximum values $\pm I_{max}$ (magnet cycling) so the magnetization is close to saturation before setting the desired current. Based on detailed magnetic measurements for the dipoles (different type) used in the bunch compressor chicanes [53], the relative deviation of the magnetic field from the quoted linear relation due to higher order fields and hysteresis effects is estimated to be $\lesssim 1.5$ %.

Quadrupole magnets

The magnetic field within the aperture of a quadrupole magnet is purely transverse and vanishes on the axis. The horizontal and vertical field components B_x and B_y depend linearly on the transverse coordinates (x, y),

$$\begin{aligned} B_y(x,y) &= -g \cdot x & (4.17)\\ B_x(x,y) &= -g \cdot y & (4.18) \end{aligned}$$

with

$$g = -\frac{\partial B_y}{\partial x} = -\frac{\partial B_x}{\partial y}. \tag{4.19}$$

[8]. The focal length f (defined in the same way as in case of optical lenses) at a particle momentum p is determined by

$$\frac{1}{f} = k \cdot L_{mag}, \tag{4.20}$$

where k is given by

$$\begin{aligned} k &= \frac{eg}{p} & (4.21)\\ k\ [\mathrm{m}^{-2}] &\approx 0.2998 \cdot \frac{g\ [\mathrm{T/m}]}{p\ [\mathrm{GeV/c}]}, & (4.22) \end{aligned}$$

and L_{mag} is the effective magnetic length of the magnet. L_{mag} is defined by the integrated transverse field gradient divided by the maximum field gradient g_{max} in the center:

$$L_{mag} = \frac{1}{g_{max}} \int g(z)dz. \tag{4.23}$$

The relation between exciting current I and field gradient g was determined by magnetic measurements at different exciting currents for each type of quadrupole. The quadrupole magnets installed in the experimental beamline are partly superferric (Q-ACC4, Q-ACC5 and since 2007 Q-ACC6, cf. Fig. 4.8) and partly conventional magnets. In case of superferric quadrupole magnets, the relation between gradient and current is given by

$$g = 0.0216\,\frac{\mathrm{T}}{\mathrm{m}} + 0.3866\,\frac{\mathrm{T}}{\mathrm{m}\cdot\mathrm{A}} \cdot I. \tag{4.24}$$

[79]. The maximum exciting current that may be set is 25 A. The magnetic length L_{mag} is 0.185 m. The relative contribution of higher harmonic fields to the integrated field gradient was measured to be $\ll 10^{-4}$ [61]. The corresponding contribution of higher order fields of the steering magnet mounted inside the yoke bore is $\ll 10^{-2}$ [61]. The relative deviation of the gradient from the quoted linear relation due to iron saturation is $\lesssim 0.01$ at the maximum current of 25 A [61]. The accuracy of the integrated field gradient is therefore estimated to be better than 1%.

The quadrupole magnets Q-TDS and Q-ACC6 (before installation of module ACC6 in 2007) are conventional magnets with a magnetic length of 0.335 m and a maximum exciting current of 100 A. The relation between field gradient g and exciting current was measured to be

$$g = 0.02\,\frac{\mathrm{T}}{\mathrm{m}} + 0.0694\,\frac{\mathrm{T}}{\mathrm{m}\cdot\mathrm{A}} \cdot I \tag{4.25}$$

[79]. Based on detailed measurements for other types of conventional quadrupole magnets installed at FLASH, the deviation from the linear relation is assumed to be < 1 % at typical currents between 5 A and 30 A. The horizontal offset of the beam within the quadrupole of up to 10 mm due to the kicker is small compared to the diameter of the yoke bore of 70 mm, so a significant change of the field gradient over this distance is not expected.

The exciting current of each quadrupole can be set remotely in steps of 1 mA. The currents of the quadrupole magnets located in the experimental beamline can be chosen independently, since each magnet is powered by a different power supply. Cycling procedures allow to prevent errors from hysteresis effects.

In order to decouple horizontal and vertical particle motion, it is important that quadrupole magnets are not rotated about the beam axis. The rotation angle of quadrupole magnets at FLASH is less than 0.1 mrad [80].

4.2.4 The kicker

A horizontal kicker deflects single bunches onto the off-axis screen OTR-2 (cf. Fig. 4.8). The kicker contains stripline electrodes arranged parallel to the beam, which generate a strong vertical dipole field. The electrodes are placed around a ceramic vacuum chamber transparent to the magnetic field. They are charged by a fast pulser. The pulse duration of 1.5 μs [81] allows to horizontally deflect single bunches of a bunch train at 1 MHz bunch repetition rate. The strength of the kick can be controlled remotely by changing the voltage of the power supply charging the capacitors of the pulser. A high voltage of about 3.8 kV is necessary to obtain a sufficiently strong magnetic field.

4.2.5 The transverse deflecting structure

The key component of the experimental setup (cf. Fig. 4.8) is a transverse deflecting structure (TDS). The structure deflects particles vertically in linear dependence on their longitudinal position within a bunch, and in this way allows to measure properties of the particle distribution as a function of the longitudinal position. Because of its importance the TDS is described in detail in the following.

Introductory remarks on transverse deflecting structures

The idea to separate charged particles with an RF deflector has its origin in particle physics. In the 1960's, much effort was devoted to the development of schemes for separating charged secondary particles of different masses but the same momentum. In uniform electric fields transverse to the direction of motion, the difference in deflection angle of two such particles is proportional to the inverse of their momentum squared. Hence, "DC deflectors" are only well-suited for low energies. For high energies, transverse RF fields are much more efficient, since the particles (if not ultra-relativistic) can be easily injected at different phases of the RF field due to different particle velocities and correspondingly different times-of-flight to the RF deflector [82].

A fundamental contribution to the development of such RF deflectors is the Panofsky-Wenzel theorem [83], which states that

1. A cavity (without beam holes) excited in a TE mode (no component of electric field parallel to the axis) imparts no transverse momentum to a high-energetic particle passing it parallel to its axis.

2. A cavity excited in a TM mode (no component of magnetic field parallel to the axis) imparts a transverse momentum

$$\Delta\vec{p}_\perp = \left(\frac{k_0}{k_g} - \frac{k_g}{k_0}\right)\frac{e}{c}\int_0^L \vec{\mathcal{E}_\perp}\left(z, t_0 + \frac{z}{v}\right)dz, \tag{4.26}$$

   where $k_0 = \omega/c$ is the free-space wave number, L is the length of the cavity, $k_g = p \cdot \pi/L,\ p \in \mathbb{N}_0$ is the guide propagation wave number of the particular mode, v is the particle velocity, $\vec{\mathcal{E}_\perp}(z,t)$ the transverse electric field vector as a function of longitudinal position z and time t, and t_0 is the time the particle enters the cavity.

Physically, the magnetic field cancels the effect of the electric field in case of TE modes, whereas in case of TM modes it multiplies the effect from the electric field with a factor which is independent of the particle velocity.

A field distribution suited for transverse RF deflection is a $\mathrm{TM}_{1,1,0}$ dipole mode. Fig. 4.12 sketches the field distribution in a pillbox cavity [84] excited in this mode. A deflector may thus be constructed from a chain of cavities excited in a $\mathrm{TM}_{1,1,0}$ mode. However, there are drawbacks associated with the use of cavities as a reduced efficiency (transit time factors) and the rather long time the fields need to reach their steady state [82]. It appeared to be more promising to use a waveguide structure with a phase velocity equal to the particle velocity, so particles “ride the crest” of the deflecting field. However, the phase velocity in uniform waveguide structures is always larger than the velocity of light [11].

A remedy to this problem are iris-loaded structures. Reflections at periodic obstacles in a structure slow down the phase velocity of the field, a mechanism that had already been used for traveling-wave accelerating

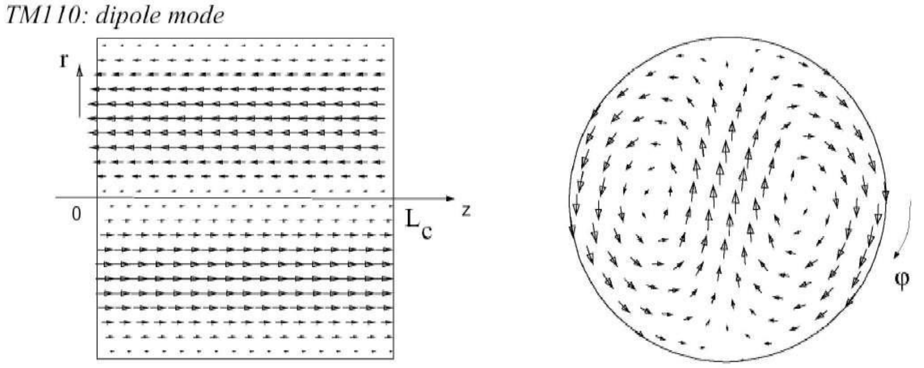

Figure 4.12: Field distribution of the $\mathrm{TM}_{1,1,0}$ *mode in a pillbox cavity [84]. The figure on the left hand side shows a side view with electric field vectors, the one on the right hand side a front view with magnetic field vectors. The electric field has no transverse component and vanishes on-axis. The magnetic field vectors have a nearly homogenous component in one transverse direction in the region near the axis, which leads to a transverse deflection of a passing charged particle.*

structures excited in a $\mathrm{TM}_{0,1}$ mode [11]. A field configuration in a periodic structure obeys the following statement [11], which is related to the Floquet theorem:

In a given mode of an infinite periodic structure, the fields at two different cross sections that are separated by one period differ only by a complex constant.

This is the case for a solution of the form

$$\vec{\mathcal{E}}(r,\varphi,z,t) = \vec{\mathcal{E}}_d(r,\varphi,z)\cdot e^{i(\omega t - k_o z)}, \tag{4.27}$$

where $\vec{\mathcal{E}}_d(r,\varphi,z)$ is a periodic function in z (with the same periodicity d as the structure) that fulfills the transverse boundary conditions, ω is the angular frequency of the field and k_0 is a longitudinal wave number yet to be determined. The field at $z+d$ is then given by

$$\vec{\mathcal{E}}(r,\varphi,z+d,t) = \vec{\mathcal{E}}(r,\varphi,z,t)\cdot e^{ik_0 d}, \tag{4.28}$$

which physically represents a cell-to-cell phase shift of $k_0 d$. Expansion of the periodic function $\vec{\mathcal{E}}_d(r,\varphi,z)$ in a Fourier series

$$\vec{\mathcal{E}}_d(r,\varphi,z) = \sum_{n=-\infty}^{n=+\infty} \vec{\mathcal{E}}_{d,n}(r,\varphi)e^{-i2\pi nz/d} \tag{4.29}$$

yields

$$\vec{\mathcal{E}}(r,\varphi,z,t) = \sum_{n=-\infty}^{n=+\infty} \vec{\mathcal{E}}_{d,n}(r,\varphi)e^{i(\omega t - k_n z)} \tag{4.30}$$

with

$$k_n = k_0 + 2\pi n/d. \tag{4.31}$$

The field can thus be expressed as a superposition of traveling waves, called space harmonics, with the same frequency ω but different wave numbers k_n. Accordingly, the space harmonics have different phase velocities $v_{p,n} = \omega/k_n$. It can be shown that if a particle moves in synchronism with one space harmonic the effect of the nonsynchronous waves on the particle averages to zero and can be ignored [11, 85].

The wavenumber k_0 of the fundamental space harmonic is determined by the structure geometry and the operating frequency ω. Generally, k_0 is modified compared to the wavenumber in the corresponding uniform waveguide such that the phase velocity v_0 is reduced. This allows to design iris-loaded structures in such a way that the phase velocity of the fundamental space harmonic, which has usually the largest Fourier amplitude, is equal to the particle velocity [11].

In case of iris-loaded accelerating structures, e.g. those used at SLAC, the fundamental space harmonic with a phase velocity equal to the speed of light shares key-properties with a $\mathrm{TM}_{0,1}$ mode (which is the desired mode for particle acceleration). In particular it has no radial dependence of the accelerating field [86]. The field distribution in iris-loaded deflecting structures is more complex. It turns out that the fundamental space harmonic in an iris-loaded deflecting waveguide can approximately be described by a so-called hybrid mode ($\mathrm{HEM}_{1,1}$), which can be considered as a linear combination of a $\mathrm{TM}_{1,1}$ and a $\mathrm{TE}_{1,1}$ mode [87]. This is related to the fact that the cut-off frequency of the $\mathrm{TM}_{1,1}$ mode is larger than that of the $\mathrm{TE}_{1,1}$ mode, so the $\mathrm{TE}_{1,1}$ mode can also exist (in contrast to the case of $\mathrm{TM}_{0,1}$ and $\mathrm{TE}_{0,1}$). The $\mathrm{HEM}_{1,1}$ mode imparts a transverse force on a synchronously moving particle, which originates from both the magnetic and electric field.

Iris-loaded RF deflecting structures were built first at SLAC in the 1960's for particle separation and called "LOLA" after their inventors G.A. **Lo**ew, R.R. **L**arsen and O.A. **A**ltenmueller [88]. A LOLA-type TDS of the

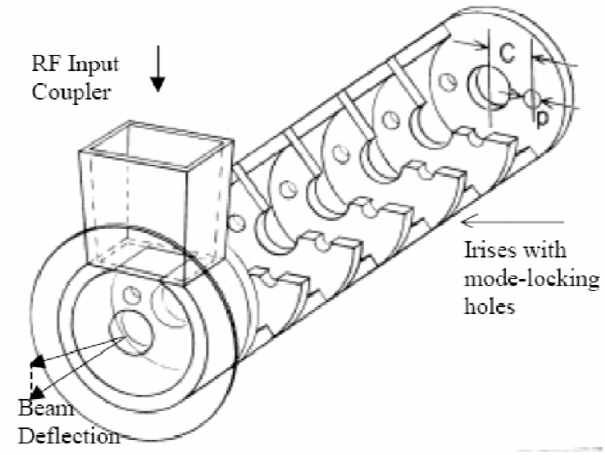

Figure 4.13: Cut-away view of an iris-loaded RF structure [88].

fourth generation built in 1968 has been installed in the FLASH linac in 2003 in a collaboration between SLAC and DESY.

Technical design

A cut-away view of the TDS at FLASH is shown in Fig. 4.13. The 3.64 m long structure is fabricated from brazed stacks of copper cylinders with a period of 3.5 cm. The iris radius is 2.24 cm. The RF input coupler is located at the end of the structure (where the beam exits). The azimuthal orientation of the coupler determines the direction of deflection, which is the vertical direction in case of this structure. Since minor imperfections in the structure could cause the field to rotate, two additional lateral holes ("mode-locking holes") are provided on either side of each iris, which allow additional coupling between the cells and thus prevent field rotations. The structure is designed such that the phase velocity of the fundamental space harmonic is equal to the speed of light. It operates in the S-band frequency range at $\nu = 2.856$ GHz, resulting in a wave length $\lambda = c/\nu \approx 10.5$ cm, a wave number $k = 2\pi/\lambda \approx 59.8\ \mathrm{m}^{-1}$ and a phase shift per cell

$$\Delta\Psi = 2\pi \cdot L_{cell}/\lambda \approx 2\pi/3, \tag{4.32}$$

where $L_{cell} \approx 3.5$ cm is the cell length.

Field pattern and forces acting on a relativistic electron

The field pattern within the structure is illustrated in Fig. 4.14 showing a snapshot of the electric field configuration in a side view of the structure as measured by means of a sapphire probe [82]. The field of the fundamental space harmonic in cylindrical coordinates (r, φ, z) is given by [82][3]

$$\begin{aligned}
\mathcal{E}_x(r,\varphi,z) &= 2\mathcal{E}_0 \cdot \cos(\varphi)\sin(\varphi)\left(\frac{1}{2}kr\right)^2 \\
\mathcal{E}_y(r,\varphi,z) &= \mathcal{E}_0\left[\left(\frac{1}{2}ka\right)^2 - \left(\frac{1}{2}kr\right)^2\left(\cos^2(\varphi)-\sin^2(\varphi)\right)\right] \\
\mathcal{E}_z(r,\varphi,z) &= i\mathcal{E}_0 kr \cdot \sin(\varphi) \qquad (4.33)\\
Z_0H_x(r,\varphi,z) &= \mathcal{E}_0\left[-\left(\frac{1}{2}ka\right)^2 + 1 + \left(\frac{1}{2}kr\right)^2\left(\cos^2(\varphi)-\sin^2(\varphi)\right)\right] \\
Z_0H_y(r,\varphi,z) &= 2\mathcal{E}_0 \cdot \cos(\varphi)\sin(\varphi)\left(\frac{1}{2}kr\right)^2 \\
Z_0H_z(r,\varphi,z) &= i\mathcal{E}_0 kr \cdot \cos(\varphi),
\end{aligned}$$

where $a = 2.24\ cm$ is the radius of the iris, $Z_0 = \sqrt{\frac{\mu_0}{\epsilon_0}}$ is the free-space impedance and $\mathcal{E}_0 = |\mathcal{E}_0|e^{i(kz-\omega t)}$ represents a traveling wave. The only components which do not vanish on-axis are $\mathcal{E}_y$ and H_x, causing a relativistic electron passing the structure on-axis to be deflected vertically. More importantly, calculating the Lorentz force yields that the electric and magnetic contribution add in such a way that the resulting deflecting force is constant over the entire aperture and thus provides an aberration-free deflection of particles moving parallel to the axis:

$$\begin{aligned}
F_y &= e\left(\mathcal{E}_y + Z_0H_x\right) \\
&= e|\mathcal{E}_0| \cdot \sin(\Psi), \qquad (4.34)
\end{aligned}$$

where the RF phase $\Psi = kz - \omega t - \Psi_0$ has been chosen relative to a zero-crossing phase Ψ_0 of the deflecting force F_y, which will be referred to as "zero-crossing phase" in the following. Away from the axis, there

---

[3] The fields have been transformed to cartesian coordinates. In order to obtain a deflecting force in vertical instead of horizontal direction, the angle φ has been replaced by $\varphi - \pi/2$.

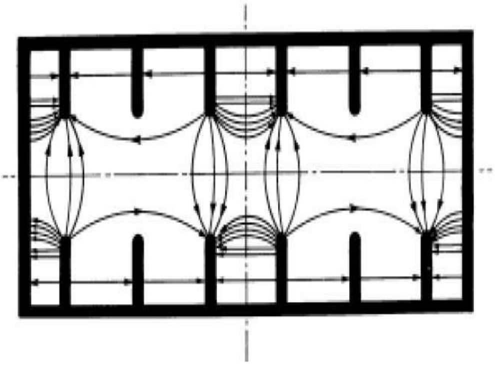

Figure 4.14: *Side-view of a LOLA-type TDS showing the electric field configuration of the deflecting mode [82]. Within the center cell there is a transverse electric field, which is almost homogenous over the aperture and contributes to the deflecting force. An electron co-moving to the field in the center of this cell, where the transverse electric field vanishes, experiences no deflection. There is a longitudinal electric fields vanishing on-axis in each cell. After three cells the field pattern repeats.*

are additionally transverse field components $\mathcal{E}_x$ and H_y, which cancel each other so there is no force in horizontal direction:

$$F_x \; = \; e\,(\mathcal{E}_x - Z_0 H_y) = 0. \tag{4.35}$$

The off-axis longitudinal electric field $\mathcal{E}_z$ is phase-shifted by 90° relative to the deflecting force and causes an accelerating or decelerating force

$$F_z(r,\varphi) = -e|\mathcal{E}_0|kr \cdot \sin(\varphi)\cos(\Psi). \tag{4.36}$$

In the following paragraphs, the forces and fields are analyzed in more detail.

Transversely deflecting force It is convenient to define an equivalent deflecting voltage V by

$$V \; = \; \frac{1}{e}\int_0^L F_y dz = \frac{F_y \cdot L}{e}. \tag{4.37}$$

From Eq. (4.34) follows

$$V = |\mathcal{E}_0| L \cdot \sin(\Psi) \tag{4.38}$$

for an electron moving in synchronism with the field at the RF phase Ψ. The deflection angle $\Delta y' = \Delta p_y/|p|$ experienced by the particle is given by

$$\begin{aligned}\Delta y' &= \frac{1}{|p|}\int_0^{L/c} F_y(t)dt = \frac{1}{c|p|}\int_0^{L} F_y(z)dz \\ &= \frac{F_y \cdot L}{E} = \frac{eV}{E}\end{aligned} \tag{4.39}$$

where E is the electron energy.

The deflecting voltage is determined by the power fed into the structure. Some power is lost by dissipation in the normal-conducting walls, which leads to a field attenuation of -4.14 dB over the entire structure[4] [78]. Moreover, power is absorbed by other space harmonics not contributing to the deflection. The effective maximum deflecting voltage $V_0 = |\mathcal{E}_0|L$ at $\Psi = \pi/2$ including these effects is related to the input power P via the relation

$$V_0 \approx 1.6\left[\frac{MV}{m\cdot\sqrt{MW}}\right]\cdot L[m]\cdot\sqrt{P[MW]}. \tag{4.40}$$

The relation has been determined experimentally and confirmed analytically [89]. The maximum input power of the TDS at FLASH is 25 MW, producing a maximum deflecting voltage of $V_0 \approx 29$ MV. For an electron energy of $E = 500$ MeV, which is a typical energy at the position of the TDS in the FLASH-linac, this results in a huge maximum deflection angle of

$$\Delta x' = eV_0/E \approx 58\ mrad. \tag{4.41}$$

However, the structure is usually operated near zero-crossing so the applied deflection is much smaller.

Longitudinal force A particle passing the structure with an offset $r = r_0$ experiences a longitudinal force (Eq. (4.36))

$$F_z(r,\varphi) = -e|\mathcal{E}_0|kr\cdot\sin(\varphi)\cos(\Psi), \tag{4.42}$$

which is maximal at zero-crossing of the deflecting force. The force can be estimated by

$$F_z \leqq e|\mathcal{E}_0|kr_0 \tag{4.43}$$

---

[4] A LOLA-type TDS is a so-called constant-impedance structure (in contrast to constant-gradient structures) with a translational symmetric geometry.

resulting in an energy change

$$\Delta E \leqq e|\mathcal{E}_0|kr_0L. \tag{4.44}$$

With $k \approx 59.8\ \mathrm{m}^{-1}$, $r_0 = 1$ mm and $|\mathcal{E}_0|L \leqq V_0 \approx 29$ MV the force causes an energy change of $\Delta E \leqq 1.8$ MeV. For a beam energy of 500 MeV, this is typically within the energy uncertainty and has no significant effect on the spatial distribution directly downstream of the structure. However, if there are correlated offsets along the bunch, e.g. linear correlation $\langle yz\rangle$ or $\langle xz\rangle$ induced by wake fields, the energy profile may be influenced.

Forces on an electron passing the structure with an angle If a particle passes the structure with an angle, the balance between magnetic and electric forces is slightly distorted. Since the magnetic field is almost horizontal near the axis, the forces in vertical and longitudinal direction change. However, for maximum angles in the order of 10^{-3}, these changes are negligible.

Energy change caused by transverse deflection The transverse electric field component contributing to the deflection causes an energy change of a passing electron given by

$$\frac{\Delta E}{E} = \frac{e\mathcal{E}_y\Delta y}{E} = \frac{1}{E}\frac{\Delta y' \cdot L}{2} \cdot e\mathcal{E}_y = \frac{(\Delta y')^2}{2} \tag{4.45}$$

according to Eq. (4.39). For deflection angles in the order of 10^{-3} this is not a significant effect.

Energy flow The time averaged power P transmitted through the structure by the fundamental space harmonic is given by integrating the complex Poynting vector for harmonic fields [3]

$$\vec{S} = \frac{1}{2}\left(\vec{\mathcal{E}} \times \vec{H}^*\right) \tag{4.46}$$

over the aperture A:

$$\begin{aligned} P &= \frac{1}{2}Re\left[\int_A \left(\vec{\mathcal{E}} \times \vec{H}^*\right)\vec{e_z}ds\right] \\ &= \frac{\pi a^2}{2}\frac{|\mathcal{E}_0|^2}{Z_0}\left(\frac{ka}{2}\right)^2\left[\frac{4}{3}\left(\frac{ka}{2}\right)^2 - 1\right], \end{aligned} \tag{4.47}$$

where $\vec{e_z}$ is the unit vector in longitudinal direction. Inserting the iris radius $a = 2.24$ cm and the wave number $k = 59.8$ m^{-1} yields $P < 0$, indicating that the fundamental space harmonic is a backward wave mode. Accordingly, the structure has a negative group velocity $v_g = -0.0189$ c [87] and thus the direction of energy flow is opposed to the beam direction. The power is therefore fed into the structure through the RF input coupler at the end of the structure as already mentioned.

Bunch deformation

In a bunch with mean energy E which is injected into the structure at an RF phase Ψ (with respect to the centroid of the bunch), the total "kick angle" imparted to an electron with energy $E + \Delta E$ at the longitudinal position ζ relative to the centroid ($\zeta = 0$) is given by

$$\Delta y'(\zeta) = \frac{eV_0}{E + \Delta E} \sin(k\zeta + \Psi). \tag{4.48}$$

In the FLASH linac, the relative RMS energy width σ_E/E at the position of the TDS is usually smaller than 0.5%, so the bunches can be considered as mono-energetic in a reasonable approximation. The RMS bunch length σ_ζ is (for standard machine settings) shorter than 2 mm, so for the wave length $\lambda \approx 10.5$ cm of the fundamental space harmonic of the TDS, Eq. (4.48) can be approximated by the first two terms of a Taylor series around $\zeta = 0$:

$$\Delta y'(\zeta) \approx \frac{eV_0}{E} \left(k\zeta \cos(\Psi) + \sin(\Psi)\right). \tag{4.49}$$

Calculating the mean kick angle $\langle \Delta y' \rangle$ and the variance

$$\sigma_{y'}^2 = \langle (\Delta y' - \langle \Delta y' \rangle)^2 \rangle \tag{4.50}$$

over the ensemble of bunch electrons yields the centroid deflection

$$\langle \Delta y' \rangle \approx \frac{eV_0}{E} \sin(\Psi) \tag{4.51}$$

and the induced angular divergence

$$\sigma_{y'} = \frac{eV_0 k}{E} \sigma_\zeta \cos(\Psi), \tag{4.52}$$

where σ_ζ is the longitudinal RMS bunch length. For the purpose of beam diagnostics, a large induced angular divergence is desirable. At the FLASH linac, the structure is operated at zero-crossing resulting in a maximum angular divergence.

In order to calculate the beam properties downstream of the structure, it is convenient to consider the structure to be a drift section with an instantaneous deflection according to Eq. (4.49) occurring at the center of the structure located at $s = s_0$. The approximation as a drift section is justified since effects other than the intended deflection are negligible as shown above. An instantaneous deflection at the center results, neglecting power attenuation along the structure, in the same change in offset $\Delta y(s_0 + L/2)$ and by definition the same angle $\Delta y'(s_0 + L/2)$ at the end of the structure:

$$\begin{aligned} \Delta y_i(s_0 + L/2) &= \int_{s_0-L/2}^{s_0+L/2} \Delta y'(s)\, ds = \int_{s_0-L/2}^{s_0+L/2} \frac{F_y \cdot s}{E}\, ds \qquad (4.53) \\ &= \frac{F_y \cdot L^2}{2E} = \frac{L}{2} \cdot \Delta y'(s_0 + L/2), \end{aligned}$$

where relation (4.39) was used. The vertical particle coordinate y at position $s > s_0 + L/2$ is therefore given by

$$\begin{aligned} y(s) &= M^y_{1,1}(s, s_0) \cdot y(s_0) + M^y_{1,2}(s, s0) \cdot (y'(s_0) + \Delta y') \qquad (4.54) \\ &= y^0(s) + M^y_{1,2}(s, s_0) \cdot \Delta y', \end{aligned}$$

where $M^y(s, s_0)$ is the transfer matrix from s_0 to s for the vertical plane including the second half of the TDS as a drift section, $y^0(s)$ the vertical particle coordinate at s without deflection from the TDS and $\Delta y'$ is the total kick angle induced by the TDS . Inserting expression (4.49) for $\Delta y'$ yields

$$y(s) = y^0(s) + S \cdot \zeta + M^y_{1,2} \cdot \frac{eV_0}{E} \sin(\Psi), \qquad (4.55)$$

with

$$S = M^y_{1,2} \cdot \frac{eV_0}{E} \cdot k \cdot \cos(\Psi). \qquad (4.56)$$

In the following, an operation of the structure near zero-crossing is assumed ($\Psi \approx 0$), resulting in

$$y(s) = y^0(s) + S \cdot \zeta, \qquad (4.57)$$

and

$$S = M^y_{1,2} \cdot \frac{eV_0}{E} \cdot k. \qquad (4.58)$$

The constant S is a proportionality constant relating longitudinal distances to vertical distances at position s downstream of the deflector. S will be called shear parameter.

In the following, the transverse density distribution of a bunch sheared by the TDS will be derived using Eq. (4.57). The charge density distribution of a bunch at a position s downstream of the TDS including effects from the TDS (TDS on) will be denoted by $\rho(x, y, \zeta)$, and the distribution at the same position with the TDS switched off by $\rho^0(x, y, \zeta)$. In order to simplify the considerations, $\rho^0(x, y, \zeta)$ will be assumed to exhibit no longitudinal-vertical correlations. The distribution can thus be decomposed into the distribution $\rho_{x\zeta}(x, \zeta)$ in the longitudinal-horizontal plane and the distribution $\rho_y^0(y)$ in the vertical direction:

$$\rho^0(x, y, \zeta) = \rho_{x\zeta}(x, \zeta) \cdot \rho_y^0(y). \tag{4.59}$$

Since the horizontal coordinate x is not changed by the TDS, the consideration can be restricted to the longitudinal-vertical plane by integrating over x, yielding

$$\rho_{y\zeta}^0(y, \zeta) = \rho_\zeta(\zeta) \cdot \rho_y^0(y) \tag{4.60}$$

with the charge density distribution in the vertical-longitudinal plane $\rho_{y\zeta}^0(y, \zeta)$ and the longitudinal distribution $\rho_\zeta(\zeta)$.

The change in vertical coordinate y_i of a bunch electron induced by the TDS (Eq. 4.57) can be written more generally as

$$y_i = y_i^0 + \chi_i, \tag{4.61}$$

with vertical offsets $\chi_i = S \cdot \zeta_i$. The corresponding distribution of induced vertical offsets χ_i in the bunch will be denoted by $P_\chi(\chi)$. The vertical charge density distribution $\rho_y(y)$ at s including effects from the TDS is thus given by the convolution

$$\rho_y(y) \;=\; \int_{-\infty}^{+\infty} d\tilde{y} \left[\rho_y^0(\tilde{y}) \cdot P_\chi(y - \tilde{y})\right]. \tag{4.62}$$

Using

$$P_\chi\left(S \cdot \left[\frac{y - \tilde{y}}{S}\right]\right) = \frac{1}{S} \cdot \rho_\zeta\left(\frac{y - \tilde{y}}{S}\right) \tag{4.63}$$

yields

$$\rho_y(y) \;=\; \int_{-\infty}^{+\infty} d\tilde{y} \left[\rho_y^0(\tilde{y}) \cdot \frac{1}{S} \cdot \rho_\zeta\left(\frac{y - \tilde{y}}{S}\right)\right]. \tag{4.64}$$

This expression shows that the vertical density distribution of a streaked bunch is a convolution of the longitudinal distribution ρ_ζ and the vertical distribution with the TDS switched off divided by the shear parameter, $\rho^0(y)/S$. The reason is that by virtue of the TDS each point in the longitudinal profile is mapped to the vertical profile of the "slice" at the same longitudinal position, so $\rho^0(y)/S$ has the meaning of a point spread function. The convolution limits the longitudinal resolution with which the longitudinal density distribution ρ_ζ can be measured. The resolution (RMS) is given by σ_y^0/S, where σ_y^0 is the overall vertical RMS bunch size (TDS off). The resolution is typically in the order of one tenth of the RMS bunch length, which corresponds to $10 - 20\ \mu$m. In general, the spatial bunch distribution $\rho^0(x, y, \zeta)$ exhibits longitudinal-vertical correlations in contrast to the assumption made here (Eq. 4.60). The resolution then becomes a function of the longitudinal position ζ and can only be roughly estimated by the overall vertical bunch size σ_y^0.

Influence of the optics on the resolution

The longitudinal resolution σ_y^0/S depends critically on the accelerator optics. For a given optics and a perfectly matched beam, the vertical transfer matrix element $M_{1,2}^y(s, s_0)$ (as defined in Eq. 4.54) can be written according to Eq. (2.38) as

$$M_{1,2}^y(s, s_0) = \sqrt{\beta_y(s)\beta_y(s_0)} \cdot \sin(\Delta\phi_y) \tag{4.65}$$

and the RMS beam size at position s as

$$\sigma_y^0(s) = \sqrt{\epsilon_y \cdot \beta_y(s)}, \tag{4.66}$$

where $\beta_y(s_0)$ and $\beta_y(s)$ are the values of the vertical beta function at the center of the deflector s_0 and position s (the screen position), respectively, $\Delta\phi_y$ is the vertical phase advance from the deflector to the screen and ϵ_y the vertical RMS emittance. Using these expressions, the definition of the shear parameter S (Eq. (4.56)) becomes

$$\begin{aligned} S &= \sqrt{\beta_y(s)\beta_y(s_0)} \cdot \sin(\Delta\phi_y) \cdot \frac{eV_0 k}{E} && (4.67) \\ &\propto \sqrt{\beta_y(s)\beta_y(s_0)} \cdot \sin(\Delta\phi_y) && (4.68) \end{aligned}$$

and the resolution can be expressed as

$$\begin{aligned}\frac{\sigma_y^0}{S} &= \frac{\sqrt{\epsilon_y \beta_y(s)} \cdot E}{\sqrt{\beta_y(s)\beta_y(s_0)} \cdot \sin(\Delta\phi_y) \cdot eV_0 k} && (4.69)\\ &= \frac{\sqrt{\epsilon_y} \cdot E}{\sqrt{\beta_y(s_0)} \cdot \sin(\Delta\phi_y) \cdot eV_0 k} && (4.70)\\ &\propto \frac{1}{\sqrt{\beta_y(s_0)} \cdot \sin(\Delta\phi_y)}. && (4.71)\end{aligned}$$

Eq. (4.70) shows that the resolution can be improved by increasing the beta function $\beta_y(s_0)$ and thus decreasing the beam divergence at the deflector and by choosing a betatron phase advance $\Delta\phi_y$ close to $(n{\cdot}\pi{+}\pi/2)$ with $n \in \mathbb{N}_0$. At the same time, the vertical beam size at the position of the screen s can be scaled by the value $\beta_y(s)$ of the beta function at the screen, as can be seen from Eq. (4.67). This is important to adapt the beam size to the screen dimensions and to the resolution of the optical system imaging the electron beam. Note that the shear parameter S does not depend on the value of the beta function at the deflector $\beta_y(s_0)$ as an independent parameter, as Eq. (4.67) might suggest, but only on the transfer matrix from the deflector to the screen. Changing the strengths of quadrupole magnets upstream of the deflector changes the beta function in such a way that

$$M^y_{1,2}(s, s_0) = \sqrt{\beta_y(s)\beta_y(s_0)} \cdot \sin(\Delta\phi_y) \qquad (4.72)$$

is unaffected. From this it follows that

$$\sqrt{\beta_y(s)} \propto \frac{1}{\sqrt{\beta_y(s_0)} \cdot \sin(\Delta\phi_y)} \propto \frac{\sigma_y^0}{S}. \qquad (4.73)$$

Hence, in case only the strengths of quadrupole magnets upstream of the TDS are changed, the resolution scales with $\sqrt{\beta_y(s)}$ or equivalently with the vertical beam size σ_y^0 without RF deflection at the screen.

Installation at FLASH

Fig. 4.15 shows a photograph of the TDS in the FLASH tunnel. The RF power is fed into the structure at the downstream end through an input coupler. The energy flow is opposed to the beam direction. At the

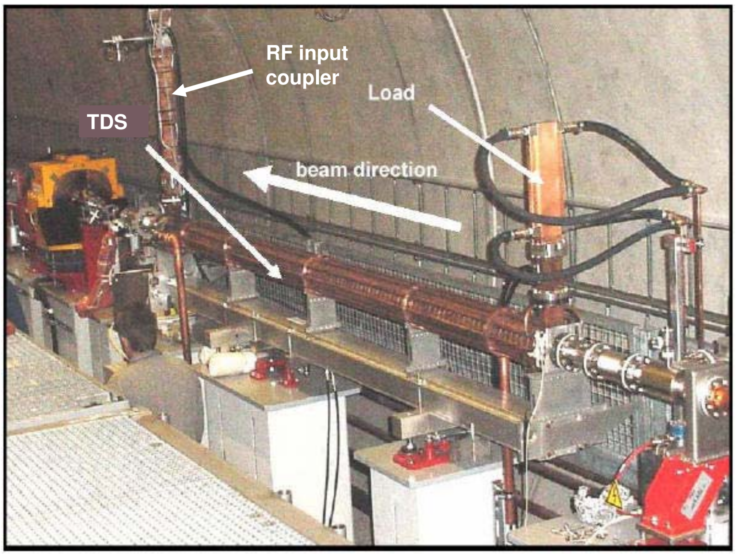

Figure 4.15: Photograph of the TDS in the FLASH tunnel. The orientation of RF input coupler, load and beam direction is drawn in.

other end, a load is installed to absorb the field and prevent reflections. The group velocity $v_g = -0.0189 \cdot c$ yields a filling time $\tau_f = L/v_g$ of 0.645 μs, after which the field reaches a steady-state. Since $2 \cdot \tau_f < 2\mu s$, the structure is suited for selectively manipulating single bunches at 1 MHz bunch repetition rate of the machine without affecting subsequent bunches.

The short RF pulses with a duration of ~ 1 μs are generated in an RF modulator and amplified by a klystron to a power of up to 45 MW. The RF signal is transported to the structure through a 75 m long waveguide with a measured attenuation of 2.6 dB [78]. The waveguide is temperature-stabilized at 45° C to prevent phase shifts. The power fed into the structure can be measured by coupling out a small fraction of the RF through drilled holes [78]. The maximum input power measured was 18 MW [87]. RF phase and input power can be remotely controlled from the control room.

An important issue for a proper operation of the structure is the synchronization to the RF system of the accelerator. At high input power of the TDS, even small drifts or fluctuations of the RF phase are translated to strong changes in the vertical offset downstream of the structure, which makes measurements difficult or even impossible. The reference timing signals for all components of FLASH are derived from a master oscillator running at 9.027775 MHz. Since the structure was originally fabricated for use in a different machine, the operating frequency of 2.856 GHz is not a multiple of the master oscillator frequency and thus disallows a simple synchronization scheme. To allow synchronization, the resonance frequency of the structure had to be shifted slightly by rising the operating temperature to 45°C. In this way, the operating frequency could be changed to a multiple of 1/11 of the master clock frequency, so a stable synchronization can be achieved by an additional synchronization circuit. More details can be found in reference [78].

Chapter 5

Experimental details

5.1 Image analysis

The raw experimental data used for determining bunch properties are digital images recorded with a CCD-camera. In order to apply the methods for phase space analysis described in chapter 3, one-dimensional transverse intensity profiles and corresponding statistical properties as mean value and standard deviation have to be extracted from the images. However, there are several disturbances such as γ-rays, stray light and noise in the camera system complicating this task. This section describes how the individual error sources are handled and the final data used for phase space analysis are determined.

Sources of spurious intensities in CCD-images

Spurious intensities caused by the electron beam: γ-rays and synchrotron radiation γ-rays may be emitted whenever beam electrons hit an obstacle like an OTR screen or the vacuum chamber. If they hit the CCD-chip of the camera, this typically results in a much higher intensity of the affected pixels than found in the direct neighborhood. Such isolated intensity spikes are corrected by using a "mean filter", which identifies individual pixels having an intensity which exceeds the mean intensity in their local neighborhood by a certain value, which was adjusted empirically, and replaces their intensity value by this mean value.

Synchrotron radiation is emitted when the beam moves on a curved trajectory, e.g. within a steering magnet or a quadrupole traversed off-axis. If this happens close to the OTR screen, the radiation may hit the screen and be reflected into the optical system of the camera. In case of the measurements presented in this thesis, synchrotron radiation plays a minor role, since steering magnets in the vicinity of the screen were operated at low currents. The quadrupole closest to the screen OTR-2 is located about 9 m upstream, so the radiation intensity, which reduces with one over distance squared, can be neglected at the location of the screen.

Background signals Spurious intensities not caused directly by the beam can be easily distinguished from the beam signal by recording "background images" with the laser of the RF gun switched off. Background images can then be subtracted from images containing beam signal ("beam images").

The main source for background intensities are electrons released from the inner surface of the accelerating modules and the gun by field emission, which generate a nearly continuous current ("dark current"). In case of the measurements using the off-axis screen OTR-2, dark current is negligible since only those electrons passing the horizontal kicker during a time window in the order of a microsecond are deflected onto the screen.

Another potential source for background signals is stray light, e.g. due to laser-based diagnostics near the screen. Stray light was not observed during the measurements.

Noise caused by the CCD-camera Noise in the camera system is usually the dominating source for spurious intensities in CCD-images. The noise is mainly caused by dark current in the pixels of the CCD sensor and signal amplifiers. The intensity distribution of this noise is in good approximation Gaussian and homogenous over the extension of the image. The mean value μ_{noise} is ideally equal to zero. If not, it has to be determined and subtracted from the measured intensities. This is automatically the case when background images are subtracted.

Restriction to a region of interest

Spurious intensities may significantly affect the statistical moments extracted from the spatial intensity distribution of a CCD-image. In particular, standard deviations, which are used to determine the transverse emittance, critically depend on intensities with a large offset to the mean beam position on the image. In case of Gaussian distributions, a Gaussian fit can be applied to determine the second moments in an accurate way. However, in many cases the bunch distribution is not Gaussian but of irregular shape, so an explicit calculation of statistical moments is preferable.

An important step is to confine the calculation to a smaller region containing the beam. Reference [32] describes a two-dimensional algorithm, in which an elliptic region around the beam center, the "region of interest" (ROI), is increased in size until the variances calculated from the image fraction contained in that region become roughly constant. This algorithm works well as long as the bunch shape is nearly elliptic, which is typically the case for transverse distributions.

Here, a different approach to define a two-dimensional ROI had to be applied, since the distributions encountered strongly deviate from an elliptical shape due to the deformation induced by the TDS (transverse deflecting structure). The algorithm will be illustrated in the following at the example of a simulated CCD-image. Figure 5.1(a) shows the transverse distribution of an electron distribution obtained from a particle tracking simulation (cf. chapter 8). Vertical shearing by means of the TDS was included, so the vertical position on the image is related to the longitudinal position within the bunch. The distribution is shown in the form of a CCD image with the same pixel size and the same intensity resolution as in case of images recorded by the cameras used for the measurements. In Fig. 5.1(b), Gaussian noise was added to the distribution. The standard deviation of the noise signal was chosen to be slightly larger than typically observed in measurements.

At first, mean value μ_{noise} and standard deviation σ_{noise} of the noise signal are determined. For this purpose, a histogram showing the distribution of pixel intensities is appropriate (Fig. 5.1(c)). As long as the largest part of the image is covered by pure noise, there is a sharp maximum at low intensities from which mean value and standard deviation of the noise signal can be determined. In the example, the mean value of the noise signal was chosen to be zero for illustrative reasons. Afterwards, the image is coarsened by introducing quadratic "macropixels" with a side length of N pixels. The intensity of each macropixel is defined to be the average intensity of the pixels enclosed. The standard deviation of the noise signal of all macropixels $\Sigma_{noise} = \sigma_{noise}/N$ is reduced by a factor of N. In case the beam intensity does not vary significantly over the extension of

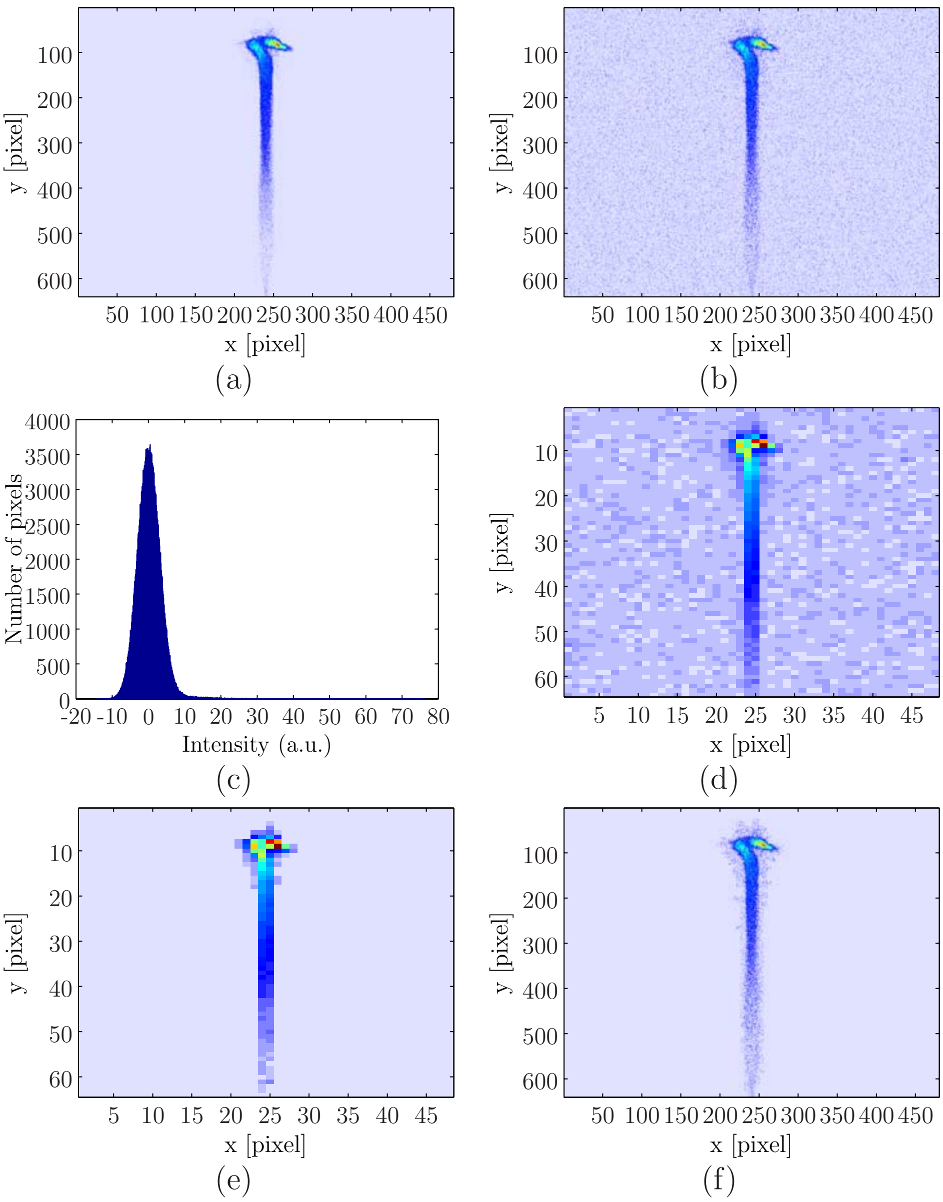

Figure 5.1: Illustration of the algorithm used for image analysis. (a) Simulated CCD-image of an electron distribution. (b) Distribution in (a) superimposed by a Gaussian distribution simulating noise. (c) Histogram showing the intensity distribution of image pixels in (b). (d) Locally averaged image with macropixels of size 10×10*. (e) Region of interest found by an iterative algorithm. (f) Final image.*

a macropixel, the signal-to-noise ratio is thus increased by the same factor. As a result, the contour of the region covered by the beam is visible (Fig. 5.1(d) with $N = 10$).

Starting from the coarsened image, a ROI is determined iteratively. First, the macropixel with maximum intensity is added to the ROI. Then all direct neighbors (at maximum eight macropixels) of this macropixel are determined. Those neighbors with an intensity above a certain threshold are added to the ROI. The threshold is chosen to be $m \cdot \Sigma_{noise}$ with typically $m = 3$, so a macropixel with an intensity above the threshold is likely to contain beam intensity. This procedure is repeated by considering all direct neighbors of macropixels within the ROI which are not element of it, until the ROI stays unchanged (Fig. 5.1(e)). Finally, the original intensities are assigned to all pixels within the ROI, whereas the intensities of all pixels outside the ROI are set to zero intensity (Fig. 5.1(f)). The resulting image allows to determine arbitrary statistical properties of the electron distribution.

The accuracy of the algorithm was tested by determining the horizontal RMS width of the test bunch shown in Fig. 5.1(a) as a function of the vertical position ("slice width") from twenty images with random background noise (Fig. 5.2). The calculated widths are in very good agreement with the original ones and have small statistical errors. At the very end of the bunch, where the beam intensity is in the same order as the standard deviation of the noise signal, the algorithm (and principally beam detection) fails. The deviations observed in the presented simulation are amplified by numerical noise resulting in strong fluctuations of the intensity from pixel to pixel in the low-intensity region.

The algorithm works provided the noise signal is gaussian in reasonable approximation and the beam covers a connected region of the image, which both is typically the case. One can consider the region with a locally averaged intensity above the noise level intuitively as the region where beam is detectable.

The size of the macropixels has to be adapted to the size and structure of the area covered by the beam. Here, 10 × 10 pixels were found to be appropriate. The sensitivity was further improved by determining regions of interest for different mean positions of the macropixels and unifying these regions afterwards. Furthermore, entire "boundary layers" containing all macropixels in the direct neighborhood of the ROI were considered and added to the ROI in case the mean intensity of these layers was above a threshold determined by the noise signal.

The noise parameters can also be determined by evaluating background images instead of using intensity histograms. This was done whenever there were no significant intensities from dark current, as was typically the case on the off-axis screen.

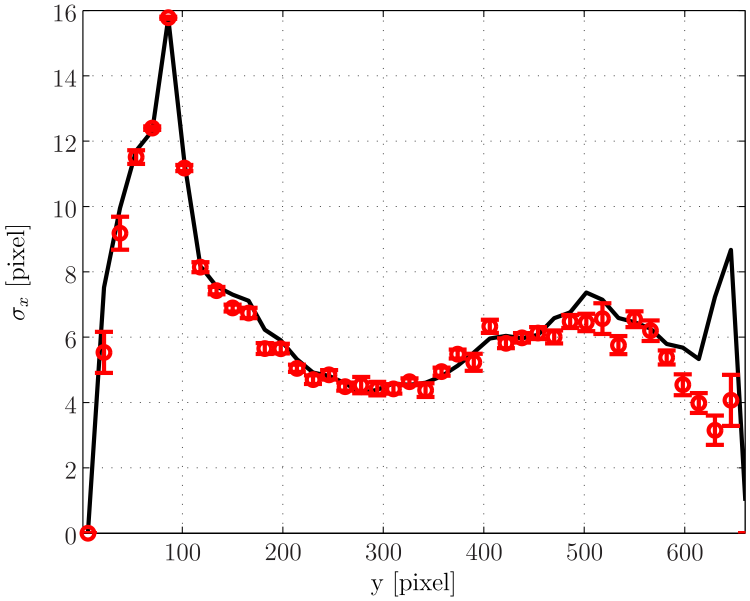

Figure 5.2: Simulation of a measurement of RMS bunch widths. The solid line shows the horizontal RMS width σ_x of the electron distribution shown in Fig. 5.1(a) as a function of vertical position. Red circles show the corresponding widths as determined from 20 images with random noise signals after processing them as described in the text. Error bars indicate the corresponding standard deviations.

The algorithm was implemented in a MATLAB environment. Including the improvements mentioned above, the runtime on the personal computer currently used for emittance analysis at FLASH ranges approximately between 0.1 s and 0.5 s per image. The runtime depends on the area covered by the beam and the chosen size of macropixels.

The analysis of images described above can be complemented by noise filters in "frequency" domain, since the noise signal is characterized by strong fluctuations from pixel to pixel, while the beam signal mainly shows variations over longer distances. One possibility to filter the noise signal is to perform a two-dimensional Fourier transformation of the image and to suppress the high frequencies before back transformation. This would, however, also smear out sharp edges of the beam density distribution. A remedy to this problem are appropriate wavelet transformations instead of Fourier transformations [32]. Since the improvements from these techniques are rather small compared to the additional expenditure of time for analyzing images, they were not applied.

Deconvolution of CCD-images

The vertical charge density profile $\rho_y(y)$ downstream of the transverse deflecting structure (TDS) can be considered as a "superposition" of the longitudinal charge density distribution $\rho_\zeta(\zeta)$ and the vertical charge density distribution $\rho_y^0(y)$ of a bunch unaffected by the TDS at the same position of the beamline. In case the charge density distribution $\rho_{y\zeta}^0(y,\zeta)$ of an unaffected bunch in the vertical-longitudinal plane can be written in the form

$$\rho_{y\zeta}^0(y,\zeta) = \rho_\zeta(\zeta) \cdot \rho_y^0(y),$$

the vertical charge density profile $\rho_y(y)$ is a simple convolution of $\rho_\zeta(\zeta)$ and $\rho_y^0(y)$ (see Eq. (4.62) in section 4.2.5). Since the vertical density profile $\rho_y^0(y)$ can be measured by switching the TDS off, the distribution in longitudinal direction can be determined by deconvolving the measured intensity distribution. Similar considerations apply to the two dimensional transverse distribution including the dependence on the horizontal coordinate x. A corresponding deconvolution of the measured CCD-images can be performed by means of the Lucy-Richardson algorithm [90, 91].

However, a bunch distribution typically exhibits correlations between the longitudinal and the vertical particle coordinate, so assumption (5.1) is a rough approximation. In particular, the vertical width is in general a function of the longitudinal position ζ within the bunch due to variations of the slice emittance and the ellipse parameters along a bunch. Also the mean vertical particle position can be function of ζ, e.g. due to wake field effects. As a result, a deconvolution using the transverse distribution measured with the TDS switched off did not deliver reliable results and was therefore not applied. The presented results are thus resolution-limited.

Subdivision into slices and averaging

An operation of the TDS close to zero-crossing of the deflecting force results in a shearing of the particle density distribution downstream of the TDS without a change of the mean particle position. However, fluctuations of the bunch arrival time with respect to the RF field of the TDS (RF phase jitter) results in jitter of the vertical beam position on the screen. To average intensity distributions and derived parameters over many images, an exact determination of the vertical beam position on the screen and a correction of position jitter is essential. Since the vertical extension of the beam on the screen is large, and occasionally only a fraction of a bunch is observed within the camera window, a determination of the mean particle position on the screen is error-prone. Instead, a reference point was defined in each vertical profile (projection of the intensity distribution onto the vertical axis). Typically, a steep slope at the head of the longitudinal charge density distribution allows a precise determination of the position of half maximum intensity in the vertical profile. The reference point was used to define an internal longitudinal bunch coordinate ζ with $\zeta = 0$ at the reference point.

In order to determine bunch properties as a function of the internal bunch coordinate, the images were subdivided into vertical intervals (slices) of the same height (typically 4 to 10 pixels) starting from the reference point. For each slice, the horizontal intensity profile (slice profile) was determined. For the purpose of slice emittance measurements, the RMS widths of the slice profiles were calculated and averaged over typically 20 to 30 images at each setting of the quadrupole magnets. For a tomographic reconstruction, average slice profiles were determined instead. Before averaging, the individual slice profiles were shifted to obtain coincidence of the slice centroid positions, thereby removing jitter of the horizontal bunch position on the screen.

5.2 Screen calibration

Calibration of longitudinal distances

When a bunch passes the TDS at zero-crossing of the RF deflecting force, the vertical distance Δy of two electrons at the screen downstream of the structure depends linearly on their longitudinal distance $\Delta\zeta$ according to $\Delta y = S \cdot \Delta\zeta$ with S the shear parameter (cf. Eq. 4.57). Owing to $\Delta\zeta \approx c\Delta t$ and $\Delta t = \Delta\Psi/\omega$ with ω the angular frequency of the TDS, Δy is also a linear function of the corresponding time difference Δt and the difference in RF phase of the TDS $\Delta\Psi$. The proportionality constants can be measured by varying the phase of the TDS around the zero-crossing phase while measuring the vertical position of the beam on the screen (see Fig. 5.3(a)).

When the shear parameter is large, small fluctuations of the RF phase from bunch to bunch result in fluctuations of the vertical beam position on the screen which are significant compared to the height of the screen. Such fluctuations may be both due to variations of the bunch arrival time and timing jitter of the RF signal. The total position jitter is typically in the order of 0.2 mm$\cdot S$ (RMS), where S is the shear parameter. The shear parameter at maximum input power of the TDS (about 18 MW) and 500 MeV beam energy amounts to $S \approx 35$, which results in position jitter of about 7 mm. In case of the screen OTR-2 (cf. Fig. 4.8), the height of the camera window amounts to 15.5 mm, so an accurate calibration is not possible at shear parameters this large. For this reason, a beam position monitor (BPM) placed directly (about 3 m) downstream of the TDS was used for calibration measurements at large shear parameters instead. Since the vertical beam offset at the position of the BPM is much smaller than at the position of the screen, it allows a measurement over a wider range of the RF phase, thus improving the signal-to-noise ratio. The calibration constant at the screen is then given by the measured calibration constant at the BPM times a constant which depends on the vertical transfer matrices from the TDS to the screen and to the BPM. Although the precision of a calibration measurement can be improved in this way, a calibration at large input power is in general clearly less precise than at low input power.

Calibration of charge density

The input power of the TDS was typically chosen such that the vertical extension of the beam at the position of the screen was slightly smaller than the height of the camera window. Since almost all electrons of a bunch are deflected onto the screen in this case, the charge density scale on a CCD-image can be calibrated by equating the integrated intensity of the image with the measured bunch charge.

Energy calibration

The current I_0 of the dipole upstream of the undulator section (dipole D1, cf. Fig. 4.8) is adjusted to bend the beam with nominal momentum p_0 by an angle α_0. The current is determined by the relation

$$\alpha_0 = \frac{-eB_0 L_{mag}}{p_0} \approx \frac{-eL_{mag} I_0}{p_0} \cdot 0.0029 \frac{T}{A} \tag{5.1}$$

with e the elementary charge, B_0 the peak magnetic field and L_{mag} the

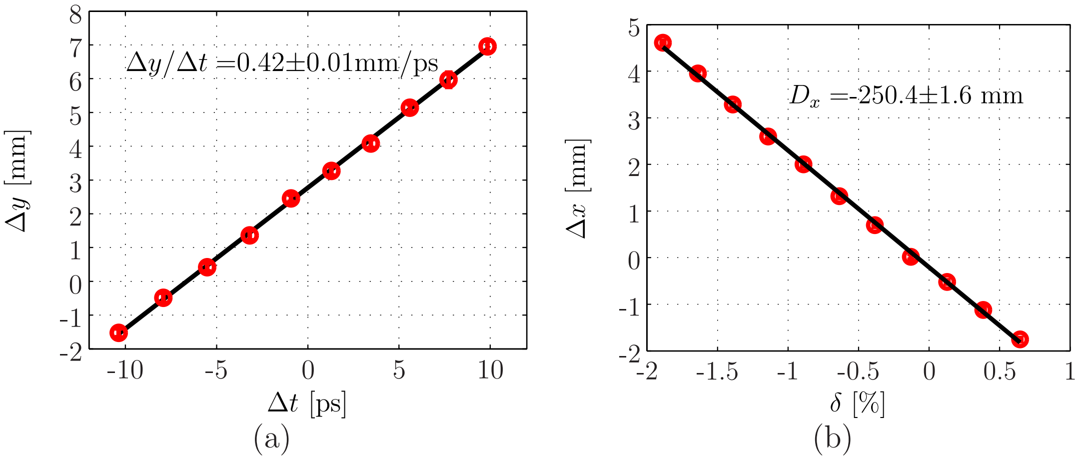

Figure 5.3: (a) Result of a calibration measurement yielding a relation between time delays Δt and vertical distances Δy on a screen . The vertical beam offset Δy (with respect to the center of the camera window) was measured at different RF phases of the TDS around zero crossing of the deflecting force. The values of the RF phase were chosen such that the bunch position significantly varies on the screen. 20 images were recorded at each step. Measured mean position and corresponding standard deviation at each step (red circles with error bars) were used to determine a regression line (black) by means of a linear least squares method. The slope of the line yields the calibration constant $\Delta y/\Delta t$. The measurement was performed using the screen OTR-2 (cf. Fig. 4.8). (b) Result of a calibration measurement yielding the relative momentum deviation δ as a function of the horizontal offset Δx on the screen OTR-3. The horizontal beam position (red circles with error bars) was measured for different currents of the upstream dipole magnet as explained in the text. The same procedure as in (a) was applied to determine the calibration constant D_x. $\Delta x = 0$ refers to the center of the screen.

magnetic length of the magnet (cf. section 4.2.3). The deflection angle of a particle with momentum $p = p_0 \cdot (1+\delta)$ slightly deviating from the nominal momentum differs from the design angle α_0 by

$$x' = \alpha_0 \cdot \frac{p_0}{p_0(1+\delta)} \approx -\alpha_0 \cdot \delta. \tag{5.2}$$

On the screen OTR-3 (cf. Fig. 4.8) downstream of the dipole magnet this angle leads to an offset

$$x = M^x_{1,2} \cdot x' \approx -M^x_{1,2} \cdot \alpha_0 \cdot \delta \equiv D_x \delta, \tag{5.3}$$

where $M^x_{1,2}$ is the element $(1,2)$ of the transfer matrix M^x from the position of the dipole to the position of the screen, and D_x the horizontal dispersion generated by the dipole at the position of the screen.

In order to calibrate the momentum deviation δ on the horizontal axis of the screen, the dispersion D_x needs to be measured. From Eq. (5.2) and

Eq. (5.1) follows that a change in momentum by a factor $(1+\delta)$ yields for $\delta \ll 1$ the same angle x' as a change of the current by a factor $(1-\delta)$. The calibration constant D_x can thus be determined by measuring the horizontal beam position on the screen as a function of the dipole current (see Fig. 5.3 (b)). Equivalently, the beam position can be measured as a function of the beam energy. Since a change in current can be quantified more precisely than a change in beam energy, the first approach was taken.

In order to optimize the energy resolution, the focal strengths of the two quadrupole magnets in-between the dipole and the screen were adjusted to maximize the dispersion D_x. Values in the range of $D_x = 250$ mm to $D_x = 290$ mm were measured. The momentum resolution δ_{resol} (RMS) is mainly determined by the horizontal beam size σ_x on the screen due to betatron oscillations,

$$\delta_{resol} \approx \frac{\sigma_x}{D_x}. \tag{5.4}$$

For a typical beam size of 100 μm and a dispersion $D_x = 290$ mm, the resolution amounts to $\delta_{resol} \approx 3 \cdot 10^{-4}$.

5.3 Details on slice emittance measurements

5.3.1 Optics

In order to be able to measure the slice emittance with good longitudinal resolution, the accelerator optics has to fulfill several boundary conditions. A good longitudinal resolution demands for a large vertical beta function at the TDS, and an appropriate betatron phase advance from the TDS to the screen, as discussed in section 4.2.5. In order to detect a large longitudinal section of the beam within the height of the camera window, the vertical beta function at the screen has to be small. The horizontal beam size at the screen should be roughly in the range of 60 to 200 μm to allow an accurate measurement of the beam size. Finally, the listed boundary conditions have to be fulfilled for different focal strengths of the quadrupole magnets, which have to be chosen such that the horizontal betatron phase at the location of the screen is varied by up to 180° (cf. section 3.1.1). It is advantageous to keep the focal strength of quadrupole magnets located in-between the TDS and the screen fixed so the shear parameter at the screen is the same for all the applied quadrupole settings.

The program MAD [92] was used to determine an appropriate optics fulfilling these boundary conditions. The optics is illustrated in Fig. 5.4. It includes the variation of six quadrupole magnets upstream of the TDS (Q-ACC4 to Q-ACC6) to obtain a sufficient change in horizontal betatron phase at the screen. A total number of eleven different settings of the magnets with stepwise increasing betatron phase ϕ_x at the screen OTR-2 were designed. The betatron phase can be changed in finer steps by interpolating the magnet currents of subsequent steps. The vertical beta function between the TDS and the screen is nearly the same in all cases, with values of about 47 m in the center of the TDS and roughly 10 m at the screen. The vertical betatron phase advance between the TDS and the screen is about 33°. At a TDS input power of 18 MW (the largest input power measured, cf. section 4.2.5) and a beam energy of 500 MeV, this yields a shear parameter of $S \approx 35$ at the screen. The horizontal beta function at the screen is in the range of 7 to 12 m, which yields a beam size of 120 μm to 160 μm at a beam energy of 500 MeV and a normalized emittance of 2 μm.

In a typical slice emittance measurements, the betatron phase ϕ_x at the screen was changed in 10 to 15 equidistant steps over an interval of 180°. At each step, 20 to 30 images were recorded and analyzed as described in section 5.1.

Beam matching

In order to match the beam to the design optics, a standard emittance measurement (based on a scan of a the focal strength of a single quadrupole magnet) was performed using an OTR screen downstream of the second bunch compressor (OTR-1, cf. Fig. 4.8). A simple matching algorithm has been implemented which adjusts the currents of five quadrupole magnets (Q-UBC3 and Q-DBC3, cf. Fig. 4.8) such that the mismatch parameter between the design optics and ellipse parameters of the bunch is minimized downstream of module ACC4.

In practice, matching the beam turned out to be problematic. The main reason is that changing the currents of quadrupole magnets upstream of the second bunch compressor may imply unwanted changes of the beam dynamics, which is especially the case for measurements under FEL operating conditions. Furthermore, the matching process was time-consuming

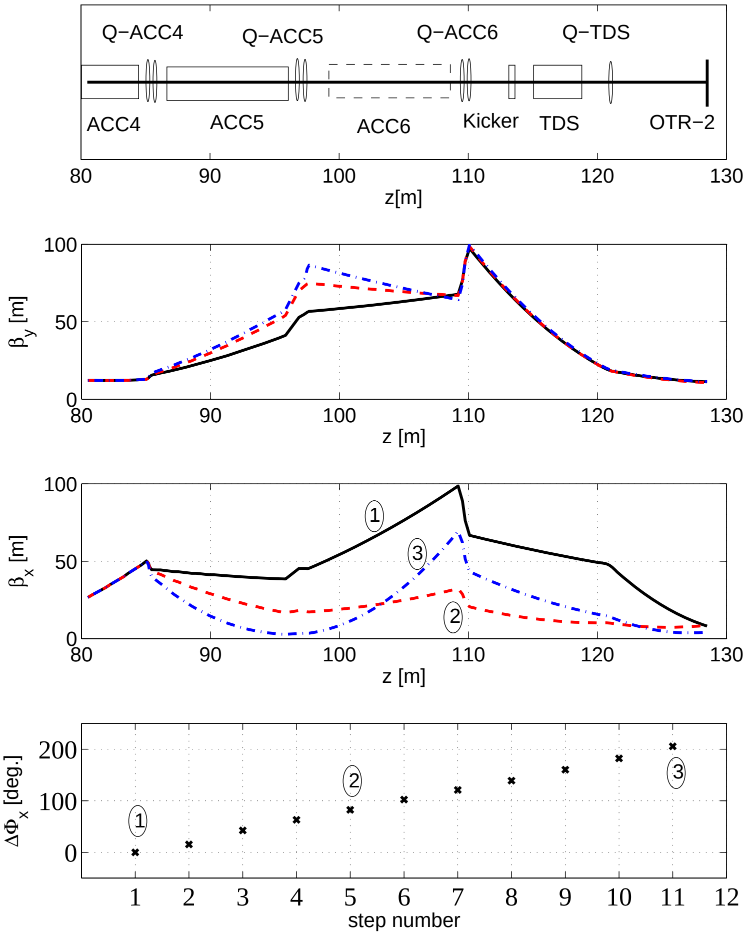

Figure 5.4: Optics for slice emittance measurements. From top to bottom: schematic of the beamline in the region around the TDS, vertical beta function β_y and horizontal beta function β_x along the beamline for three different settings of the quadrupole magnets Q-ACC4 to Q-ACC6, and difference $\Delta\phi_x$ in horizontal betatron phase at the screen OTR-2 between the different magnet settings. The numbers in the bottom plot refer to the presented betatron functions.

since the optics and the orbit had to be adjusted empirically for the emittance measurement at OTR-1. However, the optics presented above does not rely on a perfectly matched beam and thus allows accurate measurements also without a matched beam, as will be discussed in more detail in section 5.3.2.

Orbit feedback

When switching between the settings of the quadrupole magnets Q-ACC4 to Q-ACC6, beam orbit offsets at the positions of these magnets lead to variations of the beam orbit and correspondingly of the beam position on the screen. To minimize these steering effects of the quadrupole magnets, the steering magnets located directly downstream of the quadrupole magnets were adjusted automatically to compensate changes of the transverse offsets measured at BPMs.

Adjustment of camera settings

The transverse width and structure of the beam at the screen changes during a slice emittance measurement due to the variation of the accelerator optics. In order to benefit from the maximum dynamic range of the camera, the camera gain was adjusted automatically to the peak radiation intensity at each step of the measurement.

5.3.2 Error analysis

In this section, the influence of several error sources on an emittance measurement is elaborated. The discussion refers to the accelerator optics discussed in the previous section with eleven different settings of the quadrupole magnets changing the horizontal betatron phase at the screen by 180° in equidistant steps.

Statistical errors

The CCD images recorded during a measurement are subject to distortions such as noise in the camera and spurious intensities in the image, which give rise to statistical errors of the measured beam size (cf. section 5.1). Typically, the standard deviation of the beam size extracted from several images is 10 to 20 %. For a total number of 20 images for each setting of the quadrupole magnets, the standard deviation of the mean value is thus less than 5 %. The resulting statistical error of the emittance depends on the applied optics as well as the mismatch of the beam (cf. section 2.3) with respect to the optics. Figure 5.5 shows the emittance error σ_{ϵ_x} as obtained from a simulation assuming beam sizes with a random error of 5 % (RMS) and different values for the mismatch parameter M and the mismatch phase Ψ of the beam. For fixed mismatch parameter M, σ_{ϵ_x} shows a periodic dependence on the mismatch phase Ψ with a periodicity of 180° (Fig. 5.5(a)). The maximum error increases with increasing mismatch parameter M (Fig. 5.5(b)). The maximum mismatch parameter M (with

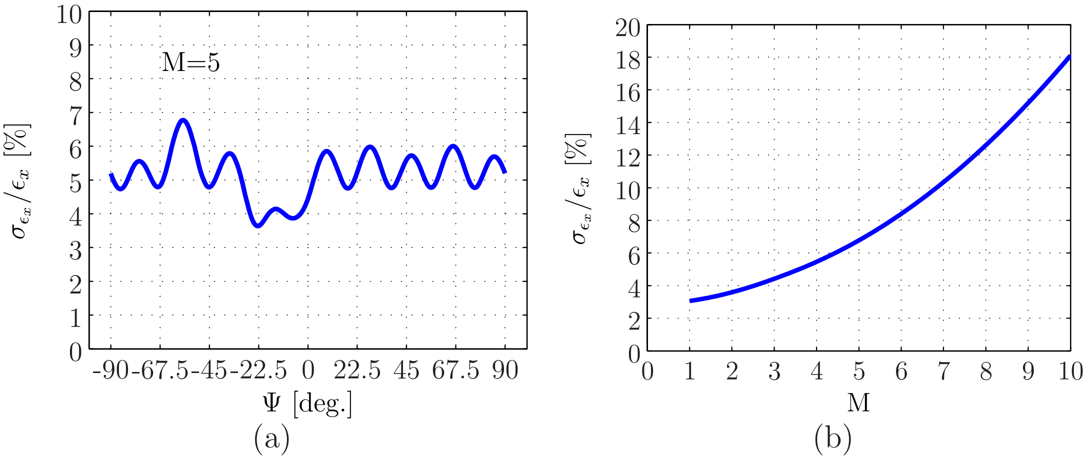

Figure 5.5: Dependence of the statistical error σ_{ϵ_x} of the emittance on the mismatch of the beam with respect to the design optics (simulation). Figure (a) shows the relative emittance error $\sigma_{\epsilon_x}/\epsilon_x$ as a function of the mismatch phase Ψ for fixed mismatch parameter $M = 5$ over one period of 180°. The error was calculated by error propagation (cf. section 3.1.1) assuming a Gaussian error of the beam size with a standard deviation of 5 %. In Fig. (b), the maximum error over one period of the mismatch phase is shown as a function of the mismatch parameter M.

respect to the overall beam ellipse parameters) encountered in case of the measurements presented in this thesis amounts to $M = 3.2$. The statistical error of the emittance is less than 5 % in this case. For individual slices the error may be larger due to a larger mismatch parameter.

Resolution errors

The spatial resolution of the OTR station used for slice emittance measurements was determined to be in the range of 14 μm to 26 μm, depending on horizontal beam position on the screen (cf. section 4.2.2). The influence of resolution limitations on an emittance measurement depends on the beam size at the position of the screen, which is determined by the optics, the mismatch of the beam with respect to this optics, the beam emittance and the beam energy. The resolution-limited beam size is given by

$$\sigma_x = \sqrt{\sigma_{x,0}^2 + \sigma_{resol}^2} \tag{5.5}$$

with σ_{resol} the RMS resolution and $\sigma_{x,0}$ the true beam size. Figure 5.6(a) shows the relative deviation $\epsilon_{rec}/\epsilon_x$ of the reconstructed emittance ϵ_{rec} from the beam emittance ϵ_x resulting from a resolution of 14 μm (RMS) as a function of the mismatch parameter M for different values of the nor-

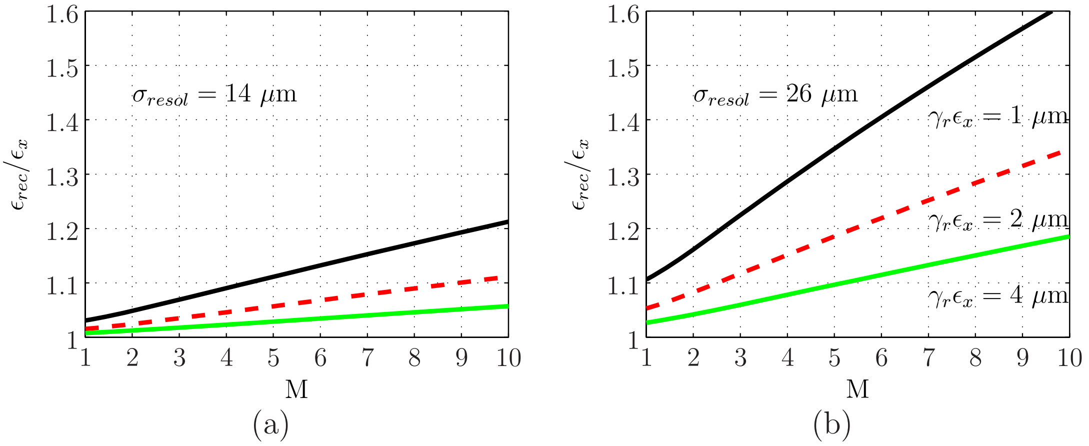

Figure 5.6: Influence of resolution limitations of the OTR station OTR-2 on emittance measurements. In (a), the relative deviation $\epsilon_{rec}/\epsilon_x$ of the reconstructed emittance ϵ_{rec} from the beam emittance ϵ_x resulting from a resolution of $\sigma_{resol} = 14\ \mu m$ is shown as a function of the mismatch parameter M. Results for different values of the normalized beam emittance of 1 μm, 2 μm and 4 μm are presented. A beam energy of 500 MeV was used for the calculations. Similar as in Fig. 5.5, the deviation $\epsilon_{rec}/\epsilon_x(M)$ is defined as the maximum value obtained over an interval of the mismatch phase Ψ of 180° at fixed mismatch parameter M. The corresponding result in case of a resolution of $\sigma_{resol} = 26\ \mu m$ is shown in (b).

malized beam emittance of 1 μm, 2 μm and 4 μm. A beam energy of 500 MeV was used for the calculations. A significant influence on the resulting emittance is seen in case of a large mismatch parameter and a small beam emittance. The reconstructed emittance is larger by up to 20 % in case of a mismatch parameter $M = 10$ and an emittance of 1 μm. In Fig. 5.6(b), the corresponding result is shown for a resolution of 26 μm. Here, a significantly stronger effect on the emittance is observed. While for moderate mismatch parameters of $M \lesssim 3$ the emittance error is less than 25 %, errors of up to 60 % are encountered at a mismatch of $M = 10$ and an emittance of 1 μm. In case of the results presented in this thesis, the mismatch parameter between the overall ellipse parameters and the design Twiss parameters was found to be $M \lesssim 3.2$, while the normalized emittance was measured to be $\gtrsim 2\ \mu$m. The error resulting from resolution limitations is thus $\lesssim 10$ %.

Influence of the kicker

In case the beam has a non-vanishing standard deviation σ_E of the beam energy, the deflection by the kicker induces an angular spread $\sigma_{x'}$. According to the results obtained in section 5.2 (Eq. (5.6)), this results in a horizontal position spread σ_x on the screen given by

$$\sigma_x \approx M^x_{1,2} \cdot \alpha_0 \cdot \sigma_\delta, \tag{5.6}$$

where M^x is the horizontal transfer matrix from the kicker to the screen, α_0 the nominal deflection angle, and $\sigma_\delta = \sigma_E/E_0$ with E_0 the nominal energy. The term $M^x_{1,2} \cdot \alpha_0 \equiv D_x$ yields the nominal offset from the beam axis at the position of the screen (10 mm when the beam is centered on the screen), and corresponds to the dispersion D_x generated by the kicker. Since the kicker is located downstream of the quadrupole magnets Q-ACC4 to Q-ACC6 which are varied during an emittance measurement, D_x is unaffected during such a measurement. The maximum relative energy spread that was measured under FEL operating conditions amounts to $\sigma_\delta \approx 0.25$ % (see chapter 7). This yields a position spread of $\sigma_x \approx 25$ μm, which is comparable to the upper limit of the resolution of the optical system. In correspondence to Fig. 5.6, Fig. 5.7 shows the ratio $\epsilon_{rec}/\epsilon_x$ of the reconstructed emittance to beam emittance assuming a relative energy spread $\sigma_\delta = 0.25$ % and a resolution $\sigma_{resol} = 26$ μm. While without mismatch the deviation of the reconstructed emittance is $\lesssim 20$ % also in case of a small beam emittance of 1 μm, large deviations up to $\epsilon_{rec}/\epsilon_x = 2$ occur if the beam emittance is small and the mismatch large. However, in case of the measurements presented in this thesis, the beam sections with large energy spread were found to have an emittance of more than 4 μm and a moderate mismatch $M \lesssim 4$ with respect to the design optics. The deviation of the reconstructed emittance from the beam emittance is therefore < 15 % also in this case. The coincidence of a large energy spread and a large emittance is related to the fact that the energy spread is mainly generated by collective effects in high-density regions of a bunch, which typically also lead to significant emittance growth.

Calibration errors

When the calibration constant of the screen specifying the horizontal distance per pixel of a CCD image is wrong by a factor $\Delta = (1 + d)$, the measured beam size deviates from the true one by the same factor Δ. The beam emittance ϵ_x is reconstructed from squared beam sizes $\sigma_x^2 = \epsilon_x \beta_x$, which are wrong by a factor Δ^2. Consequently, the emittance is also wrong

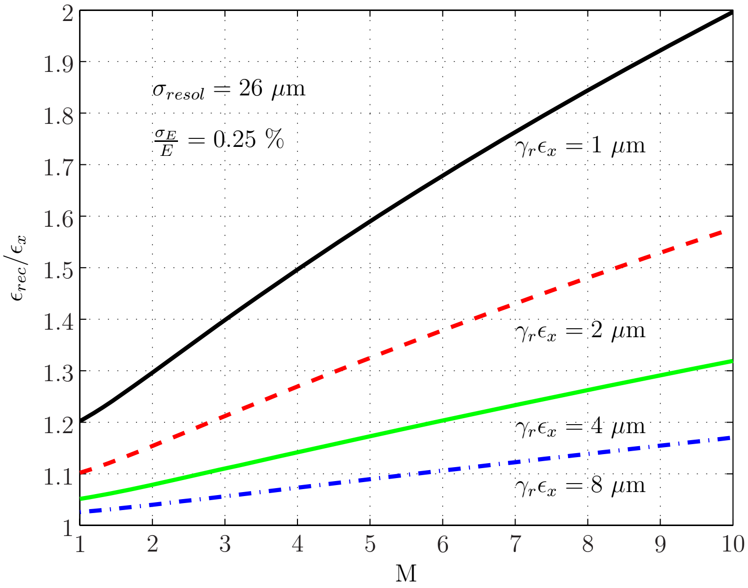

Figure 5.7: Influence of the horizontal kicker on the reconstructed emittance. The ratio of reconstructed emittance ϵ_{rec} to the beam emittance ϵ_x is shown as a function of the mismatch parameter M for different values of the normalized beam emittance as indicated in the figure. The relative energy spread used for the calculations is 0.25 % and the beam energy 500 MeV. A resolution of the OTR station of 26 μm was assumed.

by a factor Δ^2. For small relative errors $d \ll 1$ of the calibration constant, the relative error of the emittance thus amounts to $\Delta^2 - 1 \approx 2 \cdot d$.

The calibration constant of the screen OTR-2 used for emittance measurements was found to be $27 \pm 0.6\ \mu$m per pixel, with a relative error of about 2 % (RMS). Hence, the resulting error of the beam emittance amounts to about 4 %.

Erroneous beam transfer

The reconstruction of the beam emittance is based on the equation

$$\Sigma \approx R \cdot o, \tag{5.7}$$

which is an abbreviation for

$$\begin{pmatrix} (\sigma_{1,1}^{(1)}) \\ (\sigma_{1,1}^{(2)}) \\ \vdots \\ (\sigma_{1,1}^{(n)}) \end{pmatrix} \approx \begin{pmatrix} (M_{1,1}^{(1)})^2 & 2M_{1,1}^{(1)}M_{1,2}^{(1)} & (M_{1,2}^{(1)})^2 \\ (M_{1,1}^{(2)})^2 & 2M_{1,1}^{(2)}M_{1,2}^{(2)} & (M_{1,2}^{(2)})^2 \\ \vdots & & \\ (M_{1,1}^{(n)})^2 & 2M_{1,1}^{(n)}M_{1,2}^{(n)} & (M_{1,2}^{(n)})^2 \end{pmatrix} \begin{pmatrix} \sigma_{1,1}(s_0) \\ \sigma_{1,2}(s_0) \\ \sigma_{2,2}(s_0) \end{pmatrix},$$

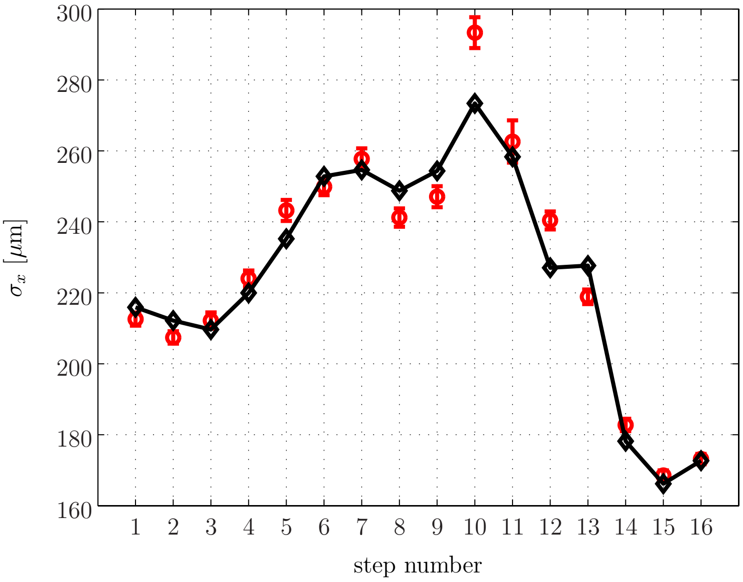

Figure 5.8: Typical result of a comparison of the reconstructed beam sizes σ_x (black) to the measured ones (red circles with error bars). The "step number" indicates the different settings of the quadrupole magnets. The RMS deviation S^* as defined in the text amounts to 3 % in this case.

where $\sigma_{1,1}^{(i)}$ is the squared beam size measured at setting (i) of the quadrupole magnets, $M^{(i)}$ is the corresponding transfer matrix from the reconstruction point s_0 to the screen, and $\sigma_{1,1}(s_0), \sigma_{1,2}(s_0), \sigma_{2,2}(s_0)$ denote the elements of the beam matrix $\sigma(s_0)$ at s_0 (cf. Eq.(3.1) in section 3.1.1). Up to now, only errors of the squared beam sizes in the vector Σ have been considered. However, also the description of the beam transfer by the matrix R may be inaccurate due to an energy error or an erroneous calibration of quadrupole magnets. An important quantity in this context is (for overdetermined systems with $n > 3$) the residual vector

$$r = R \cdot o - \Sigma$$

describing the difference between the "reconstructed" squared beam sizes $R \cdot o$ and the measured ones Σ (see Fig. 5.8). The solution of equation (5.7) is found by minimizing the sum $S = r^T r$ of the elements of r squared, optionally weighted by measurement errors (cf. section 3.1.1). The quantity S describes the accuracy of the reconstruction. In case of an accurate measurement of the vector Σ, S is a measure for the accuracy of the matrix R.

Calibration errors of the quadrupole magnets appear to be critical at first glance in case of the optics applied for emittance measurements, since the matrix R relies on the correct calibration of seven quadrupole magnets. The effect of calibration errors was investigated by randomly varying the calibration constants of the quadrupole magnets before reconstructing the emittance from experimental data. The calibration accuracy was estimated to be about 1 %, see section 4.2.3. Here, a flat top error distribution with maximum deviations of each calibration constant from its nominal value of 2 % was assumed. A typical distribution of the emittance resulting from such a simulation is presented in Fig. 5.9(a). For most combinations of calibration errors, the deviation of the emittance from its measured value is < 2 %. However, there is a long tail in the distribution with deviations up to nearly -10 %.

It is instructive to determine the deviation S between measured and reconstructed bunch widths for each combination of calibration constants. The corresponding result is presented in Fig. 5.9(b). For illustration purposes, the deviation $\Delta\sigma_x^{(i)}$ between measured widths $\sigma_x^{(i)}$ and reconstructed bunch widths is specified more intuitively as the RMS value of their relative deviation:

$$S^* = \sqrt{\frac{1}{N}\sum_{i=1}^{N}\left(\frac{\Delta\sigma_x^{(i)}}{\sigma_x^{(i)}}\right)^2}. \tag{5.8}$$

The figure reveals a correlation between the reconstruction accuracy S^* and $\Delta\epsilon_x/\epsilon_x$. In particular, combinations of calibration constants which lead to a significant deviation of the emittance from the measured value lead to large values of S^* as well, and can therefore be excluded.

The result of such a Monte Carlo simulation depends on the detailed measurement condition, in particular on the mismatch of the beam with respect to the design optics. The strong correlation between the reconstruction accuracy and the emittance error was observed in all measurements. In case of the presented measurements, the effect from calibration errors of quadrupole magnets on the reconstructed emittance can therefore safely be assumed to be < 5 % (RMS).

Aside from calibration errors of quadrupole magnets, the description of the beam transfer can be wrong because of a deviation of the beam energy from the energy assumed for the reconstruction. Such energy errors affect also the “normalization” of the emittance by multiplication of the geomet-

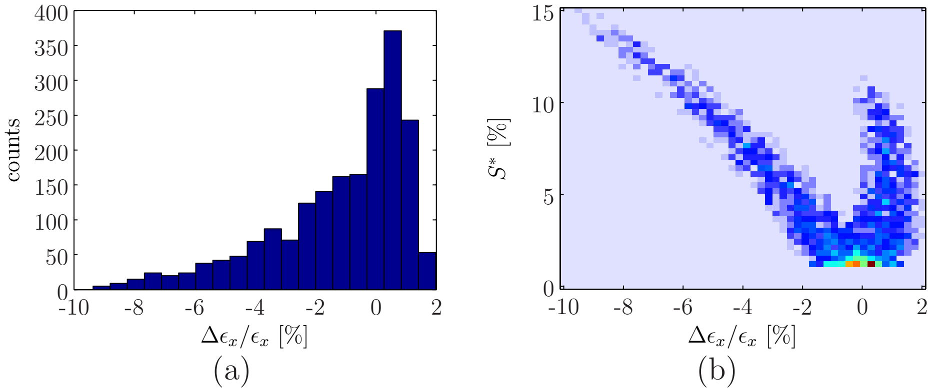

Figure 5.9: Result of an emittance reconstruction from experimental data with random calibration errors of all the seven quadrupole magnets involved. (a) Distribution of the resulting emittance error $\Delta\epsilon_x/\epsilon_x$*. (b) Correlation between the emittance error and the reconstruction error* S^**. A flat top error distribution with maximum deviations of the magnetic field gradient of* 2 % *was assumed. A total number of 2000 runs were carried out.*

rical emittance with γ_r. The influence of energy errors was checked for each measurement by determining the normalized emittance as a function of the energy in an interval of a few percent around the measured value. A typical result is presented in Fig. 5.10(a). The reconstructed normalized emittance varies by about ±5 % for an energy deviation of ±2 %. Larger deviations of up to −20 % occur for an energy deviation of −5 %.

Similar as in case of calibration errors of quadrupole magnets, it is instructive to look at the reconstruction error S^*. Figure 5.10(b) shows that large deviations of the energy from the measured value are accompanied by large reconstruction errors S^* and can therefore be excluded. Furthermore, the figure reveals that the reconstruction error exhibits a minimum close to the measured energy. This characteristic of the reconstruction error as a function of the energy was utilized to check the accuracy of the measured energy in each experiment. The measured energy was occasionally corrected by up to 2 %. The remaining energy error is assumed to be less than 1 %, and the resulting error of the normalized emittance correspondingly in the order of a few percent.

In case of off-crest operation, there is an energy gradient along a bunch, with variations of the mean energy as a function of the longitudinal position of up to 0.5 % (see chapter 7). In principle, this gradient could be determined by minimizing the reconstruction error S^* for individual longitudinal sections of the bunches. The resulting energy variations along

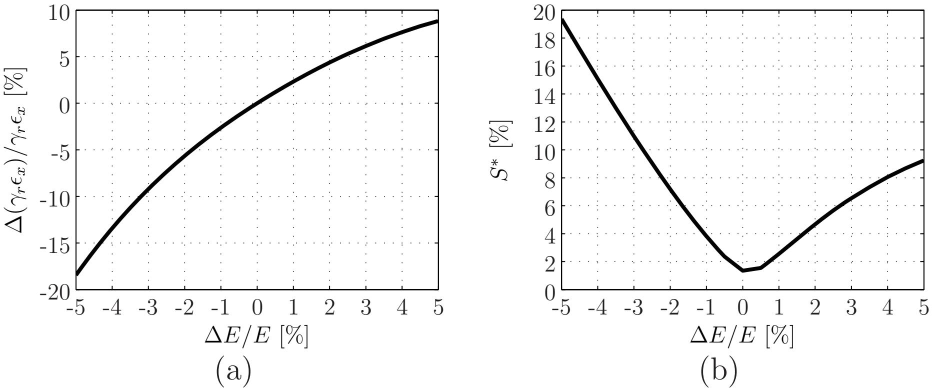

(a) (b)

Figure 5.10: (a) Sensitivity of the reconstructed normalized emittance $\gamma_r\epsilon_x$ on relative energy deviations $\Delta E/E$. Experimental data were used for the reconstruction. E denotes the measured energy. For simplicity, the energies upstream and downstream of the accelerating module ACC5 were varied by the same factor. (b) Corresponding Reconstruction error S^* as a function of the relative energy deviation $\Delta E/E$.

a bunch could be included in the reconstruction. This was, however, not done in case of the presented measurements since the energy deviations along a bunch are still within the energy uncertainty.

Discussion

In order to estimate the emittance accuracy, the variances $(\sigma_\epsilon^{(i)})^2$ due to the individual error sources have to be added to obtain the overall RMS error $\Delta\epsilon$ according to

$$\Delta\epsilon = \sqrt{\sum_{i=1}^{n}(\sigma_\epsilon^{(i)})^2}. \tag{5.9}$$

As shown in the previous section, the effect of statistical beam size errors and resolution limitations on the reconstructed emittance depends on beam parameters such as the beam energy, the beam emittance, the mismatch with respect to the design optics, and the standard deviation of the particle energy within a bunch. For typical bunch properties at FLASH ($\gamma_r\epsilon_x \gtrsim 2\ \mu$m, $\sigma_\delta \lesssim 0.25$ %, $M \lesssim 6$) and a beam energy of 500 MeV the overall emittance error is estimated to be $\lesssim 20$ %. Larger errors may occur for individual slices with a large mismatch parameter M.

Chapter 6

Results for uncompressed bunches

The beam dynamics in the linear accelerator of FLASH is well described by linear transport theory when all accelerating modules are operated on-crest. In this case the standard deviation of the particle energy is minimal, and the bunches are hardly compressed in the magnetic chicanes. Collective effects such as coherent synchrotron radiation and space charge forces are therefore greatly reduced. These conditions are suited to test the experimental methods. Moreover, initial properties of the particle distribution downstream of the RF gun can be investigated, in particular the bunch length and the slice emittance. Finally, since the bunches are much longer than in case of off-crest acceleration, time-dependent effects such as wake fields are more pronounced and can be investigated.

6.1 Current profile

A typical current profile of an uncompressed bunch is shown in Fig. 6.1 (black curve). The measurement was performed at a particle energy of 490 MeV and a bunch charge of 0.6 nC. The measured peak current amounts to about 40 A. The RMS length is 1.5 mm. The total length over which a current was detected is approximately 7 mm. The profile shows a significant asymmetry with respect to the bunch center. The asymmetry originates from a longitudinal energy gradient in both shoulders of a bunch, where particles are accelerated off-crest (see next section). The energy gradient results in an elongation (decompression) of the trailing edge and a shortening (compression) of the leading edge.

In order to suppress bunch compression effects, the current profile was measured with the dipole magnets of the bunch compressor chicanes switched

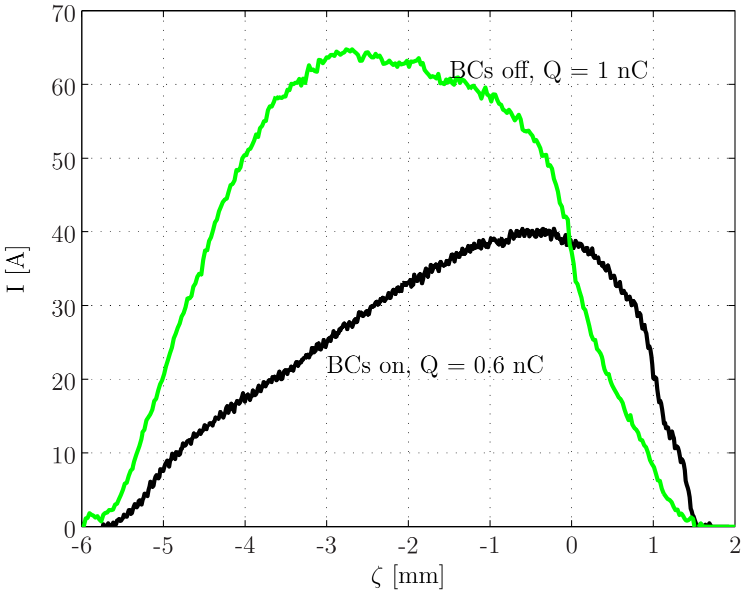

Figure 6.1: Measured current as a function of the internal coordinate ζ. The black curve shows the average current profile of a bunch obtained at nominal operation of the bunch compressor chicanes ("BCs on"). The accelerator was operated at a particle energy of 490 MeV and a bunch charge of 0.6 nC. The profile is an average over 25 bunches. The green curve shows a corresponding current profile obtained with the dipole magnets of the bunch compressor chicanes switched off ("BCs off"). Here, the accelerator was operated at a particle energy of 650 MeV and a bunch charge of 1.0 nC. The longitudinal RMS resolution of the measurements is roughly 130 μm in both cases. The bunch head is on the right hand side. The internal bunch coordinates of the two profiles were shifted to obtain coincidence at the front.

off. The orbit was adapted by steering magnets to let the particles on a straight line through the bunch compressor sections. The current profile measured under these conditions is also shown in Fig. 6.1. The measurement was performed at a particle energy of 650 MeV and a bunch charge of 1 nC. The current profile is approximately Gaussian-shaped. In particular, the profile is roughly symmetric with respect to the bunch center, in contrast to the result obtained with the bunch compressors switched on. The measured peak current amounts to about 75 A. It is significantly larger than in case of the measurement at 490 MeV due to a higher bunch charge. The RMS length is 1.6 mm. The total length over which a non-vanishing current was measured is 7.5 mm.

6.2 Longitudinal phase space

The CCD-image presented in Fig. 6.2(a) shows a single-shot measurement of the energy-dispersed charge density distribution on an OTR screen (OTR-3 in Fig. 4.8). The image is rotated so the vertical coordinate depends on the energy and the horizontal coordinate on the longitudinal position by means of the TDS. The relative energy deviation

$$\delta = \frac{E - E_0}{E_0} \tag{6.1}$$

with E the particle energy and $E_0 = \langle E \rangle$ the mean particle energy of the bunch is introduced on the vertical axis. The measurement was performed with both bunch compressors switched off. The distribution shows the curvature of the RF accelerating fields imprinted on the bunch. The bunch center was accelerated on-crest and gained the most energy, while the particles in both edges were accelerated off-crest. The energy-gradient induced in the edges leads to a change in their length in case the bunch compressors are switched on, as discussed in the previous section.

The measured standard deviation of the particle energy within a bunch is 0.09 % or 585 keV (average value over 30 bunches). The standard devi-

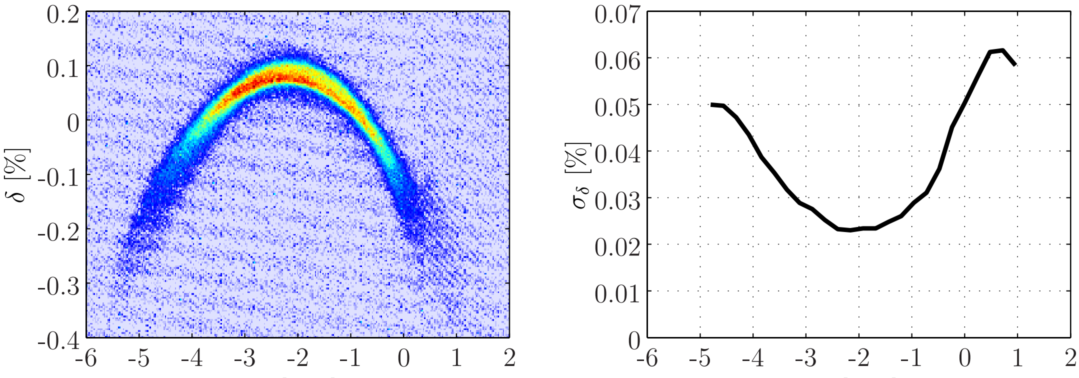

(a) (b)

Figure 6.2: (a) Single-shot measurement of the charge density distribution in longitudinal phase space (ζ, δ) *(for color code see appendix A). The measurement was performed at an energy of 650 MeV and a bunch charge of 1 nC. The bunch compressors were switched off. The dispersion at the screen was measured to be 290 mm. The longitudinal resolution is estimated to be about 130* μ*m. The bunch head is on the right hand side. (b) Average measured RMS energy spread* σ_δ *as a function of longitudinal position* ζ*. The values are averaged over 30 bunches.*

ation of the particle energy $\sigma_\delta(\zeta)$ as a function of the internal bunch coordinate ζ (energy spread) is shown in Fig. 6.2(b). The minimum energy spread measured in the center of the bunch is about 0.023 % or 150 keV. The values are resolution-limited. The energy spread in the injector section was measured to be less than 25 keV [42], and simulations suggest that the true energy spread is even smaller. The measured values thus provide an estimate for the energy resolution. The measured energy spread of 150 keV in the bunch center corresponds to a transverse bunch width of 67 μm (RMS).

6.3 Horizontal slice emittance and slice ellipse parameters

A measurement of the slice emittance of uncompressed bunches was performed at an energy of 490 MeV and a bunch charge of 0.6 nC. The result is presented in Fig. 6.3. The measured slice emittance is in the range of 1.5 to 4 μm. The largest values are found in the front section and the back section of a bunch. The slice emittance in the bunch center is below 2.5 μm, with a local maximum occurring at $\zeta \approx -2$ mm. The variation in slice emittance basically coincides with the variation in horizontal slice width observed in the measured CCD images (see figure). The accelerator settings (in particular the current of the solenoid) were not adjusted to minimize the emittance.

Aside from the slice emittance, the ellipse parameters of the RMS ellipse in horizontal phase space were determined for each longitudinal slice. RMS ellipse parameters are not intrinsic properties of a bunch, but depend on the optics and thus vary along the beamline. These variations can be suppressed by “normalizing” the slice ellipse parameters with respect to reference ellipse parameters. Here, the overall bunch ellipse parameters were chosen. The deviation from the reference ellipse parameters can be described by a deformation parameter m and a deformation phase ψ, which are defined in analogy to mismatch parameter and mismatch phase of particle beam optics. A precise definition can be found in section 2.3. Neglecting energy variations along a bunch, deformation parameter and deformation phase are invariants of linear beam optics.

A deformation parameter m close to one was measured in the bunch

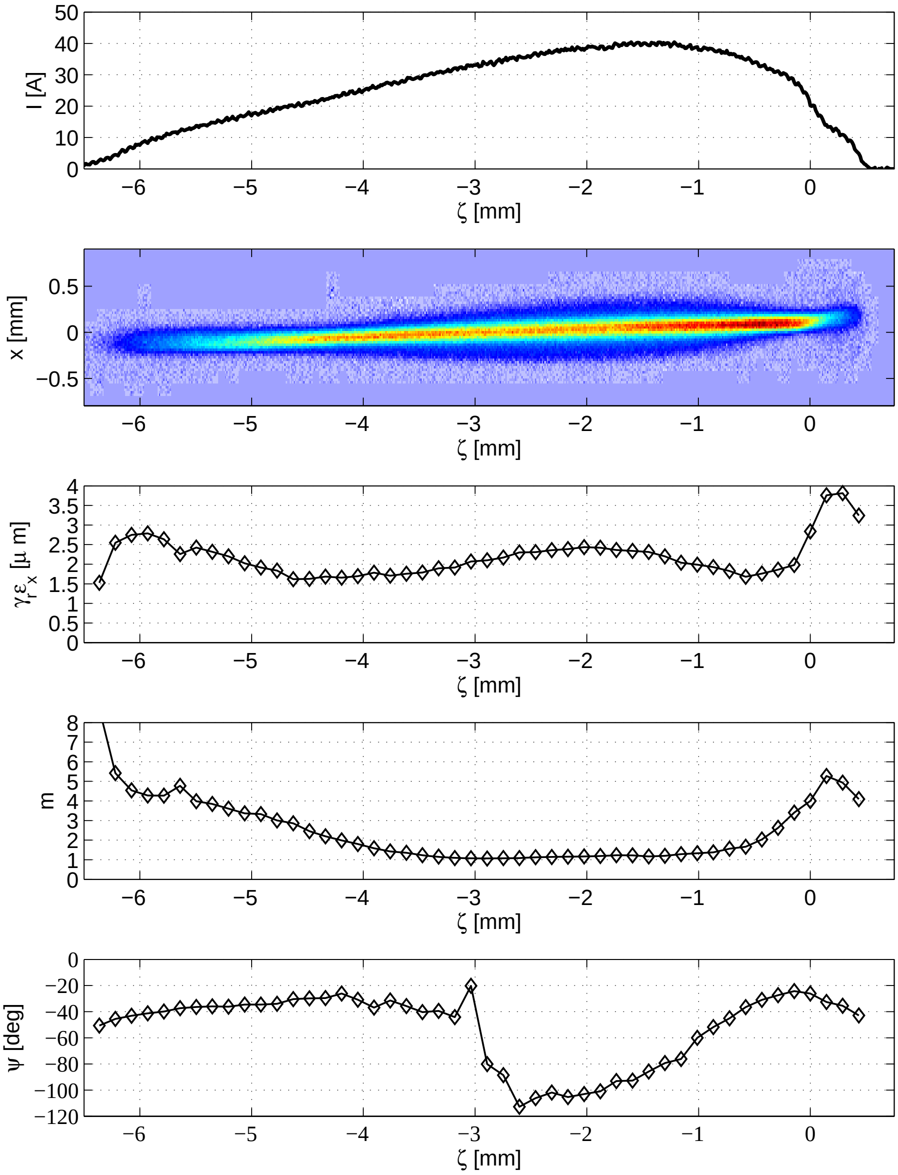

Figure 6.3: Experimental results for bunches accelerated on-crest in all acceleration modules. From top to bottom: Average current profile (cf. Fig. 6.1), typical CCD-image showing the charge density distribution in the longitudinal-horizontal plane, normalized slice emittance $\gamma_r \epsilon_x$, slice deformation parameter m, and deformation phase ψ. The head of the bunch is on the right hand side. The measurements were performed at a particle energy of 490 MeV and a bunch charge of 0.6 nC. The bunch compressors were switched on. The longitudinal resolution was estimated to be 125 μm (RMS). The slice width $\Delta\zeta$ was chosen to be 150 μm. Statistical errors of slice emittance and deformation parameters are not shown for reasons of clarity. They are in the order of a few percent.

center between $\zeta = -1$ mm and $\zeta = -3.5$ mm (see Fig. 6.3), indicating that the slice ellipse parameters nearly coincide with the overall bunch ellipse parameters. The deformation phase ψ rapidly changes in this bunch section. This is of no significance, since for $m \gtrsim 1$ the variations in ψ correspond to small variations of the underlying slice ellipse parameters. In the front section and the back section of a bunch, the deformation parameter increases to $m > 5$. At the same time, the deformation phase changes gradually between $-60°$ and $-20°$. The shape of the distributions in phase space is illustrated in the next section.

The increase in deformation parameter and slice emittance in the front and the rear section of a bunch is a well-known effect resulting from ζ-dependent transverse space charge forces and the solenoid focusing in the electron gun [93] (cf. section 4.1.2). The field of the solenoid is adjusted to compensate transverse space charge forces in the bunch center. Since the charge density and correspondingly the transverse space charge force is significantly smaller in the front and the rear section of a bunch, the particles partly diverge due to "over-focusing" in the solenoid. The divergence of a part of the beam corresponds to a bifurcation in transverse phase space and thus leads to emittance growth. The gradual variation in slice emittance in the bunch center is assumed to be caused by transverse space charge forces changing along the bunch according to the charge density.

The mean value of the slice emittance shown in Fig 6.3 (weighted by the current) amounts to 2.1 μm. The overall bunch emittance was measured [1] to be 3.8 μm. The deviation between the two values is due to slice deformation parameters $m > 1$ on the one hand, and mean particle coordinates $\langle x \rangle$, $\langle x' \rangle$ varying as a function of ζ (slice centroid offsets) on the other hand. Slice centroid offsets can be observed in the CCD-image in Fig. 6.3 in the form of a bunch tilt: The mean particle position $\langle x \rangle(\zeta)$ is about 100 μm in the front section of the bunch, while in the back section it amounts to about -100 μm. The overall bunch emittance without contributions from slice centroid offsets can be determined by calculating the mean horizontal slice width (weighted by the current) for each CCD-image. The bunch emittance determined in this way amounts to 2.5 μm. The remaining difference to the mean slice emittance of 2.1 μm is due to slice deformation parameters $m > 1$. Centroid offsets thus strongly contribute to the overall bunch emittance. Such offsets can be caused by wake

---

[1] The TDS (transverse deflecting structure) was switched off for a measurement of the overall bunch emittance. In case the TDS is switched on, the large vertical beam size on the screen makes the measurement sensitive to a roll angle of the camera (see also section 6.5).

fields in the accelerating modules. As a consequence, the overall bunch emittance may significantly change along the linac. Here, an emittance of 4.3 μm was measured in the diagnostic section downstream of the second bunch compressor.

Measurements of the slice emittance of uncompressed bunches were performed several times at different energies and bunch charges. In most cases, the resulting slice emittance was larger than in case of the presented result, with values of up to 5 μm in the bunch center. An enhanced slice emittance was found to be associated with a significant asymmetry in the horizontal charge density profiles of single longitudinal slices. Such asymmetries are an indication for a true increase in emittance due to a distortion, e.g. strong transverse wake fields. In case of the presented measurement, the profiles are Gaussian-shaped in good approximation.

6.4 Horizontal phase space

The experimental data used for determining the slice emittance shown in the previous section allow also for a tomographic reconstruction of the horizontal phase space distribution within longitudinal slices. The accuracy of the reconstruction can be checked by comparing the emittance resulting from the reconstructed distributions to the result of the slice emittance measurement using a least squares method. Such a comparison is presented in Fig. 6.4. In the bunch center, both slice emittance profiles agree within about 15 %, showing that the phase space reconstruction is accurate. In the front section, larger deviations occur due to an inferior signal-to-noise ratio. The least squares method is considered to be more reliable here.

The measured horizontal phase space distributions within the leading edge, the center and the trailing edge of a bunch are shown in Fig. 6.5. In the bunch center at $\zeta = -3$ mm (Fig. 6.5(a)), the distribution is approximately Gaussian-shaped. The emittance of the distribution is about 2 μm. A two-dimensional Gaussian fit yields an emittance of 1.6 μm (for details see section 7.6.1). At $\zeta = 0$ mm and $\zeta = -6$ mm (Fig. 6.5(b, c)), the distributions have a different shape due to large deformation parameters of $m \approx 4$ in these sections (cf. Fig. 6.3) . The measured distributions are not as smooth as in the bunch center due to an inferior signal-to-noise ratio. The phase space distribution of an entire bunch (Fig. 6.5(d)) covers

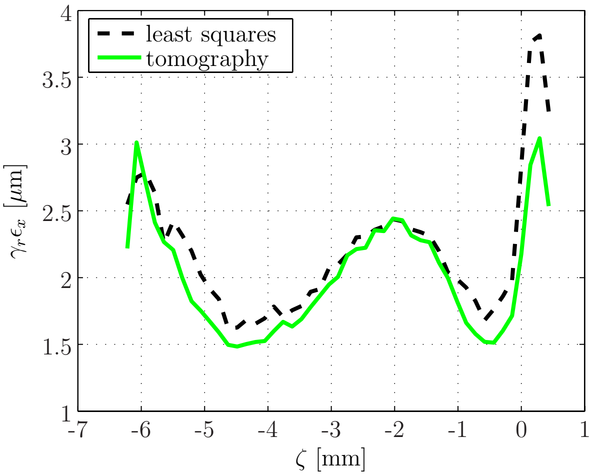

Figure 6.4: Comparison of the slice emittance obtained by a least squares method (black, dashed) and a tomographic reconstruction (green, solid). The same subdivision in longitudinal slices was used. The measurement was performed at a particle energy of 490 MeV and a bunch charge of 0.6 nC (see also Fig. 6.3).

a significantly larger phase space region, both due to slice deformation parameters $m > 1$ and slice centroid offsets. The distribution deviates from a Gaussian shape due to these effects.

In Fig. 6.6, the same distributions presented in Fig. 6.5 are shown in normalized coordinates

$$u = \frac{x}{\sqrt{\beta_e}} \tag{6.2}$$

$$v = \frac{\alpha_e}{\sqrt{\beta_e}} \cdot x + \sqrt{\beta_e} \cdot x' \tag{6.3}$$

with respect to the overall bunch ellipse parameters (β_e, α_e) [2]. In the bunch center (Fig. 6.6(a)), the iso-density contours are nearly circular in agreement with a measured deformation parameter $m \approx 1$. At $\zeta = 0$ mm and $\zeta = -6$ mm (Fig. 6.6(b, c)) , an elliptical shape is found with $m \approx 4$. The major axis of the RMS ellipse of the distributions has an angle of $\psi \approx -25°$ with respect to the $u-$axis at $\zeta = 0$ mm, and of $\psi \approx -40°$ at $\zeta = -6$ mm. The RMS ellipse of the overall bunch distribution (Fig. 6.6(d)) has circular shape per construction.

---

[2] Since the measured distributions are given in the form of digital images and not as particle distributions, a transformation can not be directly performed. Here, a distribution was generated by randomly “filling” the area of each pixel with a number of particles proportional to the pixel-intensity. The distributions can then be transformed to normalized coordinates and digital images be generated from the resulting distributions. The results were checked by comparing the emittance.

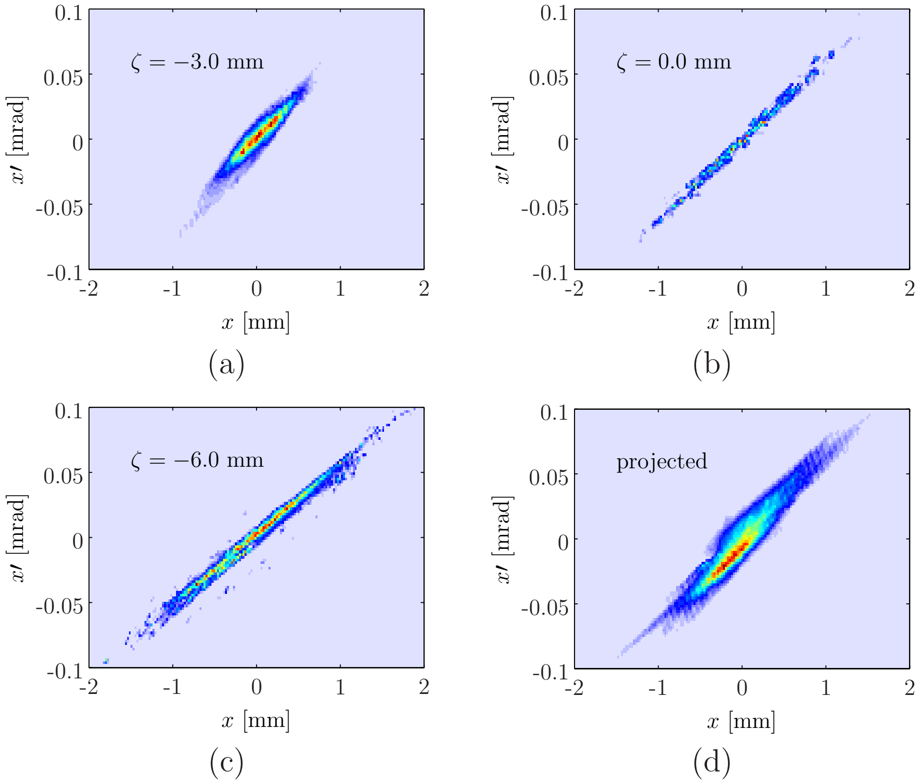

Figure 6.5: Reconstructed charge density distributions in horizontal phase space in the center (a), the leading edge (b), and the trailing edge of a bunch (c). The exact longitudinal positions are indicated in the images. Image (d) shows the corresponding distribution of an entire bunch.

6.5 Horizontal slice centroid offsets

As mentioned in section 6.3, slice centroid offsets were regularly observed in the form of a beam tilt on the screen. Owing to the shearing induced by the TDS, the mean horizontal particle position $\langle x(\zeta)\rangle$ of a tilted beam on the screen is both a function of the longitudinal coordinate ζ and the vertical coordinate y on the screen. The observed offsets may therefore originate from sources inducing a correlation $\langle x\zeta\rangle$, as well as from sources inducing a correlation $\langle xy\rangle$. Correspondingly, an offset $\Delta x(\zeta) = \langle x(\zeta)\rangle - \langle x(\zeta_0)\rangle$ at the longitudinal position ζ with respect to the reference point $\zeta_0 = 0$ can be decomposed into a ζ-correlated contribution $\Delta x^{\zeta}(\zeta)$ and a $y-$correlated contribution $\Delta x^{y}(\zeta)$:

$$\Delta x(\zeta) = \Delta x^{\zeta}(\zeta) + \Delta x^{y}(\zeta). \tag{6.4}$$

$\zeta-$ and $y-$correlated offsets can be distinguished by comparing measurements with opposite deflection in the TDS (180° difference in RF phase

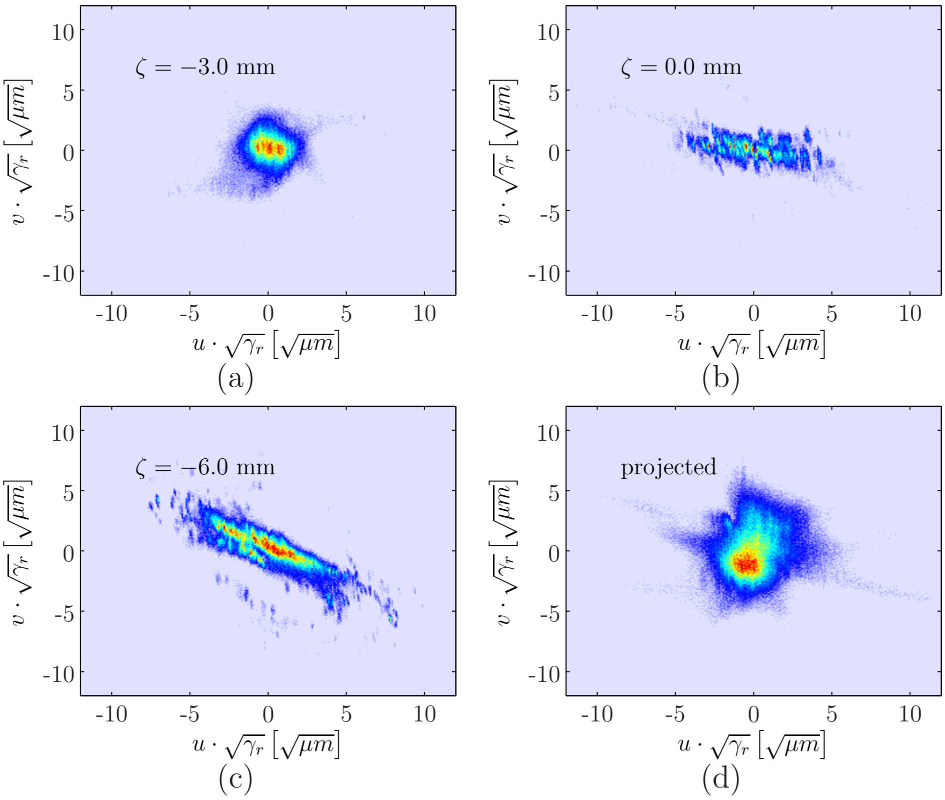

Figure 6.6: Representation of the horizontal phase space distributions shown in Fig. 6.5 in normalized coordinates (u, v). The coordinates are multiplied by $\sqrt{\gamma_r}$ so a circular RMS ellipse with radius r corresponds to a normalized emittance of $r^2[\mu m]$.

of the TDS). While the ζ-correlated contribution $\Delta x^\zeta(\zeta)$ does not change under such a "phase-flip", the y-correlated contribution $\Delta x^y(\zeta)$ does. Assuming a linear relation

$$\Delta x^y(\zeta) \propto S \cdot \zeta, \tag{6.5}$$

where S is the shear parameter induced by the TDS (vertical deflection Δy per length $\Delta\zeta$, compare section 4.2.5), a phase-flip leads to an inversion of the sign of $\Delta x^y(\zeta)$. Thus, by comparing offsets $\Delta x^{(+)}(\zeta)$ and $\Delta x^{(-)}(\zeta)$ obtained with opposite deflection in the TDS, the y- and the ζ-correlated contribution can be separated:

$$\begin{aligned} \Delta x^y(\zeta) &= \frac{1}{2}\left(\Delta x^{(+)}(\zeta) - \Delta x^{(-)}(\zeta)\right) \\ \Delta x^\zeta(\zeta) &= \frac{1}{2}\left(\Delta x^{(+)}(\zeta) + \Delta x^{-}(\zeta)\right). \end{aligned}$$

A typical result of such a comparison is shown in Fig.6.7(a). The y-

correlated part is linear in very good approximation, with an angle

$$\Theta_{xy} = \frac{\Delta x^y(\zeta)}{S \cdot (\zeta - \zeta_0)} \approx 20 \text{ mrad} \tag{6.6}$$

with respect to the y-axis. In case of the ζ-correlated part, a gradually increasing slope is observed towards the trailing end of the bunch.

y-correlated offsets are a consequence of an imprecise experimental setup. They may arise from a roll angle of the TDS, camera or quadrupole magnet downstream of the TDS about the longitudinal axis. Additional measurements (such as a scan of the vertical beam position on the OTR screen by means of a vertical steerer magnet downstream of the TDS) suggest that the largest contribution to the observed tilt comes from a roll angle of the camera of about 17 mrad $\approx 1°$. Negligible roll angles are expected for the quadrupole magnet (< 0.1 mrad [80]) and the TDS ($\ll 1°$). A roll angle of the camera leads to the linear relation (6.5) as assumed above.

The ζ-correlated part in Fig. 6.7(a) has a shape that is familiar from transverse wake field effects in RF structures (cf. appendix B). Furthermore, misalignments of components of the RF gun, time-dependent transverse fields in the RF modules (e.g. in front of the RF input couplers which induce field asymmetries) and the passage of an RF cavities with an angle $\langle x' \rangle$ may contribute. Coherent emission of synchrotron radiation within the bunch compressor chicanes, which is the dominating source for slice centroid offsets in case of compressed bunches, is not expected to play a role here.

In order to pinpoint sources of ζ-correlated offsets, measurements were performed at different focal strengths of selected quadrupole magnets. In case spatial slice centroid offsets are present at the position of a quadrupole magnet, the spatial offsets downstream of the magnet are a function of its focal strength. A measurement of the spatial offsets at different currents I_i of the quadrupole magnet allows then to determine the centroid curve $(\Delta x(\zeta), \Delta x'(\zeta))$ upstream of the quadrupole by means of a least squares method (for details see section 7.5). In contrast, offsets generated downstream of the quadrupole magnet do not depend on the focal strength of the quadrupole [3]. The observation of varying centroid offsets during such a scan which can be explained reasonably well by offsets at the position of

---

[3] In case the beam traverses the quadrupole magnet off-axis so the beam orbit depends on the focal strength of the magnet, centroid offsets may be affected indirectly.

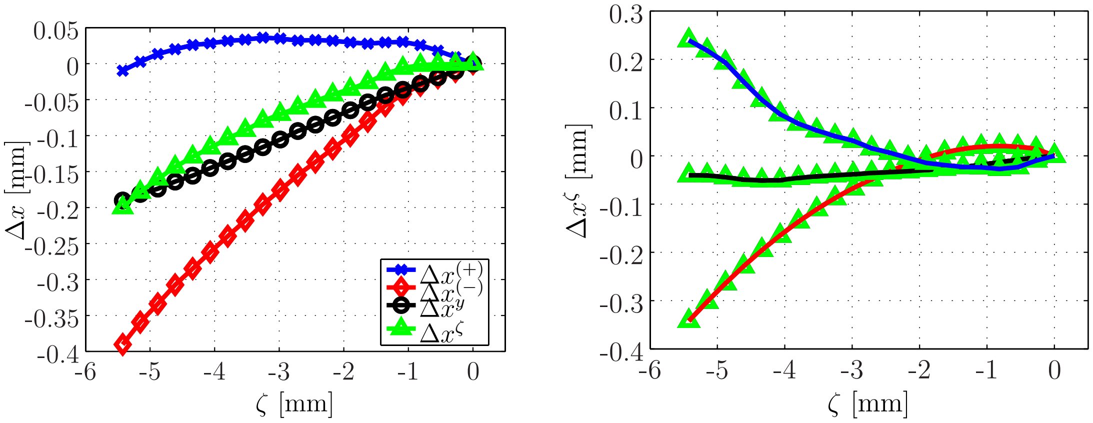

(a) (b)

Figure 6.7: (a) Typical slice centroid curves $\Delta x(\zeta)$ of uncompressed bunches measured on the screen and reconstructed contributions from $y-$ and ζ-correlated offsets. $\Delta x^{(+)}$ and $\Delta x^{(-)}$ were measured with opposite deflection in the TDS. Δx^{y} and Δx^{ζ} denote the reconstructed $y-$ and ζ-correlated offsets, see text for details. The bunch head is on the right hand side. (b) ζ-correlated offsets measured at different focal strengths of the quadrupole directly upstream of the TDS. The betatron phase advance between the quadrupole and the screen was changed by roughly 180° between the red and the blue curve.

the quadrupole are thus a strong indication for a source located upstream of the magnet.

Centroid curves $\langle x(\zeta)\rangle$ measured at different currents of the quadrupole magnet directly upstream of the TDS are presented in Fig. 6.7(b). They show a strong dependence on the focal strength of the quadrupole magnet, which can basically be explained by initial offsets at the position of the magnet. The observed centroid offsets are thus mainly generated upstream of the TDS, and therefore in particular not caused by the RF field of the TDS. However, in case the beam passes the TDS with large horizontal offsets of several millimeters, additional deflections may occur due to transverse wake fields within the TDS. Corresponding calculations are presented in appendix B. The alignment of the structure was checked by scanning its aperture with appropriate steering magnets and found to be accurate within ±1 mm.

Similar investigations using different quadrupole magnets located further upstream have not been conclusive. The offsets are assumed to be the result of various contributions along the linac as listed above. The observed shape of the centroid curves suggest that transverse wake fields play a dominant role.

Chapter 7

Results under FEL operating conditions

In this chapter, experimental results obtained under FEL operating conditions of FLASH are presented. In contrast to the results presented in the previous chapter, the bunches were accelerated off-crest and longitudinally compressed in the magnetic chicanes. The beam dynamics under these conditions is much more complicated, since the compression process is accompanied by collective effects such as the coherent emission of synchrotron radiation and space charge forces. The electrons which contribute to the SASE process, the lasing fraction of a bunch, is of particular importance. Although the lasing fraction comprises only about 15% of the total bunch charge, measurements with the transverse deflecting structure (TDS), in particular in combination with a tomographic reconstruction, allow to experimentally investigate important properties of this fraction such as transverse emittance, current profile and energy spread.

7.1 Measurement conditions

Measurements were performed at particle energies of 494 MeV, 677 MeV and 964 MeV. The energies correspond to fundamental wavelengths of the FEL radiation of 27.0 nm, 13.7 nm and 6.8 nm, respectively. Energy and fundamental wavelength were determined from a measurement of the radiation spectrum at 677 MeV and 964 MeV, whereas an energy spectrometer was used at 494 MeV (cf. section 4.1.7). The mean energy per FEL pulse was in the region of 0.5 μJ (964 MeV) to 10 μJ (494 MeV). Saturation was reached in none of the cases presented in this thesis.

Table 7.1: Measurement conditions. The conditions are labeled by the identifier specified in the first row.

Identifier	C1	C2	C3
Date	27.01.07	21.08.06	09.10.07
Energy [MeV]	494 ± 5	677 ± 1	964 ± 1
Bunch charge [nC]	0.72 ± 0.02	0.50 ± 0.02	0.67 ± 0.02
Fundamental wavelength [nm]	27.0 ± 1	13.7 ± 0.1	6.8 ± 0.1
Mean energy per FEL pulse [μJ]	10 ± 2	5 ± 1	0.5 ± 0.2
ACC1 phase [deg.]	-8.8 ± 1.0	-7.6 ± 1.0	-8.4 ± 1.0
ACC2,3 phase [deg.]	-11.0 ± 1.0	-22.0 ± 1.0	0.0 ± 1.0

The SASE process depends critically on the RF phases of the superconducting modules ACC1 and ACC2/3. The RF phases were tuned in order to initiate the SASE process and to obtain a high radiation pulse energy. The RF phases of module ACC1 were -8.8° (494 MeV), -7.6° (677 MeV) and -8.4° (964 MeV) with respect to the on-crest phase. For ACC2/3, RF phases of -11°, -22° and 0° were measured.

The accelerator was operated at a macropulse repetition rate of 5 Hz with one bunch per macropulse in each case. The bunch charges were 0.72 nC (494 MeV), 0.5 nC (677 MeV) and 0.67 nC (964 MeV). The parameters are summarized in Table 7.1.

7.2 Current profile

The current profiles of individual bunches were measured using the off-axis screen OTR-2 downstream of the TDS (cf. Fig. 4.8). The shear parameters induced by the TDS (the ratio of the vertical extension of a bunch section on the screen to its length, cf. section 4.2.5) were measured to be 25.1 ± 1.6 (494 MeV), 16.7 ± 1.0 (677 MeV) and 16.0 ± 1.0 (964 MeV). A longitudinal resolution of 9.0 μm, 8.1 μm, and 16.3 μm, respectively, was estimated using the beam size measured with the TDS switched off [1].

Average current profiles

The average current profiles that were measured are shown in Fig. 7.1(a). The profiles are characterized by a sharp spike at the head with a peak

---

[1] Throughout this chapter, resolutions are quoted in terms of RMS values.

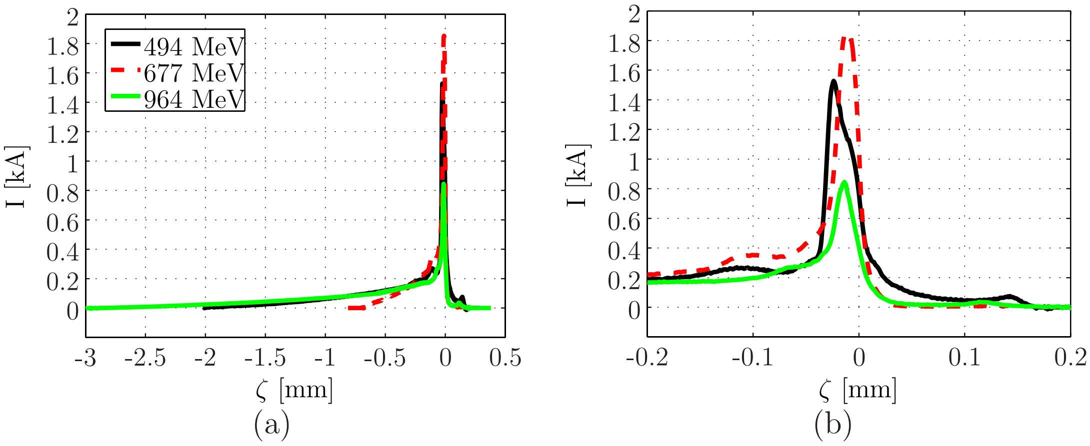

(a) (b)

Figure 7.1: (a): Average current profiles. The bunch head is on the right hand side. Each profile is an average determined from 30 (494 MeV) to 100 (677 MeV and 964 MeV) CCD-images. At 677 MeV and 964 MeV, the bunch head was measured with a higher resolution than the tail. Both parts were merged at the same internal position ζ. The internal bunch coordinate ζ is defined with respect to the half-maximum position of the leading edge of the current spike. (b): Zoom into the front region of Fig. (a).

current of up to 1.9 kA, and a long trailing tail. The current spike results from off-crest acceleration and longitudinal compression within the bunch compressors (cf. section 4.1.4). The length of the tail differs significantly between the results for different particle energies. The extension over which a detectable charge density was recorded is less than 1 mm at 677 MeV, and more than 3 mm in case of 964 MeV. The bunch length critically depends on the RF phases of the modules ACC1 and ACC2/3. While the RF phase of ACC1 is similar in all measurements, significant differences occur in case of the RF phase of ACC2/3 (cf. Table 7.1). Strong off-crest acceleration at -22° (677 MeV) results in short bunches, while on-crest acceleration (964 MeV) leads to significantly longer bunches.

A zoom into the front region of the profiles is presented in Fig. 7.1(b). The widths of the current spike amount to 33 μm (494 MeV), 23 μm (677 MeV) and 29 μm (964 MeV). The peak currents are 1.5 kA, 1.9 kA and 0.9 kA, respectively. Peak current and spike width are resolution-limited and thus to be interpreted as lower and upper bound, respectively. A charge in the range of 0.07 nC (964 MeV) to 0.13 nC (494 MeV and 677 MeV) is located within the region of the current spike (FWHM). A bunch fraction with low current extending over nearly 200 μm can be observed in front of the current spike in each profile. It is a typical indication for longitudinal space charge forces upstream of BC3 [94](cf. section 8).

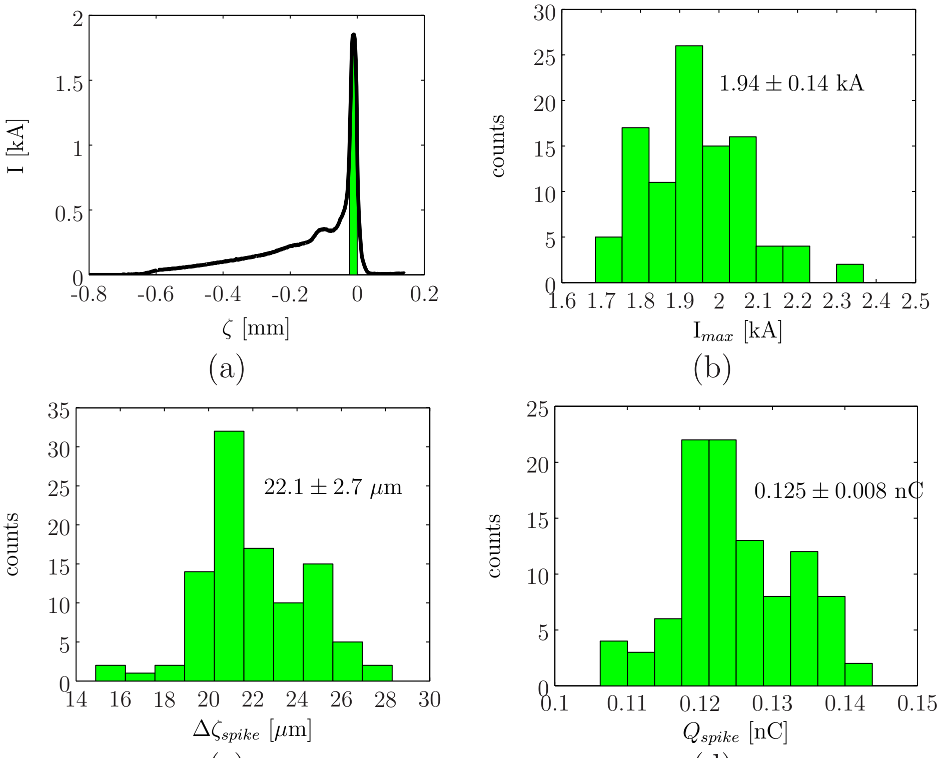

(a) (b) (c) (d)

Figure 7.2: (a): Average current profile at 677 MeV. The region of the current spike (FWHM) is indicated by the colored area. (b): Histogram of the peak current distribution of 100 subsequent bunches. (c) and (d): Corresponding histograms for the width of the current spike (FWHM) and the charge contained within the current spike.

Shot-to-shot fluctuations

The current profiles fluctuate from bunch to bunch. Figure 7.2(b),(c) and (d) show the distributions of peak current, width of the current spike, and charge of the current spike, respectively, of 100 subsequent bunches at 677 MeV. The peak current has a mean value of 1.94 kA and a standard deviation of ±0.14 kA (±7.2 %). The charge within the current spike (FWHM) is 0.13 ± 0.01 nC (±7.7 %), and the width of the current spike $22.1 \pm 2.7\mu$m (±12.3 %). Fluctuations in the range of 5 % to 15 % are also observed at 964 MeV and 494 MeV (Table 7.2). Variations of the bunch profile from shot to shot are largely due to fluctuations of the RF phase of the gun and module ACC1. The phase fluctuations typically amount to 0.06° (RMS) [95].

Table 7.2: Mean value and standard deviation of peak current, width of the current spike and charge of the current spike of 100 subsequent bunches. The mean values of peak current and spike width slightly deviate from those of the average profiles due to the averaging procedure.

Measurement	C1	C2	C3
Peak current [kA]	1.57 ± 0.14	1.94 ± 0.14	0.94 ± 0.04
Width (FWHM, [μm])	30.4 ± 1.5	22.1 ± 2.7	27.9 ± 3.6
Charge [nC]	0.13 ± 0.01	0.13 ± 0.01	0.07 ± 0.01
Charge fraction [%]	18.1 ± 1.4	25.3 ± 1.5	10.4 ± 1.5

7.3 Longitudinal phase space

The charge density distribution of bunches in longitudinal phase space was measured at 677 MeV using the screen OTR-3 (cf. Fig. 4.8) in the magnetic chicane prior to the undulator section (cf. Fig. 4.8). The first dipole magnet of the magnetic chicane disperses the beam horizontally as a function of energy. Bunches were additionally "streaked" vertically by means of the TDS. This configuration allows a single-shot measurement of the charge density distribution in longitudinal phase space.

The energy resolution σ_E of the measurement is approximately given by

$$\sigma_E \approx \frac{\sqrt{\epsilon_x \beta_x}}{D_x}, \tag{7.1}$$

where ϵ_x is the horizontal emittance (excluding dispersion), β_x the horizontal beta function, and D_x the horizontal dispersion generated by the dipole magnet at the location of the screen. A horizontal dispersion of $D_x = 233 \pm 5$ mm was measured by recording the horizontal beam position on the screen while varying the current of the dipole (cf. section 5.2). The bunch width $\sigma_x = \sqrt{\epsilon_x \beta_x}$ without dispersion cannot be directly measured. As will be shown below, the TDS allowed to measure a horizontal width of ≈ 116 μm in the bunch tail, where dispersive effects play a minor role. This width corresponds to an energy resolution of ≈ 0.05 % (340 keV).

The longitudinal resolution is determined by the vertical shear parameter induced by the TDS and the vertical bunch size as obtained when the TDS is switched off. A shear parameter of $S = 10$ and a vertical bunch size of 170 μm were measured. The resulting longitudinal resolution amounts

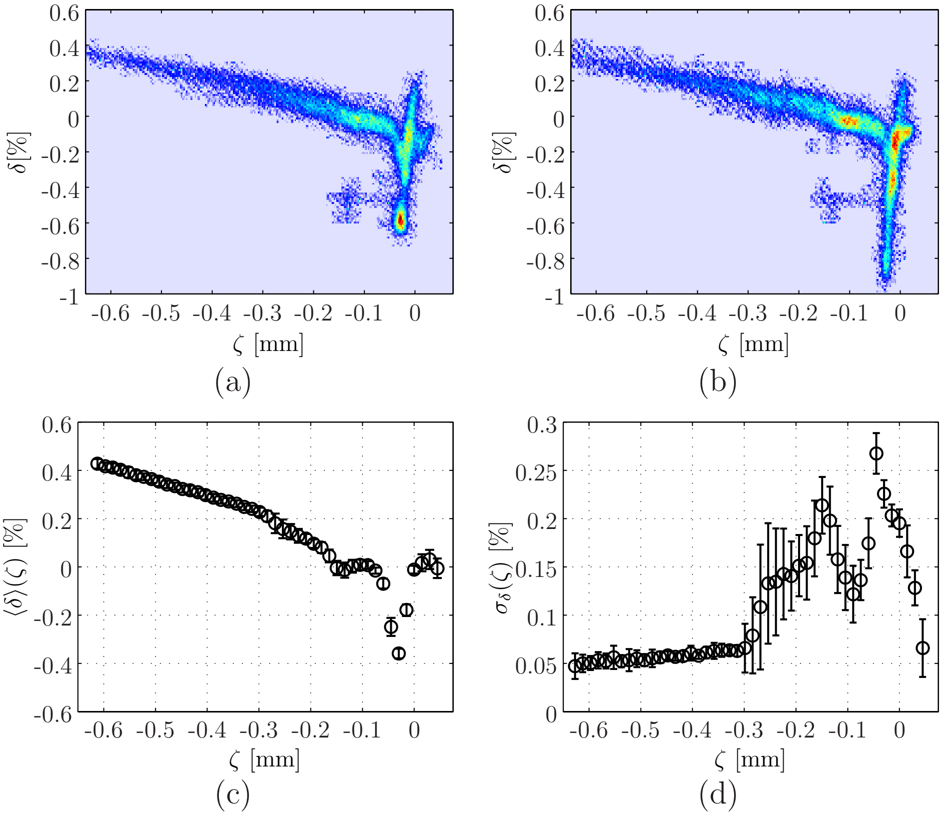

Figure 7.3: (a) and (b): Experimental results of single-shot measurements of the charge density distribution in longitudinal phase space. (c): Mean relative energy deviation $\langle\delta\rangle(\zeta)$ as a function of longitudinal position ζ. (d): Standard deviation $\sigma_\delta(\zeta)$ along a bunch. $\langle\delta\rangle(\zeta)$ and $\sigma_\delta(\zeta)$ were determined from 50 CCD-images. Error bars indicate statistical RMS errors.

to about 17 μm. A special optics downstream of the bunch compressors was used to optimize the resolution.

Experimental results at 677 MeV

The CCD-images presented in Figs. 7.3(a) and (b) show single-shot measurements of the energy-dispersed charge density distribution on the screen. The images are rotated so the vertical axis shows the energy deviation and the horizontal axis the longitudinal position. The internal bunch coordinate ζ is defined with respect to the leading edge of the current spike as in the previous section. The relative energy deviation

$$\delta = \frac{E - E_0}{E_0}, \tag{7.2}$$

with E_0 designating the mean bunch energy $E_0 = \langle E \rangle$, is introduced on the vertical axis. The plane spanned by (ζ, δ) will be called longitudinal phase space. Mean value $\langle \delta \rangle(\zeta)$ and standard deviation $\sigma_\delta(\zeta)$ as a function of ζ are shown in Figs. 7.3(c) and (d), respectively.

The bunch tail (left hand side) is characterized by a small energy spread and a longitudinal energy gradient. The gradient results from off-crest acceleration. The observed energy spread in the tail of $\sigma_E \approx 340$ keV or $\sigma_\delta \approx 0.05$ % (Fig. 7.3(d)) is expected to be resolution-limited. At the front of the bunch, longitudinal compression in the magnetic chicanes BC2 and BC3 causes bunch fractions with different energies to overlap at the same longitudinal position (full compression, cf. section 4.1.4). The energy profile is additionally broadened due to collective effects such as space charge forces and coherent emission of synchrotron radiation, which are particularly strong in the high current region. Particles at the initial front of the bunch, which gain the least energy in the accelerating modules, are now trailing behind the high current region due to over-compression. They are separated in energy from the remainder of the tail by ≈ 0.5 % (Fig. 7.3(a),(b)) and lead to an increase in energy spread in this bunch region.

The detailed structure of the high current region changes from shot to shot, as can be seen by comparing Figs. 7.3(a) and (b). The variations are assumed to be mainly due to RF phase fluctuations in the accelerating module ACC1. Corresponding fluctuations of the current profile have been discussed in the previous section. Despite these fluctuations, characteristic structures can be observed and attributed to physical processes within the bunches by comparison with typical results of particle tracking simulations [94].

At $\zeta \approx -0.03$ mm, a bunch fraction with an energy significantly below the mean energy is observed. This structure is particularly pronounced in Fig 7.3(b), where particles with an energy offset of almost 1 % below the mean energy are found. At the same position, the mean energy drops by ≈ -0.4 %, while the energy spread reaches its maximum of more than 0.25 %. Such an energy loss is a typical indication for coherent synchrotron radiation (CSR) in the bunch compressor chicanes and is seen in particle tracking simulations including CSR (cf. sections 4.1.4 and 8). Close to $\zeta = 0$, the mean energy increases. The phase space distribution exhibits a "branch" towards higher energies at this position. The maximum energy in this branch is roughly 0.2 % above the mean particle energy in both distributions presented. Increased particle energies at the front of the high current region are characteristic for longitudinal space charge forces (cf. section 4.1.4). Here, forces downstream of BC3 are presumably the main cause. In case of space charge forces occurring upstream of BC3, the large energy width of the corresponding bunch fraction involves a shearing in longitudinal phase space within BC3. Correspondingly, a small branch towards positive ζ is found at the very front of the distribution in Fig. 7.3(a), which is barely visible in Fig. 7.3(b). The extension of this bunch fraction is much smaller here than measured directly downstream of the TDS, where a length of nearly 200 μm was measured (compare previous section). The reason is supposedly a significantly higher noise level of the CCD-images obtained using the screen OTR-3 (cf. Fig. 4.8), so bunch sections with low charge density were not detected.

7.4 Horizontal slice emittance and slice ellipse parameters

Slice emittance and slice ellipse parameters were measured using quadrupole scan techniques in combination with the TDS. Measurements were performed at particle energies of 494 MeV, 677 MeV and 964 MeV. The off-axis screen OTR-2 (cf. Fig. 4.8) was used. Details on the measurement procedure and the data analysis can be found in chapter 5.

Since the SASE process depends very critically on the optics and the orbit in the undulator section, lasing is generally suppressed during a scan. Accordingly, no SASE signal was obtained after changing the optics. Bunch parameters such as the transverse emittance, which do not depend directly on the optics or the orbit, can safely be expected to be the same as during SASE operation. The optics variations were mostly[2] applied downstream of the bunch compressors, so an impact on processes within the bunch compressors can be excluded.

---

[2] At 677 MeV, two quadrupoles upstream of the second bunch compressor have been varied slightly in order to match the beam to the desired optics. The effect on the bunch parameters of interest is expected to be insignificant, too.

Table 7.3: Longitudinal resolution of the slice emittance measurements at 494 MeV (C1), 677 MeV (C2) and 964 MeV (C3). All parameters refer to the location of the screen (OTR-2, cf. Fig. 4.8). The specified errors are statistical RMS errors. The errors of the quoted beam sizes are below 5%. The calibration constant specifies the length corresponding to the vertical size of one pixel of the CCD camera.

	C1	C2	C3
Max. vertical RMS beam size [μm]	240	180	540
Min. vertical RMS beam size [μm]	225	130	260
Mean vertical RMS beam size [μm]	230	155	357
Shear parameter	29 ± 4	12.9 ± 0.8	16 ± 1
Long. Resolution estimate [μm]	8.0	12.2	22.1
Slice width [μm]	6.7	15.0	12.1
Calibration constant [μm/pixel]	0.9 ± 0.3	1.9 ± 0.1	1.5 ± 0.1

Resolution

In order to optimize the longitudinal resolution of the measurements, a small vertical beam size at the screen throughout the measurements is crucial. For this purpose, several optics with a small vertical beta function $\beta_y \leq 10$ m at the location of the screen were worked out on the basis of the design optics of the FLASH linac (cf. section 5.3.1). Applying these optics one after another by changing appropriate quadrupoles ("multi-quadrupole scan") allows a measurement of the horizontal slice emittance with a good longitudinal resolution. This technique was applied at 494 MeV and at 677 MeV. At 677 MeV, the beam was matched to the design optics downstream of the second bunch compressor prior to the measurement (cf. section 5.3.1). At 964 MeV, the focal strength of a single quadrupole was scanned instead. The optics was adapted empirically in order to optimize the resolution.

The vertical bunch width was measured with the TDS switched off during each quadrupole scan. The minimal, maximal and mean vertical widths during the scans are quoted in Table 7.3. While in case of the multi-quadrupole scans (494 MeV (C1) and 677 MeV (C2)) the vertical beam size varies by less than 20 % around the mean value, strong changes of more than 50 % are observed in case of the single-quadrupole scan (964 MeV (C3)). The resulting variation in longitudinal resolution is the main drawback of the latter technique.

The shear parameter was measured to be $S = 29$ (494 MeV), $S = 12.9$

(677 MeV) and $S = 16$ (964 MeV). An estimate of the longitudinal RMS resolution is obtained by dividing the mean vertical bunch width by the shear parameter, resulting in 8.0 μm (494 MeV), 12.2 μm (677 MeV), and 22.1 μm (964 MeV). Note that the resolution varies along a bunch and may significantly deviate from this estimate (cf. section 7.2). The slice width used for calculating bunch properties as a function of the longitudinal position was therefore determined empirically as described at the end of this section. The parameters are summarized in Table 7.3.

Measurement at 494 MeV

At 494 MeV, a large shear parameter of $S = 29$ was used in order to obtain a good longitudinal resolution. As a consequence, the total vertical extension of a bunch exceeded the size of the camera window so only a limited bunch section was observed on the screen. The experimental results are presented in Fig. 7.4. The average current profiles measured during the quadrupole scan (top) exhibit a peak current of about 1.6 kA and the spike width of 32 μm in agreement with the results presented in section 7.2. The two profiles presented in the figure were measured at different currents of the quadrupoles which were varied during the scan. Small differences between the profiles can be observed at the trailing edge of the current spike. They are due to a slightly different longitudinal resolution, which is caused by different vertical bunch widths. The presented profiles exhibit the largest (red, dashed) and the smallest (black, solid) spike width that was measured during the quadrupole scan. The good agreement between the two profiles demonstrates that the longitudinal resolution hardly changes.

A CCD-image recorded during the quadrupole scan reveals the density distribution of a single bunch in the (x, z)-plane. Although this distribution changes significantly during a quadrupole scan, some intrinsic bunch properties already become obvious. The maximum intensity coincides with the spike in the current profile (note that the ζ-axis is the same in each layer of Fig. 7.4). Compared to the tail, the horizontal width is strongly increased throughout the current spike, in particular at the position of the trailing edge. The distribution is horizontally asymmetric at this position. The entire high-intensity region is shifted horizontally with respect to the remainder of the bunch. As in the current profile, a significant intensity

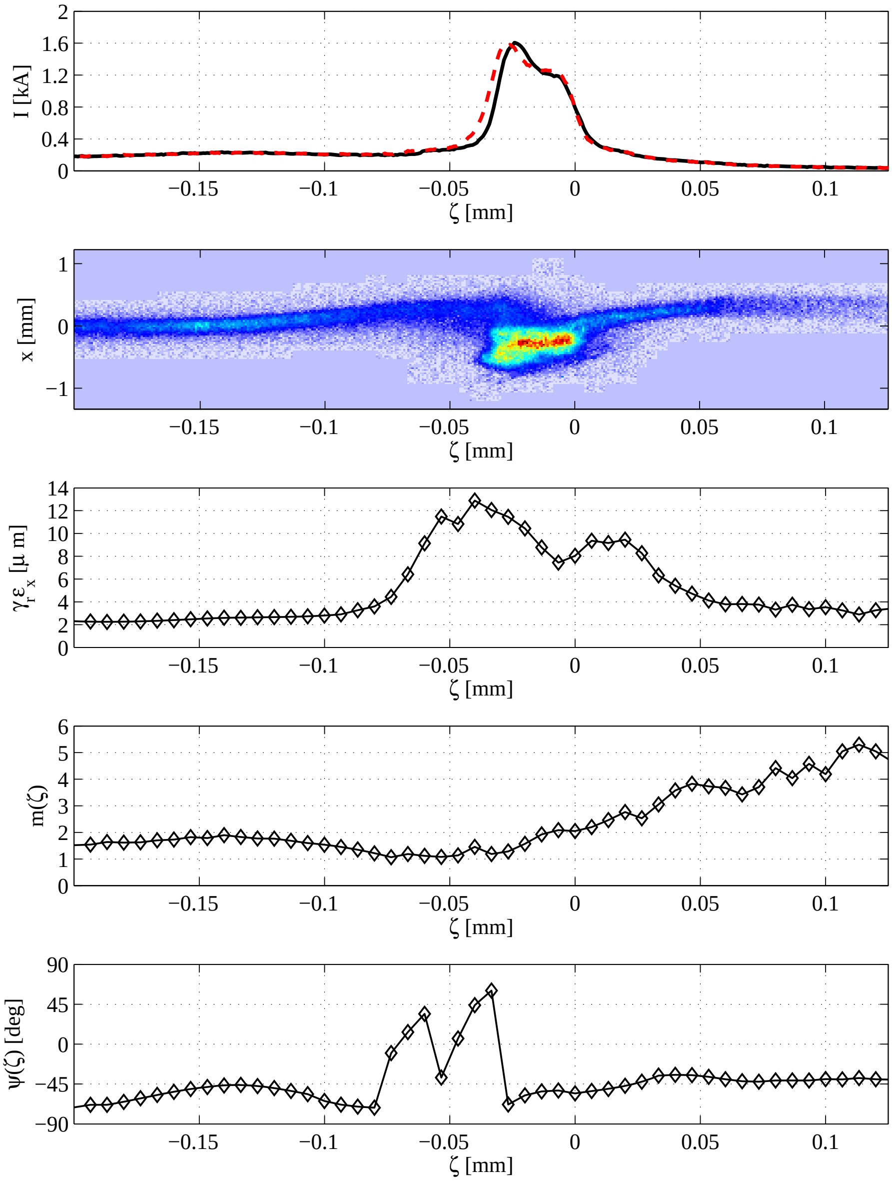

Figure 7.4: Experimental results at 494 MeV (C1 in Table 7.1): Average current profiles, typical CCD-image (for color code see appendix A), slice emittance, deformation parameter and deformation phase (from top to bottom). The head of the bunch is on the right hand side. The top layer shows the average current profile of 20 bunches measured with best (black, solid) and worst (red, dashed) longitudinal resolution during the quadrupole scan. Statistical errors of slice emittance and deformation parameters are not shown for reasons of clarity. They are typically below 5 *%.*

can be observed in front of the current spike.

The slice emittance[3] (Fig. 7.4) is strongly increased in the region around the current spike. The maximum value is nearly 13 μm and occurs close

---

[3] Throughout this chapter, the term "emittance" refers to a normalized RMS emittance.

to the trailing edge of the current spike, where a large slice width and a horizontal asymmetry can be observed in the CCD-image. Within the spike, the normalized slice emittance is in the range of 7.5 μm to 12 μm, with a local minimum of 7.5 μm close to the leading edge. The region with an increased slice emittance is significantly broader than the current spike. Within the tail, the emittance drops to values of ≈ 2 μm. The bunch fraction in front of the spike has a slice emittance of 3 μm to 4 μm. The mean slice emittance (weighted by the current) of an entire bunch, which was measured at a smaller shear parameter of the TDS, amounts to ≈ 6 μm. An overall bunch emittance of 13 μm was determined by a measurement with the TDS switched off. The difference between mean slice emittance and overall bunch emittance is largely due to offsets of the mean particle coordinates $\langle x \rangle$ and $\langle x' \rangle$ of bunch slices. Such offsets are discussed in detail in section 7.5.

The deformation parameter (cf. sections 2.3, 6.3) is smaller than $m \lesssim 2$ up to $\zeta = 0$ and then continuously increases to about $m = 5$ at the very front of the bunch. The deformation phase changes smoothly except for the region around the trailing edge of the spike, where it rapidly varies. The deformation parameter is close to $m = 1$ within this region, meaning that this section of the bunch has about the same ellipse parameters as the entire bunch. Recall that a deformation phase is not defined for $m = 1$ and that for $m \gtrsim 1$ variations of the deformation phase correspond to small variations of the underlying slice ellipse parameters (cf. section 2.3).

Measurement at 677 MeV

The results obtained at an energy of 677 MeV are presented in Fig. 7.5. The shear parameter induced by the TDS was adapted to enable the observation of entire bunches on the OTR screen. The peak current of the average current profiles measured is ≈ 1.4 kA and the spike width ≈ 37 μm (FWHM). These values deviate from those quoted in section 7.2 (1.85 kA and 23 μm) due to an inferior longitudinal resolution. As in case of an energy of 494 MeV, the measured profiles hardly change during the quadrupole scan.

The density distribution in the (x, z)-plane shows again an increased horizontal slice width throughout the region of the current spike. At the position of the trailing edge of the current spike, two “branches” with a

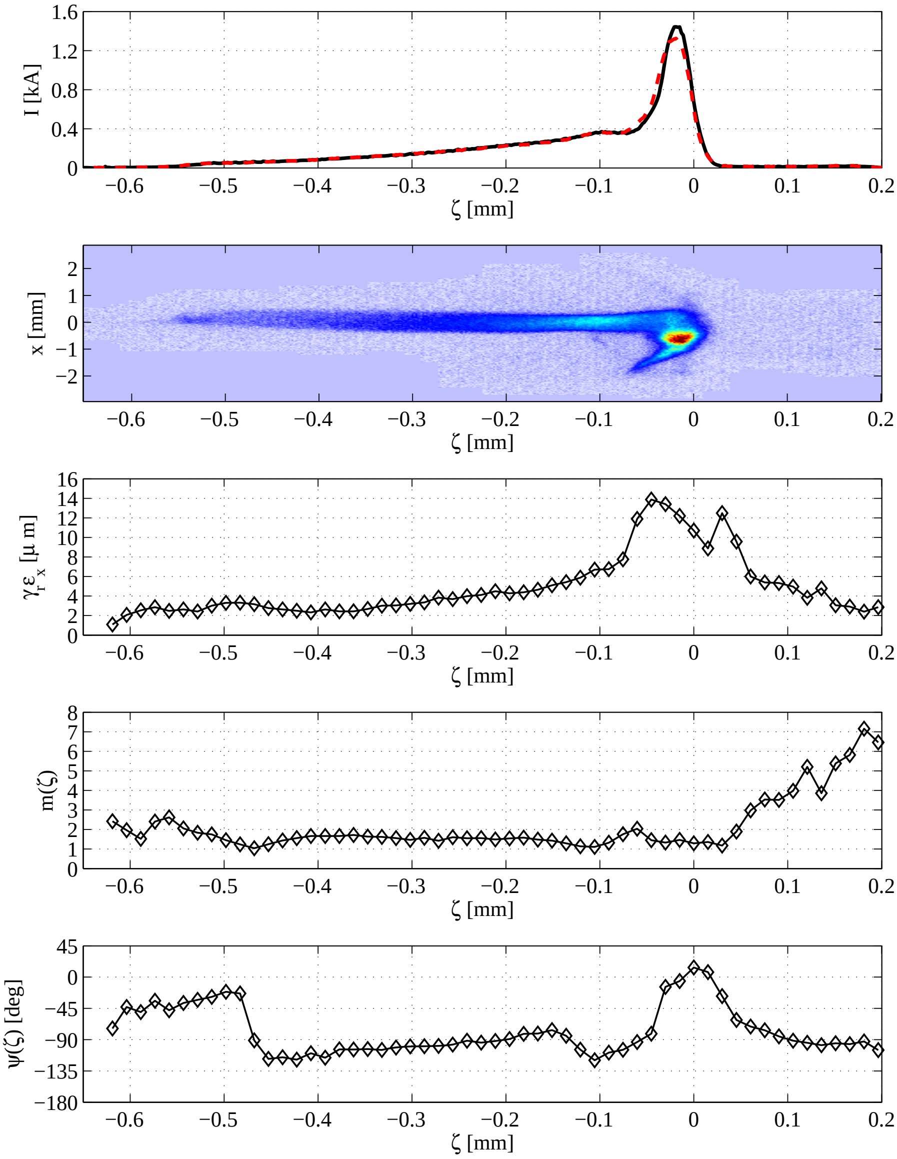

Figure 7.5: Experimental results at 677 MeV (C2). See Fig. 7.4 and text for details.

horizontal offset of about 1.5 mm are observed at the same longitudinal position. Such a strong transverse separation can only occur due to coherent synchrotron radiation (CSR) within the bending magnets of the compressor chicanes. An energy loss of particles due to CSR within a horizontal chicane leads to horizontal angle and position offsets at the end of the chicane. A comparison with the longitudinal phase space distribution measured under the same conditions (Fig. 7.3) indeed shows that the energy width is maximal at about the same longitudinal position. This suggests that the branch at $\zeta \approx -0.05$ mm, $x \approx -1.5$ mm in Fig. 7.5

corresponds to the low-energy branch in longitudinal phase space, which is supposedly caused by CSR in the second bunch compressor. The maximum energy difference of bunch fractions measured at $\zeta \approx -0.05$ mm is $\approx 0.9\%$. The ratio 1.5 mm/0.9% $\approx$ 167 mm is only slightly smaller than the maximum horizontal dispersion of $D_x \approx 192$ mm [53] between the fourth and fifth bending magnet in BC3. Dispersion due to beam steering and the horizontal kicker is expected to be in the order of ±10 mm and thus plays a minor role.

The slice emittance assumes its maximum value of 14 μm in the region where the separated branches occur. Within the region of the current spike, the slice emittance is in the range of 10 μm to 14 μm. A local minimum of 8.5 μm can be observed right in front of the current spike, before it rises again to more than 12 μm. In the tail of the bunch, the slice emittance drops to values between 2 μm and 4 μm. The mean slice emittance amounts to ≈ 8 μm. As at $E = 494$ MeV, an overall bunch emittance of 13 μm was determined in a separate measurement.

The deformation parameter is smaller than $m = 3$ except for the part in front of the current spike, where it increases up to $m \approx 7$. The deformation phase rapidly changes at the position of the edges of the current spike. The jump in deformation phase at the end of the bunch at about $\zeta = -0.45$ mm is accompanied by a deformation parameter close to one. The corresponding change of the underlying ellipse parameters is therefore small.

Measurement at 964 MeV

The results obtained at a particle energy of 964 MeV are presented in Fig. 7.6. As in case of $E = 494$ MeV, the shear parameter was maximized so only the front region of each bunch was observed on the screen. The average current profiles measured during the quadrupole scan show a peak current in the range of 0.5 kA (red, dashed) to 0.85 kA (black, solid), and a spike width in the range of 70 μm (black, solid) down to 29 μm. The deviations between the results obtained at different quadrupole currents are significantly stronger than observed at 494 MeV and 677 MeV. The reason for this is a stronger variation of the vertical beam size during the single-quadrupole scan used in this case. The consequence is an inferior longitudinal resolution of slice emittance and slice ellipse parameters.

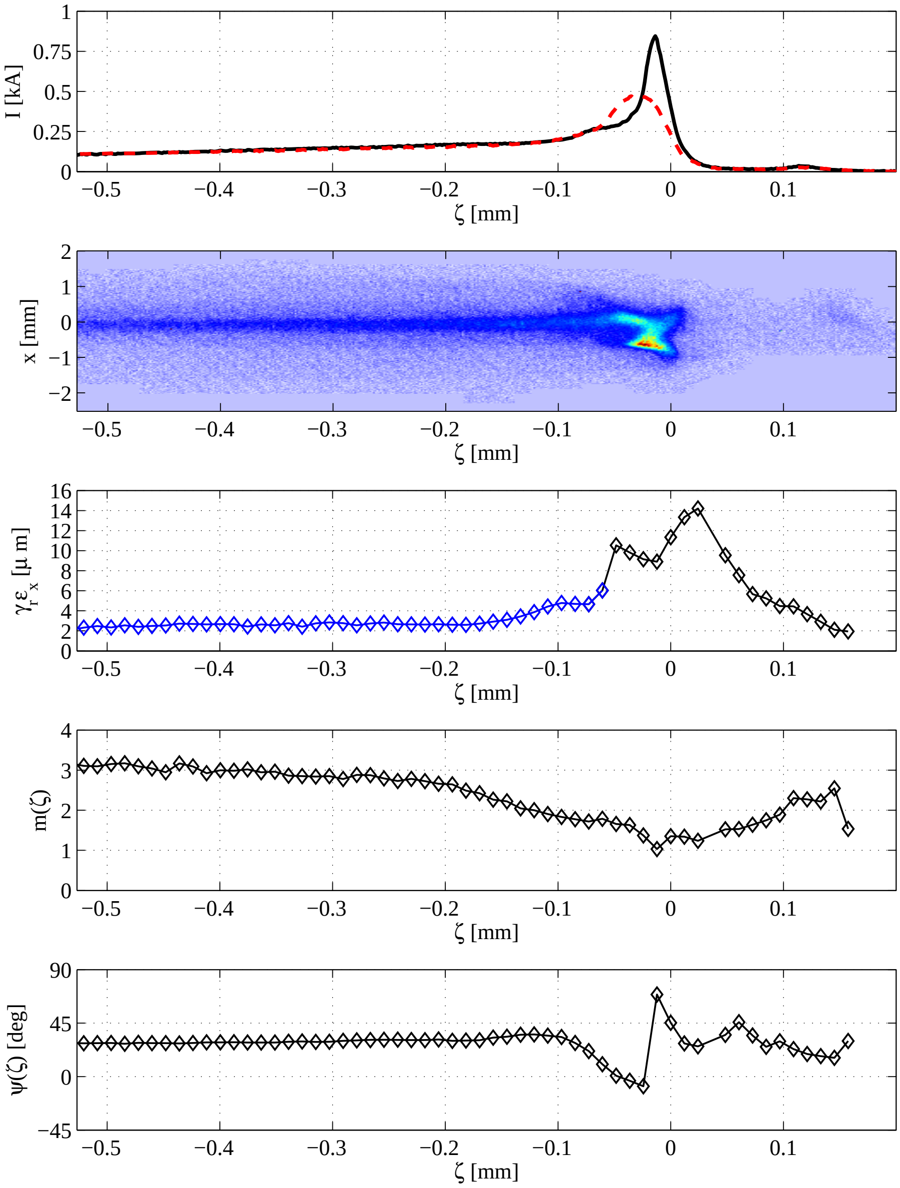

Figure 7.6: Experimental results obtained at a particle energy of 964 *MeV (C3 in Table 7.1). The slice emittance values in the tail (blue) were determined using standard deviations of Gaussian fits to the measured horizontal slice profiles. Within the bunch head (black), the standard deviations of the profiles were used.*

A strong beam halo of unknown cause can be observed in the region of the bunch tail in the presented CCD-image. The beam halo significantly contributes to the slice width. The high-current region is characterized by bunch fractions with a significant horizontal offset. Correspondingly, an increase in slice emittance is found in this region. In contrast to the results at $E = 494$ MeV and $E = 677$ MeV, the maximum in slice emittance of about 14 μm occurs at the position of the leading edge of the current spike. Within the high current region, the slice emittance lies in the range between 8 μm and 12 μm. In the tail, the slice emittance drops to $\approx 2\ \mu m$. Here, standard deviations of Gaussian fits to the horizontal slice profiles were used in order to suppress the beam halo [4]. The overall bunch emittance was measured to be 10 μm.

A slice deformation parameter of $m \approx 3$ was measured in the bunch tail. This value is significantly larger than observed at 494 MeV and 677 MeV and most likely caused by the beam halo. Within the region of the current spike, the deformation parameter is smaller than $m = 2$ and then increases up to $m = 2.5$ in front of the spike. The jump in mismatch phase close to $\zeta = 0$ occurs at a position with $m \approx 1$ and is thus not accompanied by a strong variation of the underlying ellipse parameters.

Reproducibility

The reproducibility of slice emittance profiles was checked by performing seven slice emittance measurements at 964 MeV within about one hour. The result is presented in Fig 7.7. The figure shows the mean slice emittance $\langle\gamma_r\epsilon_x\rangle(\zeta)$ obtained from the measurements. Error bars indicate the minimum and the maximum values. The results are in very good agreement. The average standard deviation $\sigma_{\gamma_r\epsilon_x}(\zeta)$ (not weighted by the current) within the bunch section presented in the figure amounts to 4.5 %. The statistical errors of the individual slice emittance measurements due to measurement errors of the horizontal widths are typically less than 5%, which is in agreement with the observed standard deviation $\sigma_{\gamma_r\epsilon_x}(\zeta)$. The accuracy of the results is mainly determined by systematical errors and resolution-limitations, which are discussed in detail in chapter 5.

Choice of the slice width

The influence of the selected slice width $\Delta\zeta_{slice}$ on the reconstructed slice emittance is demonstrated in Fig. 7.8. The figure shows the slice emittance obtained at 494 MeV using slice widths of $\Delta\zeta_{slice} = 10\ \mu$m, $\Delta\zeta_{slice} = 3.4\ \mu$m

---

[4] Gaussian fits are less sensitive to long tails in the horizontal profiles and suited as long as the profiles are Gaussian shaped in the center in good approximation, which is the case in the bunch tail.

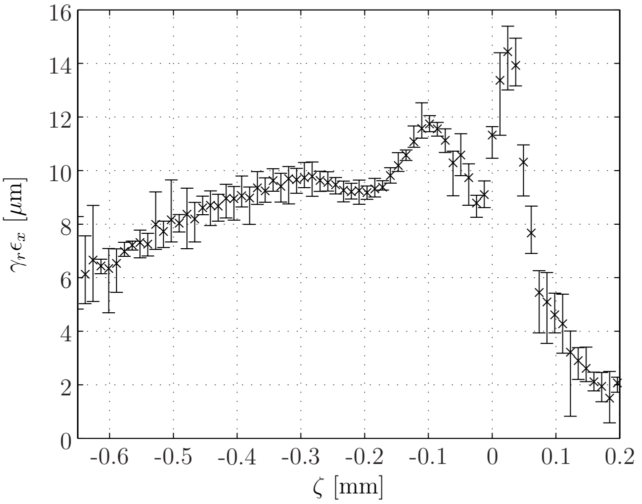

Figure 7.7: Reproducibility of slice emittance results. The plot shows the mean slice emittance values of seven measurements performed in about one hour at 964 MeV. Error bars indicate the maximum and the minimum slice emittance measured. All values are calculated from the standard deviations of the slice profiles. The large slice emittance in the tail of up to 10 μm is caused by the beam halo, which is not suppressed here by Gaussian fits.

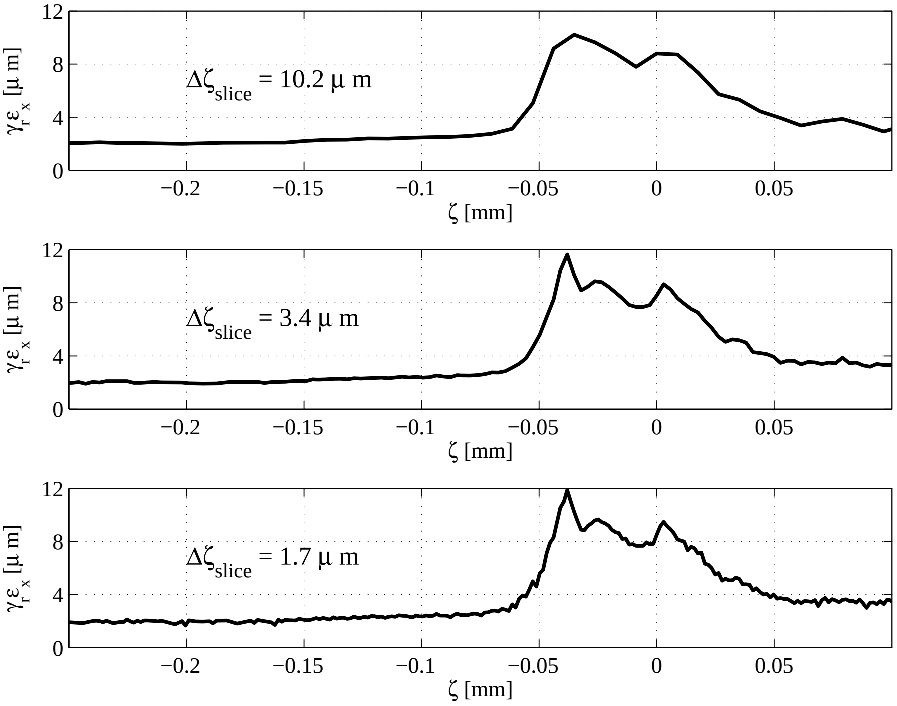

Figure 7.8: Dependence of slice emittance results on the choice of the slice width. The vertical slice widths are 300 μm (top), 100 μm (middle) and 50 μm (bottom) which corresponds to longitudinal slice widths of 10 μm, 3.4 μm and 1.7 μm, respectively. The particle energy is 494 MeV (conditions C1, see Table 7.1).

and $\Delta\zeta_{slice} = 1.7$ μm. A significant difference can be observed between the slice emittance profiles obtained with $\Delta\zeta_{slice} = 10$ μm and $\Delta\zeta_{slice} = 3.4$ μm, indicating that the longitudinal resolution is better than 10 μm. In contrast, the results for $\Delta\zeta_{slice} = 3.4$ μm and $\Delta\zeta_{slice} = 1.7$ μm agree well. This behavior is in agreement with the resolution estimate of 8.0 μm deduced from the overall vertical bunch width. At $\Delta\zeta_{slice} = 1.7$ μm, the slice emittance starts to oscillate slightly from slice to slice indicating numerical noise. For data evaluation, the slice width was adjusted to resolve all details while at the same time keeping numerical noise as small as possible (here: $\Delta\zeta_{slice} = 3.4$ μm).

7.5 Horizontal slice centroid offsets

As mentioned in the previous section, the overall bunch emittance measured under FEL operating conditions is typically larger than 10 μm. At the same time, the mean slice emittance (weighted by the current) is in

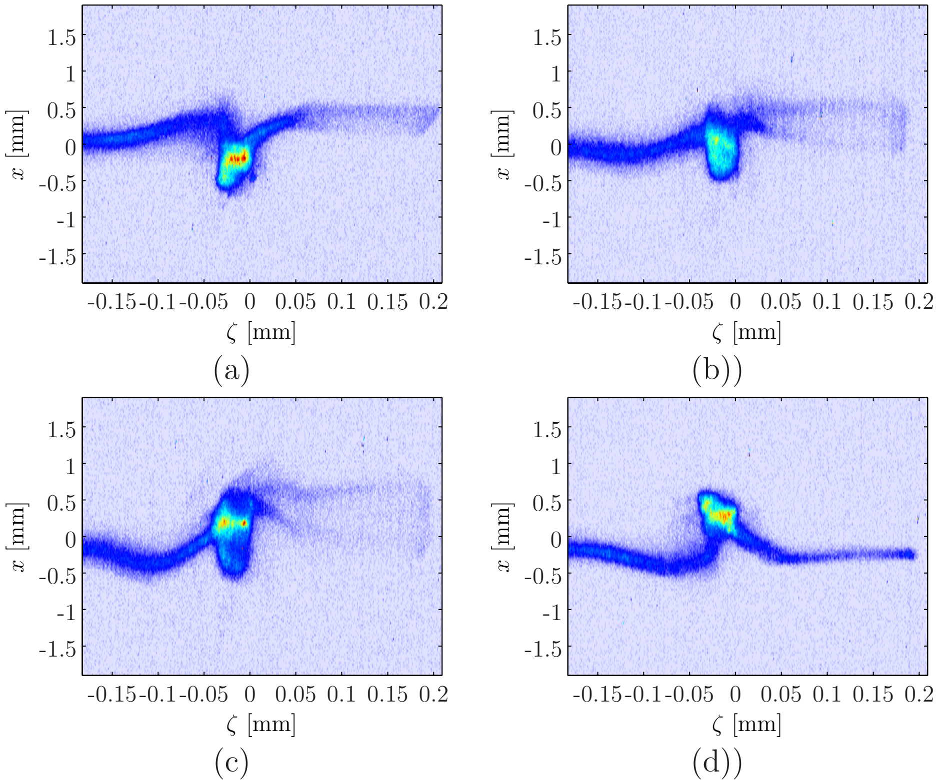

(a) (b)) (c) (d))

Figure 7.9: CCD-images showing the density distribution in the front region of single bunches in the (x, z)-plane at 494 MeV. The images were recorded with different strengths of the upstream quadrupoles.

the range of 6 μm to 8 μm. The apparent deviations are to a large extent caused by variations of the mean particle coordinates $\langle x\rangle$, $\langle x'\rangle$ in dependence on the longitudinal position ζ within a bunch. The offsets $\Delta x(\zeta)$, $\Delta x'(\zeta)$ of bunch slices with respect to the overall mean particle position will be called slice centroid offsets. Slice centroid offsets may be caused e.g. by dispersion, transverse wake fields and coherent synchrotron radiation (CSR) within the magnetic bunch compressor chicanes. While wake fields mainly affect the tail of a bunch, dispersion and CSR are the dominant sources for centroid offsets in the high current region of a compressed bunch (see also section 6.5).

Spatial offsets $\langle x\rangle$ can be investigated by measuring the charge density distribution in the (x,ζ)-plane with the TDS. They change as a bunch moves along a transfer line. As an example, Fig 7.9 shows typical distributions (CCD-images) in the (x,ζ)-plane measured at 494 MeV. Each CCD-image was recorded with different focal strengths of the upstream quadrupole magnets. Strong slice centroid offsets are found in each image. The distance between the centroid positions of two individual slices changes from image to image, revealing the dependence on the optics.

The dependence on the optics can be easily understood in the linear optics approximation (see section 2.1). Given the centroid coordinates $(x_1(s_0), x_1'(s_0))$ and $(x_2(s_0), x_2'(s_0))$ of two slices at the position s_0 of a beamline and a horizontal transfer matrix $M(s,s_0)$ from s_0 to s, the linearity of the transformation yields

$$\begin{bmatrix} \Delta x(s) \\ \Delta x'(s) \end{bmatrix} = M(s,s_0)\cdot\begin{bmatrix} \Delta x(s_0) \\ \Delta x'(s_0) \end{bmatrix}, \tag{7.3}$$

where

$$\Delta x(s) = x_2(s) - x_1(s) \tag{7.4}$$

$$\Delta x'(s) = x_2'(s) - x_1'(s). \tag{7.5}$$

The difference of the horizontal centroid position of two slices thus transforms along the linac like a particle trajectory. In contrast to the absolute horizontal offsets with respect to the design orbit (beam orbit offsets), slice centroid offsets do not depend on the dipole fields of steering magnets, provided the mean particle energy in each slice is about the same. Beam orbit offsets may be in the order of several millimeters and are typically clearly larger than slice centroid offsets.

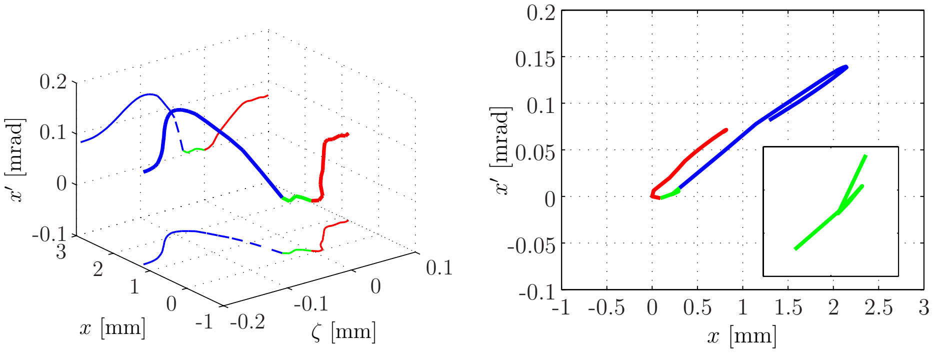

(a) (b)

Figure 7.10: (a) Reconstructed slice centroid offsets in trace space along the front part of a bunch at 494 MeV. The solid line shows the three-dimensional centroid curve in (x, x', ζ)-space. The thin lines show the projections of the curve onto the (x, ζ)-plane and (x', ζ)-plane, respectively. The spatial centroid offsets were determined with respect to the position of a "reference slice" close to $\zeta = 0$ instead of the mean bunch position, since only a limited section of a bunch could be observed on the screen. Different colors are used for the longitudinal sections defined by $\zeta > 0$ (red), -0.035 mm $\leq \zeta \leq 0$ (green), and $\zeta < -0.035$ mm (blue). The middle section (green) corresponds to the longitudinal section of the current spike (FWHM). (b) Projection of the centroid curve in (a) onto the horizontal trace space plane (x, x'). Different colors indicate the longitudinal position according to (a). The plot in the lower right corner shows a zoom into the section of the current spike. Note that the x-axis in (a) is reversed for reasons of clarity.

The described transformation of slice centroid offsets can be utilized to reconstruct the underlying position and angle offsets in trace space (x, x') by using quadrupole scan techniques. The measurement of spatial centroid offsets during a quadrupole scan allows to determine initial offsets $(\Delta x_i, \Delta x'_i)$ for each slice i at the reconstruction point of the scan (the starting point of the transfer matrices) in such a way that the measured spatial centroid offsets are reproduced best in a least-square sense (cf. section 3.1.2).

Figure 7.10(a) and (b) show the result of such a reconstruction at a particle energy of 494 MeV. The centroid offsets strongly vary within the region around the current spike. Two extremal values can be observed, one occurring at $\zeta \approx 0$ and one at $\zeta \approx -0.1$ mm. The spatial offset between these two regions is more than 2 mm. The centroid offsets within the current spike are comparably small, with spatial offsets of $\lesssim 200$ μm. A zoom into the region of the current spike (small plot in Fig. 7.10(b)) reveals a bifurcation in horizontal trace space.

The centroid offset curves presented in Fig 7.10 strongly depend on the optics. In order to minimize this dependence and to reveal the underlying bunch properties, the centroid coordinates can be transformed to normalized coordinates (u, v)

$$u = \frac{x}{\sqrt{\beta_e}} \tag{7.6}$$

$$v = \frac{\alpha_e}{\sqrt{\beta_e}} \cdot x + \sqrt{\beta_e} \cdot x' \tag{7.7}$$

using the measured beam ellipse parameters β_e and α_e of an entire bunch. Defined in this way, relative centroid offsets describe a circle in (u, v)-space as the bunch moves along the beamline, provided that the transverse dynamics is purely linear (cf. section 2.3). The relative centroid coordinates (u, v) of a slice can thus be expressed in phase-amplitude form by

$$u = \sqrt{a_C} \cdot cos(\phi) \tag{7.8}$$

$$v = -\sqrt{a_C} \cdot sin(\phi), \tag{7.9}$$

where

$$a_C = u^2 + v^2. \tag{7.10}$$

$\sqrt{a_C}$ is the radius of the circle in (u, v)-space defining the possible values of (u, v). It corresponds to the Courant-Snyder invariant in single-particle dynamics and remains constant under linear beam transfer.

Combining Eq. (7.6) and Eq. (7.8) yields the spatial separation

$$\Delta x \leq \sqrt{a_C \cdot \beta_e}. \tag{7.11}$$

It is instructive to compare the offset Δx to the bunch width $\sigma_x = \sqrt{\epsilon_x \beta_e}$ by forming the ratio

$$\frac{\Delta x}{\sigma_x} \leq \sqrt{\frac{a_c}{\epsilon_x}} = \sqrt{\frac{\gamma_r a_c}{\gamma_r \epsilon_x}}. \tag{7.12}$$

The product $\gamma_r a_c$ will be called offset amplitude.

The offset amplitudes measured at 494 MeV, 677 MeV and 964 MeV are presented in Fig. 7.11. An oscillation within the high current region with a steep slope around $\zeta = -0.05$ mm is found in each case. The zeros at $\zeta \approx 0$ show the position of the reference slices. At 494 MeV and 677 MeV, a maximum of $\gamma_r a_C \approx 55$ μm and $\gamma_r a_C \approx 35$ μm, respectively,

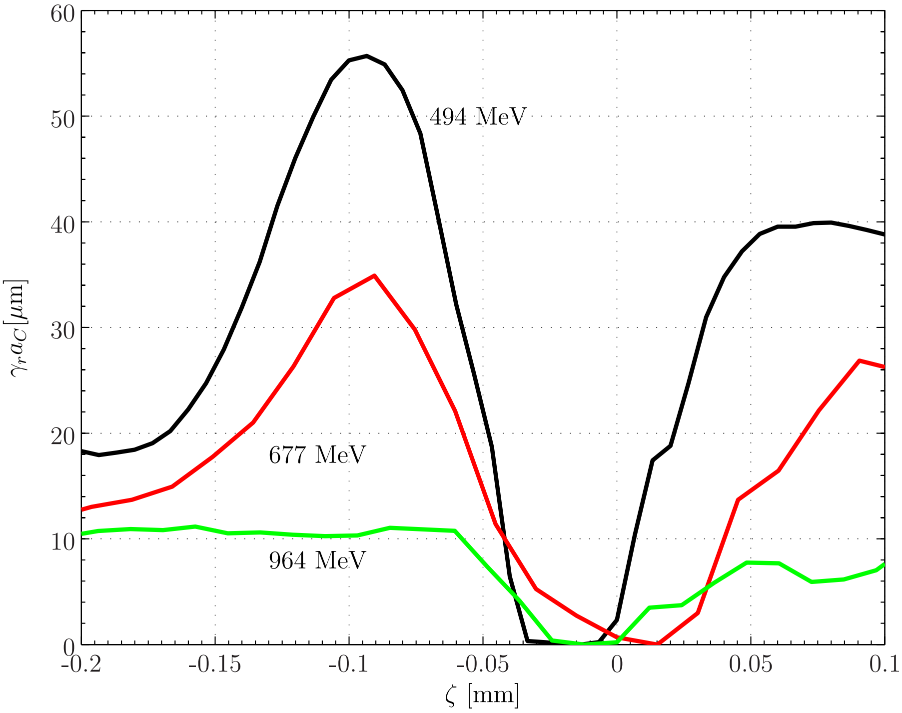

Figure 7.11: Offset amplitude $\gamma_r a_C$ at 494 MeV, 677 MeV and 964 MeV.

occurs at $\zeta \approx -0.1$ mm. A comparison to the overall bunch emittance of 13 μm according to Eq. (7.12) yields large maximum spatial offsets of $\approx 2\sigma_x$ (494 MeV) and $\approx 1.6\sigma_x$ (677 MeV). The offset amplitude is smallest in case of the measurement at 964 MeV. Here, limiting factors such as the beam halo and the inferior longitudinal resolution (cf. Table 7.3) supposedly play a role.

7.6 Horizontal phase space

In the previous sections, the first and second moments of spatial density profiles were used to determine properties of the density distribution in phase space. As elaborated in sections 8.9 and 4.2.5, a detailed tomographic reconstruction of the horizontal phase space distributions of individual slices is possible by utilizing the full information contained in the spatial profiles. Tomographic reconstructions greatly contribute to an understanding of the slice emittance results presented in section 7.4. Moreover, it will turn out that they are indispensable for an estimation of the emittance of the lasing fractions of bunches at FLASH.

Results at 494 MeV

The accuracy of a tomographic reconstruction can be checked by comparing the emittance resulting from the tomographic reconstruction to the result of a corresponding slice emittance measurement using a least squares method. Figure 7.12(a) shows a comparison of the slice emittance determined via tomography and least squares method at a particle energy of 494 MeV (C1 in Table 7.1). The results agree well within the bunch tail and the region of the current spike (from $\zeta \approx -0.035$ mm to $\zeta = 0$). Significant deviations occur mainly around $\zeta = -0.05$ mm, close to the trailing edge of the current spike. The reason for these deviations are reconstruction artefacts in trace space with a large distance to the centroid of the distribution. They may result from noise in the long tails of the spatial profiles which contribute significantly to the emittance in case the signal-to-noise ratio is too small[5]. The deviations therefore occur in the region around $\zeta = -0.05$ mm where the horizontal profiles are broad while the current is small. Despite these deviations, the comparison underpins that the reconstruction of the “bunch core” is accurate.

Figure 7.13 shows trace space distributions of selected slices measured at a particle energy of 494 MeV. The longitudinal positions of the individual slices are indicated in Fig. 7.12(b). Image (1) in Fig. 7.13 shows the distribution of a slice in front of the current spike. The distribution exhibits

---

[5] In the tails of spatial profiles, noise contributions with positive and negative sign occur after subtraction of a background. When calculating RMS widths, the contributions from noise therefore approximately cancel each other. Negative intensities are, however, not included by the tomography algorithm.

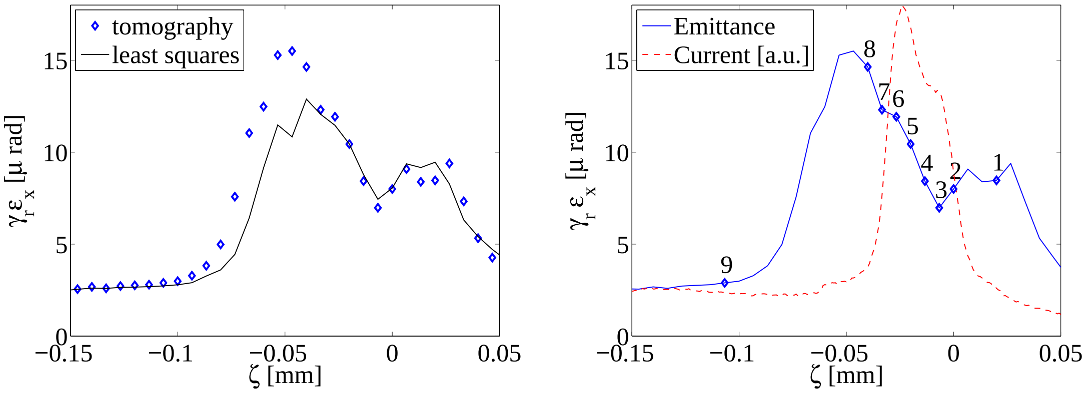

(a) (b)

Figure 7.12: (a): Comparison of the slice emittance obtained using tomography and a least squares method. The same experimental data and the same subdivision into slices was used in both cases. (b): Longitudinal positions of selected slices considered in Fig. 7.13. The numbers refer to the images shown in Fig. 7.13.

two local intensity maxima and therefore has an increased slice emittance of about 8 μm. At the position of the leading edge of the current spike (2), one density maximum occurs in the center of the distribution. The density increases within the current spike (3) while the slice emittance decreases. In the center of the current spike, a bifurcation into two "branches" can be observed (4). The branch on the right supposedly corresponds to the low-energy branch observed in longitudinal phase space (cf. Fig. 7.3) which is caused by CSR (cf. section 8). The branch on the left is assumed to contain particles with higher energy and to pass into the bunch tail, which would be in agreement with the measured slice centroid curve in trace space (Fig. 7.10(b)). The bifurcation results in an increasing slice emittance, which further increases as the bifurcation gets stronger (5) and the maximum density in the center reduces (6). At the trailing edge of the current spike, the density maximum vanishes (7). Within the region around the maximum slice emittance, the distribution is diffuse and shows again two separated regions with local maxima in charge density (8). The upper bunch fraction in the image supposedly corresponds to the tail, while the lower one is likely to contain low-energy particles. In the tail, a nearly Gaussian distribution covering a significantly smaller trace space area can be observed (9).

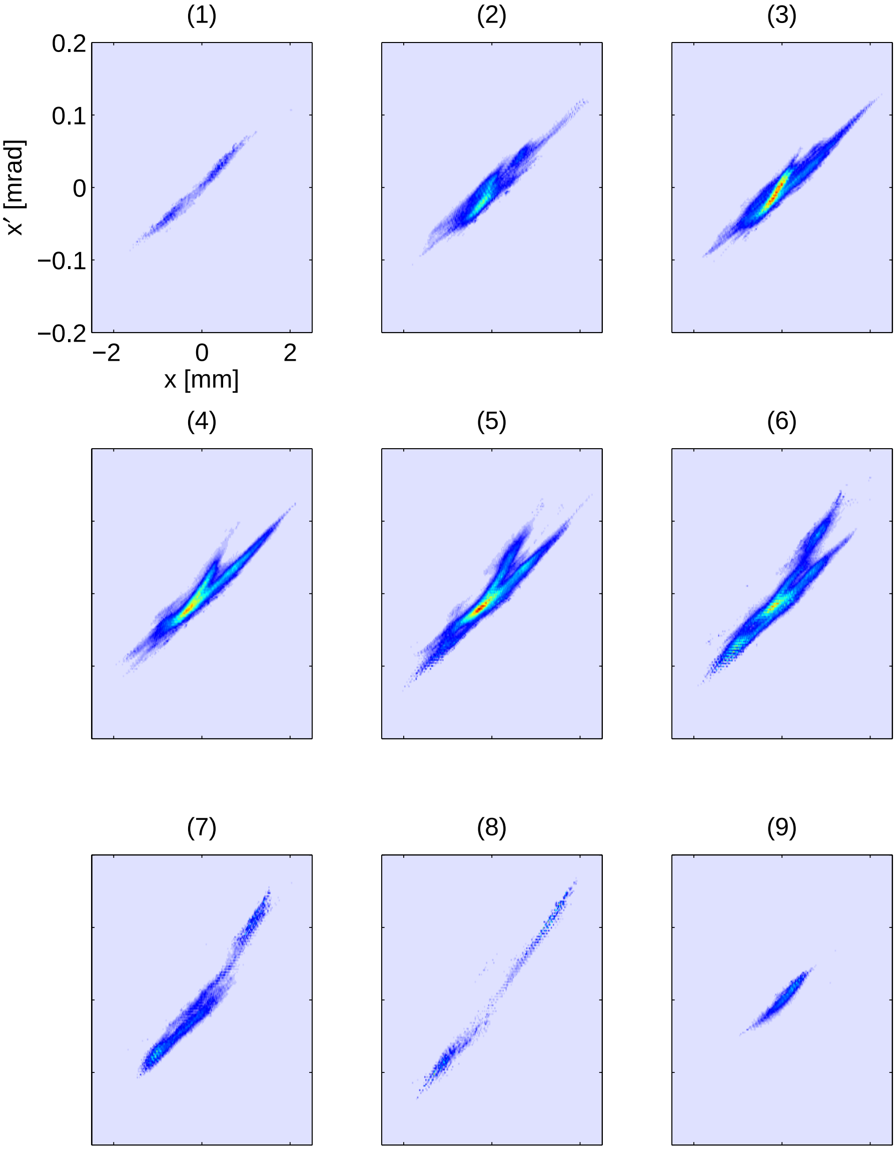

Figure 7.13: Reconstructed trace space distributions of selected slices (for color code, see appendix A). The longitudinal position of the individual slices within a bunch is shown in Fig. 7.12(b). The intensity of each image was normalized to the integrated intensity and multiplied by the total charge within the corresponding slice, so the charge density scale is the same in each image. Note that the mean coordinates $(\langle x\rangle, \langle x'\rangle)$ *in each image define the origin* $(0, 0)$, *so the coordinates in different images cannot be directly compared.*

Distributions in normalized coordinates

The overall "shape" of the reconstructed trace space distributions depends strongly on the ellipse parameters at the reconstruction point. In order to reveal basic bunch properties and to be able to compare results of different measurements, a transformation to normalized coordinates (u, v) (cf.

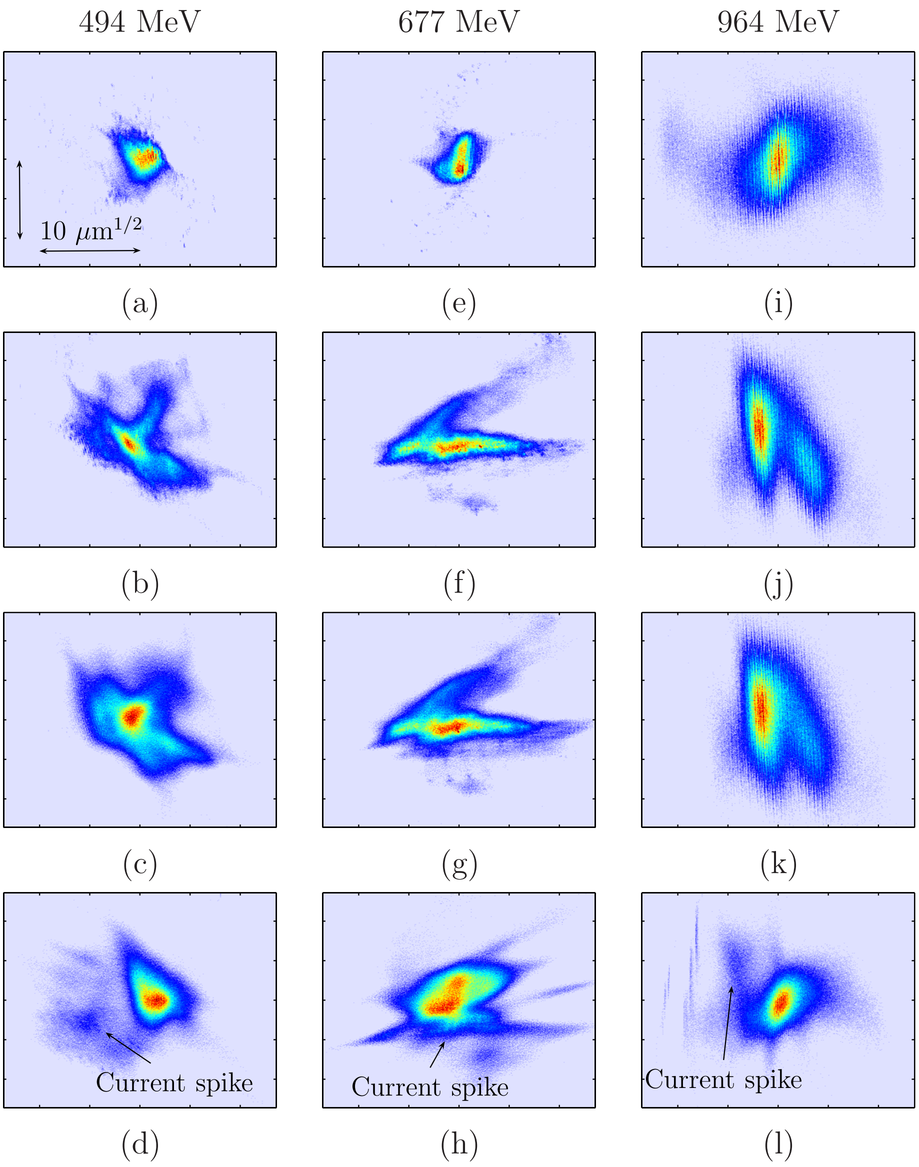

Figure 7.14: Comparison of reconstructed phase space distributions under FEL operating conditions at different particle energies. The distributions are shown normalized coordinates $(u, v) \cdot \sqrt{\gamma_r}$ *with* $u\sqrt{\gamma_r}$ $[\mu\mathrm{m}^{1/2}]$ *on the horizontal and* $v\sqrt{\gamma_r}$ $[\mu\mathrm{m}^{1/2}]$ *on the vertical axis. A circular RMS ellipse with radius* r *corresponds to a normalized emittance of* $r^2[\mu m]$*. The scale is indicated in (a). The left column shows the distribution within a slice in the bunch tail (a), a slice in the current spike (b), the entire current spike (FWHM) (c), and an entire bunch (d) at 494 MeV. The arrow in (d) indicates the position of the intensity maximum in (c). (e)-(h) and (i)-(l): Corresponding results at 677 MeV and 964 MeV, respectively.*

section 2.3) with respect to the beam ellipse parameters of an entire bunch is appropriate [6] (cf. section 2.3). In case the beam optics is linear and the

---

[6] Since the measured distributions are given in the form of digital images and not as particle distributions, a transformation cannot be directly performed. Here, a distribution

particles are not accelerated, a bunch distribution rotates about its mean coordinates in the (u, v)-plane as the bunch proceeds along a beamline and retains its basic structure.

Figure 7.14 shows density distributions in normalized coordinates obtained at particle energies of 494 MeV, 677 MeV and 977 MeV. The distribution within a slice in the tail at 494 MeV (Fig. 7.14(a)) confirms the regular shape observed in Fig. 7.13. The iso-density contours are nearly circular, revealing a small deformation parameter of the distribution with respect to the ellipse parameters of an entire bunch. The distributions within a slice in the current spike (b) and within the entire current spike between FWHM-boundaries (c) exhibit a bifurcation into two branches and a high-intensity core as discussed above. The density distribution of an entire bunch (d) was determined from a separate measurement (TDS off). The distribution is dominated by the long trailing tail typically containing more than 75% of the total bunch charge. The head of the bunch is significantly separated from the tail by slice centroid shifts.

The corresponding distributions at 677 MeV (e-h) and 964 MeV (i-l) exhibit similar properties. In particular, a bifurcation and a high-density region within the current spike can be observed also in these cases. The distribution within the tail covers a significantly larger area at 964 MeV (i) due to the beam halo.

7.6.1 Emittance analysis

The trace space distribution within the bunch tail can be approximated by a two-dimensional Gaussian distribution. Figure 7.15(b) shows the results of a two-dimensional Gaussian fit (least-square) to a typical distribution within the tail (Fig. 7.15(a)), and a comparison of the corresponding one-dimensional intensity profiles in x- and x'-direction (Fig. 7.15(c, d)). The profiles of the Gaussian distribution and the measured distribution agree reasonably well, corroborating that a Gaussian fit is justified. The emittance of the Gaussian distribution is 1.6 μm, compared to 2.1 μm in case of the measured distribution.

---

was generated by randomly "filling" the area of each pixel with a number of particles proportional to the pixel-intensity. The distributions can then be transformed to normalized coordinates and digital images be generated from the resulting distributions. The results were checked by comparing the emittance.

In order to quantify the deviation of the measured distribution from the Gaussian distribution, the quantity

$$\sigma_1 = \sqrt{\frac{\sum_{(x,x')\in A_1} \left[\rho(x,x') - \rho_{fit}(x,x')\right]^2}{\sum_{(x,x')\in A_1} [\rho_{fit}(x,x')]^2}} \tag{7.13}$$

can be used. Here, $\rho(x, x')$ is the measured distribution and $\rho_{fit}(x, x')$ the distribution of the Gaussian fit. A_1 is the trace space area defined by

$$\frac{\rho_{fit}(x,x')}{max(\rho_{fit}(x,x'))} \geq 0.01. \tag{7.14}$$

Thus, σ_1 is a measure of the deviation of the two distributions within the trace space area with a significant intensity of the Gaussian distribution. The aim of this parameter is to allow a comparison of deviations rather than quantify the deviations in an absolute sense. In case of the distributions presented in Fig. 7.15, the deviation amounts to $\sigma_1 = 24\%$.

A similar approach can be applied in order to determine the emittance of the high-density core observed within the current spike. To do so, the high-density core of the distribution shown in Fig. 7.16(a) (image (3) of Fig. 7.13) was isolated by applying an intensity threshold to the distribution. The threshold was chosen to be the half-maximum value of the intensity of the distribution. A three-dimensional representation of the distribution (Fig. 7.16(b)) reveals more clearly that such a threshold separates the core from the remainder of the distribution. The Gaussian distribution obtained by a two-dimensional Gaussian fit to the core (Fig. 7.16(c, d)) yields an emittance of 1.8 μm, compared to 7.5 μm slice emittance of the measured distribution. The integrated intensity of the Gaussian distribution corresponds to about 52% of the integrated intensity of the entire slice distribution. Consequently, the “equivalent charge” of the Gaussian distribution and the corresponding “equivalent current” are 52% of the total charge within the slice and the slice current, respectively.

As shown in Fig. 7.13, a high-density core in horizontal phase space can be observed throughout the extension of the current spike. A Gaussian fit can thus as well be applied to the trace space distribution of the entire current spike (FWHM). At 494 MeV, the resulting emittance of the high-density core is 2.9 μm and the equivalent charge 49% of the slice charge. The method is only applicable as long as the main part of the high-density

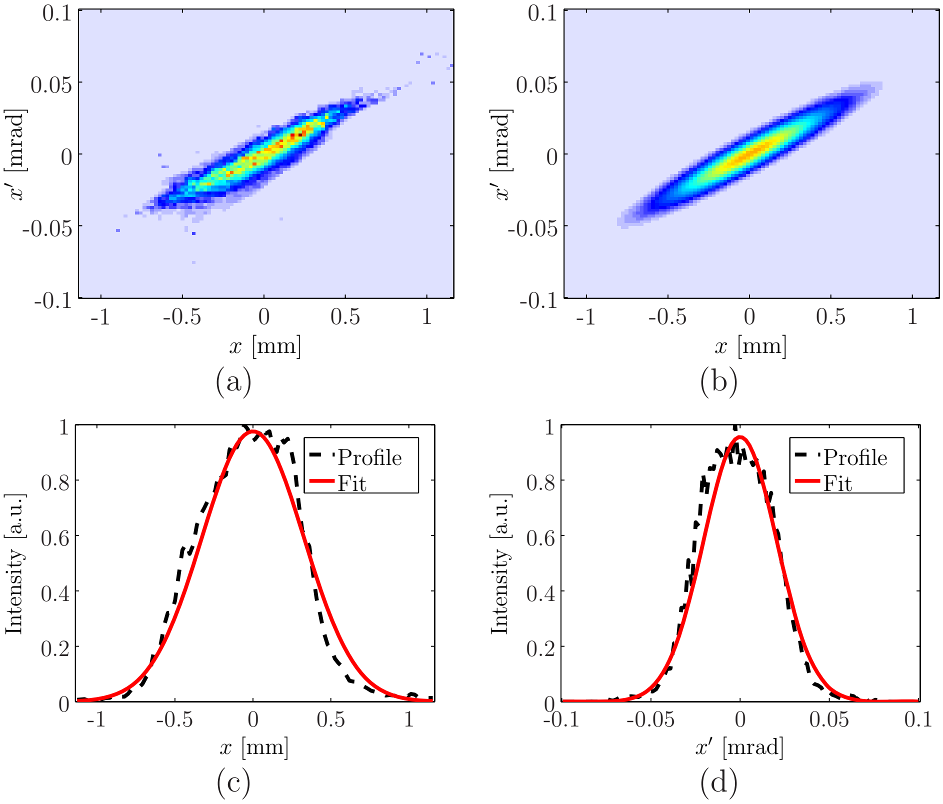

Figure 7.15: Two-dimensional Gaussian fit to the trace space distribution of a single slice in the tail. (a): Measured distribution. (b): Distribution of the Gaussian fit. The color code is defined in appendix A. (c) and (d): Comparison of the resulting x- and x'-profiles, respectively.

region in horizontal phase space is located in one branch of the observed bifurcation. This is the case when considering the overall distribution in the current spike, but not for each slice within this section, as is apparent from Fig. 7.13.

In case of a fit to the high-density core of a trace space distribution, the error σ_1 defined above is typically dominated by contributions outside the core region, where the density of the measured distribution $\rho(x, x')$ may be significantly larger than the density of the Gaussian distribution $\rho_{fit}(x, x')$. Since such deviations are not relevant here, a different quality measure needs to be introduced. One can define an error σ_2 similar to σ_1 (7.13) which includes only contributions satisfying $\rho_{fit}(x, x') \geq \rho(x, x')$:

$$\sigma_2 = 2 \cdot \sqrt{\frac{\sum_{(x,x')\in A_2} \left[\rho(x, x') - \rho_{fit}(x, x')\right]^2}{\sum_{(x,x')\in A_1} [\rho_{fit}(x, x')]^2}}, \tag{7.15}$$

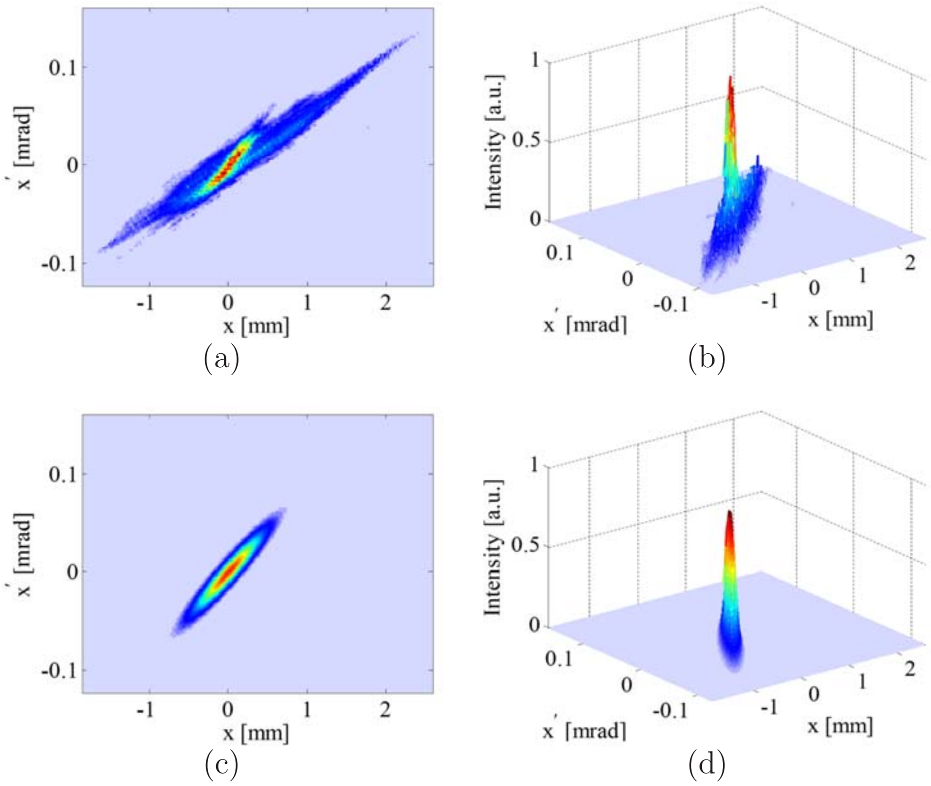

(a) (b)

(c) (d)

Figure 7.16: Two-dimensional Gaussian fit to a high-density core. (a) and (b): Measured distribution of a slice within the current spike at 494 MeV (cf. image (3) of Fig. 7.13). The color code is defined in appendix A. (c) and (d): Gaussian fit to the high-intensity core.

Table 7.4: Properties of the reconstructed phase space distributions determined by Gaussian fits. The column "bunch section" specifies the longitudinal section considered: "spike" refers to the current spike within FWHM-boundaries, "head slice" refers to a typical slice within the current spike, and "tail slice" to a typical slice within the tail.

conditions	bunch section	$\gamma_r \epsilon_x$ [μm]	$\sigma_{1/2}$ [%]	Q_e/Q_{slice} [%]	Q_e/Q_{bunch} [%]	I_e [kA]]
494 MeV (C1)	spike	2.9	26	49	9	0.6
	head slice	1.8	34	52	-	0.6
	tail slice	1.6	24	94	-	0.2
677 MeV (C2)	spike	4.0	36	72	18	0.9
	head slice	4.7	54	92	-	1.2
	tail slice	1.3	24	89	-	0.2
964 MeV (C3)	spike	3.2	32	52	5	0.4
	head slice	4.2	56	67	-	0.5
	tail slice	2.6	30	69	-	0.2

where A_2 is defined by the condition

$$\rho_{fit}(x, x') \geq \rho(x, x'). \tag{7.16}$$

The factor of two in Eq.(7.15) is introduced in order to allow a quantitative comparison between σ_1 and σ_2. In case of the distributions presented in Fig. 7.16, the deviation amounts to $\sigma_2 = 34\%$.

Corresponding procedures were applied to the experimental data obtained at 677 MeV and 964 MeV. The results are summarized in Table 7.4. The emittance of the high-density region within the entire current spike is in the range of 2.9 μm (C1) to 4.0 μm (C2). The values are significantly smaller than the emittance of the entire current spike of about 10 μm (cf. section 7.4). The ratio of equivalent charge and slice charge (Q_e/Q_{slice}) ranges between 49 % (C1) and 72 % (C2). This yields an equivalent current I_e between 0.4 kA (C3) and 0.9 kA (C2). Multiplying the ratio Q_e/Q_{slice} with the charge fraction contained within the current spike (Table 7.2) yields a ratio of equivalent charge to bunch charge (Q_e/Q_{bunch}) between 5 % (C3) and 18 % (C2).

The emittance of the high-density region of slices within the current spike lies between 1.8 μm (C1) and 4.7 μm (C2). The charge fraction varies between 52 % (C1) and 92 % (C2), resulting in equivalent currents of 0.4 kA (C3) to 1.2 kA (C2). Smaller errors σ_2 and a better agreement between the measurements suggest that a fit to the entire current spike is more reliable.

The core emittance within slices of the tail is found to be in the range of 1.3 μm (C2) to 2.6 μm (C3). The comparably large emittance of 2.6 μm and the small equivalent charge fraction of 69 % under conditions C3 are due to the beam halo.

In case of Gaussian fits to a high-density core, the result may significantly depend on the choice of the threshold applied prior to the Gaussian fit. This is the case when the distribution within the core significantly deviates from a Gaussian distribution. For instance, in case of conditions C2, emittance and charge fraction of the high-density region within the spike drop from 4.0 μm to 2.7 μm and from 72 % to 50 %, respectively, if the threshold is increased. A strong dependence on the threshold and corresponding deviations from a Gaussian distribution are reflected in large errors σ_2. The resulting uncertainty concerning the emittance is, however, rather small compared to the difference to the measured slice emittance.

7.6.2 Discussion

Aside from a direct measurement, beam parameters of the lasing fraction of an electron bunch can be deduced from measured properties of the FEL radiation. A characterization of the FEL radiation was performed at a wavelength of 13.7 nm and a saturated average radiation pulse energy of 40 μJ [1]. In particular, the radiation pulse energy was measured as a function of the longitudinal position within the undulator section (gain curve) by interrupting the FEL gain process at several positions with suited steering magnets. The measurement yielded a field gain length of 2.5 m [1], which corresponds to a power gain length L_g of about 1.25 m. The measurement allowed also to estimate the coherence time[7] τ_{coh} of the radiation to be about 4 fs. An average number of 1.9 coherence regions or "modes" per pulse was determined from statistical fluctuations of the radiation pulse energy. The pulse duration is thus about $M \cdot \tau_{coh} \approx 8$ fs.

The FEL code FAST [96] was used to determine the beam parameters of the lasing fraction needed to reproduce the measured radiation properties, in particular the gain length. A peak current of 2 to 2.5 kA, a width of the current spike of about 10 μm (FWHM), and a normalized transverse emittance of 1 to 1.5 μm were determined in this way [1].

The presented measurement at the same particle energy using the TDS yielded a peak current of 1.9 kA, a width of the current spike of 22 μm, and a normalized transverse slice emittance of about 10 μm in the high current region. A tomographic reconstruction allowed to determine a phase space region with an estimated emittance of 4 μm and a current of about 1 kA. This high-density region in phase space is expected to contain the lasing fraction, while the slice emittance includes particles not contributing to the lasing process.

Although the emittance determined by a tomographic reconstruction is much closer to the result deduced from radiation properties than the slice emittance, there is still a significant deviation between the results, concerning both the emittance and the current. These deviations may have several reasons. At first, it must be noted that the measurement conditions were not exactly the same. While a saturated average pulse energy of 40 μJ was obtained during the characterization of the FEL radiation, an average pulse energy of 5 μJ (not saturated) was obtained during the measurement

---

[7] The time over which the radiation can be considered coherent.

of electron beam properties. The gain length was thus larger in the latter case, so a slightly smaller current and a larger emittance are not contradictory to the measured gain length. Furthermore, the measurement took place upstream of the dispersive collimator section (cf. Fig. 4.8), in which modifications, in particular of the peak current, are to be expected.

The main reason for the observed deviations is, however, assumed to be the longitudinal resolution. The length scale on which the amplification process takes place and on which the conditions for normalized emittance and current have to be fulfilled, is the coherence length $\Delta\zeta_{coh}$ defined by $\Delta\zeta_{coh} = c\tau_{coh}$ with τ_{coh} the coherence time of the radiation. The measured coherence time of 4 fs corresponds to a coherence length of 1.2 μm, which is significantly below the estimated RMS resolution of the measurement of 12 μm. Resolution limitations affect in particular the measured current, but also the emittance may be smaller on this length scale in view of the strong distortions observed in the high current region.

Moreover, it is important to note that the emittance measurements and the tomographic reconstruction refer to the average phase space distribution of beam bunches. Strong fluctuations of the structure of the phase space distribution from shot-to-shot necessarily lead to a dilution of the average phase space distribution. Such fluctuation are mainly due to jitter of the RF phase of module ACC1, and are particularly strong in the high current region (cf. Fig. 7.3). The measured emittance, in particular that of high density regions in phase space, is thus an upper limit for the corresponding emittance within a single bunch.

Finally, systematic errors of the reconstruction may occur due to strong transverse space charge forces and the significant energy spread within the high current region, as is shown in chapter 8. While the effect on the measured slice emittance is shown to be negligible, the detailed structure of the reconstructed distribution in horizontal phase may be slightly distorted because of these effects. Resolution limitations of the optical system are assumed to play a minor role, since an emittance below 2 μm was measured in the bunch tail.

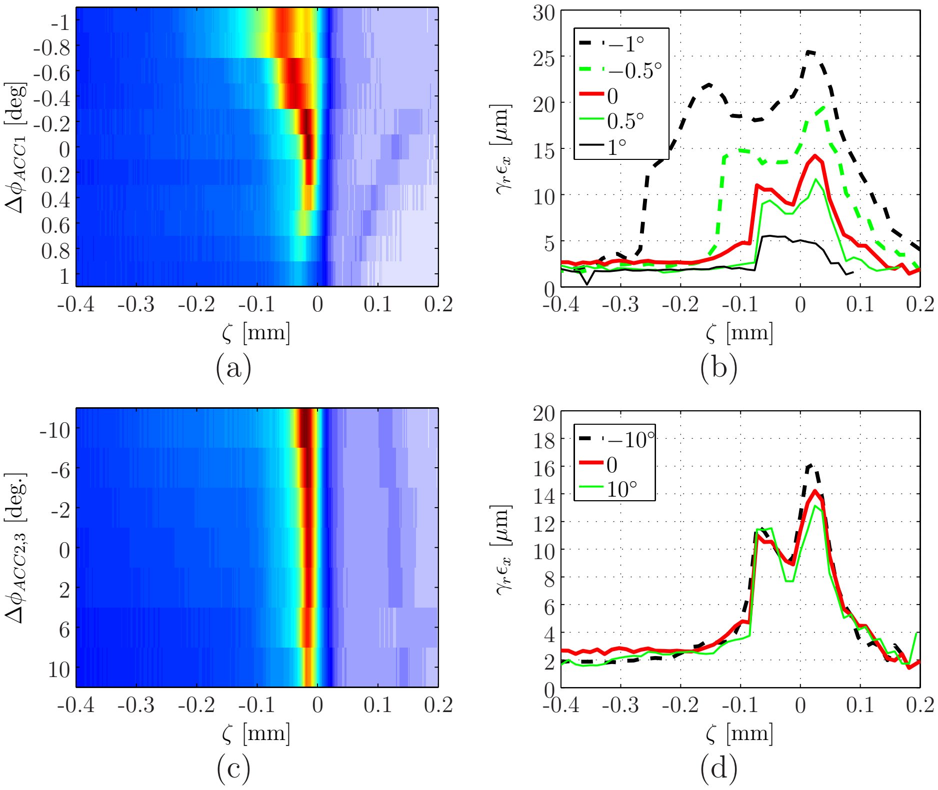

(a) (b)

(c) (d)

Figure 7.17: Comparison of current profiles (a) and slice emittance profiles (b) measured during a scan of the RF phase ϕ_{ACC1} of module ACC1 at 964 MeV. $\Delta\phi_{ACC1}$ specifies the difference to the RF phase at SASE operation ($\phi_{ACC1} = -8.4°$). The profiles are average current profiles determined from 20 CCD-images. They are normalized to the maximum peak current measured during the scan. The color code of Fig. (a) can be found in appendix A. (c) and (d): Corresponding results obtained by scanning the RF phase of module ACC2/3.

7.7 Measurements at different acceleration phases

In order to study the dependence of current profile and slice emittance on the RF phases of the accelerating modules ACC1 and ACC2/3, measurements at several RF phases around the setpoints for SASE operation were carried out. Figure 7.17(a) shows a comparison of the average current profiles measured at different RF phases of module ACC1. The measurements were performed at a particle energy of 964 MeV. $\Delta\phi_{ACC1}$ specifies the difference of the chosen RF phase to the RF phase at SASE operation, which was measured to be $-8.4°$. Although the RF phase was changed within an interval of only ±1°, the profiles significantly change during the scan. The maximum peak current (≈ 0.9 kA) and the minimum width of the current spike ($\approx 29\ \mu$m) are obtained at the phase for

SASE operation ($\Delta\phi_{ACC1} = 0$). Stronger compression ($\Delta\phi_{ACC1} < 0$) results in an increased width of the current spike of more than 100 μm at $\Delta\phi_{ACC1} = -1°$. At the same time, the peak current drops to ≈ 0.74 kA. A larger spike width can be explained by over-compression in this region, while a decreasing peak current supposedly arises from stronger collective effects such as CSR and space charge forces. Shifting the phase towards on-crest-operation ($\Delta\phi_{ACC1} > 0$) leads to less longitudinal compression. Accordingly, the peak current drops until the current spike nearly disappears at $\Delta\phi_{ACC1} = +1°$.

The slice emittance was measured (additionally to SASE conditions) at $\Delta\phi_{ACC1} = \pm 0.5°$ and $\Delta\phi_{ACC1} = \pm 1.0°$ (Fig. 7.17(b)). Within the high current region, the slice emittance continuously increases with decreasing RF phase. At $\Delta\phi_{ACC1} = -1.0°$, maximum values of up to 25 μm were measured, whereas at $\Delta\phi_{ACC1} = 1.0°$ a slice emittance of $\lesssim 5$ μm is found. This behavior originates from a critical dependence of the slice emittance on collective effects, in particular CSR. Dispersive effects from beam steering and the horizontal kicker are assumed to play a minor role (cf. section 8).

The RF-phase of module ACC2/3 was varied within an interval of ± 10° around the phase for SASE operation ($\phi_{ACC2/3} = 0$). It was scanned over a wider range than ϕ_{ACC1} since the longitudinal compression is less sensitive to changes of $\phi_{ACC2/3}$. The average current profiles measured during the scan are presented in Fig. 7.17(c). Peak current and spike width change moderately compared to the results of the scan of ϕ_{ACC1}. The peak current continuously increases from ≈ 0.74 kA at $\Delta\phi_{ACC2/3} = 10°$ (less compression) to ≈ 0.9 kA at SASE operation, and ≈ 1.0 kA at $\Delta\phi_{ACC2/3} = -10°$ (more compression). The spike width (FWHM) is ≈ 29 μm at $\Delta\phi_{ACC2/3} = 0$ and ≈ 39 μm at $\Delta\phi_{ACC2/3} = -10°$ and does not significantly change for phases $\Delta\phi_{ACC2/3} > 0$.

The slice emittance (Fig. 7.17(d)) shows a weak dependence on the RF-phase of ACC23 within the range of the scan. The most significant change is found around $\zeta = 0$, where the slice emittance increases by $\approx 23\%$ as the RF phase is changed from $\Delta\phi_{ACC2/3} = 10°$ to $\Delta\phi_{ACC2/3} = -10°$.

A tomographic reconstruction of the horizontal phase space distribution at different RF phases $\phi_{ACC2/3}$ allows a more detailed analysis. Figure 7.18 shows the phase space distributions of the current spike (FWHM) at $\Delta\phi_{ACC2/3} = 10°$ (a), $\Delta\phi_{ACC2/3} = 0$ (b), and$\Delta\phi_{ACC2/3} = -10°$ (c). The

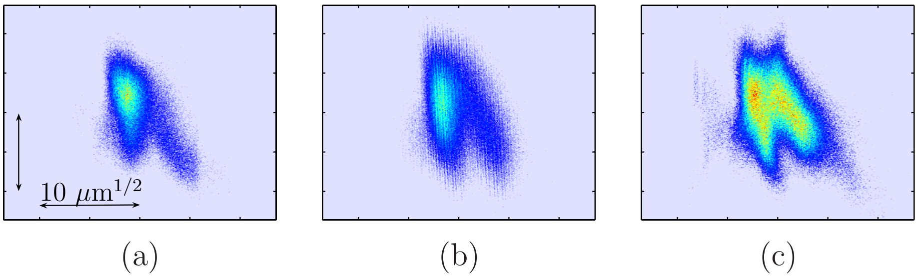

(a) (b) (c)

Figure 7.18: Charge density distribution of the current spike (FWHM) in horizontal phase space at $\Delta\phi_{ACC2/3} = 10°$ (a), $\Delta\phi_{ACC2/3} = 0°$ (b), and $\Delta\phi_{ACC2/3} = -10°$ (c). Normalized coordinates $(u, v) \cdot \sqrt{\gamma_r}$ are used. The charge density scale is the same in each image.

intensity of each image was normalized to the integrated intensity and multiplied with the total charge located within the current spike. The charge density scale is thus the same in all images. The populated phase space area and the overall shape of the distribution is similar in all three cases, which is in agreement with small differences in slice emittance. At $\Delta\phi_{ACC2/3} = 10°$ and $\Delta\phi_{ACC2/3} = 0$, a high-density region occurs in one branch of a bifurcation. The maximum charge density is slightly higher at $\Delta\phi_{ACC2/3} = -10°$ than under SASE conditions. At $\Delta\phi_{ACC2/3} = -10°$, the total charge within the current spike is nearly 50% larger than at $\Delta\phi_{ACC2/3} = 0$. The phase space distribution reveals that a large fraction of this additional charge is located in the branch on the right which supposedly does not contribute to the SASE process. The charge stems from the part of the tail directly behind ($\zeta > 0$) the current spike at $\Delta\phi_{ACC2/3} = 0$, which is longitudinally compressed at off-crest acceleration in module ACC2/3 and thus becomes part of the current spike.

7.8 Experimental studies of resolution limitations

Measurements at different input powers of the TDS

An experimental approach to study the influence of resolution-limitations is to compare experimental results obtained at different input powers of the TDS, which result in different shear parameters at the location of the screen. Fig. 7.19 shows current profiles (a) and slice emittance profiles (b) measured at different shear parameters of $S_1 = 7$, $S_2 = 13$, $S_3 = 25$ and $S_4 = 29$. It is apparent from the figures that an insufficient resolution has a significant impact on the resulting peak current and the width of the current spike as well as the slice emittance at $S_1 = 7$ and $S_2 = 13$. The impact on the slice emittance can be explained by large slice centroid offsets observed around the region of the current spike (cf. section 7.5). Between $S_3 = 25$ and and $S_4 = 29$, no significant differences are observed. The difference in resolution between S_3 and S_4 is, however, too small to conclude that resolution-limitations play a minor role in these cases.

Figure 7.20 shows the horizontal trace space distribution within the current spike (FWHM) measured at the same shear parameters S_1 to S_4. Although there are significant differences between the results for current profile and slice emittance, basically the same structures in phase space are found in each case. Additional charge fractions occur at low shear parameters around $x = 1$ mm, $x' = 0.1$ mrad. They stem from the bunch tail which is not sharply separated from the current spike due to an inferior longitudinal resolution. The separation of these charge fractions from the remainder is in agreement with the slice centroid curve (Fig. 7.10(b)) discussed in section 7.5. It can also be observed that the sharpness of the maximum in intensity drops with decreasing shear parameter. The results demonstrate that the tomographic reconstruction is less sensitive to the longitudinal resolution than the current profile or the slice emittance, since longitudinal sections are partly separated in trace space by centroid offsets.

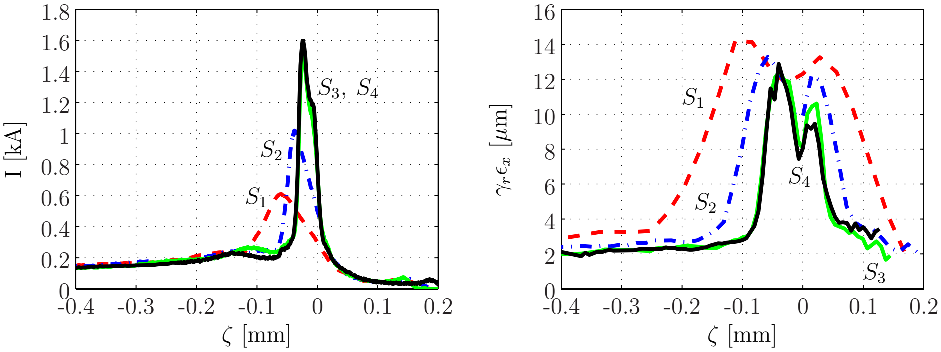

(a) (b)

Figure 7.19: Comparison of current profiles (a) and slice emittance profiles (b) measured at different shear parameters $S_1 = 7$ (red, dashed), $S_2 = 13$ (blue, dashed), $S_3 = 25$ (green, solid) and $S_4 = 29$ (black, solid). The measurements were carried out at a particle energy of 494 MeV.

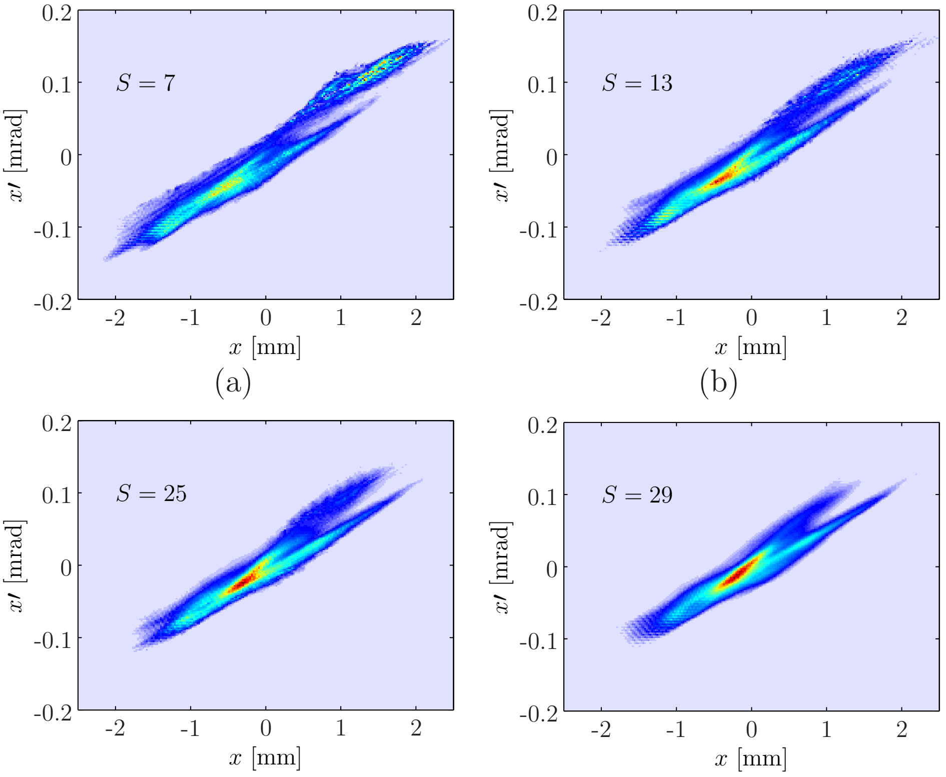

(a) (b) (c) (d)

Figure 7.20: Influence of TDS input power on measured phase space distributions. The figures show the reconstructed trace space distribution of the head for shear parameters of 29 (a), 25 (b), 13 (c) and 7 (d). The measurements were done at a particle energy of 494 MeV (C1).

Measurements at different RF phases of the TDS

The TDS is operated at a zero-crossing phase of the RF deflecting force, so the trajectory of the bunch centroid is not affected by the TDS. If the phase is shifted by 180°, the sign of the shear parameter is inverted. Performing measurements at both signs of the shear parameter allows to determine the impact of asymmetries in the vertical bunch profiles on the measurements. Such asymmetries may for instance arise from vertical slice centroid shifts due to wake fields and dispersion.

Measurements at both signs of the shear parameter were carried out at 494 MeV. A comparison of the measured current and slice emittance profiles is presented in Fig 7.21(a) and (b), respectively. The results obtained at both RF phases are basically in agreement. Moderate deviations in current as well as slice emittance of $\approx 20\%$ are unveiled within the high current region. In particular, the current and the slice emittance measured

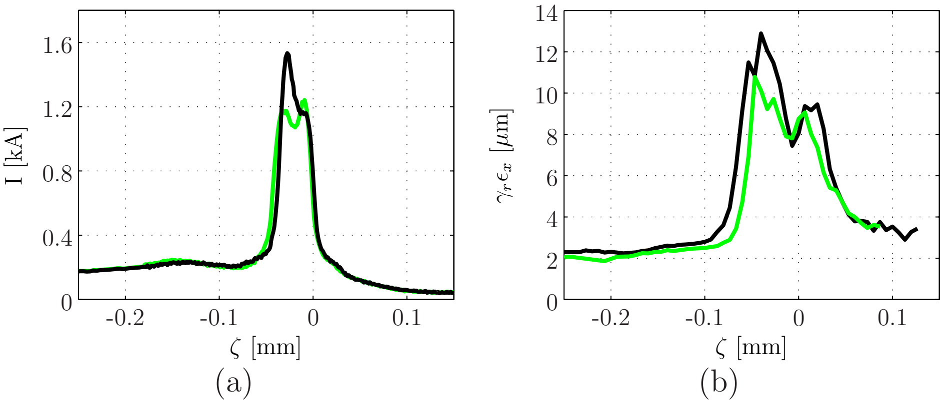

(a) (b)

Figure 7.21: Comparison of average current profile (a) and slice emittance profile (b) obtained at opposite signs of the shear parameter.

at the position of the trailing edge of the current spike drop if the shear parameter is inverted (green).

The strong energy variations measured in this bunch region at 677 MeV (cf. Fig. 7.3) suggest that the differences originate from vertical dispersion. A vertical separation of bunch fractions at the screen due to dispersion adds to the offsets induced by the TDS and may introduce non-linearities of the vertical position $y(\zeta)$ as a function of the longitudinal position ζ. Vertical dispersion may originate from beam steering and off-crest acceleration on the one hand, and the deflection of the TDS on the other hand. An inversion of the shear parameter is suited to reveal such effects, since the distorting vertical offsets add and subtract, respectively, to the offsets induced by the TDS.

The dispersion at the screen is assumed to be in the order of $D_y \lesssim$ 20 mm, with a contribution of less than 7.5 mm (half the screen hight) from the TDS. Assuming variations of the mean slice energy of $\lesssim 0.4\%$ as measured at 677 MeV (cf. section 7.3), the vertical separation of corresponding bunch fractions on the screen amounts to $\lesssim 80$ μm. At a shear parameter of $S = 29$ as in the presented measurements, this corresponds to an apparent longitudinal separation of $\lesssim 3$ μm. The difference in apparent longitudinal separation between the measurements with inverted shear parameters amounts to twice this value, which is close to the estimated resolution of 8 μm. Vertical dispersion may thus explain the observed differences.

The results show that vertical asymmetries may influence the experimental results for current profile and slice emittance. The impact is the larger the smaller the shear parameter. Generally, a dependence of the results on the sign of the shear parameter is an indication for resolution-limitations. Averaging of results obtained with inverted shear parameters may lead to improvements, as discussed in section 6.

Chapter 8

Numerical simulations

8.1 Particle tracking simulations for FEL operating conditions

This section is concerned with a comparison of the experimental results presented in this thesis with particle tracking simulations. Particle tracking simulations were performed for the entire beamline from the RF electron gun to the position of the screens, including both external fields from accelerating structures and magnets, and self-fields of the bunches. For this purpose, the computer codes ASTRA and CSRTrack were used. ASTRA ("A Space Charge Tracking Algorithm") tracks particles through user defined external fields taking into account the space charge field of the particle cloud. The tracking is based on a Runge-Kutta integration with fixed time step [55]. ASTRA was used for particle tracking along straight sections of the beamline, including in particular the accelerating modules. CSRTrack focuses on the treatment of coherent synchrotron radiation (CSR) fields and provides various models for field calculations [56, 97, 98, 99, 100, 94]. Here, an efficient one-dimensional method has been used, in which electron bunches are approximated by line charge densities along the beam trajectory [57, 97]. CSRTrack was used within the magnetic bunch compressor chicanes, where strong effects from CSR may occur.

The electron distribution of a bunch depends critically on the RF phase ϕ_{ACC1} of the accelerating module ACC1. As will become clear in this section, changes of the RF phase in the order of 0.1° may lead to significant changes of current profile and slice emittance. However, the RF phases were determined only with an accuracy of about 1°. Variations in the order of 1° are also critical in case of the RF phase $\phi_{ACC2/3}$ of module ACC2/3. For this reason, simulations for several RF phases of ACC1 and ACC2/3 close to the measured values were performed. A comparison of the resulting current profile to the measured current profile allows to confine the RF phases to a smaller range of values, since the width of the current spike and the peak current sensitively depend on these parameters. A detailed quantitative comparison between experimental results and simulations is, however, not possible without knowing the RF parameters more precisely. The comparisons shown in this section are therefore mainly of qualitative character. Nevertheless, they allow to interpret important experimental observations.

The simulations were performed for the case of a final particle energy of 494 MeV (conditions C1 in Table 7.1). Module ACC4/5 was set to on-crest operation and the bunch charge to 0.76 nC in correspondence with the measurements (cf. Table 7.1). Results for different RF phases $-7.0^\circ \leq \phi_{ACC1} \leq -9.0^\circ$ (in steps of 0.25°) and $-10^\circ \leq \phi_{ACC2/3} \leq -12^\circ$ (in steps of 1.0°) around the measured values $\hat{\phi}_{ACC1} = -8.8^\circ$ and $\hat{\phi}_{ACC2/3} = -11.0^\circ$ were compared to the experimental results. A reasonable agreement with the measured current profile was obtained at $\phi_{ACC2/3} = -10.0^\circ$ and $-8.0^\circ \leq \phi_{ACC1} \leq -8.25^\circ$. The results of these simulations will be presented in more detail in the remainder of this section. In all simulations, an input distribution with 10^5 particles obtained for standard settings of the RF-gun and a standard optics was used. An adaption to the conditions during the measurements was not carried out in view of the dominating dependence on the RF parameters of ACC1 and ACC23.

8.1.1 Comparison to experimental results

In the following, properties of the simulated particle distributions are compared to experimental results. Unless otherwise specified, the particle distributions are considered at the reconstruction point of the emittance measurement at 494 MeV, which is located upstream of the accelerating module ACC5 (cf. section 7).

Current profile Figure 8.1(a) shows a comparison of the current profiles obtained in the simulations with the experimental result. The current profiles in the simulations exhibit a current spike as observed experimentally. In case of $\phi_{ACC1} = -8.0^\circ$, the current spike is much narrower than

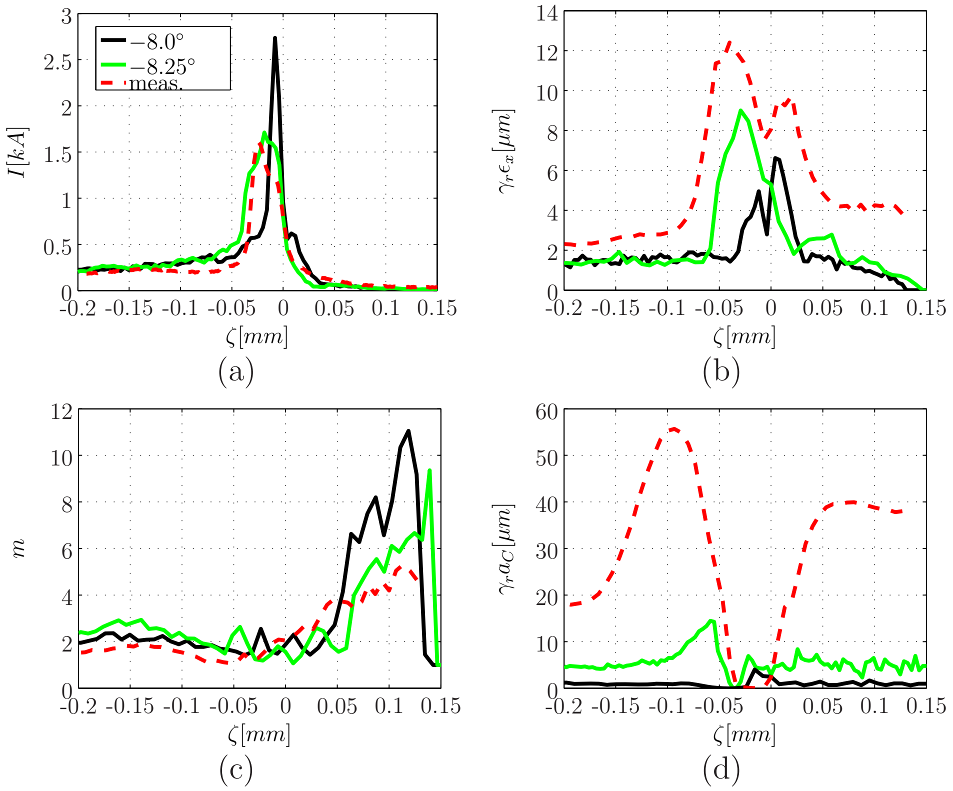

(a) (b) (c) (d)

Figure 8.1: Comparison of experimental results obtained at a particle energy of 494 MeV with results of simulations. (a) Current profile. (b) Slice emittance. (c) Deformation parameter (cf. section 2.3). (d) Amplitude of slice centroid offsets (cf. section 7.5). Solid lines show the results of simulations for RF phases ϕ_{ACC1} of $-8.0°$ (black) and $-8.25°$ (green). Dashed lines show experimental results.

measured, while the peak current is larger by more than 50 %. The total charge located within the current spike is roughly the same as measured. At $\phi_{ACC1} = -8.25°$, peak current and width of the current spike are in good agreement with the experimental results. The current spike is broader at this phase than at $\phi_{ACC1} = -8.0°$ due to over-compression in the front region of the bunch. The spike width further increases for $\phi_{ACC1} < -8.25°$. For $\phi_{ACC1} > -8.0°$, the peak current decreases and the amount of charge located in the high current region falls below the measured value. The RF phase of module ACC1 during the measurement is therefore assumed to be in the range of $-8.0°$ to $-8.25°$.

Slice emittance The slice emittance significantly increases in the region around the current spike at both RF phases of ACC1 considered (Fig. 8.1(b)). This behavior is in agreement with experimental observations. The maximum slice emittance is about 6.5 μm at $\phi_{ACC1} = -8.0°$ and 9 μm at $\phi_{ACC1} = -8.25°$. At $\phi_{ACC1} = -8.25°$, the maximum value occurs at the position of the trailing edge of the current spike. The slice emittance increases by up to a factor of 6 compared to the value of about 1.5 μm in the tail. A similar increase is observed experimentally. At $\phi_{ACC1} = -8.0°$, the maximum slice emittance is found in front of the current spike. As in case of the measurement, a local minimum occurs at the position of the leading edge of the current spike.

Throughout the considered bunch region, the slice emittance values found in simulations are smaller than the measured ones. The deviation in the tail may be due to an improper initial distribution, since the detailed settings of the RF gun such as the laser spot size on the cathode were not adapted to the conditions during the measurements. In the high current region, imprecise RF parameters play the dominant role, as can be seen from the difference in slice emittance between the simulation results for $\phi_{ACC1} = -8.0°$ and $\phi_{ACC1} = -8.25°$. Furthermore, at a particle energy of 494 MeV the one-dimensional approximation used for the calculation of CSR tends to underestimate slice emittance growth due to CSR [101]. The approximation gets more accurate for larger particle energies in the order of 1 GeV. Measurement errors were estimated to be $\lesssim 20$ % (cf. section 5.3.2).

Deformation parameter The deformation parameter (Fig. 8.1(c)) shows the same behavior at both RF phases considered. The parameter varies in the range of $m = 1$ to $m = 3$ in the tail and the current spike in both cases. In front of the current spike, the parameter strongly increases up to $m \approx 10$. Apart from the deviations in the low current region in front of the current spike, which may originate from a limited sensitivity of the measurement for low charge densities, the measured deformation parameter is in reasonable agreement with these results.

Slice centroid offsets Slice centroid offsets (cf. section 7.5) are shown in Fig. 8.1(d). At $\phi_{ACC1} = -8.0°$, hardly any offsets can be observed. At $\phi_{ACC1} = -8.25°$, variations are found around the position of the trailing edge of the current spike, with two extremal values and a steep slope at $\zeta = -0.05$ mm. The shape of the profile is very similar to the one observed

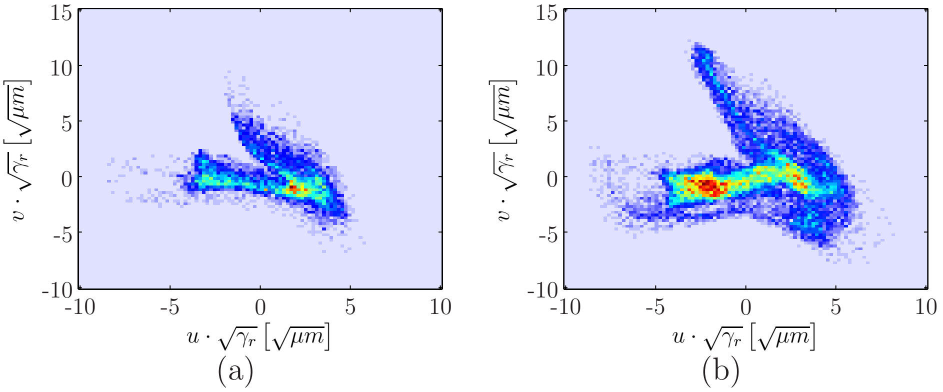

(a)
(b)

Figure 8.2: Simulated horizontal phase space distribution of the particles located within the current spike (FWHM) for $\phi_{ACC1} = -8.0°$ (a) and $\phi_{ACC1} = -8.25°$ (b). Normalized coordinates (u, v) (defined by means of the Twiss parameters of the entire bunch) are used in order to minimize the dependence of the phase space distribution on the optics (cf. sections 2.3 and 7.6).

in the measurement. However, the absolute values are about four times larger in case of the measurement than found in the simulation. These deviations are not fully understood. They may arise from physical effects not included in the simulations, such as wake fields and space charge forces within the magnetic chicane and an imperfect beam alignment. Further studies need to be done to clarify this observation.

Horizontal phase space The horizontal phase space distribution of the particles located within the current spike (FWHM) is shown Fig. 8.2(a) for $\phi_{ACC1} = -8.0°$ and in Fig. 8.2(b) for $\phi_{ACC1} = -8.25°$. Both distributions are characterized by a bifurcation into two branches. At $\phi_{ACC1} = -8.0°$, the maximum charge density occurs in the region where the branches split up, while at $\phi_{ACC1} = -8.25°$ it is found within the lower branch. The maximum in charge density is more pronounced in the latter case. The total phase space area occupied by the particles is significantly larger at $-8.25°$, which is in agreement with a larger slice emittance. The basic structure of the distributions in phase space is very similar to that of measured distributions, in which also a bifurcation and a high-density region were observed (cf. Fig. 7.14).

Longitudinal phase space The density distributions in longitudinal phase space at $\phi_{ACC1} = -8.0°$ (Fig. 8.3(a)) and $\phi_{ACC1} = -8.25°$ (Fig. 8.3(b))

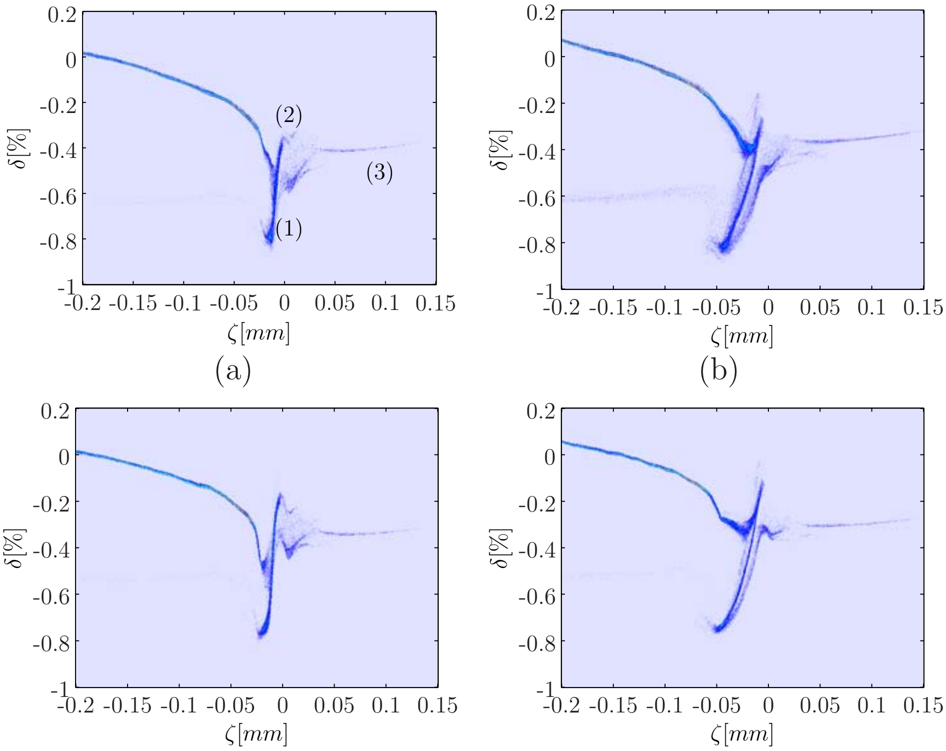

(a) (b) (c) (d)

Figure 8.3: Distribution in longitudinal phase space at $\phi_{ACC1} = -8.0°$ (a) and $\phi_{ACC1} = -8.25°$ (b) upstream of the accelerating module ACC5. δ denotes the relative energy deviation from the mean bunch energy, which is slightly lower at $\phi_{ACC1} = -8.25°$ due to stronger CSR effects. Only the front part containing the high-current region is shown. In (a), characteristic deformations due to CSR (1) and space charge forces downstream (2) and upstream (3) of the second bunch compressor are indicated. Figures (c) and (d) show the corresponding distributions at the position of the OTR screen used for measuring the distribution in longitudinal phase space (downstream of the final accelerating modules).

show essentially the same characteristic structures seen in simulations for standard settings (cf. section 4.1.4) and the results of measurements (cf. section 7.3). In particular, branches towards lower energies due to CSR, towards higher energies due to space charge forces downstream of the second bunch compressor, and towards positive ζ due to space charge forces in between the bunch compressors can be observed in the high-current region of the bunches. The branch towards lower energies due to CSR has a positive slope in longitudinal phase space in case of $\phi_{ACC1} = -8.25°$, which indicates over-compression in this bunch region (cf. section 4.1.4). At $\phi_{ACC1} = -8.0°$, the branch has minimum spatial extension, showing that the bunch section is close to full compression. This is in agreement with a larger peak current and narrower current spike observed at $\phi_{ACC1} = -8.0°$.

The experimental result at a particle energy of 677 MeV (cf. Fig. 7.3) suggests that a slight over-compression of the high-current region is favorable for SASE operation.

Figures 8.3(c) and (d) show the corresponding distributions at the position of the OTR screen used for measuring longitudinal phase space, which is located downstream of the final acceleration modules. Here, the relative deviations δ from the mean energy are reduced since the mean particle energy is larger. Moreover, the spikes towards higher energy are more pronounced due to longitudinal space charge forces acting along the additional beamline segment.

Structure of the high-current region

A key observation in simulations as well as experiments is a bifurcation of the bunch section around the current spike in horizontal phase space. As is shown in Fig. 8.4 for the case of $\phi_{ACC1} = -8.25^\circ$, the bifurcation is related to the structure observed in longitudinal phase space. The majority of the particles in the lower branch of the bifurcation have an energy only slightly below the mean energy, while the upper branch mainly contains low-energy particles (Fig. 8.4(a) - (d)). In both branches, there is a correlation between longitudinal position and energy. While in the lower branch particles at the front have lower energy than those trailing behind, the situation is reversed in the upper branch due to over-compression. The correlations can be utilized to raise the peak current by longitudinally compressing one of these bunch sections in the magnetic chicane prior to the undulator section. Upstream of this magnetic chicane, the maximum current carried by the two regions is about 1 kA (Fig. 8.4(e) and (f)) and thus in good agreement with the measured current of the high density region in horizontal phase space (cf. section 7.6).

8.1.2 Effects from coherent synchrotron radiation within the second bunch compressor

As shown in section 8.1.1, remarkable experimental results such as a strong increase in slice emittance, a bifurcation in transverse phase space and varying slice centroid offsets in the high-current region can basically be reproduced in particle tracking simulations. In this section, it will be shown that CSR in the second bunch compressor (BC3) is the dominating physical origin for these effects. The results obtained for $\phi_{ACC1} = -8.25°$ will be considered since the agreement between experimental results and simulations is best in this case.

The direct consequence of coherent emission of synchrotron radiation

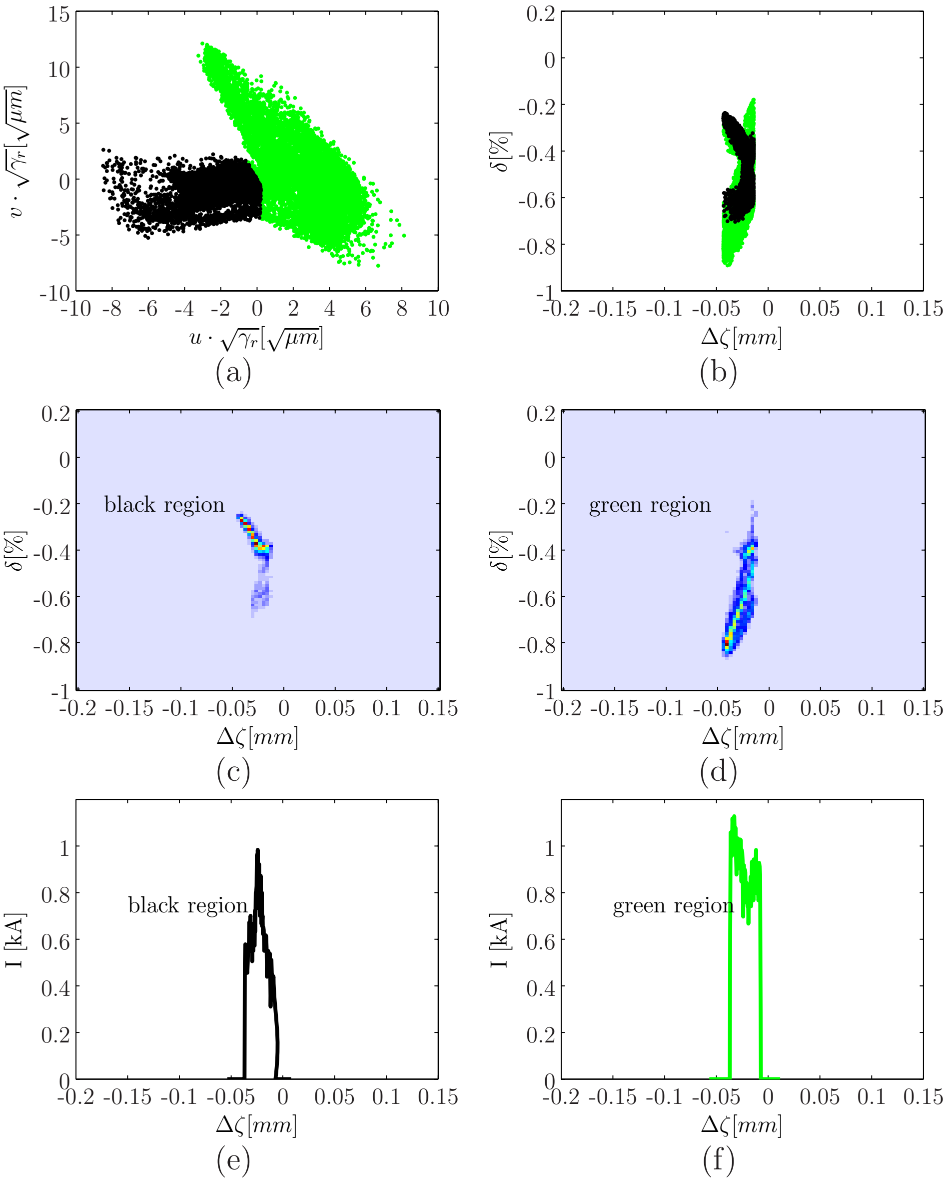

(a) (b) (c) (d) (e) (f)

Figure 8.4: Structure of the high-current region in horizontal and longitudinal phase space at $\phi_{ACC1} = -8.25°$. *(a) Horizontal phase space distribution of the particles located within the current spike (cf. Fig. 8.2). Different colors are used for the two branches. (b) Corresponding distribution in longitudinal phase space using the same color-code. (c, d) Charge density distribution of the two branches in longitudinal phase space. (e, f) Current profiles of the two bunch fractions.*

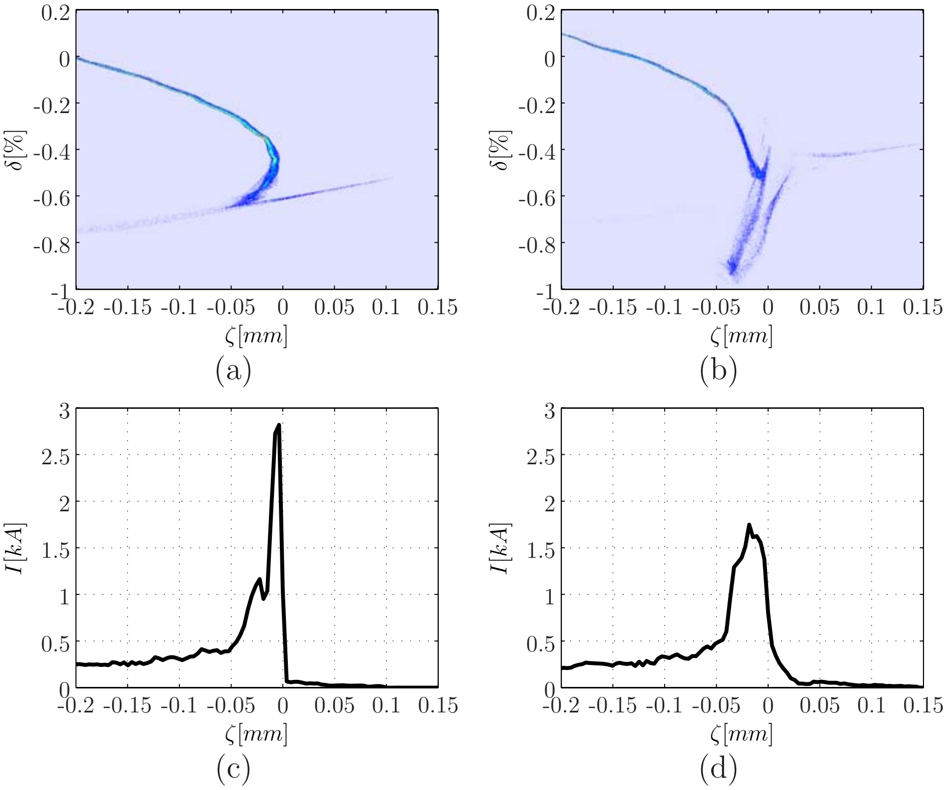

Figure 8.5: Simulated distributions in longitudinal phase space (a) excluding and (b) including CSR in the second bunch compressor. (c, d) Corresponding current profiles.

is an energy loss of the radiating electrons. CSR effects can thus be seen directly in longitudinal phase space (Fig. 8.5). When CSR is excluded in the simulations, the distribution shows hardly deviations from the "ideal shape", which results from bunch compression. A spike towards positive ζ is found due to longitudinal space charge forces upstream of BC3. If CSR is included, the entire bunch fraction in the high current region between $\zeta = 0$ and $\zeta = -0.05$ mm is shifted towards lower energies. As a result, the mean particle energy is reduced. The distribution is additionally deformed since the energy loss varies as a function of longitudinal position and energy. This results in particular in a branch towards lower energies.

Significant effects can also be observed in the current profiles. CSR leads to a reduction of the peak current from about 2.7 kA to 1.7 kA (cf. Fig. 8.5(c) and (d)). At the same time the current spike is broadened. A reduction of the peak current is an important consequence for the dynamics in the remainder of the accelerator, where space charge forces, which sensitively depend on the peak current, play a dominant role. CSR influences the current profile since energy variations within the magnetic chicane affect the path length within the chicane. In this way radiating bunch fractions fall slightly behind. Typically, the emission of CSR is strongest within the last three dipoles (fourth to sixth dipole of the chicane), where the peak current is highest. The induced path length differences are therefore small.

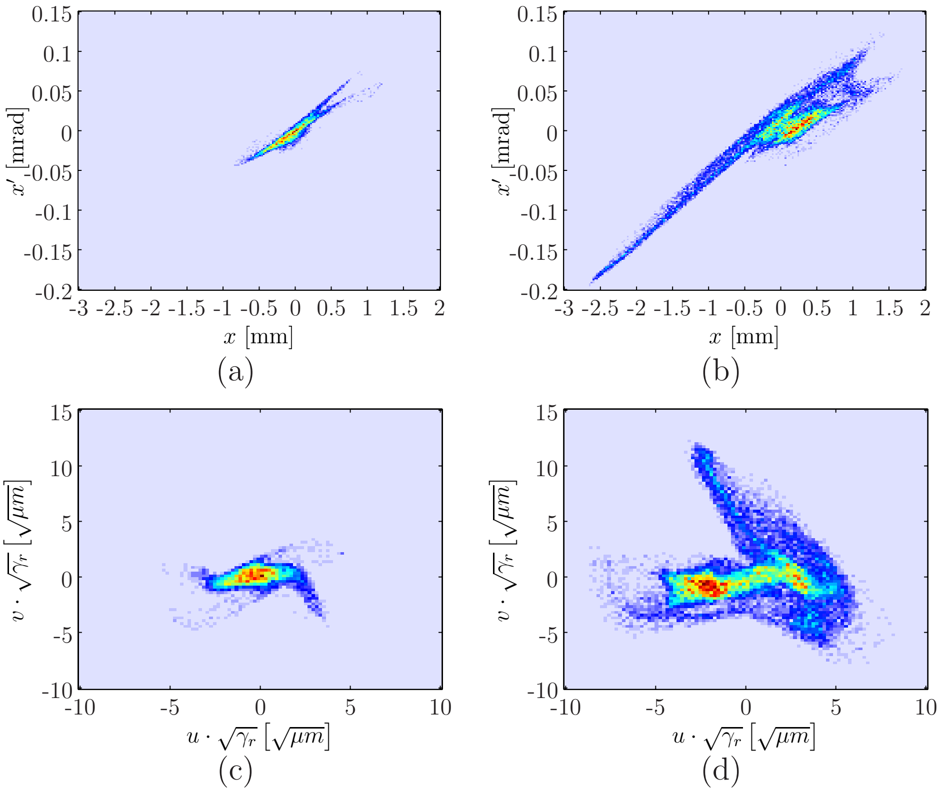

(a) (b)

(c) (d)

Figure 8.6: Effects from CSR in the second bunch compressor BC3 at $\phi_{ACC1} = -8.25°$ on the distribution in horizontal phase space. (a) Charge density distribution in horizontal phase space directly downstream of BC3 if CSR is not included in the simulation. (b) Corresponding distribution if CSR is included. (c, d) Horizontal phase space distribution further downstream at the reconstruction point of the emittance measurements (upstream of module ACC5) excluding and including CSR, respectively. Normalized coordinates are used (cf. section 7.6).

An energy loss within the magnetic chicane leads to changes of the bending angles within the dipole magnets. In this way CSR also affects the charge density distribution in horizontal phase space. CSR in the last dipole primarily leads to a horizontal angle offset $\Delta x'$ of the radiating bunch fractions at the exit of the chicane. CSR in the fourth and the fifth dipole magnet additionally induces a spatial offset Δx. Figure 8.6(a) and (b) show the charge density distribution in horizontal phase space at the exit of the magnetic chicane excluding and including CSR in BC3, respectively. Bunch fractions with huge spatial offsets of up to 2.5 mm and angle offsets of up to 0.2 mrad are found if CSR is included. The largest contribution to these offsets stems from CSR in the fifth dipole of the chicane. The offsets transform into a bifurcation further downstream of the machine (Fig. 8.6(c) and (d)).

The phase space area covered by the particles is significantly increased due to CSR. Correspondingly, a slice emittance of up to 9 μm occurs if CSR is included, compared to maximum values of about 3 μm without CSR (Fig. 8.7(a)). Also horizontal slice centroid offsets can be attributed to CSR in the second bunch compressor. The offsets vanish if CSR is excluded (Fig. 8.7(b)).

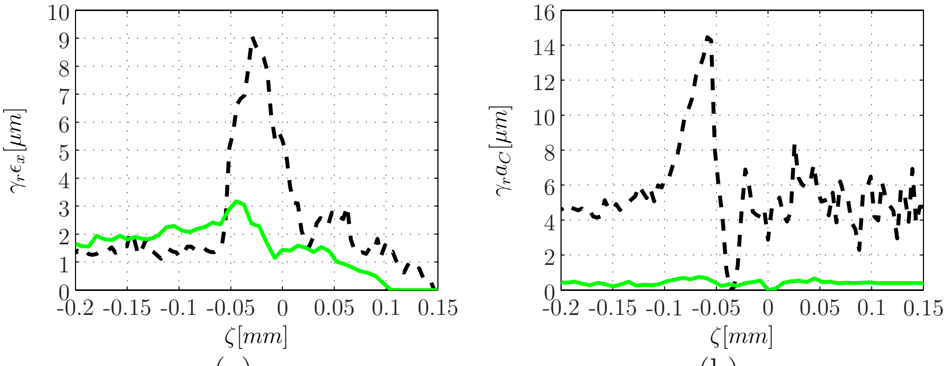

(a) (b)

Figure 8.7: Effects from CSR in the second bunch compressor on slice emittance and centroid offsets. (a) Comparison of the slice emittance which is obtained if CSR in the second bunch compressor is included (black, dashed) and excluded (green, solid), respectively. (b) Corresponding comparison of slice centroid offsets. $\gamma_r a_C$ denotes the offset amplitude as defined in section 7.5.

8.1.3 Discussion

The presented comparison between experimental results and numerical simulations shows that key observations such as a strong increase in slice emittance in the high current region and a bifurcation in horizontal phase space can basically be reproduced in simulations. These distortions were shown to arise largely from CSR in the second bunch compressor. However, the observed slice centroid shifts at the trailing edge of the current spike could not be explained satisfactory, indicating that there may be significant effects which were not included in the simulations.

An exact comparison between simulations and experimental results is difficult in view of the multitude of parameters that affect the beam properties at the position of the measurement. In particular, in turned out that the RF phase of the accelerating module ACC1 needs to be known with an accuracy of $\lesssim 0.1°$ for this purpose.

8.2 Simulation of an emittance measurement under FEL operating conditions

The accuracy of the emittance measurements presented in chapter 7 depends on properties of the electron bunches under investigation. Energy deviations of bunch fractions from the mean energy lead to different focusing effects of the quadrupole magnets and consequently to a different beam transfer. Energy spread is transformed into a spread of the horizontal position by means of the kicker and may thus influence the measurements. Finally, strong transverse space charge forces in the high current region provide a defocusing force, which is not included in the transfer matrices used to determine the emittance and the distribution in horizontal phase space.

In order to investigate the measurement accuracy under FEL operating conditions, the electron distribution obtained from the tracking simulation discussed above ($\phi_{ACC1} = -8.25°$) was taken as an input distribution for a simulation of an emittance measurement. The distribution was tracked to the position of the OTR screen (OTR-2) for all quadrupole settings applied during the corresponding emittance measurement at 494 MeV. The particle tracking was performed by the program ASTRA which takes the detailed energy distribution of the bunch as well as space charge forces into account. The action of the TDS was simulated by inducing a time-dependent vertical deflection at the position of the center of the TDS with the same strength as used in the actual experiment. The kicker was included by adding an energy-dependent horizontal offset Δx to the final distribution at the screen according to $\Delta x = D_x \cdot \delta$ with $D_x \approx 10$ mm. Finally, the transverse particle distributions were converted into digital images with 8 bit intensity resolution and 640×480 pixels of the same size as in case of the recorded images. Gaussian noise with a similar intensity as observed during the measurements was added. Ten images were stored for each setting of the quadrupoles and used as input for the data evaluation programs.

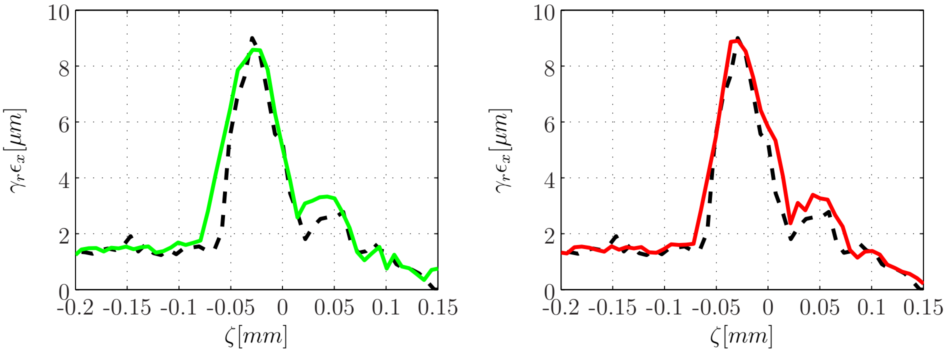

(a) (b)

Figure 8.8: (a) Comparison of the reconstructed slice emittance profile (green, solid) with the original profile of the input distribution (black, dashed) used for the reconstruction. The particle tracking was performed with ASTRA. Space charge forces and effects from the horizontal kicker were included. (b) Reconstructed slice emittance profile using linear transfer matrices for particle tracking (red, solid), and original profile (black, dashed).

Figure 8.8(a) shows a comparison of the reconstructed slice emittance profile with the original slice emittance profile of the input distribution. Nearly perfect agreement between both profiles is obtained in the bunch tail, where energy spread and current are comparably small. Also within the region of the current spike, reconstructed and original slice emittance agree very well, despite of the complicated energy distribution within this region. Around the edges of the current spike, deviations of up to 50 % occur. Similar deviations are found when the linear transfer matrices used for reconstructing the emittance are also used for particle tracking (Figure 8.8(b)). The deviations are thus mainly due to the limited longitudinal resolution of the measurement. Effects from space charge forces and the detailed energy distribution are negligible in the case considered here.

The accuracy of a phase space reconstruction is illustrated in Fig. 8.9(a) - (f). Figure 8.9(a) shows the original horizontal phase space distribution within the region of the current spike (FWHM) in normalized coordinates. A reconstruction of this distribution was simulated using different methods for particle tracking. In order to investigate the accuracy that may principally be obtained, linear transfer matrices were used. The reconstructed distribution (Fig. 8.9(b)) is in very good agreement with the original distribution. The distribution is smeared out due to the limited longitudinal resolution as well as the maximum entropy algorithm used for the tomographic reconstruction.

In order to include the detailed energy distribution of the bunch, particle tracking was performed with ASTRA. If space charge forces and effects from the kicker are excluded, deviations between reconstructed and original distribution mainly occur in the upper branch of the bifurcation in horizontal phase space, which primarily contains low-energy particles

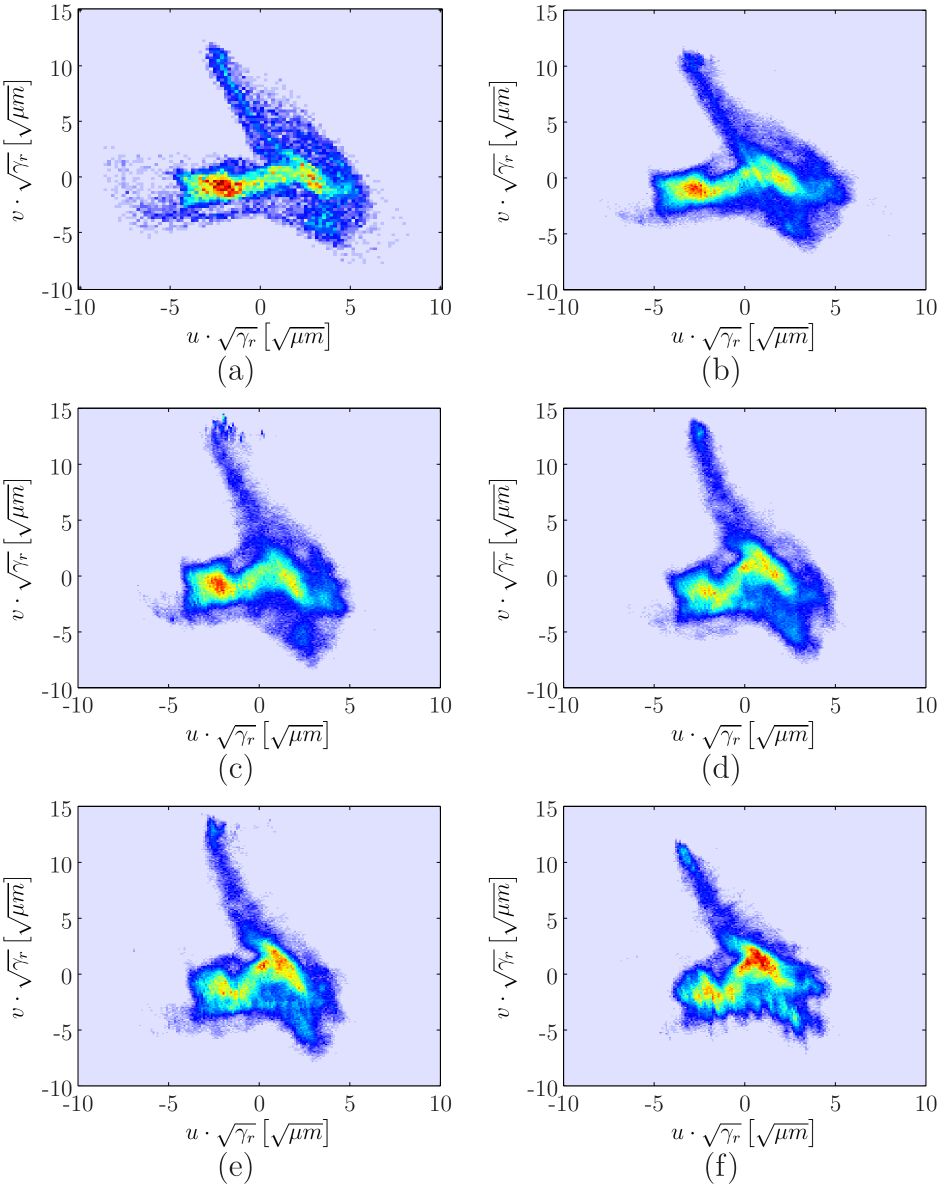

(a) (b) (c) (d) (e) (f)

Figure 8.9: Demonstration of the accuracy of a phase space reconstruction. The horizontal phase space (a) of a test particle distribution was reconstructed using different methods for particle tracking: (b) Linear transfer matrices. (c) Tracking with ASTRA excluding space charge forces. (d) Tracking with ASTRA including space charge forces. (e) Tracking with ASTRA including space charge forces and horizontal dispersion induced by the kicker. (f) Same particle tracking as in (e), but assuming an energy of 2 % below the mean energy for the reconstruction. The charge density scale is the same for all reconstructed distributions. Normalized coordinates are used.

(Fig. 8.9(c)). If space charge forces are included, deviations are also found in the high-density regions of the distribution (Fig. 8.9(d)). Including also the horizontal kicker has no significant influence (Fig. 8.9(e)). In case the mean energy of the bunch is not known precisely, additional reconstruction errors may occur. Fig. 8.9(f) shows the distribution obtained using an energy 2% below the mean bunch energy for the reconstruction.

The presented comparison of reconstructed and original phase space distributions show that the structure of the high-current region in horizontal phase space can be reconstructed with a reasonable accuracy. Errors occur mainly due to energy-dependent focusing in the quadrupoles and space charge forces. Effects from the kicker are negligible. This is related to the fact that bunch fractions of different energy are generated by CSR in the second bunch compressor, which also leads to a separation in horizontal phase space. Under FEL operating conditions, the resulting spatial separations are significantly larger than those induced by the kicker.

Chapter 9

Conclusions and Outlook

A transverse deflecting structure (TDS) installed at the Free-Electron Laser in Hamburg (FLASH) was successfully used to investigate the phase space distribution of electron bunches. Single-shot measurements of the current profile and the distribution in longitudinal phase space were performed with an unprecedented longitudinal resolution on the order of 10 μm and an energy resolution on the order of 10^{-4}. For the first time, the transverse slice emittance (averaged over several bunches) was also measured with a longitudinal resolution of about 10 μm. A maximum entropy algorithm was applied in order to reconstruct the horizontal phase space distribution as a function of the longitudinal position within a bunch.

Experimental results for uncompressed bunches showed a peak current of 40 A to 70 A (depending on the bunch charge) and a bunch length of about 1.6 mm (RMS). A horizonal slice emittance between 1.6 μm and 2.5 μm was measured in the bunch center. The values are significantly below the overall bunch emittance of 3 μm to 4 μm, which was shown to be influenced significantly by slice centroid offsets along the bunch. The difference between overall bunch emittance and slice emittance underpins the necessity of longitudinally resolved measurements. A measurement of the particle distribution in longitudinal phase space clearly displays the nonlinear dependence of the particle energy on the position within the bunch caused by the harmonic time dependence of the RF accelerating field.

Measurements under FEL operating conditions at radiation pulse energies of up to 10 μJ (not saturated) were performed at particle beam energies of 494 MeV, 677 MeV and 964 MeV. Peak currents of up to 2 kA and a width of the leading current spike down to 22 μm (FWHM) were resolved. A measurement of the charge density distribution in longitudinal phase space at 677 MeV revealed structures which can be attributed to longitudinal space charge forces and coherent synchrotron radiation emitted in the dipole magnets of the bunch compressor chicanes. A peak slice energy spread of 1.8 MeV or 0.26 % was measured in the high-current region.

The overall bunch emittance under FEL operating conditions was measured to be > 10 μm. It was found to be significantly influenced by large slice centroid offsets along a bunch. While a slice emittance of 2 to 3 μm was measured in the bunch tail, a surprisingly strong increase in slice emittance in the high current region to more than 10 μm was observed. The apparent contradiction to FEL theory could to a large extent be resolved by a tomographic reconstruction revealing a bifurcated charge density distribution in horizontal phase space with a high-density region. The RMS emittance of this high-density region was estimated to be in the range of 2 to 4 μm. This result demonstrates that due to the complex phase space structure of bunches at FLASH under FEL operating conditions a tomographic reconstruction is essential for an estimate of the emittance of the lasing portion of a bunch. The origin of the structures in horizontal phase space has been identified to be coherent synchrotron radiation in the second bunch compressor with the help numerical simulations.

An appropriate accelerator optics for slice emittance analysis is crucial to obtain a good resolution and accurate results. A corresponding optics was designed for FLASH and investigated in detail. The analysis revealed that great care has to be taken to adapt the optics to the spatial resolution of the imaging system, in particular at large beam energy, small transverse emittance and the possibility of mismatched beams. The RMS error of slice emittance measurements at FLASH including resolution errors, statistical errors, energy errors, and calibration errors of quadrupole magnets and OTR screens was estimated to be < 15 %. In order to push the longitudinal resolution and the accuracy to its limits, a precisely known accelerator optics for FEL operation which simultaneously fulfills the requirements for measurements using the TDS is highly desirable for the future.

Principal limitations of the accuracy of slice emittance measurements and phase space tomography result from machine instabilities, which lead to shot-to shot fluctuations of the phase space distribution. As a consequence, the measured average transverse phase space distribution is diluted. Furthermore, the achieved longitudinal resolution of about 10 μm is still significantly above the coherence length of about 1 μm deduced from a measurement of the gain length at 677 MeV. Finally, a numerical simulation of an emittance measurement under FEL operating conditions showed that transverse space charge forces and the complicated energy distribution in the high current region slightly distort the result of the tomographic reconstruction. An incorporation of transverse space charge effects into the reconstruction by means of a linear approximation might further improve the results.

Appendix A

Abbreviations and color code

Table A.1: Abbreviations repeatedly used in the text.

Abbreviation	Definition
FLASH	Free Electron Laser in Hamburg
TDS	transverse deflecting structure
CSR	coherent synchrotron radiation
SCF	space charge forces
OTR	optical transition radiation
BPM	beam position monitor
RF	radio frequency
FEL	free electron laser
SASE	self-amplified spontaneous emission
BC	bunch compressor
FWHM	full width at half maximum
RMS	root mean square

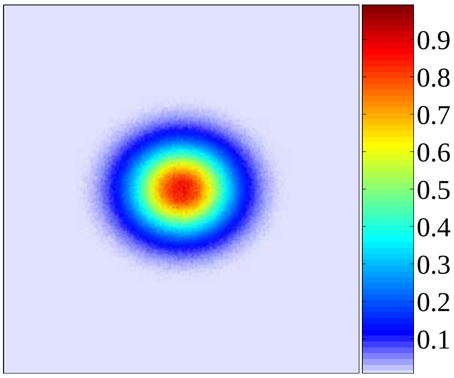

Figure A.1: Color code used in figures of this thesis. The image shows a two-dimensional Gaussian distribution.

Appendix B

Wake fields of the transverse deflecting structure

A bunch of electrons traversing the transverse deflecting structure (TDS) interacts with the conducting wall of the structure. Due to the varying geometry along the structure, an electromagnetic field (geometrical wake field) is generated behind the bunch. The field generated by the head of the bunch acts on the bunch tail (short-range wake field effects), and the field generated by the entire bunch may act on subsequent bunches (long-range wake field effects). Before discussing wake field effects of the TDS, a few concepts need to be introduced.

Consider a charge distribution with total charge q_1 traversing a cylindrically symmetric structure with a transverse offset r_1 parallel to the symmetry axis (z-axis) with the speed of light c. Then the wake potential is defined as [102]

$$W(r_1, \zeta) = \frac{1}{q_1} \int_{-\infty}^{+\infty} dz \left[\mathcal{E}(r_1, z, t) + c e_z \times B(r_1, z, t) \right]_{t=(\zeta+z)/c}, \qquad \text{(B.1)}$$

where $\mathcal{E}$ and B are the electric and magnetic (wake) field, respectively, e_z is the unit vector along the z-axis, and the internal bunch coordinate ζ is measured from the head of the bunch towards its tail. The change of momentum of a test charge q_2 trailing behind the bunch at a distant s on the same path is given by

$$\Delta p(\zeta) = q_1 q_2 W(\zeta). \qquad \text{(B.2)}$$

For a point-like charge q_1, the wake potential is called wake function $w(\zeta)$. The wake potential for an arbitrary charge distribution $\rho(\zeta)$ is given by the convolution with the wake function

$$W(\zeta) = \frac{1}{q_1} \int_{-\infty}^{+\infty} w(\zeta - \zeta')\rho(\zeta')d\zeta'. \tag{B.3}$$

The short-range and long-range wake function of the TDS have been estimated both numerically and analytically in reference [103]. Here, only short-range wake fields are considered. Long-range wake fields are much weaker and not relevant for the measurements presented in this thesis. The longitudinal and transverse short-range wake functions $w_{\parallel}^{0}(\zeta)$ and $w_{\perp}^{1}(\zeta)$, respectively, can be approximated by the expressions [103]

$$w_{\parallel}^{0}(\zeta) \approx 257.6 \cdot \exp\left[-\sqrt{\frac{\zeta}{3.96 \cdot 10^{-3}}}\right] + 1.16 \frac{\cos(1760 \cdot \zeta^{0.72})}{\sqrt{\zeta} + 1600 \cdot \zeta^{1.23}} \left[\frac{V}{pC}\right] \tag{B.4}$$

and

$$\begin{aligned} w_{\perp}^{1}(\zeta) \approx & \quad 10200 \quad \left(1 - \left(1 + \sqrt{\frac{\zeta}{11.7 \cdot 10^{-3}}}\right) \exp\left(-\sqrt{\frac{\zeta}{11.7 \cdot 10^{-3}}}\right)\right) \\ + & \quad 9200\sqrt{\zeta} \left[\frac{V}{pC \cdot m}\right] \end{aligned} \tag{B.5}$$

with $\zeta > 0$. These expressions are the lowest-order terms of a multi-pole series. The transverse wake function $w_{\perp}^{1}(\zeta)$ is normalized by the particle

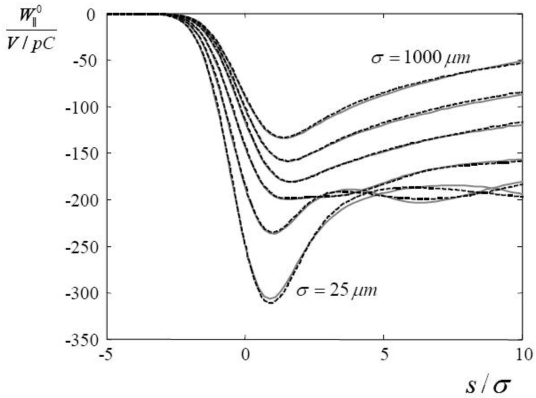

Figure B.1: Comparison of numerical (solid lines) and analytical (dashed lines) longitudinal wake potentials in the TDS for Gaussian bunches with RMS lengths σ of 25,50,100,250,500,1000 μm [103]. The internal bunch coordinate in units of σ is designated by s in contrast to the convention used in this thesis. The head of the bunch is on the left hand side.

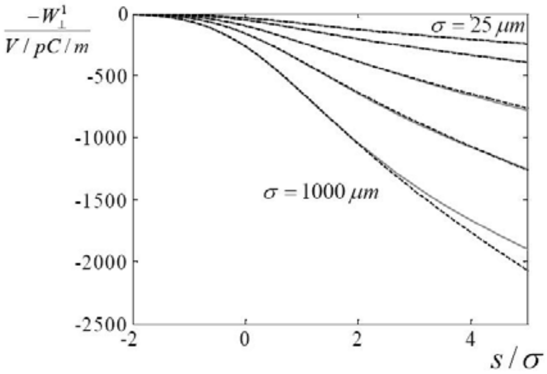

Figure B.2: Comparison of numerical (solid lines) and analytical (dashed lines) transverse wake potentials in the TDS for Gaussian bunches with RMS lengths σ of 25,50,100,250,500,1000 μm [103]. The head of the bunch is on the left hand side.

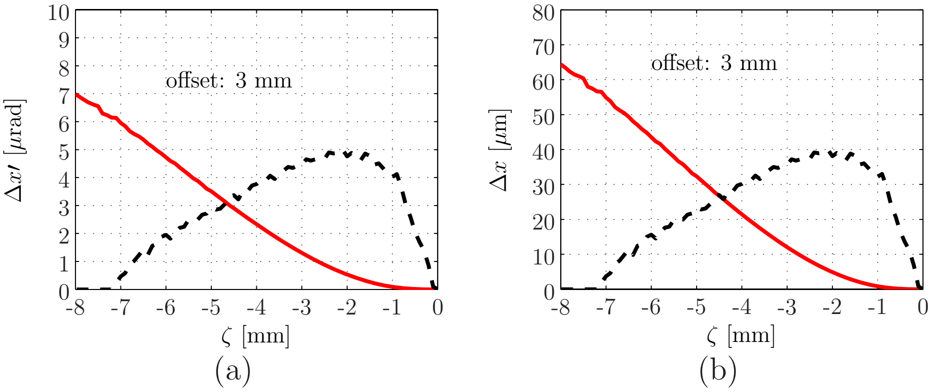

(a) (b)

Figure B.3: Effects from transverse wake fields in the TDS. (a) Horizontal kick $\Delta x'$ (red, solid) as a function of the longitudinal position ζ for a measured current profile (dashed line, arbitrary units) at a bunch charge of 0.67 nC and a beam energy of 490 MeV. (b) Resulting offset Δx at the screen (OTR-2, cf. Fig. 4.8) as a function of ζ (nominal optics). The head of the bunch is on the right hand side.

offset r_1 in the structure, so the change in transverse momentum of a charge q_2 trailing a distance ζ behind a point-like charge q_1 is given by

$$\Delta p_\perp(\zeta) = q_1 q_2 r_1 w_\perp^1(\zeta), \tag{B.6}$$

while the change in longitudinal momentum is given by

$$\Delta p_\parallel(\zeta) = q_1 q_2 w_\parallel^0(\zeta). \tag{B.7}$$

The longitudinal and transverse wake potentials for Gaussian bunches with RMS lengths σ between 25 and 1000 μm are shown in Figs. B.1 and B.2. For a bunch charge of 1 nC and a bunch length $\sigma = 25$ μm, the maximum energy loss of bunch particles due to the longitudinal wake potential is about 300 keV, which is negligible at a typical beam energy of 500 MeV. Significant effects may arise from the transverse wake potential in case of long bunches. For $\sigma = 1$ mm, a bunch charge of 1 nC, and a beam energy of 500 MeV, the transverse (here: horizontal) kick

$$\Delta x' = \frac{\Delta p_\perp}{|p|} \tag{B.8}$$

at the trailing end of the bunch is about 4 μrad per millimeter offset in the TDS. Figure B.3(a) shows the horizontal kick as a function of the longitudinal position ζ for a measured current profile (uncompressed bunch) and a mean horizontal offset of 3 mm in the TDS. In Fig. B.3(b), the corresponding offsets resulting at the screen are shown (nominal optics). A transverse offset of up to 60 μm between head and tail of a bunch is observed. The maximum offsets measured and the screen are typically about four times larger. Since the mean offset within the TDS is typically smaller than 3 mm (the alignment of the structure was found to be accurate within ±1 mm), the contribution from the TDS to slice centroid offsets can be considered small in agreement with the experimental results presented in section 6.5.

Bibliography

[1] W. Ackermann et al. Operation of a free-electron laser from the extreme ultraviolet to the water window. *Nature Photon.*, 1:336–342, 2007.

[2] P. Schmüser, M. Dohlus, and J. Rossbach. *Introduction to Ultraviolet and X-Ray Free-Electron Lasers*. Springer, to be published.

[3] J. D. Jackson. Classical electrodynamics. John Wiley & Sons, 1999.

[4] C. Pellegrini and S. Reiche. Lasers, Free-Electron. Optics Encyclopedia, p. 1111-1134, Wiley-VCH Verlag, Berlin 2003.

[5] E. D. Courant and H. S. Snyder. Theory of the alternating-gradient synchrotron. *Ann. Phys.*, 3:1–48, 1958.

[6] L. A. Pipes. Applied mathematics for engineers and physicists. New York, USA: McGraw-Hill (1958) 723 pp.

[7] H. Wiedemann. Particle accelerator physics: Basic principles and linear beam dynamics. Berlin, Germany: Springer (1993) 445 p.

[8] J. Rossbach and P. Schmüser. Basic course on accelerator optics. In *Jyvaeskylae 1992, Proceedings, General accelerator physics, vol. 1* 17-88. CERN Geneva - CERN-94-01 (94/01,rec.Mar.) 17-88.

[9] O. R. Sander. Transverse emittance: Its definition, applications, and measurement. *AIP Conf. Proc.*, 212:127–155, 1990.

[10] A. W. Chao and M. Tigner. Handbook of accelerator physics and engineering. Singapore, Singapore: World Scientific (1999) 650 p.

[11] T. P. Wangler. Principles of rf linear accelerators. New York, USA: Wiley (1998) 382 p.

[12] P. M. Lapostolle. Possible emittance increase through filamentation due to space charge in continuous beams. (talk). *IEEE Trans. Nucl. Sci.*, 18:1101–1104, 1971.

[13] H. Goldstein. Klassische Mechanik. Akademische Verlagsgesellschaft, 1963.

[14] M. Sands. A beta mismatch parameter. SLAC-AP-085.

[15] P. Castro. Monte carlo simulations of emittance measurements at ttf2. DESY-TECHNICAL-NOTE-2003-03.

[16] M. G. Minty and F. Zimmermann. Measurement and control of charged particle beams. Berlin, Germany: Springer (2003) 364 p.

[17] K. T. McDonald and D. P. Russell. Methods of emittance measurement. In *Capri 1988, Proceedings, Frontiers of particle beams* 122-132. (see HIGH ENERGY PHYSICS INDEX 29 (1991) No. 15582).

[18] V. Bobel and E. Lohrmann. Statistische und numerische Methoden der Datenanalyse. Stuttgart, Teubner (1998) 358 p.

[19] R.L. Branham. Scientific Data Analysis. An Introduction to Overdetermined Systems. New York, Springer-Verlag (1990) 237 p.

[20] C. Gerth, M. Roehrs, and H. Schlarb. Layout of the diagnostic section for the European XFEL. Prepared for Particle Accelerator Conference (PAC 05), Knoxville, Tennessee, 16-20 May 2005.

[21] J. Radon. Über die Bestimmung von Funktionen durch ihre Integralwerte längs gewisser Mannigfaltigkeiten. *Ber. Verh. Saechs. Akad. Leipzig, Math. Phys. Kl.*, 69:262, 1917.

[22] Jack D. Gaskill. Linear Systems, Fourier Transforms, and Optics. New York, John Wiley & Sons (1978).

[23] David W. Townsend and Michel Defrise. Image reconstruction methods in positron tomography. CERN-93-02.

[24] F. Natterer. The Mathematics of Computerized Tomography. Stuttgart, Teubner (1986).

[25] J. J. Scheins. Tomographic reconstruction of transverse and longitudinal phase space distributions using the maximum entropy algorithm. DESY-TESLA-2004-08.

[26] E.T. Jaynes. On the rationale of maximum entropy methods. *Proc. IEEE*, 70:939–952, 1982.

[27] B. R. Frieden. Restoring with Maximum Likelihood and Maximum Entropy. *J. Opt. Soc. Am.*, 62:511, 1972.

[28] A. Papoulis and S. Pillai. Probability, Random Variables and Stochastic Processes. McGraw Hill, 2002.

[29] G. Minerbo. MENT: A Maximum Entropy Algorithm for Reconstructing a Source from Projection Data. *Computer Graphics and Image Processing*, 10:48–68, 1979.

[30] C. T. Mottershead. Maximum entropy beam diagnostic tomography. *IEEE Trans. Nucl. Sci.*, 32:1970, 1985.

[31] Markus Hüning. Analysis of surface roughness wake fields and longitudinal phase space in a linear electron accelerator. DESY-THESIS-2002-029.

[32] Florian Löhl. Measurements of the transverse emittance at the VUV-FEL. DESY-THESIS-2005-014.

[33] V. Yakimenko, M. Babzien, I. Ben-Zvi, R. Malone, and X. J. Wang. Electron beam phase-space measurement using a high- precision tomography technique. *Phys. Rev. ST Accel. Beams*, 6:122801, 2003.

[34] O. R. Sander, G. N. Minerbo, R. A. Jameson, and D. D. Chamberlin. Beam Tomography in Two Dimensions and Four Dimensions. Submitted to 1979 Linear Accelerator Conf., Montauk, N.Y., Sep 10-14, 1979.

[35] G. N. Minerbo, O. R. Sander, and R. A. Jameson. Four-Dimensional Beam Tomography. *IEEE Trans. Nucl. Sci.*, 28:2231–2233, 1981.

[36] Massimo Altarelli et al. XFEL: The European X-Ray Free-Electron Laser. Technical design report. DESY-06-097.

[37] R. Brinkmann et al. TESLA XFEL: First stage of the X-ray laser laboratory. Technical design report, supplement. DESY-02-167.

[38] V. Ayvazian et al. Generation of GW radiation pulses from a VUV free-electron laser operating in the femtosecond regime. *Phys. Rev. Lett.*, 88:104802, 2002.

[39] V. Ayvazian et al. A new powerful source for coherent VUV radiation: Demonstration of exponential growth and saturation at the TTF free-electron laser. *Eur. Phys. J.*, D20:149–156, 2002.

[40] SASE FEL at the TESLA facility, phase 2. DESY-TESLA-FEL-2002-01.

[41] H. Schlarb. Collimation system for the VUV free-electron laser at the TESLA test facility. DESY-THESIS-2001-055.

[42] S. Schreiber. First lasing at 32-nm of the VUV-FEL at DESY. 2005.

[43] S. Schreiber et al. Experience with the photoinjector laser at FLASH. Prepared for 28th International Free Electron Laser Conference (FEL 2006), Berlin, Germany, 27 Aug - 1 Sep 2006.

[44] K. Abrahamian et al. Experimental characterization and numerical simulations of the electron source at PITZ. *Nucl. Instrum. Meth.*, A558:249–252, 2006.

[45] H. Schlarb, N. Heidbrook, H. Kapitza, F. Ludwig, and N. Nagad. Precision RF gun phase monitor system for the VUV-FEL. Prepared for European Particle Accelerator Conference (EPAC 06), Edinburgh, Scotland, 26-30 Jun 2006.

[46] J. H. Han, M. Krasilnikov, and K. Flottmann. Secondary electron emission in a photocathode rf gun. *Phys. Rev. ST Accel. Beams*, 8:033501, 2005.

[47] S. Schreiber. Commissioning of the VUV-FEL injector at TTF. Prepared for 9th European Particle Accelerator Conference (EPAC 2004), Lucerne, Switzerland, 5-9 Jul 2004.

[48] K. Abrahamian et al. Characterization of the electron source at the photo injector test facility at DESY Zeuthen. *Nucl. Instrum. Meth.*, A528:360–365, 2004.

[49] J. Rosenzweig and L. Serafini. Transverse particle motion in radio-frequency linear accelerators. *Phys. Rev. E*, 49(2):1599–1602, Feb 1994.

[50] B. Aune et al. The superconducting TESLA cavities. *Phys. Rev. ST Accel. Beams*, 3:092001, 2000.

[51] H. Padamsee, J. Knobloch, and T. Hays. RF superconductivity for accelerators. New York, USA: Wiley (1998) 523 p.

[52] P. Schmüser. Superconductivity in high energy particle accelerators. *Prog. Part. Nucl. Phys.*, 49:155–244, 2002.

[53] P. Castro. Beam trajectory calculations in bunch compressors of TTF2. DESY-TECHNICAL-NOTE-2003-01.

[54] M. Dohlus, T. Limberg, and P. Emma. Bunch compression for linac-based FEL's. Electron bunch length compression. *ICFA Beam Dyn. Newslett.*, 38:15–37, 2005.

[55] K. Flöttmann. Astra user manual. http://www.desy.de/ mpy/ astra dokumentation.

[56] M. Dohlus, A. Kabel, and T. Limberg. Efficient field calculation of 3D bunches on general trajectories. *Nucl. Instrum. Meth.*, A445:338–342, 2000.

[57] E. L. Saldin, E. A. Schneidmiller, and M. V. Yurkov. On the coherent radiation of an electron bunch moving in an arc of a circle. *Nucl. Instrum. Meth.*, A398:373–394, 1997.

[58] Frank Stulle. A bunch compressor for small emittances and high peak currents at the VUV Free-Electron Laser. DESY-THESIS-2004-041.

[59] J. Pfluger, U. Hahn, B. Faatz, and M. Tischer. Undulator system for the VUV-FEL at the TESLA Test Facility phase-2. *Nucl. Instrum. Meth.*, A507:228–233, 2003.

[60] C. Martens. Status of the TTF-2 Collimator Section. Presentation, Salzau, 2003.

[61] A. Koski, R. Bandelmann, and S. Wolff. Superconducting magnet package for the TESLA test facility. *IEEE Trans. Magnetics*, 32:2155–2158, 1996.

[62] J. Fusellier and J. M. Joly. Beam intensity monitoring and machine protection by toroidal transformers on the TESLA Test Facility. Prepared for 5th European Particle Accelerator Conference (EPAC 96), Sitges, Spain, 10-14 Jun 1996.

[63] H. Schlarb. private communication.

[64] J. Lund-Nielsen, N. Baboi, and W. Reisch. Button beam position monitors for FLASH. To be published in the Proceedings of 8th European Workshop on Beam Diagnostics and Instrumentation for Particle Accelerators (DIPAC 2007), 20-23 May 2007, Venice, Italy.

[65] D. Nölle and M. Wendt. TTF2 Beam Monitors for Beam Position, Bunch Charge and Phase Measurements. Proceedings of LINAC 2004, Lbeck, Germany.

[66] D. A. Edwards. TESLA Test Facility Linac: Design report. Version 1.0, March 1, 1995. DESY-TESLA-95-01.

[67] M.A. Geitz. Investigation of the transverse and longitudinal beam parameters at the TESLA test facility linac. DESY-THESIS-1999-033.

[68] M. Castellano and V. A. Verzilov. Spatial resolution in optical transition radiation (OTR) beam diagnostics. *Phys. Rev. ST Accel. Beams*, 1:062801, 1998.

[69] V. A. Lebedev. Diffraction-limited resolution of the optical transition radiation monitor. *Nucl. Instrum. Meth.*, A372:344–348, 1996.

[70] X. Artru et al. Experimental investigations on geometrical resolution of optical transition radiation (OTR). *Nucl. Instrum. Meth.*, A410:148–158, 1998.

[71] B. Schmidt. private communication.

[72] M. Castellano, V. A. Verzilov, and L. Catani. Spatial resolution of the optical systems for beam profile measurements at TTF. DESY-TESLA-2001-24.

[73] V. L. Ginzburg and V. N. Tsytovich. Several Problems of the Theory of Transition Radiation and Transition Scattering. *Phys. Rept.*, 49:1–89, 1979.

[74] K. Honkavaara. Optical Transition Radiation in High Energy Electron Beam Diagnostics. Helsinki Institute of Physics. Internal report HIP-1999-04.

[75] A. Bychkov et al. Development of MCP-based photon diagnostics at the TESLA Test Facility at DESY. *Nucl. Instrum. Meth.*, A528:254–257, 2004.

[76] K. Honkavaara et al. Design of OTR beam profile monitors for the TESLA Test Facility, phase 2 (TTF2). Prepared for Particle Accelerator Conference (PAC 03), Portland, Oregon, 12-16 May 2003.

[77] A. Cianchi et al. Commissioning of the OTR beam profile monitor system at the TTF / VUV-FEL injector. Presented at the 9th European Particle Accelerator Conference (EPAC 2004), Lucerne, Switzerland, 5-9 Jul 2004.

[78] Andy Bolzmann. Investigation of the longitudinal charge distribution of electron bunches at the VUV-FEL using the transverse deflecting cavity LOLA. DESY-THESIS-2005-046.

[79] Magnet data base of FLASH.

[80] M. Schlösser. private communication.

[81] H. Schlarb. Horizontal kicker and cable distribution. Electronic Logbook of FLASH.

[82] Otto H. Altenmueller, Rudolf R. Larsen, and G. A. Loew. Investigation of traveling wave separators for the stanford 2-mile linear accelerator. SLAC-0017.

[83] W. K. H. Panofsky and W. Wenzel. Some considerations concerning the transverse deflection of charged particles in radiofrequency fields. *Rev. Sci. Instrum.*, 27:967, 1956.

[84] L. Lilje and P. Schmüser. Superconducting rf. http://hep.uchicago.edu/ kwangje/LectureNotes_Lilje.pdf.

[85] J. Le Duff. Dynamics and acceleration in linear structures. Prepared for CERN Accelerator School: Introduction to Accelerator Physics, Loutraki, Greece, 2-13 Oct 2000.

[86] G. A. Loew and R. Talman. Elementary principles of linear accelerators. Presented at 2nd Summer School on High Energy Particle Accelerators, Stanford, CA, Aug 2-13, 1982.

[87] M. Nagl. Physics of the transverse r.f. deflecting structure. Presentation at DESY, 2004.

[88] G. A. Loew and Otto H. Altenmueller. Design and applications of rf separator structures at slac. Paper presented at the fifth Int. Conf. on High-Energy Accelerators, Frascati, Italy, 1965.

[89] P. Emma, J. Frisch, and P. Krejcik. A transverse rf deflecting structure for bunch length and phase space diagnostics. LCLS-TN-00-12, 2000.

[90] L. B. Lucy. An iterative technique for the rectification of observed distributions. *Astron. J.*, 79:745, 1974.

[91] The MathWorks. Image processing toolbox. 3.1 edition, 2001.

[92] H. Grote and F. C. Iselin. Recent developments in MAD: Version 8. *Nucl. Instrum. Meth.*, A293:464–467, 1990.

[93] X. Qiu, K. Batchelor, I. Ben-Zvi, and X-J. Wang. Demonstration of emittance compensation through the measurement of the slice emittance of a 10-ps electron bunch. *Phys. Rev. Lett.*, 76(20):3723–3726, May 1996.

[94] M. Dohlus. Modelling of space charge and CSR effects in bunch compressor systems. Prepared for European Particle Accelerator Conference (EPAC 06), Edinburgh, Scotland, 26-30 Jun 2006.

[95] H. Schlarb et al. Beam Based Measurements of RF Phase and Amplitude stability at FLASH. Proceedings of the DIPAC 2007, Venice, Italy.

[96] E. L. Saldin, E. A. Schneidmiller, and M. V. Yurkov. FAST: Three-dimensional time-dependent FEL simulation code. *Nucl. Instrum. Meth.*, A429:233–237, 1999.

[97] M. Dohlus. Two methods for the calculation of CSR fields. DESY-TESLA-FEL-2003-05.

[98] M. Dohlus et al. Start-to-end simulations of SASE FEL at the TESLA Test Facility, phase 1. *Nucl. Instrum. Meth.*, A530:217–233, 2004.

[99] M. Dohlus. CSRtrack Version 1.2 Users Manual. http://www.desy.de/xfel-beam/csrtrack.

[100] M. Dohlus and T. Limberg. Calculation of coherent synchrotron radiation in the TTF- FEL bunch compressor magnet chicanes. *Nucl. Instrum. Meth.*, A407:278–284, 1998.

[101] T. Limberg and M. Dohlus. Impact of optics on csr-related emittance growth in bunch compressor chicanes. Prepared for Particle Accelerator Conference (PAC 05), Knoxville, Tennessee, 16-20 May 2005.

[102] T. Weiland and R. Wanzenberg. Wake fields and impedances. *Lect. Notes Phys.*, 400:39–79, 1992.

[103] I. Zagorodnov, T. Weiland, and M. Dohlus. Wake fields generated by the LOLA-IV structure and the 3rd harmonic section in TTF-II. DESY-TESLA-2004-01.

Acknowledgments

First of all, I would like to thank Prof. Dr. P. Schmüser and Prof. Dr. G. Mack for their effort in supervising my PhD thesis, and for their great support in particular during the final stage of this thesis. I am grateful to Prof. Dr. P. Schmüser and Dr. B. Schmidt for providing the opportunity to work on a very interesting subject, and for their aid and encouragement during this time.

I want to express may gratitude to Dr. H. Schlarb for advising me during my thesis, and for introducing me to the field of accelerator physics and to the FLASH facility. His many ideas and his support substantially contributed to the outcome of this work.

I very much appreciate the enjoyable collaboration with Dr. C. Gerth, who greatly supported me at various occasions, in particular during the measurements and during the final stage of my thesis.

Thanks goes to F. Löhl for providing a convenient interface for using the computer code for tomographic reconstructions, and for fruitful discussions about related issues. I want to thank B. Polzin, Dr. V. Kocharyan and Dr. B. Steffen for support related to the "LOLA-camera", and Dr. E.A. Knabbe, U. Djuanda, G. Grygiel and Dr. J. Menzel for support in computer issues. I thank A. Bolzmann for introducing me into details on the transverse deflecting structure and the experimental setup, and Dr. M. Hüning and R. Jonas for providing technical support for operating "LOLA". Thanks goes also to Dr. M. Dohlus, Dr. I. Zagorodnov, Dr. K. Flöttmann and Dr. B. Beutner for showing me how to use the computer codes for numerical simulations. I want to thank I. Nikodem for her help in organizational issues.

I am indebted to Prof. Dr. J. Rossbach for supporting the presentation of my work at international conferences. Special thanks goes to Dr. T. Limberg and Dr. W. Decking for organizing a stay at LCLS at SLAC, and Dr. P. Emma, Dr. H. Loos and the entire LCLS team for their great hospitality and the possibility to gain insight into their work.

I am grateful to Dr. C. Gerth, Dr. H. Schlarb and K. Hacker for reading my manuscript and helping to improve it, both in content and language.

For fruitful discussions I want to thank (aside from the people mentioned above) E. Prat, Dr. B. Faatz, Dr. K. Honkavaara, Dr. S. Schreiber, Dr. A. Winter, Dr. E. Schneidmiller, H. Delsim-Hashemi, L. Fröhlich, Dr. M. Yurkov, Dr. P. Craievich, Dr. R. Brinkmann, M. Schlösser and Dr. F. Stephan.

I would like to thank the entire FLASH team for enabling me to do experiments at a fascinating facility. Special thanks goes to Dr. B. Faatz and Dr. K. Honkavaara for providing always enough time for performing the experiments.

Finally, I would like to thank my family and my girlfriend Antje Krüger for their moral support.